Sea ice effects on the upper ocean: internal waves, ice-covered gyres and the seasonal ice zone.



Kevin Thielen
Wadham College
University of Oxford

A thesis submitted for the degree of
Doctor of Philosophy

Trinity 2021

Andrew made me decide between watching ice melt or paint dry.
He then taught me how to see that both were fascinating.

Acknowledgements

The list of people who helped make this thesis as it is seen here is longer than the actual thesis. The most significant of which, is my supervisor Andrew Wells whose patience I've empirically determined to be endless. You allowed me to explore topics far afield from whatever the intended scope of this thesis used to be. Without your infectious curiosity and patient indulgence this thesis would not be what it's.

Further thanks due to colleagues and friends within AOPP and the ocean-climate group as well as within Wadham College who supported me in my intellectual and personal growth - Jamie, Joe, Joel, Jules, and Marcus in particular. The Polar Glider group at the University of Gothenburg who graciously welcomed me into their team and broadened my scientific horizons: Louise, Marcelle, Seb, Martin, and Isabelle. Thanks as well to all those involved in the ROAM MIZ Project, especially the crew of the S. A. Agulhas II.

For funding this experience and allowing me to experience a number of once in a lifetimes - Thanks to the Swedish Fulbright Commission who made my stay in Sweden possible and as a result greatly shaped the content of this thesis. Similarly, I would not have been able to pursue this degree in any form without the generous financial support of the David Richards Scholarship in Climate Research and Wadham College.

To my previous teachers whether at my Undergraduate - Eckerd College, or before, thank you for fostering in me an intellectual curiosity which has allowed me to ultimately find a way through this thesis: Stephen Weppner, Nazarré Merchant, Walter Walker, Eduardo Fernandez, Anne Cox, Harry Ellis, Donna Oglesby, Susan Harris, Michael Brooks, Stephen Foster, Coach Harder, and so many others.

A more intimate thanks to my family - Mom, Dad, Michael, Matthew and the kids, Aunt Cebby and Uncle Robert for providing me with emotional support and grounding.

And lastly, to my partner Sidney who has put up with moving across multiple countries multiple times over multiple years, thank you.

Abstract

The polar oceans are currently experiencing significant changes. Arctic and Antarctic sea ice extent and volume are changing, with a poorly constrained implication for future climate. Understanding the interactions between sea ice and the underlying ocean is fundamental for understanding current changes, and predicting future ice-states.

In this thesis I study several aspects of the under-ice boundary layer and the coupling to the deeper polar ocean. First I conduct numerical simulations of fluid flow using the Lattice Boltzmann Method to investigate the effects of stratification and roughness on ice-ocean drag and heat flux below a ridged ice floe overlaying a stably stratified ocean. It is found that sea ice generated internal waves can cause order of magnitude variations in the simulated drag coefficient and modest variations in area-integrated heatflux and its spatial distribution.

A parameterization is developed for wave drag as a scaling law in terms of upper ocean velocity, stratification, and ridge geometry. To understand the potential impact, this parameterization is applied to an idealized conceptual model of an ice-covered ocean gyre. The model extends previous descriptions of ocean density variation subject to applied wind stress to account for ice-ocean wave drag and a simple treatment of ocean surface stress redistribution within the ice via a viscous ice rheology. I find that in certain stratification regimes, inclusion of internal wave effects significantly alters ice-velocity and ice-ocean stress with implications for the freshwater content of the gyre.

I also explore how seasonal variations in ice cover impact the water mass properties of the Southern Ocean. A 1D ice-ocean model is adapted and compared to oceanographic float observations in the Antarctic seasonal ice zone. I find that Ekman upwelling has a leading order impact on the seasonal evolution of the upper ocean water masses and stratification.

Contents

1 Introduction **1**

1.1 Thesis structure and motivation . . . 3
1.2 Sea ice . . . 6
1.2.1 Formation of sea ice . . . 7
1.2.2 Evolution of sea ice . . . 8
1.3 Turbulent boundary layers . . . 11
1.3.1 Boundary layer theory . . . 11
1.3.1.1 Reynolds fluxes . . . 12
1.3.2 Oceanic boundary layer . . . 13
1.3.2.1 Rotational effects . . . 14
1.3.2.2 Wind and wave driven ocean . . . 16
1.3.2.3 Buoyancy driven flow . . . 17
1.3.3 Under ice boundary layer . . . 20
1.3.3.1 Ice-ocean buoyancy fluxes . . . 21
1.3.3.2 Ice-ocean momentum flux . . . 22
1.4 Summary . . . 24

2 Lattice Boltzmann Method **26**

2.1 Theory . . . 27
2.1.1 Lattice Bhatnagar-Gross-Krook model . . . 29
2.1.2 Scalar fields in the LBM . . . 30
2.2 Discretization of the physical system . . . 32
2.2.1 Understanding error: choosing Δx_{lb} and Δt_{lb} . . . 34
2.3 Boundary conditions . . . 35
2.3.1 No-slip no-penetration condition . . . 35
2.3.2 Boundary condition with known velocity . . . 36
2.3.3 Isothermal boundary conditions . . . 37
2.3.4 Absorbing boundary conditions . . . 38

2.4 Parallel implementation . . . 39
2.5 Computational algorithm . . . 40
2.6 Benchmarking . . . 41
2.6.1 Flow around a cylinder asymmetrically placed in a channel . . . 41
2.6.2 Rayleigh-Bénard . . . 45
2.7 Summary . . . 46

3 Sea ice generated internal waves: effects on ice-ocean heat and momentum balance 48
3.1 Stratified shear flow over topography (SSFOT) . . . 49
3.1.1 Theoretical developments of SSFOT . . . 49
3.1.1.1 The Taylor-Goldstein equation . . . 50
3.1.1.2 Long's model . . . 52
3.1.2 Atmospheric development of SSFOT . . . 55
3.1.3 Oceanic SSFOT . . . 56
3.1.4 Under ice internal wave generation . . . 58
3.1.5 Summary of SSFOT background . . . 62
3.2 Internal wave generation under a ridged summer ice floe . . . 64
3.2.1 Schematic . . . 64
3.2.2 Mathematical setting . . . 67
3.2.3 Simulation calibration . . . 70
3.3 Results . . . 72
3.3.1 Simulation flow field . . . 73
3.3.2 Drag results . . . 80
3.3.3 Ice-ocean heat flux . . . 85
3.3.4 Sensitivity to ridge geometry and position . . . 98
3.4 Summary and future work . . . 101

4 The effects of internal wave drag and ice rheology on an ice-covered gyre 106
4.1 The Beaufort Gyre . . . 109
4.2 Sea ice rheology . . . 114
4.3 Idealized model of Beaufort Gyre structure . . . 118
4.3.1 Transformed Eulerian mean framework . . . 119
4.4 The steady state gyre . . . 122
4.4.1 Effects of internal wave drag and sensitivity . . . 124
4.5 Rheological model . . . 131

4.5.1 Model derivation . . . 131
4.5.2 Robin boundary condition physical interpretation . . . 133
4.5.3 Parameter values for rheological model . . . 134
4.5.4 Rheology model with linear drag . . . 134
4.5.5 Rheological model with quadratic drag . . . 137
4.5.6 Sensitivity of idealized rheological model. . . . 139
4.6 Summary . . . 152
4.A Coupled ice-ocean model . . . 159
4.A.1 Description of coupled model Algorithm . . . 159
4.A.2 Coupled ice-ocean model results. . . . 161

5 Seasonal evolution of upper ocean water masses in the Antarctic seasonal ice zone 165
5.1 Introduction . . . 165
5.1.1 1D ocean models . . . 166
5.1.2 Water masses of the Antarctic seasonal ice zone . . . 168
5.2 Data acquisition and processing . . . 171
5.2.1 SOCCOM Floats . . . 171
5.2.2 Ice concentration . . . 173
5.2.3 Atmospheric forcing . . . 175
5.3 Observations of the seasonal evolution . . . 175
5.4 1D ice ocean model . . . 179
5.4.1 Open Ocean Exchanges . . . 180
5.4.2 Sea ice model . . . 182
5.4.3 Mixed Layer Model . . . 185
5.4.4 Model Parameters and Initialization. . . . 189
5.5 Model Results . . . 191
5.5.1 Model Sensitivity . . . 199
5.6 Conclusion . . . 204

6 Conclusions 207
6.1 Summary of scientific results . . . 208
6.1.1 Effects of sea ice generated internal waves on the ice-ocean boundary layer . . . 208
6.1.2 Effects of internal wave drag and rheology on the vertical structure of the Beaufort Gyre. . . . 211

6.1.3 Seasonal evolution of upper ocean water masses in the Antarctic seasonal ice zone 213
6.1.4 Future work and broader perspectives 215

Bibliography **219**

Chapter 1

Introduction

Covering about 12% of the Earth's oceans and 7% of its surface (Weeks, 2010), sea ice is a fundamental component of the Earth system. Formed by the freezing of ocean water, the sea ice covered polar oceans are disproportionately affected by anthropogenic climate change (Pithan and Mauritsen, 2014) and currently undergoing significant changes in ice-state.

Satellite measurements show that Arctic sea ice is declining rapidly. Over the past 40 years, September sea ice extent[1] of the Arctic has decreased at a rate of 13.4% per decade relative to the 1981 to 2020 average (National Snow and Ice Data Center, 2020). Alongside the shrinking areal coverage, the ice thickness, and hence ice volume has also been in decline (Kwok and Untersteiner, 2011). Over 8 trillion tonnes of sea ice has been lost since 1979 (Slater et al., 2021). Due to this decline, some predictions suggest a seasonally ice-free Arctic ocean will occur as early as the middle of this century (Guarino et al., 2020; Holland et al., 2006). Antarctic sea ice extent has until recently stood in contrast to this pattern. A positive increase in ice extent (Parkinson and Cavalieri, 2012) was suddenly reversed in 2014 (Parkinson, 2019) with a 40 year low occurring in 2017. The multi-decadal increase in Antarctic sea ice and the subsequent collapse have yet to be fully characterized (Roach et al., 2020).

These changes in sea ice volume and extent heavily influence a number of environmental processes such as large scale ocean and atmospheric circulation (Williams et al., 2016; Vihma, 2014), as well as the stability of high latitude ecosystems (Kahru et al., 2016; Hamilton et al., 2015). Furthermore, understanding the factors driving changes in ice-state is essential in order to make informed decisions about topics ranging from emissions regulations (Notz and Stroeve, 2016) and shipping routes (Melia

[1]Extent is not the same as sea ice area. Extent defines a region as "ice-covered" or "not ice-covered." For satellite data, extent refers to the total area of ice-covered data cells.

et al., 2016) to those of governance (Nuttal, 1998) and resource extraction (Harsem et al., 2011). In this thesis we will exam a number of understudied processes that are both subject to, and feedback on the observed changes in ice-state. Specifically we focus on exchanges of heat, salt and momentum within the ice-ocean boundary layer and corresponding impacts on key features of the polar oceans: the Beaufort Gyre, and the Antarctic Seasonal Ice Zone.

The main pathway for sea ice to affect climate is via modifications of the typical pathways for air-sea exchanges of heat, salt, momentum, and various tracers. The atmosphere and ocean exert a stress on sea ice which then sets it into motion. The difference between the ice velocity and the underlying ocean current then sets the ocean surface stress. A number of processes further influence this process such as sea ice roughness due to floe edges, melt ponds or pressure ridges, internal stresses within the ice, viscous skin drag, and generation of internal waves (Tsamados et al., 2014). In most models of the air-sea-ice interface the internal wave drag is neglected and a drag coefficient is either calculated based on the other factors (as in Tremblay and Mysak (1997); Steiner et al. (1999); Tsamados et al. (2014) or is held to be a constant (Hibler, 1979). Understanding how these processes of sea ice which determine the ice-ocean drag have changed alongside the observed change in sea ice volume is important for predictions of future climate (Martin et al., 2016; Castellani et al., 2018).

Understanding the processes that set the air-sea-ice surface stress is also relevant for understanding the ice-ocean heat flux (Tsamados et al., 2014). The Arctic sea ice cover in particular is known to be sensitive to small increases in basal heat flux to the ice with a change from 1 to 2 W m^2 resulting in a change in the equilibrium ice state thickness of 1 m yr^{-1} (Kwok and Untersteiner, 2011). In the Arctic, cold fresh surface water is underlain by warm salty North Atlantic water at depth. If mixed upward, the warm Atlantic water possesses enough heat to melt the entire sea ice cover (Polyakov et al., 2020b,a). Variations in the turbulent momentum flux from changing ice characteristics are then of great importance for determining the rates of upward mixing of heat stored at depth.

The commonly excluded contribution of internal wave drag of sea ice is known to correlate with changes in heat and momentum fluxes at the ice-ocean interface (Skyllingstad et al., 2003; McPhee and Kantha, 1989; Cole et al., 2018). Improving the understanding of internal wave processes under sea ice is thus important for understanding the sea ice state both in the present and in the future. Furthermore, modifications to the drag coefficient on local scales may influence large scale polar processes such as the structure of the Beaufort Gyre in the Arctic Ocean (Meneghello

et al., 2018b; Proshutinsky et al., 2009b; Manucharyan et al., 2016; Doddridge et al., 2019) or water-mass transformation in the Antarctic Ocean (Abernathey et al., 2016; Pellichero et al., 2017, 2018).

The Beaufort Gyre is a large anticyclonic ocean circulation in the Arctic Ocean (Manucharyan et al., 2016; Manucharyan and Spall, 2016; Meneghello et al., 2018b; Doddridge et al., 2019; Timmermans and Marshall, 2020). The atmospheric wind pattern drives a surface stress which in turn drives the accumulation of fresh Arctic surface waters within the gyre via lateral Ekman transport at the surface (Proshutinsky et al., 2009b). As a result of this persistent forcing, the gyre is the largest reservoir of freshwater in the Arctic Ocean (Proshutinsky et al., 2019). Periodically the accumulated freshwater can be released at depth, which has the potential to influence deepwater formation and in turn affect the Atlantic meridional overturning circulation (Proshutinsky et al., 2002). Alterations to the processes that set sea ice drag or affect the ice-ocean state are thus important for setting both the rate of fresh water accumulation within the gyre and its equilibrium state.

In the Antarctic, sea ice formed close to the continent is transported northwards towards the equator (Sun and Eisenman, 2021). This formation and subsequent seasonal freshwater transport has been suggested to play a key role in the global overturning ocean circulation (Abernathey et al., 2016). Furthermore, the northward transport and subsequent melt of sea ice combines with surface heat fluxes to set up meridional buoyancy gradients in the ice-influenced Southern Ocean, which in turn set up patterns of water-mass transformation (Pellichero et al., 2018). The ocean stress field created by this northward transportation of sea ice may also create regions of vertical upwelling or downwelling with the potential to further affect water-mass transformation.

Each of the above processes are fundamental for the climate system. Understanding understudied small scale processes of the under-ice boundary layer and their potential impact on the large scale ocean features will be the core of this work. With this we proceed to outline the specific trajectory taken within the thesis.

1.1 Thesis structure and motivation

This thesis aims to tackle a number of topics relevant to the relationship between sea ice, the underlying oceanic mixed layer, and wider consequences for the evolution of the deeper ocean. This is an area of increasing research activity (Peterson et al., 2017; Neggers et al., 2019; Parkinson, 2019; Timmermans and Marshall, 2020; Lee,

2020; Brenner et al., 2020) due in part to the relatively recent development of novel observational methods such as ice mass-balance buoys (Planck et al., 2019), ice-tethered profilers, and others (Swart et al., 2019; Toole et al., 2010; Charrassin et al., 2008). The theoretical development of the under-ice boundary layer is slightly older and most completely laid out in McPhee (2008).

This chapter will serve as an introduction and broad literature review to the shared topics of this multifaceted thesis. We will overview the broad topics of sea ice formation and evolution, as well as the relevant aspects of boundary layer theory as it applies to the oceanic and under ice boundary layers. Later chapters will focus on a specific scientific question and contain a more detailed literature review of the particular subjects dealt with.

In chapter 2, we develop the computational framework to be used for simulating fluid flow in the upper ocean in chapter 3, which uses the Lattice Boltzmann method (Succi, 2001; Mohamad, 2011). The overarching theory of the approach as well as the particular implementation and relevant boundary conditions are discussed in §2.1 through §2.3 and the parallelization scheme implemented is described in §2.4. The logical structure of the computational algorithm is outlined in §2.5 and a summary wraps up the chapter in §2.6 with a number of benchmark problems to validate the various aspects of the written code.

Chapter 3 tackles the first research topic on the interaction between large scale sea ice roughness, such as pressure ridges, and the under-ice boundary layer. In the summer melt period, this setting becomes one of a stably stratified flow beneath a rough boundary. The resulting turbulent fluxes of heat and momentum are important for determining sea ice melt rates, and the ocean surface stress. Using computational simulations, I examine the interactions between stratification and sea ice roughness along with resultant impacts on ice-ocean heat and momentum fluxes. In §3.1 I present an overview of the field of stratified shear flow, reviewing the prevailing theoretical framework as well as previous research related to stratified shear flows in the atmosphere and ocean. Following this literature review, in §3.2 we consider internal wave generation by sea ice roughness in stably stratified ocean flow. In §3.3 I find that, due to internal wave generation, the drag coefficient follows a power law relationship dependent on stratification strength, roughness scale, and ice-ocean relative velocity and compare this to the contrasting array of previous theoretical results. Over a range of geophysically motivated parameter values, an order of magnitude change in the drag coefficient was observed. Furthermore it is established that internal wave generation also influences the net heat flux and its spatial distribution at

the ice-ocean interface. The chapter is concluded with a summary and discussion of future work in §3.4.

Chapter 4 considers the potential impact on the Beaufort Gyre of the variable ice-ocean drag established in chapter 3 and a simple treatment of sea ice internal stresses via a viscous rheology using a theoretical model. I begin with an overview of existing research on the Beaufort Gyre mechanisms, observations, and its role in the larger Arctic Ocean in §4.1, followed by a review of sea ice rheological models in §4.2. Following this literature review, in §4.3 I extend an existing theoretical model of the Beaufort Gyre from Manucharyan and Spall (2016), and couple it with the wave drag formulation of the previous chapter to examine the role of wind stress, ice mechanics, ice-ocean drag and the upper ocean stratification on the gyre structure and freshwater content. Here I find that alteration to the ice-ocean drag coefficient has the potential to vary the freshwater content of an idealized gyre by $\approx \pm 20\%$ given an imposed ice-ocean relative velocity (but neglecting feedbacks of wave-drag on the ice and upper ocean velocities). A sensitivity study is done for this ocean model examining the role of a variety of ocean, atmosphere, and wave drag parameters on the results. In §4.5 I then develop a simple model of the sea ice rheological response to imposed atmosphere and ocean stress with the goal of understanding how differential stress within the ice may influence the impact of the wave drag parameterization. This model is applied in an uncoupled manner in §4.5.6 where we examine the influence of a variety of boundary conditions, and parameter values. The resulting ice velocity is seen to depend strongly on the ice state beyond the gyre edge with markedly decreased ice-ocean torque being applied in the case where the ice pack surrounding the gyre is rigid.

In Chapter 5, I look at the role of vertical Ekman transport on the water-mass transformation and seasonal evolution of the Antarctic seasonal ice zone. We begin with an introduction and overview of 1-D ocean models in §5.1.1 alongside a discussion of the vertical distribution of water masses in the study region and the data to be used in this study within §5.1.2. In §5.2, we introduce the observational and reanalysis products to be used in this chapter followed by an examination of the observed seasonal evolution of the region according to float data in §5.3. I then develop a 1-D ice-ocean mixed layer model in §5.4 to investigate seasonal water mass transformation in the Antarctic seasonal Ice Zone. In §5.5 this model is applied to demonstrate that vertical Ekman transport is an essential factor in the seasonal evolution of the vertical structure and stratification of the region. Specifically we see that Ekman upwelling

has a strong control on the transformation of Upper Circumpolar Deep Water in the study region with potential impact on multiyear ice trends.

Lastly, in Chapter 6 I summarise the key results from each topic, and discuss the limitations of the current work as well as future steps and broader implications.

1.2 Sea ice

The presence or absence of sea ice in the polar seas has a leading order impact on many fundamental processes via modifications to the typical air-sea fluxes of momentum, heat, moisture, and salt (Post et al., 2013; Tsamados et al., 2015; Bourassa et al., 2013; Thomas and Dieckmann, 2010). One such example of this alteration to air-sea exchanges is the "ice-albedo feedback" (Budyko, 1969). Compared to the ocean, sea ice is highly reflective and thus much of the incoming solar radiation in ice-covered oceans is reflected away from the Earth surface, as opposed to being absorbed in the near-surface ocean. Thus the presence of sea ice in the polar regions provides a leading order impact on the heat balance of the polar oceans with broad implications for climate (Perovich and Polashenski, 2012). Thoroughly understanding all of the mechanisms through which sea ice modifies the exchanges from the atmosphere to the oceanic boundary layer and vice versa is thus a key aspect of accurately representing ocean dynamics in a changing climate (Swart et al., 2019; Frew et al., 2019).

Current sea-ice observational records provide valuable context, but have distinct gaps. Observations that cover large spatial extents, such as those using satellites, typically have spatial resolutions of several kilometers. Hence small scale features of sea ice, such as leads, are not easily detected (Parkinson, 1987). Even when satellites can provide a finer scale resolution of 100-250m , such as the MODIS[2] or the Synthetic Aperture Interferometric Radar Altimeter aboard ESA's CryoSat and CryoSat 2, they can have trouble reliably measuring fundamental properties such as ice thickness (Haas et al., 2010) and albedo (Stroeve et al., 2006). The reason for this error is multifaceted, but the leading causes of uncertainty for satellite sea ice thickness retrieval are uncertainties in ice-snow total freeboard (Kwok et al., 2004), snow depth (Giles et al., 2007) and in the densities of sea ice and snow (Kern and Spreen, 2015; Nandan et al., 2017). On the other hand, field observations cover very fine spatial scales (O(1 - 100) m) for bulk properties or even as low as O(10^{-3}m) for turbulence measurements, but have a very localized sampling region. Enough is known about ice

[2]Moderate Resolution Imaging Spectroradiometer operated by NASA:https://modis.gsfc.nasa.gov/

to understand that many key properties, such as ice thickness, albedo, snow cover and more are determined by local processes that are subject to wide regional variations (Haapala et al., 2013; Parkinson and Cavalieri, 2012; Cavalieri and Parkinson, 2012; Massom et al., 2013). These local processes give rise to the fine scale differences in sea ice, the average of which defines the observable bulk properties such as albedo or mechanical strength (Thomas and Dieckmann, 2010). Hence, understanding the small scale aspects controlling the formation and evolution of sea ice is essential to understanding its role in the climate system.

1.2.1 Formation of sea ice

Though sea ice can technically form year round if the conditions permit, the vast majority of sea ice formation occurs in the polar winters. During winter, the surface layer of the ocean is cooled primarily by a net outgoing longwave radiation due to the negligible incoming short-wave during the longer polar nights (Serreze et al., 2009). Further contributions to the winter net cooling of the ocean surface are fluxes of sensible heat from the ocean to the cold winter atmosphere directly or via conductive processes through the sea ice, as well as latent heat fluxes from evaporation and sublimation (Semtner, 1976; Maykut and McPhee, 1995). In general, the initial onset of sea ice formation occurs in two distinct regimes depending on the sea state as discussed in Thomas and Dieckmann (2010, Chapter 2) and summarized below.

In calm waters, small ice crystals called frazil ice form within the cool surface layer and float to the ocean surface where they slowly congeal into a smooth, thin sheet of ice (Rees Jones and Wells, 2018). This type of ice is commonly referred to as grease ice due to its visual resemblance to an oil slick. Once formed, grease ice slowly grows downwards and transitions from a thin and optically transparent sheet to a thicker and optically reflective sheet. During this stage the lightweight ice sheets are easily pushed about by winds and can slide over each other (so-called rafting) and fuse together (Vella and Wettlaufer, 2008).

In sufficiently rough sea states, the formation of the thin fragile plates of ice cannot occur. Instead, the frazil ice accumulates into roughly shaped "pancakes"referred to as pancake ice (Doble et al., 2003). These pancakes are characterized by raised edges from collisions with other discs and the constant battering of waves. Similarly to the calm water case, pancake ice can raft and fuse together. If the ice is thick enough, these collisions and pile ups can lead to ridging as well. Ridging occurs when the sea ice bends or breaks, and then piles up to form ridges of dramatically increased

thickness (Parmerter and Coon, 1972). Ridging can occur at any stage of the sea ice life cycle and will be examined in more detail in §1.2.2.

After the initial ice mass has formed, the sea ice continues to grow as surface cooling and conduction through the ice removes latent heat from the water below (Cox and Weeks, 1988). In this process, water molecules freeze into a regular crystalline structure while salt ions are mostly rejected (Thomas and Dieckmann, 2010, Chapter 2). This "brine rejection" forms a high salinity liquid that is either enveloped in the forming ice matrix or drains into the ocean layer below. By creating a thin layer of comparatively dense fluid, the salty brine from sea ice formation can create an instability in the stratification profile. Depending on the underlying stratification, this brine rejection can create buoyancy driven convection and deepen the mixed layer (Thomas and Dieckmann, 2010, Chapters 1 & 3).

1.2.2 Evolution of sea ice

After the initial formation of an ice floe it is known as First Year Ice (FYI). FYI is typically $\sim$ 2m thick or less and has a relatively high brine content and a thin snow layer (Perovich and Polashenski, 2012). As ice ages, a number of mechanisms continue to alter both the composition and morphology of the ice such as melt pond drainage, precipitation, and mechanical deformation due to floe collisions (Thomas and Dieckmann, 2010, Chapter 2). These mechanisms, which operate over months or years, change key properties of sea ice including mechanical strength, albedo, and thickness (e.g. Polashenski et al., 2017, 2012; Perovich and Polashenski, 2012; Perovich and Jones, 2014; Andreas et al., 2010). Ice that survives a full growth and melt cycle is called Multi-Year Ice (MYI).

After the first growth season, ice undergoes its first season of melt. During spring and summer, the period of sunlight for the Arctic increases shifting the radiative heat balance to a net incoming of heat (Stanton et al., 2012). This heat is, in part, reflected by sea ice with an importance illustrated by the ice-albedo feedback (Budyko, 1969; Perovich and Polashenski, 2012). The heat that is not reflected is then absorbed by the ice or the ocean (Polashenski et al., 2012). Absorption of heat via the ocean or the ice provide two distinct pathways for the erosion of sea ice: from above via the melting of the snow/ice at the atmospheric interface, or from lateral/basal heat fluxes at the ice-ocean boundary (Perovich and Jones, 2014).

As ice ages, the brine pockets within the porous sea ice can drain and freeze shut. This turns pockets previously full of liquid brine to air pockets. Depending on the

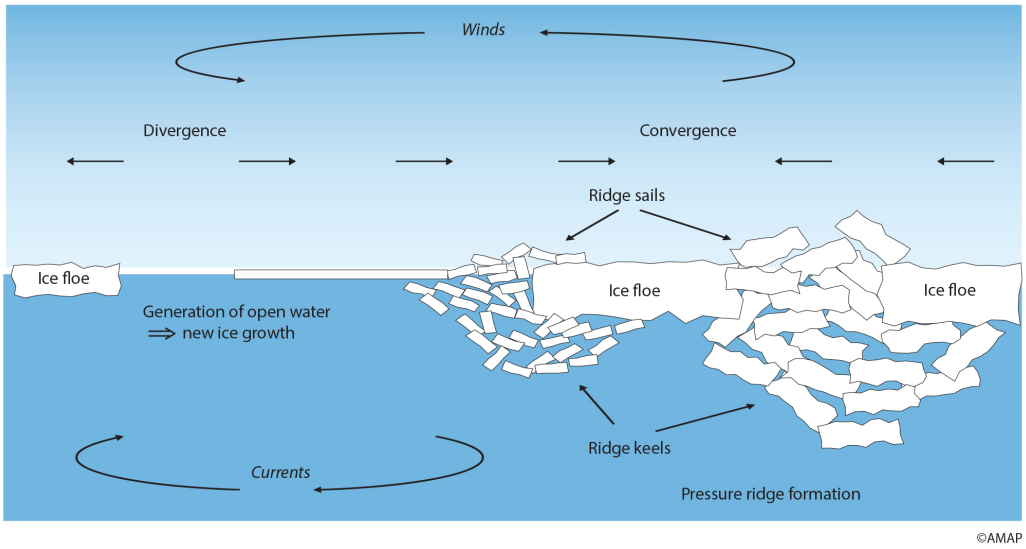


Figure 1.1: Diagram of sea ice mechanical evolution. Leads are formed under divergent stress as on the left hand side of the image, and pressure keels are formed under convergence as on the right. The specific shape and properties of pressure ridges depend on the ice they are formed from (Wadhams et al., 2012). Image courtesy of the Arctic Monitoring & Assessment Programme, Arctic Climate Issues 2011: Changes in Arctic Snow, Water, Ice and Permafrost.

temperature, sea ice may have three distinct inclusions: liquid brine pockets, haline crystals, and air bubbles (Light et al., 2003). These inclusions determine many macroscopic properties of sea ice such as its characteristically high albedo (Perovich and Polashenski, 2012), habitability for micro-organisms (Boetius et al., 2015) and mechanical strength (Timco and Weeks, 2010). Studies of these inclusions are typically done with either lab grown ice or in the field with fresh ice cores (Thomas and Dieckmann, 2010; Eicken, 2009, Chapter 2).

Throughout the evolution of sea ice, the ice is subject to dynamical processes driven by both the atmosphere and ocean. Wind and waves place mechanical stresses on the floes that can accelerate or fracture them (Dumont et al., 2011; Horvat and Tziperman, 2015). A simple schematic of these processes is shown in figure 1.1. Under a divergent wind stress, ice-floes are torn apart creating fractures which grow and propagate creating regions of open ocean between the resulting ice floes called leads (Smith et al., 1990). These leads are also important both dynamically and biologically as they allow direct air-sea exchanges to occur within the ice pack (Smith et al., 1990; Assmy et al., 2017). These mechanical interactions, alongside local variations in thermodynamic growth and melt of ice, generate the characteristic roughness of the ice ocean interface, and a distribution of sea ice thickness (von Albedyll et al.,

2020; Rothrock and Thorndike, 1980; Thorndike et al., 1975; Hutchings et al., 2011).

In the case of convergent wind stress, floes are pushed together causing collisions. During this collision the thicker ice floe may raft on top of the other. This pile up often leads towards the brittle fracture of the thinner, submerged, floe. As the ice fractures, fragments pile up creating a pressure ridge (Parmerter and Coon, 1972).

Studies investigating pressure ridges have been based predominantly on airborne and underwater measurements (Wadhams, 1986; Wadhams and Davis, 2000; Haas et al., 2010). Pressure ridges have been observed as having a wide range of geometries with distinct pressure ridges potentially extending laterally for tens to hundreds of meters across an ice floe (Petty et al., 2016). Newly formed ridges from FYI can be well approximated by the simple shape of an isosceles triangle (Davis and Wadhams, 1995). Older ridges and those formed from MYI are instead typically characterized more accurately by a picture of rubble fields (Wadhams et al., 2012). For FYI in the Arctic ocean, the median slope of these pressure ridges has been found to lie within the ranges of 21.7° to 26.5° (Davis and Wadhams, 1995; Wadhams et al., 2012) and an average keel depth of 5m, though keels exceeding 40m have been observed (Davis and Wadhams, 1995; Wadhams et al., 2012). Hence pressure ridges can occupy a significant fraction of the under-ice mixed layer depth and are thus an important factor in the mass, momentum, and energy balance of the polar oceans (Fer and Sundfjord, 2007; Skyllingstad et al., 2003).

Accurate representation of ridges within models is a critical component of air-ice-ocean momentum exchange (Martin et al., 2016). Such representation necessitates not only the geometry of the ridge above and below the ice floe, but also an understanding of their spatial distribution, the porosity of the ridge, and their formative processes. Many basin scale or larger models including sea ice processes approximate these dynamics by implementing an empirical ridging parameterization based on frictional effects (Lipscomb et al., 2007). In general these characteristics can be determined by either observations (e.g. Haas et al. (2010); Davis and Wadhams (1995); Wadhams et al. (2012)) or modelling (e.g. Roberts et al., 2019). The motivation for accurately characterizing the formation and evolution of ridges is primarily for more accurate calculation of the form drag (Martin et al., 2016; Tsamados et al., 2014). However ridges are known to also influence the generation of internal waves which may in turn further impact ice-ocean fluxes of momentum and heat (Tsamados et al., 2014; McPhee and Kantha, 1989). The impact of sea ice on ice-ocean fluxes will be elaborated on in §1.3.3 and the topic of sea ice generated internal waves specifically is the subject of Chapter 3 and is discussed in more detail in §3.1.

1.3 Turbulent boundary layers

The surface ocean boundary layer moderates the exchanges of heat, salt, and momentum between the atmosphere and the deep ocean (Vallis, 2017). Despite this essential role in the climate system, this O(1-100m) deep region at the air-sea interface is unresolved in the majority of climate models (D'Asaro, 2014). Because these boundary layers can not be resolved they are instead parameterized. As a result, current climate models typically have large errors in ocean boundary layer thickness (Belcher et al., 2012; Sallée et al., 2013).

In this chapter I will summarize the broad theory of boundary layers and the necessary modifications to this theory for the case of the oceanic surface, and under-ice boundary layers.

1.3.1 Boundary layer theory

Fluid flows are often modelled using the well known Navier-Stokes equation for momentum conservation, here written in a rotating reference frame using the f-plane approximation and ignoring centrifugal effects (Vallis, 2017),

$$\frac{D\mathbf{u}}{Dt} = -\mathbf{g} - \frac{1}{\rho}\nabla p + \nu\nabla^2\mathbf{u} + f\mathbf{k}\times\mathbf{u}. \tag{1.1}$$

We have here assumed the flow is incompressible such that $D\rho/Dt = 0$, and so our accompanying equation for mass conservation is

$$\nabla\cdot\mathbf{u} = 0. \tag{1.2}$$

The fluid velocity is $\mathbf{u} = (u, v, w)$, t is time, $\mathbf{g}$ is the acceleration due to gravity, ρ is the fluid density, p is the pressure, ν is the kinematic viscosity, f is the Coriolis parameter used to denote the strength of rotational effects, and $\mathbf{k}$ is the vertical unit vector.

Often scalar fields are incorporated via a general advection-diffusion equation

$$\rho\left[\frac{\partial\phi}{\partial t} + \mathbf{u}\cdot\nabla\phi\right] = \nabla\cdot(\rho K_\phi\nabla\phi) \tag{1.3}$$

where ϕ is the conserved quantity (typically heat or salt), and K_ϕ is the diffusivity of said quantity. Scalar quantities can sometimes affect the flow such as through buoyancy driven turbulence to be discussed in §1.3.2.3, or act as passive tracers.

Early attempts at solving hydrodynamical problems involved a variety of simplifications (see reviews by Tani, 1977a; Anderson, 2005; Schlichting and Gersten, 2016).

One such simplification was to assume zero viscosity, $\nu = 0$, in the limit of large Reynolds number, where $Re = UL/\nu$ is the Reynolds number with U, L the characteristic speed and length scales of the problem. This inviscid case however removed the ability to solve for the viscous force on a boundary as discussed in Anderson (2005). One attempt to remedy this was via the imposition of a no-slip boundary condition ($\mathbf{u} = 0$ at the boundary) (as reviewed by Tani, 1977b). Unfortunately with this boundary condition, the inviscid solutions failed to match observations (Schlichting and Gersten, 2016). A remedy to these issues was introduced via Prandtl's seminal work *"On the motion of a fluid with very small viscosity"* published in 1905.

Prandtl's solution to this problem was the establishment of a so called 'boundary layer' within which viscous effects of the fluid are significant and beyond which the fluid relaxes towards the inviscid states previously examined (Prandtl, 1905). Due to the small thickness of the boundary layer, one can make certain approximations in order to simplify the Navier-Stokes equations within this thin layer: the variation of pressure normal to the wall is negligibly small, and the variation of velocity along the wall is much smaller than its variation normal to it (Schlichting and Gersten, 2016). With these assumptions, (1.1), (1.2) can be simplified drastically.

This original formulation of boundary layer theory is recognizable now as a singular perturbation problem (Bender and Orszag, 2013). Another important result for understanding boundary layer physics are the Reynolds fluxes that result from perturbations to the Navier-Stokes equation.

1.3.1.1 Reynolds fluxes

We consider fluids that are well represented within the incompressible limit where $\nabla \cdot \mathbf{u} = 0$. For turbulent flow, one can represent the velocity as turbulent fluctuations around a mean flow state written as

$$u_i = \overline{u_i} + u_i' \tag{1.4}$$

where $\overline{u_i}$ is a mean value and $u_i^{'}$ represents turbulent fluctuations about the mean value. A similar construction is used for pressure. This substitution is usually used alongside averaging the momentum equation, using the following rules for the averaging operator denoted by $\overline{...}$

$$\begin{aligned} \overline{\overline{a}} &= \overline{a} \\ \overline{a + b} &= \overline{a} + \overline{b} \\ \overline{a\overline{b}} &= \overline{a}\overline{b}. \end{aligned}$$

Substituting u_i into (1.1) with ρ constant, neglecting the Coriolis term and taking the average of both sides, one can derive the Reynolds-Averaged Navier–Stokes here written in Einstein notation:

$$\rho\overline{u_j}\frac{\partial\overline{u_i}}{\partial x_j} = -\rho\overline{\mathbf{g}} + \frac{\partial}{\partial x_j}\left[-\overline{p}\delta_{ij} + 2\mu\overline{S_{ij}} - \rho\overline{u_i'u_j'}\right] \tag{1.5}$$

where δ_{ij} is the Kronecker delta tensor, $S_{ij} = \frac{1}{2}\left(\frac{\partial\overline{u_i}}{\partial x_j} + \frac{\partial\overline{u_j}}{\partial x_i}\right)$ is the mean rate of strain tensor, $\mu = \rho\nu$ is the dynamic viscosity, and the quantity $\rho\overline{u_i'u_j'}$ is known as the Reynolds stress. The Reynolds stress as it appears in (1.5) represents the effect of turbulent fluctuations on the mean flow. In the ocean, turbulent fluxes of heat and salt in the direction of x_i can be ascertained the same way via (1.3) and are given by $\rho c_p\overline{T'u_i'}$ and $\overline{S'u_i'}$ with temperature T, specific heat c_p and salinity S.

The Reynolds stress is sometimes represented as the product of an eddy viscosity, K_ν and the shear by

$$-\rho\overline{u_i'u_j'} = \rho K_\nu\frac{d\overline{u_i}}{dx_j}. \tag{1.6}$$

From this relation one can define a friction velocity, u_* as

$$u_*^2 = K_\nu\frac{d\overline{u_i}}{dx_j}. \tag{1.7}$$

The friction velocity can be used to examine the impact of boundary layer turbulence on the mean flow.

The Reynolds-Averaged Navier-Stokes equation (1.5) is an important foundation for approaching a wide variety of geophysical applications. In most settings, however, modifications need to be made to include specific features. In the ocean, and under ice, these include the effects of planetary rotation, the specific boundary conditions, and the effects of buoyancy due to fluxes of heat and salt.

1.3.2 Oceanic boundary layer

At the surface of the ocean, the boundary layer is commonly represented as a so-called "mixed layer." The mixed layer is often used as a proxy for the layer of the ocean surface undergoing active mixing. Observationally, this active turbulence has been more difficult to detect (Brainerd and Gregg, 1995) so a density dependent definition is widely used. This definition typically diagnoses the mixed layer depth as the depth where the density at depth varies from the surface measurement by some threshold (de Boyer Montégut et al., 2004), though other methodologies also exist (Holte and Talley, 2009).

Current climate models typically have difficulty when it comes to approximating the dynamics of the mixed layer with the implemented parameterizations giving large errors in mixed layer thickness (D'Asaro, 2014). This difficulty is apparent when looking at the large errors in mixed layer depth and of ventilated water masses originating in the mixed layer (Sallée et al., 2013). In general, a wide ensemble of processes govern the surface ocean's dynamics, including surface gravity waves and wave breaking, evaporation and precipitation patterns, radiative heat transfer as well as planetary rotation (Vallis, 2017). Herein I will focus primarily on some key processes elaborated upon later in this work such as rotational effects on lateral and vertical water-mass transport, as well as buoyancy driven flow. We proceed with a discussion of the open ocean case, which we will then modify to include the effects of sea ice in §1.3.3.

1.3.2.1 Rotational effects

For the oceanic boundary layer, or a general boundary layer with rotational effects, a key physical process is the Ekman layer first described in V.W. Ekman's seminal work from the voyage of Nansen's Fram. During the voyage, Nansen observed that the drift of the boat was at an angle of $20° - 40°$ to the surface winds (Ekman, 1905). This can be investigated by looking at (1.1) and assuming that the dominant terms are Coriolis forces, pressure gradients, and viscous drag in a neutrally stratified boundary layer such that

$$-fv = -\frac{1}{\rho_0}\frac{\partial p}{\partial x} + \nu\frac{\partial^2 u}{\partial z^2}, \tag{1.8}$$

$$fu = -\frac{1}{\rho_0}\frac{\partial p}{\partial y} + \nu\frac{\partial^2 v}{\partial z^2}, \tag{1.9}$$

$$0 = -\frac{1}{\rho_0}\frac{\partial p}{\partial z}, \tag{1.10}$$

where u and v are the horizontal components of the flow velocity, ρ_0 is a reference density, and p describes the pressure perturbation relative to a hydrostatically balanced state. Here we have also assumed a constant viscosity.

From here, one can impose wind stress as the boundary conditions at the air-sea surface ($z = 0$)

$$\rho\nu\frac{\partial u}{\partial z} = \tau_x \qquad \text{and} \qquad \rho\nu\frac{\partial v}{\partial z} = \tau_y \tag{1.11}$$

where τ_x and τ_y are the x and y components of the surface wind stress, τ. Solving (1.8) to (1.11) provides the well known solution of the Ekman spiral (Vallis, 2017)

$$u = u_g + \frac{\sqrt{2}}{\rho_o f d} e^{z/d} \left[\tau^x \cos(z/d - \pi/4) - \tau^y \sin(z/d - \pi/4)\right], \tag{1.12}$$

$$v = v_g + \frac{\sqrt{2}}{\rho_o f d} e^{z/d} \left[\tau^x \sin(z/d - \pi/4) + \tau^y \cos(z/d - \pi/4)\right], \tag{1.13}$$

$$d = \sqrt{2\nu/|f|}. \tag{1.14}$$

Here d is known as the Ekman layer depth, which represents the penetration depth of wind induced mixing and u_g, v_g are the geostrophic velocities below the surface boundary layer. These velocities can be integrated over the Ekman layer depth to determine the net transport of water due to wind stress. This Ekman transport indicates a deflection of the surface ocean current to the right of the wind direction in the northern hemisphere or to the left in the southern hemisphere.

To conserve mass, lateral Ekman transport must be balanced by vertical transport. In the case of divergent Ekman transport, as surface waters are moved outward, deeper water within the region upwells from below, in turn replaced by deep water outside the region. In the convergent case, surface waters accumulate and depress water in the interior to depth via down-welling. In general the vertical and lateral Ekman transport is given by.

$$w_{ek} = \mathbf{k} \cdot \nabla \times \left(\frac{\tau}{f\rho}\right), \quad \mathbf{U}_{ek} = -\frac{\mathbf{k} \times \tau}{\rho f}. \tag{1.15}$$

Where $\mathbf{U}_{ek}$ is the depth integrated velocity ($\mathrm{m}^2\ \mathrm{s}^{-1}$). This Ekman transport both laterally and vertically has important impacts such as equatorial upwelling (Vallis, 2017), water mass transformation and ventilation (Sallée et al., 2010), and freshwater build up in the Beaufort gyre (Timmermans and Marshall, 2020; Proshutinsky et al., 2009b; Meneghello et al., 2018b; Manucharyan et al., 2016). Note that the results of (1.15) do not rely on constant viscosity or an Ekman spiral and can also be derived for any turbulent stresses that can be approximated as the vertical derivative of the relevant stress components (Vallis, 2017).

In addition to the effects of rotation, the boundary layer is subject to mechanical influences on the flow field, as well as changes in density and thus buoyancy. In the oceanographic setting, the primary influencers are atmospheric winds, and exchanges of heat and salt/freshwater at the oceans surface.

1.3.2.2 Wind and wave driven ocean

The classical paradigm of ocean dynamics treats the influence of waves and wind shear as a single effect neglecting a direct treatment of wave breaking and Langmuir circulation (D'Asaro, 2014). In many climate models this forcing is represented as a modified shear stress on the upper ocean that obeys the empirically determined relation

$$\tau = C_D \rho_{air} U_{10}^2,$$

where U_{10} is the wind speed at 10m above the sea surface, $\rho_{air} = 1.22\ \mathrm{kg\,m^{-3}}$ is the atmospheric density near the surface and C_D is a dimensionless drag coefficient. The drag coefficient is chosen to approximate the effect of surface roughness due to swells and waves (a typical value is $C_D = 0.0013$) (Cronin and Sprintall, 2009). Based on this wind stress, and in the absence of strong buoyancy forcings, the air-sea boundary layer momentum fluxes are broadly consistent with the turbulent shear of the Reynolds fluxes described in §1.3.1.1.

Early measurements supported the idea of purely shear driven turbulence (Jones and Kenney, 1977). Since then wave breaking, Langmuir turbulence, and mesoscale and submesoscale processes have been found to contribute to the mixed layer turbulence (D'Asaro, 2014; Sutherland et al., 2013).

For most cases, the classical combination of wind and wave stresses appears to work decently, though it falls short when events such as wave breaking occur (Melville, 1996). With wave breaking, observations show that the kinetic energy dissipation close to the boundary layer is greater than that expected due to the Reynolds stress framework (D'Asaro, 2014). It is still not clear to what degree wave breaking influences mixed layer dynamics.

Another poorly understood phenomena tied to wave-wind coupling is Langmuir circulation (Thorpe, 2004). First described by Irving Langmuir, Langmuir circulation takes the ideal form of wind aligned vortices. The rotating roll vortices are thought to arise due to the interaction of the mean flow with the wave averaged flow of surface waves (Thorpe, 2004). In the ice-covered oceans, surface gravity waves are damped due to the presence of ice floes (Zhang et al., 2015). Due to this, wave induced effects are likely weak deep in the ice pack, though potentially relevant in the wave influenced marginal ice zone.

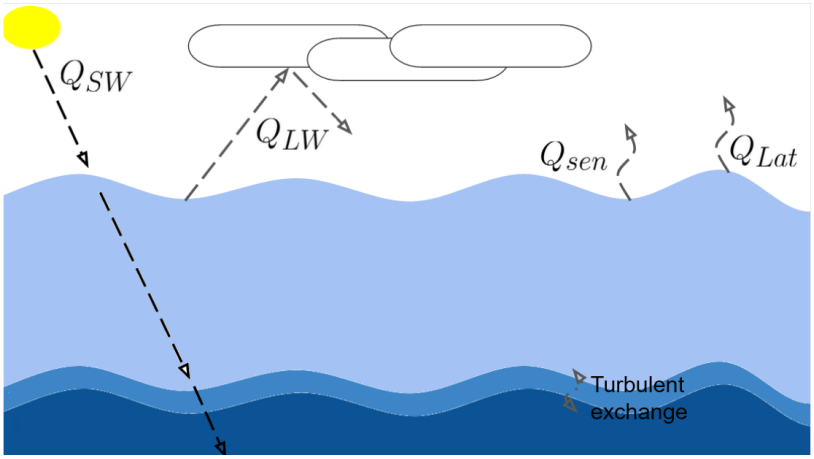


Figure 1.2: Simplified sketch of the upper ocean heat sources and sinks. Q_{sw} indicates the downwelling shortwave radiation from the sun, Q_{LW} the balance of longwave radiation emitted via blackbody radiation and the fraction subsequently reflected back towards the surface by cloud cover, Q_{sen} the net sensible heat-flux, Q_{lat} the latent heat flux.

1.3.2.3 Buoyancy driven flow

The primary factors affecting density changes in the ocean are temperature, salinity and pressure, with minor variation of density due to pressure in the surface boundary layer. The relative importance of temperature and salinity varies depending on location (Johnson et al., 2012). Together the salinity and temperature fluxes lead to variations in the density and may drive or inhibit convection in the upper ocean.

Assuming that the ocean is warmer than the atmosphere, the thermodynamic inputs to the surface layer are short-wave radiation from sunlight, long-wave radiation from the atmosphere and clouds, sensible heat transfer at the air-sea interface, latent heat from evaporation at the surface and upwelling heat from the deep ocean at the base of the mixed layer as shown in figure 1.2. These heat inputs are balanced by sensible heat loss at the ocean-atmosphere interface as well as long-wave radiation emitted from the ocean surface according to the blackbody curve[3]. The incoming short-wave radiation penetrates to depth as controlled by radiative scattering and absorption. Examining the surface heat fluxes using the net shortwave absorbed at the surface and net long-wave (outgoing due to black body radiation, and incoming from absorption and re-emission from the atmosphere and cloud cover), the heat

[3]Though both sources of radiations are technically broadband radiation, the solar radiation curve peaks in the wavelength band (0.1μm - 4μm). Because the earth is much cooler than the sun, its peak is in the long wave spectrum (4μm - 100μm).

balance at the surface can be written in the form

$$Q_{SW} - Q_{LW} - Q_{Sen} - Q_{Lat} + Q_{Turb} + \rho_o c_o H_{ML} \frac{\partial T}{\partial t} = 0,$$

where Q_{SW} is the depth-integrated short-wave flux through the surface, Q_{LW} the net surface flux of longwave radiation, Q_{Sen} the net sensible heat flux from the ocean surface to the atmosphere, Q_{Lat} the latent heat flux, Q_{Turb} is the turbulent heat flux from the underlying deep ocean, and the last term represents the heat storage of the surface layer with specific heat capacity c_o and thickness of the surface layer H_{ML}. Satellite measurements of incoming and outgoing radiation are able to tell us the short-wave and long-wave components of the surface heat budget. However the so called turbulent heat fluxes from sensible heat and latent heat usually need to be estimated from wind speed and air-sea humidity/temperature differences. The typical bulk parameterization for these fluxes into and out of the ocean are given by

$$Q_{Sen} = \rho_a c_a c_h U_{10}(T_o - T_a)$$

and

$$Q_{Lat} = \rho_a \mathcal{L} c_e U_{10}(q_o - q_a),$$

where c_a and $\mathcal{L}$ are the specific and latent heat of the atmosphere and c_h, c_e are turbulent exchange coefficients for each process and T_o/q_o and T_a/q_a are the temperature/specific humidity for the ocean and atmosphere respectively (Taylor, 2009). Similar turbulent exchange relations exist for the ice-ocean and ice-atmosphere boundaries (Sirevaag, 2009; McPhee, 1992).

Penetration of short-wave radiation with depth is usually treated via a two stream approximation as reviewed in Meador and Weaver (1980). In brief, with the two stream approximation radiation is separated into a downwards flux of radiation and an upwards one with absorption and scattering changing the intensity of each beam. This method has been used in global climate models (Chou, 1992) for solar radiation in the atmosphere and ocean as well as for snow and melt-pond covered ice (Taylor and Feltham, 2004).

In the open ocean, salt/freshwater fluxes are driven primarily by evaporation and precipitation with locally focused fluxes such as river run off playing a role as well. This salinity flux and the aforementioned heat flux can modify the dynamics of the ocean mixed layer by changing the density of sea water. Within the ocean these effects due to buoyancy forcing can be investigated using the Boussinesq approximation to the Navier-Stokes equation (1.1).

The Boussinesq approximation (see Vallis (2017) for example) implies that the density variation is only important when multiplied by gravity in the buoyancy terms. With this assumption, the continuity equation has the form of (1.2) and so (1.1) becomes

$$\rho_0 \frac{D\mathbf{u}}{Dt} = -\rho \mathbf{g} - \nabla p + \rho_0 \nu \nabla^2 \mathbf{u} + \rho_0 f \mathbf{k} \times \mathbf{u} \tag{1.16}$$

with reference density ρ_0. In the buoyancy term, the full density, ρ, is given by the equation of state for seawater which in its full form depends on temperature, salinity and pressure. For the case of the surface boundary layer we here will neglect the role of pressure and for an illustrative case consider a linear equation of state with

$$\frac{\Delta \rho}{\rho_0} = \beta \Delta S - \alpha \Delta T \tag{1.17}$$

where β is the haline contraction coefficient, α is the thermal expansion coefficient and T and S are temperature and salinity fields. Here $\Delta\rho$, ΔS and ΔT represent the change from the reference values (e.g. $\Delta S = S - S_0$). These equations are used along with appropriate equations for heat and salt of the form (1.3). The use of a linear equation of state neglects some important dynamics that occur due to the non-linearity such as cabelling or thermobaricity (McDougall, 1987) which we omit here.

The molecular diffusion of heat is much faster than the molecular diffusion of salt, and so the dependence of the buoyancy force on salinity in (1.17) can give rise to interesting double diffusive effects (e.g. see Radko, 2013) This allows either quantity to be stably stratified (density increases with depth) or unstably stratified (density decreases with depth). There are four different regimes depending on gradients in T and S as

1. T and S stably stratified (stable)
2. S stable, T unstable (diffusive regime)
3. T stable, S unstable (salt fingering)
4. T and S unstable (unstable).

Each of these regimes appear in the world's oceans, with double diffusive effects being observed in the Arctic (as in Shibley et al., 2017). For a more complete treatment of double diffusive effects, we direct the reader to Radko (2013).

The forcings that cause changes in temperature and salinity, such as solar radiation and precipitation, have a seasonal cycle. Thus the buoyancy driven flow has a seasonal cycle as well. Typically during the summer months, a net stabilizing buoyancy flux serves to re-stratify the mixed layer and thus shallow it (de Boyer Montégut et al., 2004). If mixing is inhibited for a sufficiently long period of time, a seasonal pycnocline is formed (Cronin and Sprintall, 2009). During the winter months, cooling at the ocean surface through sensible heat loss and emitted long-wave radiation leads to an unstable stratification as cold ocean water sits over warmer water. As a result of this unstable stratification, convection occurs. This convection acts to slowly entrain water from the pycnocline underneath the mixed layer. Under sufficient forcing, entrainment of deeper waters may continue once the seasonal pycnocline is eroded. Below the seasonal pycnocline established during the shallow summer mixed layer is a persistent region of strong stratification known as the main or 'permanent' pycnocline (Cronin and Sprintall, 2009). In oceans where buoyancy forces are salinity dominated, such as the Arctic, this stratification is set by salt and referred to as the halocline (Polyakov et al., 2020a). If strong forcing events occur such as storms, water from the main pycnocline may be entrained through the same mechanisms that served to erode the seasonal pycnocline (Price et al., 1978). In the Arctic, concern has grown regarding the impact of reduced sea ice coverage and the corresponding increase of wind and wave driven mixing on increased heat entrainment from below the main halocline, as a substantial amount of heat is stored at depth in this region and could melt the ice if mixed to the surface (Polyakov et al., 2020a; Carmack et al., 2015).

In the ice-covered oceans, the fundamental processes described here are all potentially present, though the typical air-sea exchanges of heat, salt, and momentum become modified due to the interrupting presence of sea ice.

1.3.3 Under ice boundary layer

The above upper ocean processes are heavily modified by the presence of sea ice. Rotational effects, such as Ekman transport or Ekman pumping, are determined by the wind stress transmitted through the ice instead of directly acting on the ocean surface. In addition to the typical fluxes of heat and salt previously discussed, buoyancy exchanges at the ocean surface are modified by the introduction of ice formation and melt as well as alterations to the surface heat budget.

1.3.3.1 Ice-ocean buoyancy fluxes

Thermodynamically, the presence of snow-covered sea ice complicates the previous picture of direct air-sea exchanges. The snow layer atop sea ice is less efficient at conducting heat than the underlying sea ice due to its air filled porous space. In this case, the direct influence of atmospheric temperatures near the ocean surface is communicated through a conductive heat flux based on the ice/snow thickness and conductivities as in Semtner (1976). This complicates the picture of the typical open ocean heat and salt exchanges as the ice acts as an extra storage reservoir for energy depending on its specific and latent heat. There is an energy flux balance at the upper boundary of the ice that determines surface melting or temperature as a result of the net budget of heat fluxes through the atmosphere to the ice, and conduction through the ice. There is also a corresponding energy flux balance at the lower ice boundary, with basal melt/growth further depending on conductive heat flux through the ice, and sensible heat transfer with the underlying ocean (Maykut and Untersteiner, 1971). Each pathway of heat and salt exchange with the atmosphere previously set out in the air-sea case is altered depending on ice presence, ice type, melt ponds, and snow cover (Perovich and Polashenski, 2012; Lu et al., 2016; Thomas and Dieckmann, 2010).

For the saline contribution, formation of sea ice increases the salinity of the surrounding water due to rejection of salts as the crystal structure starts to develop. The ice covered ocean also restricts evaporation and precipitation fluxes to the ocean (Thomas and Dieckmann, 2010). During ice melt, the comparatively fresh sea ice serves as a source of positive buoyancy flux which can inhibit convection (Rudels et al., 1996).

The heat and salt fluxes between the ice and the ocean are set by the ablation or formation of the ice. In general, ablation can be due to dissolution, or melting (Notz et al., 2003). In each case, the heat and salt fluxes are often primarily turbulent fluxes which depend on the freezing point of the water calculated via a a liquidus curve using the interfacial salinity (Keitzl et al., 2016; Notz et al., 2003). Salt released during ice growth can (as discussed in §1.2) result in dense water near the ice-ocean interface which can enhance turbulence (Maykut and McPhee, 1995; McPhee et al., 2003).

The full energy and salt budget determining ablation or freezing rates is given by the so called three equation formulation (Holland and Jenkins, 1999). The three equations are

$$T_{int} = aS_{int} + b + cp_{int} \tag{1.18}$$

$$Q_i^T - Q_o^T = Q_{latent}^T \tag{1.19}$$

$$Q_i^S - Q_o^S = Q_{brine}^S. \tag{1.20}$$

where the subscript int denotes a property of the ice-ocean interface and a, b, and c are empirical constants. It is important to note (1.18) utilizes a linearized version of the liquidus curve and the particular values of a, b and c used in Holland and Jenkins (1999) are intended for use between 4-40 psu. Q represents fluxes of heat or salt denoted by superscript T or S, respectively, and the subscripts i and o denote fluxes into the ice, or into the mixed layer. The right hand side of (1.19) is the latent heat flux given by $Q_{latent}^T = -\rho_i w_{int} L_f$ with w_{int} the evolution of the ice interface, which is positive if melting and negative if growing, and L_f the latent heat of fusion. Analogous to the latent heat flux, in (1.20) the growth/melt of ice has a corresponding salt flux of $Q_{brine}^S = \rho_i w_{int}(S_i - S_{int})$. These three equations, though an improvement on simpler models (Schmidt et al., 2004a), require one to know the ratio of heat and salt fluxes at the interface (Keitzl et al., 2016). Better characterization of this ratio is an ongoing topic of research.

1.3.3.2 Ice-ocean momentum flux

Many of the boundary layer processes discussed in §1.3.1 and §1.3.2.2 are also active in ice covered oceans, but with some modifications in the relevant parameterizations. Namely, the presence of sea ice alters the eddy diffusivity and the characteristic drag coefficient as discussed in §1.3.2.2 through the inhibition of waves, and modified surface roughness (Tsamados et al., 2014).

Within the ice-covered oceans, waves attenuate exponentially as they propagate into ice covered regions for small wave heights ($H < 3$m), and linearly for large wave heights (Kohout et al., 2014). For small wave heights, wave energy is strongly attenuated via an increasing exponential decay with increasing frequency (Dumont et al., 2011). Hence wave effects are likely to be relatively insignificant outside of the Marginal Ice Zone (a region of relatively low ice concentration at the ice edge). Within the Marginal Ice Zone, breaking of sea ice due to mechanical stress caused by ocean waves is an increasing point of concern as Arctic sea ice extent continues to decline and wave energy increases in the now open regions of the Beaufort and Chukchi seas (Zippel and Thomson, 2016). The attenuation of these surface waves in

the MIZ, and into the deeper ice pack, suggests that Langmuir circulation is heavily suppressed within the Arctic ice pack. Recent model studies suggest that this process is absent from the perennial ice covered oceans (Schultz et al., 2020).

Understanding the momentum flux at both the air-sea interface and the ice-ocean interface is essential for understanding the effect of sea ice on boundary layer processes. Many of the process discussed in §1.2 regarding ice formation and evolution influence the sea ice drag force via their impact on ice geometry and resulting modifications to the ice-ocean form drag, skin drag, and wave drag as in Tsamados et al. (2014). To determine the magnitude of the net ice-ocean drag one can either measure the shear profile or look at turbulent flux measurements (Cole et al., 2014). These measurements can then be used to derive a drag coefficient for the common quadratic drag stress used in numerical models. For example, ice tethered profilers in the Arctic have been used to show that the magnitude of derived ice-ocean drag coefficients can vary by more than an order of magnitude from $C_d \approx O(10^{-3} - 10^{-2})$ (Cole et al., 2018; Shirasawa and Ingram, 1991; Lu et al., 2011). The cause for such dramatic variation in the drag coefficient is attributable to varying ice roughness, atmospheric or oceanic stresses, internal wave generation, sea ice floe size and other properties of the atmospheric and oceanic boundary layers (Tsamados et al., 2014). Each of these components of the ice-ocean drag coefficient varies on seasonal timescales, therefore so do the air-ice and ice-ocean drag coefficients (Tsamados et al., 2014).

The effects of large morphological features of sea ice such as pressure ridges is known to play an important role in local ice-ocean drag values (McPhee and Kantha, 1989; Skyllingstad et al., 2003; Fer and Sundfjord, 2007; Tsamados et al., 2014). Enhanced turbulence due to the presence of a pressure ridge has been observed in Fer and Sundfjord (2007) and Perovich et al. (2003) and modelled in Skyllingstad et al. (2003) and McPhee and Kantha (1989). Around the pressure ridge, ice draft was observed to increase the eddy diffusivity of the mixed layer contributing to increased heat transported to the ice-ocean interface. Furthermore, a downstream turbulent wake was observed that may affect heat transfer down stream of the ridge.

These processes are attributable to generation of internal waves due to the rough sea ice (McPhee and Kantha, 1989). Internal waves have been observed to play a role in the turbulent fluxes under sea ice in data from ice tethered profilers (Cole et al., 2014). Similarly, model studies have used the inclusion of sea ice generated internal waves to explain observed changes reported in heat flux measurements as in Skyllingstad et al. (2003) and McPhee and Kantha (1989). Observations of the Arctic internal wave field suggest that younger ice is associated with reduced internal wave

generation (Cole et al., 2018). Understanding the role of internal wave drag is then potentially important for predicting Arctic ocean circulation in a future ice-state. The effects of pressure ridges and internal waves on the under ice boundary layer is the primary subject of §3.1. As such a more detailed review of these works occurs in §3.1.4.

On larger scales, the difference in drag between ice-covered and open ocean creates a variable ice-ocean stress that depends on the ice concentration. The area-weighted ocean surface stress is given by

$$\tau_o = \tau_{io} A + \tau_{ao}(1 - A) \tag{1.21}$$

where τ_o is the ocean surface stress, τ_{io} is the ice-ocean stress, τ_{ao} is the air-ocean stress, and A is the fractional ice coverage with $A = 1$ indicating a completely ice covered surface (Zippel and Thomson, 2016).

This variation in surface stress also plays a role in the strength of Ekman transport and pumping discussed in §1.3.2.1. One manifestation of this is the structure of the Beaufort gyre which we will explore using a simple conceptual model to be discussed in chapter 4.

Measuring the boundary layer (i.e., within a meter below the base of the sea ice) remains incredibly difficult. Even with the advent of novel observational methods such as ice mass balance buoys, ice-tethered profilers, autonomous unmanned vehicles and animal attached CTDs, observations within the surface five meters are few and far between. Under some circumstances the under-ice boundary layer is entirely contained within this surface five meters leaving the details of the air-sea-ice interface to parameterizations (McPhee, 1992). Therefore, a detailed picture of this boundary layer does not exist. Within this thesis we attempt to fill in some of this knowledge gap.

1.4 Summary

The processes governing sea ice formation and evolution, as discussed in §1.2, define the dynamics of the under-ice boundary layer as discussed in §1.3.3. Ice ablation or formation rates control the buoyancy fluxes in the ice-covered oceans via complex processes discussed within Notz and Stroeve (2016); McPhee and Kantha (1989); Malyarenko et al. (2020); McPhee (2008). Ice formation rates along with subsequent mechanical deformation of sea ice also sets the macroscopic properties of sea ice that influence the under ice boundary layer dynamics (Tsamados et al., 2014; Parmerter

and Coon, 1972; Wadhams et al., 2012; Nuber et al., 2013; Thomas and Dieckmann, 2010).

The under ice boundary layer has a strong similarity to that of the open ocean boundary layer discussed in §1.3.1. Key modifications are the reduced influence of surface gravity waves, and thus Langmuir circulation, within the ice pack, and a modified ice-ocean roughness and thus a modified surface stress. The nature of this ice roughness is determined by a wide variety of factors including pressure ridge geometry and spacing or floe size and thickness distributions as discussed in Tsamados et al. (2014). An understudied effect of this boundary layer is the generation of internal waves due to sea ice roughness, examined using linear theory in McPhee and Kantha (1989) and large eddy simulations of a particular configuration in Skyllingstad et al. (2003). Periods of elevated internal wave activity have recently been observed to be associated with changes in the ice-ocean heat and salt flux (Cole et al., 2018). Furthermore, observations of these processes in the Arctic suggests that the sea ice state is particularly sensitive to mixing of heat from depth through boundary layer processes (Kwok and Untersteiner, 2011). As we will discuss in §5 these processes are also important for understanding the state of Antarctic sea ice and, in turn, water-mass transformation in the Southern Ocean (Pellichero et al., 2018).

In this thesis we will examine a number of topics regarding understudied processes of the ice-ocean boundary layer and the impacts on deeper ocean structure. In chapter 3, we examine the effects of sea ice generated internal waves due to a ridged ice flow above a stably stratified upper ocean on the ice-ocean exchanges of momentum, heat, and salt in an idealized model. For this work we observe modest adjustments to the average values of these fluxes as well as changes in their spatial structures when compared to the same properties under a neutral stratification. In chapter 4 we further develop this idea and examine the potential impact of the modified ice-ocean drag and a simple ice-rheology on the vertical structure of the Beaufort Gyre. Lastly, In chapter 5 we switch geographical focus to the Antarctic seasonal ice zone to examine the role of ice dynamics on the transformation of water-masses in the upper branch of the Southern Ocean. Before chapter 3, however, we must first develop the computational infrastructure to be used.

Chapter 2

Lattice Boltzmann Method

When attempting to solve fluid dynamics problems, one usually thinks first of the many traditional methods of discretization of the Navier-Stokes equations (Cuvelier et al., 1986). Since the 1980s, an alternative approach to computational fluid dynamics has emerged in the tail of the lattice gas methods (Chen and Doolen, 1998; Aidun and Clausen, 2010): the Lattice Boltzmann Method (LBM).

The lattice gas methods of the mid-late 20th century attempted to create a simple atomistic way of calculating fluid flows. Focusing on the motions of individual particles moving on a hexagonal grid, the method enforces conservation laws of mass and momentum at the particle scale. These early lattice gas methods were shown to be able to simulate hydrodynamics, though with an astronomical computational cost and an extreme amount of noise (Succi, 2001; Higuera and Jiménez, 1989, Chapter 2).

One large step to remedying these failings while maintaining the advantages of a discretized velocity lattice was to advect a particle density function (PDF), instead of individual particles (Higuera and Jiménez, 1989). By following the evolution of a particle distribution function instead of a single particle, one considers ensemble averages over an infinite number of systems. This sort of ensemble averaging eliminates the noise associated with following a single particle (Succi, 2001).

Since this development, the LBM has emerged as a promising alternative for a variety of fluid dynamics problems. Particular applications of the LBM include problems such as turbulence, aerodynamics, multiphase flows, magnetohydrodynamics, chemically-reactive flows, and hemodynamics (Chopard et al., 2002; Artoli et al., 2006; Peters et al., 2009; Jahanshaloo et al., 2013; Martinez et al., 1994; Mishra and Roy, 2007; He and Luo, 1997). Modern versions of the LBM are easily developed and parallelized (Mohamad, 2011), scale well with increased processors (Jahanshaloo et al., 2013), and allow for simple implementation of boundary conditions for vector

and scalar fields (Guo et al., 2002; Ladd, 1994). This allows for explicit computation of fluxes at the boundary (Ladd, 1994) instead of by calculating the Reynolds fluxes as done in Skyllingstad et al. (2003); McPhee and Kantha (1989). A disadvantage of using a direct numerical simulation (via LBM or otherwise) is the need to resolve the viscous length-scales, which might be parameterised in an LES model.

Herein we will lay out the relevant theory of the LBM used to develop the computational model used in the next chapter. This includes the general background of the LBM in §2.1, and its particular form to be used in §2.1.1. The inclusion of scalar fields, such as salt and temperature, within the model is outlined in §2.1.2. The unit conversion process from dimensional systems to the lattice units is covered in §2.2. The implementation of boundary conditions is covered within §2.3, followed by a description of the parallelization scheme in §2.4, and then a description of the computational algorithm in §2.5. Finally, a number of benchmarks are used to validate our LBM code in §2.6 and we wrap up this chapter with a summary in §2.7.

2.1 Theory

The LBM is well established, and the physical and theoretical underpinnings are described in detail in a number of textbooks and review articles (Mohamad, 2011; Succi, 2001; He and Luo, 1997; Chen and Doolen, 1998). In this section and the following, we summarise the key ideas and details drawn from the above body of work, as relevant to this thesis.

In the statistical mechanics view of fluid dynamics taken by the LBM, fluids are represented by an unnormalized probability distribution function (PDF) $f(\mathbf{r}, \mathbf{v}, t)$ of finding particles at some position $\mathbf{r}$ with some velocity, $\mathbf{v}$ at time t. The cornerstone of this approach is Boltzmann's equation

$$\frac{\partial f}{\partial t} + \mathbf{v} \cdot \nabla f + \frac{\mathbf{F}}{m} \cdot \frac{\partial f}{\partial \mathbf{v}} = \Omega. \tag{2.1}$$

In (2.1) the first two terms of the left hand side represent the so-called 'streaming process' of particle advection and the remaining term accounts for an external force, $\mathbf{F}$ where m is the mass of the particles. The right hand side describes effects of inter particle collisions on the distribution function through a collision operator Ω. From these equations, the macroscopic properties of density, momentum, and energy

density, $\rho\epsilon$ are given by the moments of (2.1) as

$$\rho = \int f d\mathbf{v} \tag{2.2}$$

$$\rho\mathbf{u} = \int \mathbf{v} f d\mathbf{v} \tag{2.3}$$

$$\rho\epsilon = \frac{1}{2}\int (\mathbf{v}-\mathbf{u})^2 f d\mathbf{v}. \tag{2.4}$$

The "lattice" of the Lattice Boltzmann Equation (LBE) comes from the discretization of time and velocity for (2.1). When discretizing the momentum space, the discretization must maintain the conservation rules of quantities in (2.2) to (2.4). Additionally, the discretization of the configuration space must be that of a lattice and the mesh must be evenly spaced. Many 1D, 2D, and 3D lattices are well established (Succi, 2001; Mohamad, 2011). In this work we will be using the so-called 'D2Q9' lattice (Dimension 2, with 9 velocities) shown in figure 2.1. All following discussion will use this lattice. By satisfying isotropy and symmetry, the speed of sound for a suitable lattice can be derived as in Mohamad (2011). For the D2Q9 lattice the dimensionless speed of sound is $c_s = 1/\sqrt{3}$.

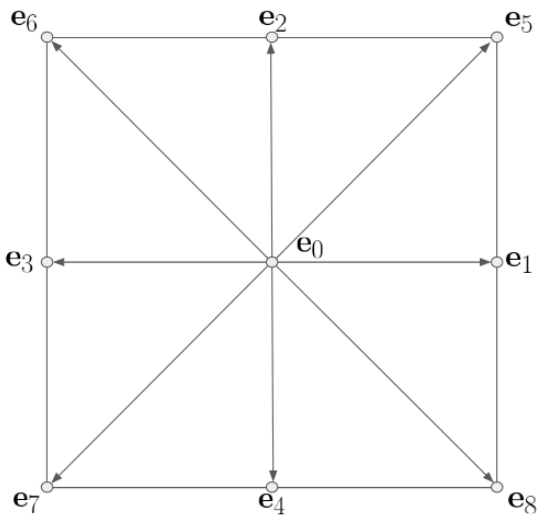


Figure 2.1: Discrete velocity vector lattice for typical 2D velocity discretization (D2Q9). $e_0, e_1, ..., e_5$ have lattice speed 1, and e_i for $i \geq 5$ have speed $\sqrt{2}$.

In this picture, a particle traveling with some discretized velocity $\mathbf{e_i}$ for the discretized time step Δt would then move to the adjacent grid point in the direction of $\mathbf{e_i}$. The resultant discretization of (2.1) with a valid lattice is given by

$$f_i(\mathbf{r} + \mathbf{e}_i\Delta t, t + \Delta t) = f_i(\mathbf{r}, t) + \Omega(f_j^{eq}(\mathbf{r}, t), f_i(\mathbf{r}, t)) + \Delta t F_i \tag{2.5}$$

where the subscript i is used to index the set of discrete velocities shown in figure 2.1. In this discretization, $f_i(\mathbf{r}, t)$ is the particle distribution such that there exists $f(\mathbf{e}_i, \mathbf{r}, t)$ particles by mass at time, t, position $\mathbf{r}$, and velocity $\mathbf{v} = \mathbf{e_i}$. The *equilibrium* value of the distribution function,f_i^{eq}, is typically given by a Maxwellian distribution as discussed in §2.1.1. The collision matrix, Ω, is a function of f whose eigenvalues give the time scales for relaxation to the local equilibrium and is assumed to be linear in f.

To verify that this formulation of (2.5) is actually applicable for hydrodynamics, one can derive the Navier-Stokes equations in the weakly compressible limit. To do this, we need to first identify appropriate forms of the collision matrix and the discrete local equilibrium f_i^{eq}. The most commonly used forms of these objects are those given by the Lattice Bhatnagar-Gross-Krook Model (Bhatnagar et al., 1954).

2.1.1 Lattice Bhatnagar-Gross-Krook model

Inspired by the Bhatnagar-Gross-Krook operator of the traditional Boltzmann Equation (Bhatnagar et al., 1954), the Lattice-Bhatnagar-Gross-Krook model (LBGK) is probably the most widely used form of the LBM (Mohamad, 2011) and is the simplest form of the collision matrix. In the LBGK, the collision operator takes the form

$$\Omega = -(f_i - f_i^{eq})/\tau \tag{2.6}$$

where τ is the relaxation timescale of the system corresponding to a diagonal collision matrix Ω_{ij}. In this formulation, momentum exchange from particle collisions is treated as a relaxation process of the local distribution, f_i, towards the equilibrium distribution, f_i^{eq}. Substituting (2.6) into (2.5) yields

$$f_i(\mathbf{r} + \mathbf{e}_i\Delta t, t + \Delta t) = f_i(\mathbf{r}, t) - \frac{1}{\tau}[f_i(\mathbf{r}, t) - f_i^{eq}(\mathbf{r}, t)] + \Delta t F_i. \tag{2.7}$$

Using (2.2) and (2.3), we can recover the macroscopic equations in the discretized system using the D2Q9 lattice depicted in figure 2.1 via

$$\sum_{i\in\{0,1,\ldots,8\}} f_i = \rho, \qquad \sum_{i\in\{0,1,\ldots,8\}} f_i\mathbf{e_i} = \rho\mathbf{u}. \tag{2.8}$$

With the collision operator of (2.6), the only unknown remaining in (2.7) is the form of the equilibrium distribution.

From Succi (2001), the equilibrium distribution for this system is given by a Maxwellian distribution. The Maxwellian (or Maxwell-Boltzmann) distribution is the

equilibrium distribution of molecular speeds predicted for an ideal gas from kinetic theory in statistical mechanics. For a 2D fluid in equilibrium, the probability of finding a particle of velocity $\mathbf{e_i}$ moving in a medium with macroscopic velocity $\mathbf{u}$ is given by

$$f_i^{eq} = \left[\sqrt{\frac{\rho}{2\pi c_s^2}}\right]^3 e^{-\frac{(\mathbf{e_i}-\mathbf{u})^2}{2c_s^2}}. \tag{2.9}$$

Using a discretized velocity distribution such as the D2Q9 of figure 2.1, the form of this Maxwellian for implementation in (2.7) is typically expanded to 2nd order as

$$f_i^{eq} = \rho w_i \left[1 + \frac{\mathbf{e}_i \cdot \mathbf{u}}{c_s^2} + \frac{(\mathbf{e}_i \cdot \mathbf{u})^2}{2c_s^4} - \frac{u^2}{2c_s^2}\right] \tag{2.10}$$

where w_i is the weight of the ith velocity of the distribution function determined by enforcing isotropy and a normalization condition as in Mohamad (2011). For the D2Q9 lattice of figure 2.1 this has values $w_0 = 4/9$, $w_1 = w_3 = w_5 = w_7 = 1/9$ and $w_2 = w_4 = w_6 = w_8 = 1/36$.

With both a collision operator, and this form of the equilibrium distribution, similarity to the Navier-Stokes equations can be demonstrated via a multi-scale expansion known as the Chapman Enskog method. The Chapman Enskog method uses the timescale separation between the mean free time between successive collisions and the time scale of evolution of the fluid to recover the Navier-Stokes equations from (2.7) with the equilibrium distribution of (2.10). This method successfully recovers the Navier-Stokes stress tensor up to second order in the Mach number $u/c_s = Ma$ where u is a typical velocity scale of the flow (Succi, 2001, Chapter 4). The assumption of the separation of scales chosen also implies that this similarity is valid for $Ma << 1$ which will be important for the discretization choices in later sections.

2.1.2 Scalar fields in the LBM

The implementation in the LBM of scalar fields, such as salt or temperature, has been done in several different ways (Guo et al., 2002; Eggels and Somers, 1995; He et al., 1998). The method used in this work is the Multiple Distribution Function (MDF) approach first developed in Eggels and Somers (1995). Another popular method derives an LBE thermal model by discretizing the continuous evolution equation for the internal energy distribution using the same method used to derive the standard LBM (He et al., 1998). The primary difference between these two methods is that the methodology of He et al. (1998) is able to incorporate viscous heat dissipation and compression work done by the pressure. Neither of these are required in the problem

to be addressed in this work. Furthermore, the implementation of the MDF approach is simpler.

The MDF method includes scalar fields in much the same way as the velocity field outlined above. We define an unnormalized PDF of a scalar field $g_i(\mathbf{r}, t)$ as in the vector case. The relaxation time of the scalar PDF is governed by the diffusion coefficient as opposed to how the relaxation of velocity is related to the viscosity (see §2.2). The macroscopic value of the scalar is recovered in the same manner as (2.8). For some scalar χ, and the D2Q9 lattice of figure 2.1, the value of χ at a grid cell is

$$\sum_{i \in \{0,1,\ldots,8\}} g_i = \chi. \tag{2.11}$$

Scalar fields utilize a slightly different equilibrium function in order to reflect the characteristics of advective and diffusive transport. In general these can be determined via non-dimensionalizing the relevant equations and scaling as in Mohamad (2011), here we skip the derivation and present the results. For diffusion only, g_{eq} is given by

$$g_i^{eq} = w_i \chi(\mathbf{r}, t), \tag{2.12}$$

which is the formulation used in (2.10) with $\mathbf{u} = 0$. With advection, we add the 2nd term of (2.10) and this becomes

$$g_i^{eq} = w_i \chi(\mathbf{r}, t) \left[1 + \frac{e_i \cdot \mathbf{u}}{c_s^2} \right]. \tag{2.13}$$

In our model, we also want to use scalar fields to provide a buoyancy force based on changes in density due to temperature and salinity. To do this we use the Boussinesq approximation, and implement a body force as developed in Guo et al. (2002). If density depends on a single component χ, the dimensionless buoyancy force is given as

$$\mathbf{F} = -\rho_0 \mathbf{g} \beta \frac{(\chi_{x,y} - \chi_{ref})}{\Delta \chi}$$

where ρ_0 is the density of the fluid with $\chi = \chi_{ref}$, $\chi_{x,y}$ is the macroscopic value of the scalar at a particular grid cell as determined by (2.11), $\mathbf{g}$ is the gravitational acceleration, and β is the coefficient of expansion of the fluid by changing values of χ. If we use multiple scalar fields, such as for temperature and salt, then we can easily include the effects of both in this body force term as done in §2.2.

2.2 Discretization of the physical system

Like all computational methods, we must first discretize the simulation both spatially and temporally. To do this, we first convert the dimensional system to a non-dimensional form. We will do this step as it pertains to the mathematical system of chapter 3 in §3.2.2. For this section, we assume that the governing equation is already represented in dimensionless form. Following this, we take the dimensionless system and through scaling arguments derive appropriate 'lattice units', which are the appropriate increment of the non-dimensionalized physical variables that correspond to the unit grid cell spacing and velocities of the LBM grid. The subscript "lb" in this section refers to 'lattice units.' Dimensionless variables of the Navier-Stokes system will be denoted with a subscript d.

The scaling to determine the length of a grid element in the physical system from the unit lattice scale of the LBM, Δx_{lb}, is defined to be the characteristic length H_d of the dimensionless system divided by the number of grid cells of unit lattice length, N, used to discretize said length within the LBM. Similarly, Δt_{lb} is given by the number of iterations of the LBM, N_{iter}, used to reach the characteristic time of the dimensionless system $t_{0,d}$ so that Δx_{lb}, Δt_{lb} have units (1/lattice length) and (1/lattice time) respectively, with

$$\Delta x_{lb} = H_d/N, \quad \Delta t_{lb} = t_{0,d}/N_{iter}.$$

To set the discretization of the computation one can choose Δx_{lb} and Δt_{lb} and thus set the number of unit lattice grid cells N and time-steps N_{iter} of the simulation as we will do in the next section §2.2.1. In the dimensionless system, if H_d, $t_{0,s}$ are set to unity we have

$$\Delta x_{lb} = 1/N \quad \Delta t_{lb} = 1/N_{iter}.$$

To convert the dimensionless quantities of viscosity (ν_d), diffusion of heat and salt ($D_{q,d}$ and $D_{s,d}$ respectively) as well as the dimensionless velocity, u_d into lattice units, we use Δx_{lb} and Δt_{lb} (units 1/lattice length, and 1/lattice time, respectively) to non-dimensionalize the values of the corresponding lattice quantities as

$$
\begin{aligned}
u_d &= \frac{\Delta x_{lb}}{\Delta t_{lb}} u_{lb} \\
\nu_d &= \frac{1}{Re} = \frac{\Delta x_{lb}^2}{\Delta t_{lb}} \nu_{lb} \\
D_{q,d} &= \frac{1}{Pr \cdot Re} = \frac{\Delta x_{lb}^2}{\Delta t_{lb}} D_{q,lb} \\
D_{s,d} &= \frac{1}{Sc \cdot Re} = \frac{\Delta x_{lb}^2}{\Delta t_{lb}} D_{s,lb}.
\end{aligned}
$$

Dimensionless salt and temperature (S_d and T_d) are scaled as

$$
\begin{aligned}
T_d = \frac{T_{lb}}{\Delta T_{lb}} &\implies T_{lb} = T_d \Delta T_{lb} \\
S_d = \frac{S_{lb}}{\Delta S_{lb}} &\implies S_{lb} = S_d \Delta S_{lb}.
\end{aligned}
$$

Here ΔT_{lb}, ΔS_{lb} must be chosen, though it is not a crucial choice as the scaling simply sets the conversion to the physical system and doesn't alter any properties of the flow (Latt, 2008). In this work we set these to unity so that $T_{max} = S_{max} = 1$ and $T_{min} = S_{min} = 0$. Lastly, we can convert the buoyancy force by

$$
F_{b,d} \equiv \frac{(S_d - T_d R_\rho)}{Fr^2} = \frac{\Delta x_{lb}}{\Delta t_{lb}^2} F_{b,lb},
$$

or

$$
F_{b,lb} = \frac{\Delta t_{lb}^2}{\Delta x_{lb}} \frac{1}{Fr^2} \left(\frac{S_{lb}}{\Delta S_{lb}} - \frac{T_{lb}}{\Delta T_{lb}} R_\rho \right). \tag{2.14}
$$

where the full non-dimensionalization and expression for $F_{b,d}$ is derived in §3.2.2 with the Froude number, Fr, and density ratio, R_ρ, to be derived in §3.2.1.

Furthermore, under this scaling, it can be shown that the relaxation timescale τ is related to the non-dimensional parameters of the physical system by (as shown in Mohamad, 2011, Chapter 8)

$$
\tau = \frac{\nu_{lb}}{c_s^2} + \frac{\Delta t_{lb}}{2} \tag{2.15}
$$

or for the scalar case with timescale τ_χ

$$
\tau_\chi = \frac{D_{\chi,lb}}{c_s^2} + \frac{\Delta t_{lb}}{2} \tag{2.16}
$$

where $D_{\chi,lb}$ is the diffusion coefficient of χ in lattice units.

2.2.1 Understanding error: choosing Δx_{lb} and Δt_{lb}

To complete the scaling of the dimensionless system to lattice units we must select the discretization values for Δt_{lb} and Δx_{lb}. The first concern for choosing Δt_{lb} is to ensure that $u_{lb} < c_s$ where c_s is the speed of sound in the LBM. This is primarily because the LBM is unstable with supersonic flows as the equilibrium is based on an expansion for small Mach numbers as mentioned in §2.1.1 (Chen and Doolen, 1998). From above, $u_{0,lb} = u_{0,d}\Delta t_{lb}/\Delta x_{lb}$ with the 0 subscript indicating the characteristic value. Using the D2Q9 lattice we have $c_s = 1/\sqrt{3}$ (Mohamad, 2011). So then a maximal constraint is given as $\Delta t_{lb} < \Delta x_{lb}/\sqrt{3}$ if the dimensionless velocity is scaled with $u_{0,d} \leq 1$.

Furthermore, because the LBM is a quasi-compressible solver, the model enters a weakly compressible regime for the pressure of the fluid (Mohamad, 2011; Bhatnagar et al., 1954). As we are trying to solve for incompressible flow, these compressibility effects impact the numerical accuracy of simulations with an error that scales as $O(Ma^2)$ (Latt, 2008; Mohamad, 2011; Succi, 2001). Thus to keep the error due to compressibility effects low, it is necessary to keep the Mach number low. The Mach number is given in the LBM by $u_{0,lb}/c_s$ and so is proportional to $\Delta t_{lb}/\Delta x_{lb}$. Therefore the error due to compressibility scales as $O[(\Delta t_{lb}/\Delta x_{lb})^2]$.

In the LBM, the general form of error dependence is given by

$$\begin{aligned} E_{total} &= E_{\Delta x_{lb}} + E_{\Delta t_{lb}} + E_{Ma} \\ &= O(\Delta x_{lb}^2) + O(\Delta t_{lb}^2) + O[(\Delta t_{lb}/\Delta x_{lb})^2]. \end{aligned} \tag{2.17}$$

where the first two terms describe the usual spatial and temporal discretization error, and the last is the Mach number dependent error discussed above. To minimize the error one can thus let $\Delta t_{lb} \sim \Delta x_{lb}^2$ as this keeps the Mach number dependent error and the grid resolution error on the same order. This is not always desirable however as this may make the simulation run time too long to be feasible. An alternative approach is to prescribe a Mach number and Δx_{lb} thus fixing Δt_{lb} as $\Delta t_{lb} = Ma\Delta x_{lb}/\sqrt{3}$. This method introduces a discretization error of a few percent for $\Delta t_{lb}/\Delta x_{lb}$ but dramatically reduces computational cost. With this restriction all that is left to do is fix Δx_{lb}, and choose $Ma << 1$

A number of ad-hoc guides for choosing Δx_{lb} exist to ensure the stability of the simulations (Mohamad, 2011; Succi, 2001). One we will follow here is to require that $N \cdot \nu_{lb} = \nu_{lb}/\Delta x_{lb} > 1$. To do this we first give an initial choice of N and then check if the condition is met, if not we increase the choice for N by 10 and then check again, repeating this process until the inequality is satisfied. This ensures that a Reynolds

number using the lattice velocities, $\mathbf{e_i}$, is order one or smaller which implies the grid scale Reynolds number in physical units is much smaller than one, if $Ma << 1$.

2.3 Boundary conditions

A distinct advantage of the LBM is the ease with which complex geometries and irregular boundary conditions can be implemented. We firstly consider the implementation of a no-slip and no-penetration boundary condition in §2.3.1, followed by boundary conditions with a known velocity in §2.3.2, isothermal boundary conditions in §2.3.3 and then absorbing boundary conditions in §2.3.4 and the parallelization scheme in §2.4.

2.3.1 No-slip no-penetration condition

No-slip and no penetration boundary conditions can be given by enforcing

$$\mathbf{u}(\mathbf{r}_w) = 0,$$

where $\mathbf{r}_w$ refers to an arbitrary location on the wall. To achieve this, we simply want the particles streaming in to the wall nodes to be reflected as outgoing populations

$$f_{\text{in}}(r_w) = f_{\text{out}}(r_w), \tag{2.18}$$

where 'in' and 'out' denote incoming/outgoing populations. In the case of a stationary boundary, we can then calculate the force at the boundary from the momentum exchange in each time step of unit length via (Ladd, 1994)

$$\mathbf{F_b} = 2 * (f_{in} - f_{out}) \cdot \mathbf{e_i}. \tag{2.19}$$

When the boundaries are aligned with the lattice (2.18) yields a perfectly elastic collision. In this formulation, particles are reflected directly back along the line of impingement as shown in Figure 2.2. With this implementation, the wall is actually mid way between the fluid nodes and a 'ghost node' which lies outside of the simulation domain but is used to determine the the reflections of f_i as in (2.18). For the scenario depicted in figure 2.2, a solid boundary at the top of the domain has incoming populations f_5, f_6 with their reflections f_7 and f_8 respectively. In this picture f_2 is also reflected the same way with f_4 (not shown). This method is sufficient to ensure conservation of mass and allows for increased accuracy and numerical stability as opposed to putting the boundary exactly on a specific index (Chun and Ladd, 2007).

Many different interpolation schemes for handling misaligned or curved boundaries have also been developed (Mei et al., 1999) but are not pursued here.

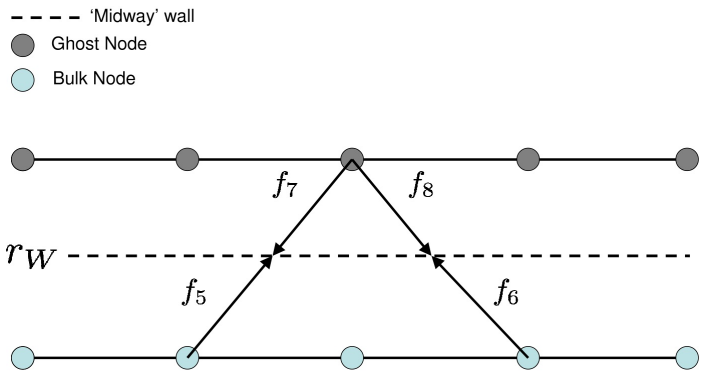


Figure 2.2: Flat solid boundary at the top boundary of a simulated flow with wall location $\mathbf{r_w}$. In this picture the wall is located halfway between the two computational rows with 'ghost-nodes' outside of the computational domain and bulk nodes within the fluid flow. The ghost nodes are used to calculate the reflection of particles at the wall which can then simulate reflection at the boundary by inward streaming from the ghost nodes to the bulk nodes. The incoming populations using the lattice of figure 2.1 are f_5, f_6 (shown), and f_2 (not shown) with their reflections given by f_7, f_8, and f_4 respectively. This formulation is known as the mid-way bounce back scheme for lattice Boltzmann models in the D2Q9 lattice (He and Luo, 1997). Figure credit: Mid-way bounce back scheme by Stefano Ubertini licensed under CC BY-NC-SA 3.0 uploaded to http://www.scholarpedia.org/article/Lattice_Boltzmann_Method

2.3.2 Boundary condition with known velocity

Here we recreate the derivation from Chapter 8.3 of Mohamad (2011) assuming the boundary is parallel to the grid. For the boundary at the left side of the domain, we need to identify the reflected values of f_5, f_1, and f_8 as well as the fluid density at the wall ρ_w. With a known velocity profile to be specified at a boundary we can use the first and second moments of the distribution function, (2.2),(2.3) to write

$$\rho = f_0 + f_1 + f_2 + f_3 + f_4 + f_5 + f_6 + f_7 + f_8 \tag{2.20}$$

and the momentum equations

$$\rho_w \mathbf{u} = f_1 + f_5 + f_8 - f_6 - f_3 - f_7 \tag{2.21}$$

$$\rho_w \mathbf{v} = f_5 + f_2 + f_6 - f_7 - f_4 - f_8 \tag{2.22}$$

with $\mathbf{u}$, $\mathbf{v}$ the prescribed x and y components of velocity. We can enforce that the flow is in equilibrium normal to the surface as in Zou and He (1997) yielding

$$f_1 - f_1^{eq} = f_3 - f_3^{eq}. \tag{2.23}$$

where f_1^{eq} and f_3^{eq} can be calculated using (2.10) with $\mathbf{u} = \mathbf{u}_{wall}$. We can substitute f_1^{eq} and f_3^{eq} to arrive at

$$f_1 = f_3 + \frac{2}{3}\rho_{wall}\mathbf{u}_{wall}. \tag{2.24}$$

.

Solving (2.20) -(2.24) for the remaining unknowns yields,

$$\rho_w = \frac{1}{1-\mathbf{u}_w}[f_0 + f_2 + f_4 + 2(f_3 + f_6 + f_7)], \tag{2.25}$$

$$f_5 = f_7 - \frac{1}{2}(f_2 - f_4) + \frac{1}{6}\rho_w\mathbf{u}_w + \frac{1}{2}\rho_w\mathbf{v}_w, \tag{2.26}$$

$$f_8 = f_6 + \frac{1}{2}(f_2 - f_4) + \frac{1}{6}\rho_w\mathbf{u}_w - \frac{1}{2}\rho_w\mathbf{v}_w, \tag{2.27}$$

Functionally this is similar to (2.18) with a modification for the wall velocity. We will use this in a number of our benchmark cases, and our primary simulation section for specifying inflow at fluid inlets. Establishing the same condition for boundaries at the top, bottom or right side of the domain follows a symmetric argument but is presented in Mohamad (2011).

2.3.3 Isothermal boundary conditions

We will also make use of isothermal/isohaline boundary conditions. In this section we will overview their implementation into the LBM using the PDF for scalars discussed in §2.1.2.

At the boundary, the system is in equilibrium, and therefore, the non-equilibrium part of the distribution functions must be zero such that the incoming/outgoing populations at the boundary must be equal and opposite and thus sum to zero such that

$$(g_{in}^{eq} - g_{in}) + (g_{out}^{eq} - g_{out}) = 0. \tag{2.28}$$

We can rewrite this using (2.12) assuming a no-slip boundary ($\mathbf{u} = 0$) as

$$g_i^{eq} - g_{in} + g_{out}^{eq} - g_{out} = w_{in}T_b - g_{in} + w_{out}T_b - g_{out} = 0. \tag{2.29}$$

As an example, let us consider a vertical wall on the left side of the domain with constant temperature $T = T_b$. The populations being 'streamed' into the boundary

from (2.5) using the D2Q9 lattice from figure 2.1 are g_3, g_6, g_7 with their opposites g_1, g_8, and g_6, respectively. In this scenario, the incoming populations are known from the streaming step, so all that remains is to solve for their reflections using (2.29). For g_1

$$g_1 = w_1 T_b + w_3 T_b - g_3 \tag{2.30}$$

and similarly for each other outgoing population. It is also possible to specify T_b as a function of position as we will do later in §3.2.

The non-dimensional heat flux at the boundary can be calculated similarly to (2.19) as in Mohamad (2011)

$$Q = \frac{k_d}{c_s^2 \tau_\chi}(g_{in} - g_{out}). \tag{2.31}$$

with k_d the dimensionless conductivity of the medium and τ_χ is the relaxation time. Other scalar fluxes, such as salt flux, can be calculated similarly with $D_{s,d}$ replacing k_d and g and τ_χ for the appropriate scalar field. This is equivalent to using a finite difference approach with $\Delta x = 1$:

$$Q = k_d(T[0] - T[1]) \tag{2.32}$$

This can be integrated over the boundary to determine an integrated heat flux at the interface, or re-arranged to establish a boundary condition for a constant heat flux. The process is identical for other scalar fields.

2.3.4 Absorbing boundary conditions

Internal wave propagation is a key feature of stratified flow. Initial simulations for this thesis generated internal waves, which were able to reflect off the domain boundaries. This reflection then caused a numerical instability in the simulation that made initial runs crash. To remedy this, we investigated a series of "non-reflecting boundary conditions" for the LBM as described in Kam et al. (2007). The implemented method is that of a sponge region, or "Absorbing Boundary Condition" (ABC). In typical direct numerical simulation solvers this scheme consists of extending the domain and adding an absorbing region established through the addition of dissipative forcing terms to the Navier-Stokes equations. Through these extra terms, a prescribed flow is achieved on the boundaries by the dissipation of disturbances within the 'sponge' via a relaxation towards specified flow properties. If tuned correctly, no reflections

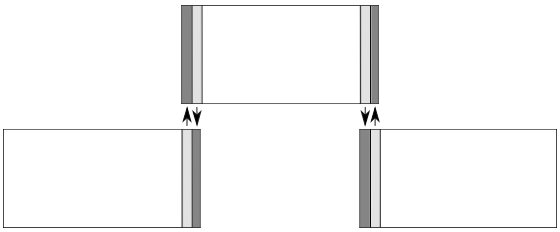


Figure 2.3: A minimalist representation of the parallel scheme. At the end of each time step, the segmented domains exchange information in the buffer region as shown. In this schematic, the light gray region is the last column in the domain before the buffer region represented by the darker gray. This same pattern would carry on for the beginning and end of the domain if periodic boundary conditions were in effect.

are detected at the boundary and thus no waves are reflected back into the domain. In a 2D LBM problem, this can be accomplished for the velocity field using

$$\frac{\partial f}{\partial t} + v \cdot \nabla f = -\frac{1}{\tau}\left[f_i(\mathbf{r},t) - f_i^{eq}(\mathbf{r},t)\right] - \sigma(f_i^{eq} - f_a) \tag{2.33}$$

where $f_a = f^{eq}(\mathbf{u}_0)$ is the equilibrium distribution function consistent with the target velocity $\mathbf{u}_0$, the damping rate is given by $\sigma = \sigma_m(\delta/d)^2$ where σ_m is a constant to be specified, d is the length of the sponge region and the variable δ is the distance inside the sponge region from the unmodified domain. In our simulation we divide the sponge region into sides, bottom and the overlapping corners with, σ/σ_m given by $(\delta_x/d_x)^2$, $(\delta_y/d_y)^2$ and $(\delta_x/d_x)^2 + (\delta_y/d_y)^2$ in each case where δ_x and δ_y indicate the horizontal and vertical distance inside the sponge domain.

The ABC method gradually relaxes the local distribution function towards the prescribed equilibrium distribution and through doing so dissipates the waves. As we will discuss in §3.2.3, care is needed when choosing both the length of the domain, d, as well as the strength of dissipation, σ_m. The implementation of this in the scalar fields follows a symmetric argument.

2.4 Parallel implementation

For the LBM, parallelization is mostly straightforward as the computation is entirely local, with the exception of the streaming process which communicates via a shift of values between adjacent cells. Thus the only thing to consider is when and how to communicate the streaming information between the sub-divided processes. Within my code I use the mpi4py package to implement the parallelization. In this case I split the domain into n subdomains, where n is the number of separate processes

(mpi ranks) and each subdomain extends the full vertical extent of the simulation. To illustrate this concept, consider a domain width, w, that is divisible by n such that $w/n = m \in \mathbb{Z}$. In the chosen implementation, each computational subdomain effectively has a width of $m+2$, the m columns in its domain and then a buffer column on each side that stores upstream and downstream information for the streaming step. After each time-step information is propagated from the adjacent ranks for the subsequent streaming as shown in figure 2.3.

2.5 Computational algorithm

The above LBM and boundary conditions were taken and coded into a series of scripts using the Python programming language for the purposes of simulating stably stratified flow beneath a pressure ridge. In this section I will outline the general procedure of the LBM code developed.

Prior to beginning the time stepping, we calculate the lattice values of Δx_{lb}, Δt_{lb}, u_{lb}, ν_{lb} and the diffusivities as in §2.2 based on the chosen values of the non-dimensional variables. With the relevant length and time scales chosen, we then initialize boolean arrays to indicate the location of the solid boundaries and sponge regions. Next, arrays are initialized for macroscopic density, velocity, and scalar values if required. With the domain extent arrays established we then subdivide each array into the desired number of sub-domains for parallelization as shown in figure 2.3.

With the initial setup of the lattice units and arrays, we then calculate the starting value of the momentum and scalar equilibrium distributions based on the specified initial conditions using (2.10). This distribution is copied for the initial PDFs such that $f = f_{eq}$ before the main loop. With the initialization of all necessary arrays, the algorithm now begins the main computation loop.

If it is not the first iteration, the macroscopic properties are recalculated, and the equilibrium distributions are then recalculated with said values using (2.10). At this time any body forces are calculated such as the buoyancy force of (2.14).

We now proceed to the 'collision step' of calculating the right hand side of (2.7) with buoyancy and sponge calculations included based on the problem being examined, or if the region is in the sponge region by including the last term of (2.33). Before proceeding to the 'streaming step' where particle advection occurs, information of the populations in the buffer regions as in figure 2.3 is exchanged. With this, the resultant PDF f_i is allowed to propagate in the direction $\mathbf{e}_i$ in the streaming step. A similar process is used for scalar PDFs.

With the streaming process concluded we can implement the relevant boundary conditions by modifying the values of the PDFs as discussed in the subsections of §2.3. During this step we can also calculate momentum and scalar fluxes as in (2.19) and (2.31).

The above process is then repeated for each iteration. In all the benchmark cases, as well as our simulations in §3.2, the simulations run until steady state. The method for verifying steady state differs depending on the case, but is most often achieved by placing thresholds on the variation in heat or momentum flux over a time period.

2.6 Benchmarking

As we develop the specific computational framework used in the following chapter, we first benchmark a number of relevant test cases. The first problem is that of flow around a cylinder placed asymmetrically in a channel, to verify the treatment of immersed no-slip, no-penetration boundaries of §2.3.1, velocity inlet, as in §2.3.2, and momentum exchange calculations of (2.19). For inclusion of scalar fields, we test the classic problem of Rayleigh-Bénard convection to validate the advective-diffusive heat transports discussed in §2.1.2, the scalar field boundary conditions of §2.1.2, and the treatment of the buoyancy force of (2.14). We note that salt and heat are treated in the same way, so this problem is sufficient to demonstrate the infrastructure for scalar fields in general. Each of these benchmarks were calculated using the parallel construction discussed in §2.4. The calibration of the sponge coefficient for the particular application of §3.2 will be examined later on in §3.2.3.

2.6.1 Flow around a cylinder asymmetrically placed in a channel

The first test case is to solve for flow past a cylinder asymmetrically placed in a channel. This problem has been used extensively as a benchmark for a large collection of fluid mechanics code (Schäfer et al., 1996) as well as for implementations of the LBM (Mussa et al., 2009). The flow configuration is the same as in Schäfer et al. (1996) and Mussa et al. (2009) and is illustrated in figure 2.4.

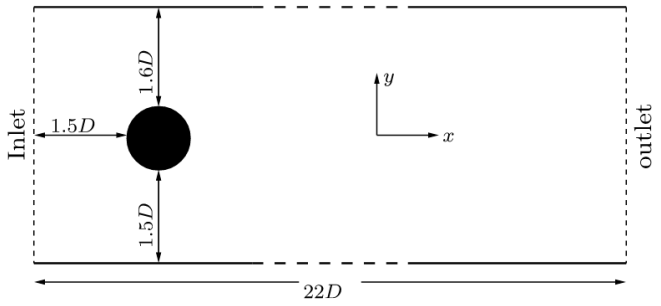


Figure 2.4: An inlet boundary condition of $U(0, y) = 4U_{max}y(H-y)/H^2$, $V(0, y) = 0$ is imposed on the left side, where U_{max} is the max inlet velocity, and H is the height of the domain, and flows past a cylinder slightly displaced from the centerline of the channel. No-slip no-penetration boundaries are imposed on the top and bottom. No normal gradient boundary condition is imposed on the right hand side. Diagram of cylinder placed asymmetrically in a channel from Schäfer et al. (1996).

In both cases to be considered, the inlet boundary condition in the horizontal direction is given by $U(0, y) = 4U_{max}y(H - y)/H^2$, $V(0, y) = 0$, where U_{max} is the max inlet velocity, V is the vertical component of the velocity, and H is the height of the domain. The Reynolds number in this scenario is given by $Re = \bar{U}D/\nu$ with $\bar{U} = 2U_{max}/3$ the average velocity of the inlet and D the cylinder diameter. At the outlet, a no gradient boundary condition $\mathbf{n} \cdot \nabla \mathbf{u} = 0$ is used. This no normal gradient condition is enforced by copying the populations normal to the boundary at the final grid cell and enforcing these values at the penultimate grid cell. Top and bottom boundaries as well as the immersed cylinder use the no-slip condition of §2.3.1. With this, (2.19) is applied on the cylinder to calculate the force. From this force we calculate the drag coefficient assuming a quadratic drag relationship as in Schäfer et al. (1996)

$$c_d = \frac{2F_x}{\rho \bar{U}^2 D} \quad , \quad c_l = \frac{2F_y}{\rho \bar{U}^2 D}$$

where F_x, F_y are the x and y components of (2.19).

In this benchmark we will look at two cases: laminar flow around the cylinder ($Re = 20$) and unsteady flow with periodic vortex shedding ($Re = 100$). In this section we will not enforce the selection of Δx_{lb} as outlined above in §2.2.1 as we will be comparing to the LBM scheme of Mussa et al. (2009) and so will match their resolution. We will also define $\Delta t_{lb} = \Delta x_{lb}^2$ for the same reason.

Case 1 (Re=20)

For the first case (Re=20), the flow is steady and a re-circulation bubble is formed behind the cylinder. The quantities of interest are the drag coefficient, c_d, and the

lift coefficient, c_l. We run simulations at a variety of resolutions as in Mussa et al. (2009) and compare the values of c_d and c_l with those of Schäfer et al. (1996) and Mussa et al. (2009).

	$D/\Delta x_{lb}$	10	20	30	40	80	NS
$\mathbf{c_d}$	BB	5.188	5.270	5.373	5.398	5.472	5.5700-5.5900
	Ref	6.171	5.816	5.755	5.6855	5.6108	
$\mathbf{c_l}$	BB	0.0889	0.0322	0.0208	0.0164	0.0119	0.0104-0.0110
	Ref	0.0354	0.0223	0.0186	0.0164	0.0129	

Table 2.1: Flow past a cylinder asymmetrically placed in a channel at Re=20. c_d and c_l refer to the drag and lift coefficients and BB denotes our bounce-back method outlined in §2.3.1, Ref refers to results of the LBM implementation of Mussa et al. (2009) which uses a higher order boundary condition and NS is the average result range from Schäfer et al. (1996)

In the first case of $Re = 20$ shown in table 2.1 and the first column of figure 2.5, at high resolution our results agree well with that of both Mussa et al. (2009) and Schäfer et al. (1996) at larger values of N with errors of order 1-2% for the drag coefficient c_d. The percentage difference is larger for c_l because this is a smaller quantity and thus has a larger % error from our discretization, but we achieve clear agreement with the benchmarks at large N. The convergence of the drag occurs from the opposite side of the value of Schäfer et al. (1996) compared to Mussa et al. (2009), though at high N the error is similar. This slightly increased error at small Re can be attributed to the use of higher order bounce-back methods for curved boundaries in Mussa et al. (2009) that are not implemented in our LBM code, which instead uses a staircase approximation to the curved surface. With the selection of Δx_{lb} and Δt_{lb}, the criterion mentioned in §2.2.1 of $N \cdot \nu_{lb} = \nu_{lb}/\Delta x_{lb} > 1$ is met at $N > 20$.

Case 2 (Re=100)

For the second case (Re=100), the flow is unsteady with a periodic oscillation on the down-wind side of the cylinder. Because of this oscillation, the drag and lift coefficients become time dependent. Therefore, we record the maximum values of the drag and lift for comparison to the simulations of Schäfer et al. (1996) and the LBM simulation of Mussa et al. (2009).

	D/N	10	20	40	80	NS
$\mathbf{c_d}$	BB	3.641	3.266	3.246	3.247	3.2200-3.2400
	Ref	3.951	3.329	3.241	3.266	
$\mathbf{c_l}$	BB	0.859	0.867	1.007	1.047	0.9900-1.0100
	Ref	0.974	0.844	0.922	1.007	

Table 2.2: Flow past a cylinder asymmetrically placed in a channel for $Re = 100$. c_d and c_l refer to the maximum drag and lift coefficients over time and BB denotes our bounce-back method taken from Ladd (1994) outlined in §2.18. Ref refers to Mussa et al. (2009) and NS to Schäfer et al. (1996).

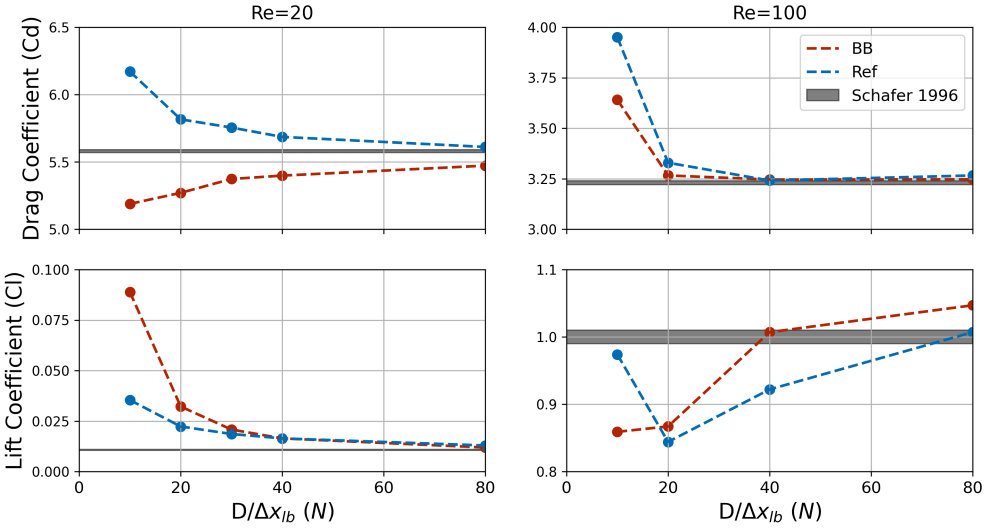


Figure 2.5: Plots of data within tables 2.1 and 2.2. The rows correspond to the drag and lift coefficient comparisons, respectively, and each column to a Reynolds number test case. The red circles, correspond to the points in each table for the LBM method developed here (Ref), and the blue circles the data from Mussa et al. (2009) (BB). The gray shaded region represents the data of Schäfer et al. (1996).

Similarly to the $Re = 20$ case we notice that both the LBM code developed here and that of Mussa et al. (2009) have a similar error when compared to the benchmark of Schäfer et al. (1996). At higher N these simulations have lower total error in c_d when compared with the earlier error in our results for $Re = 20$. This again suggests that the comparative accuracy with our boundary implementation compared to the higher order scheme used in Mussa et al. (2009) is restricted to low Re. For these simulations, $N \cdot \nu_{lb} = \nu_{lb}/\Delta x_{lb} > 1$ is met at $N > 100$. Failing to meet this criteria using only the mid-grid bounce back of §2.18 as opposed to the curved boundaries of Mussa et al. (2009) accounts in part for the observed error in c_l. This error was

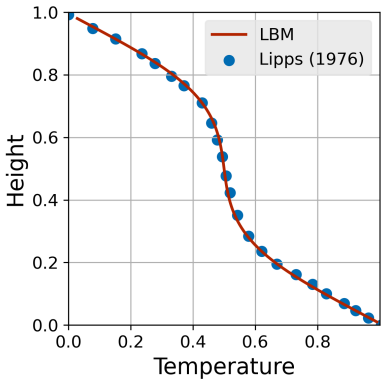
typically of a few percent, with errors of $\approx 5\%$ for the lift coefficients when compared to the results of Mussa et al. (2009) for the higher resolution cases.

2.6.2 Rayleigh-Bénard

The classic problem of Rayleigh-Bénard convection is used to benchmark the accuracy of the scalar MDF approach outlined in §2.1.2, as well as the scalar boundary conditions and buoyancy force outlined in §2.3.3 and (2.14), respectively. We consider similar metrics to the benchmarking test of Toppaladoddi et al. (2015). For this simulation, we examine a rectangular box of fluid with height, H, and width, L determined by the aspect ratio of the desired benchmark ($L = 3.117H$ for Clever and Busse (1974), $L = 1.222H$ for Lipps (1976)). The fluid is cooled at the top by a horizontal plate maintained at temperature $T_0 - \Delta T/2$ and heated from below by a plate with $T_0 + \Delta T/2$. In these simulations, the initial temperature profile is a linear profile from $T_0 + \Delta T/2$ at $y = 0$ and $T_0 - \Delta T/2$ at $y = H$. The initial flow field is stationary with $\mathbf{u} = 0$. At the start of the simulation, an arbitrary perturbation to the flow field is introduced to accelerate the onset to convection as $T(x, H/2) = T_0 + 10^{-2}\sin(x/L)$.

The physical parameters of the fluid are the kinematic viscosity, ν, thermal diffusivity, κ, and the coefficient of thermal expansion, β. In this setup with fixed aspect ratio, the relevant non-dimensional parameters that govern the flow are the Rayleigh number, $Ra = g\beta\Delta T H^3/\nu\kappa$, and the Prandtl number, $Pr = \nu/\kappa$. With these conditions the critical Rayleigh number for the onset of convection is $Ra_c = 1708$ for all values of Pr (Clever and Busse, 1974). We expect for simulations run with $Ra < Ra_c$ that the perturbation to the flow will decay to a state of no flow. If $Ra > Ra_c$, buoyancy driven convection will occur.

In the first test, we compare the horizontally averaged temperature profile for $Ra = 4000$ and $Pr = 0.71$ to the results from Lipps (1976) as shown in figure 2.7.



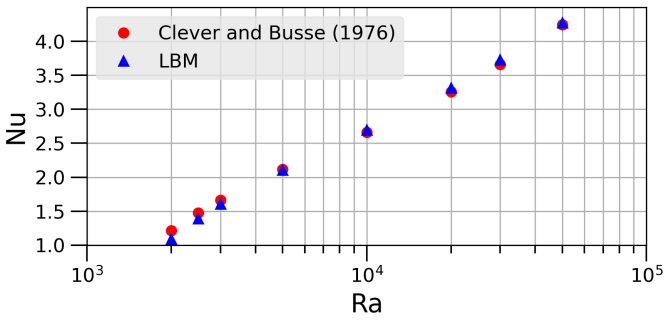


Figure 2.6: Comparison of results (red) and the present LBM code (blue)

Figure 2.7: Profiles of horizontally averaged temperature for Ra=4000 and Pr=0.71 (left) and Nusselt number vs Rayleigh number (right). In the left plot, the LBM (red line) is compared to results from Lipps (1976) (blue dots). In the right plot, our LBM code, (blue triangles) is compared to the results of Clever and Busse (1974) (red dots).

In the second test, we compare the effect of the Rayleigh number on the transport of heat through convection as measured in terms of the Nusselt number. The Nusselt number is defined as the ratio of total heat flux to the heat flux solely due to conduction and is given by

$$Nu = -\frac{k\langle\frac{d\overline{T}}{dz}\rangle + \rho c\langle\overline{wT}\rangle}{k\Delta T/H},$$

where k and c are the thermal conductivity and specific heat of the fluid, w is the vertical velocity component, $\overline{\ldots}$ and $\langle\ldots\rangle$ indicate temporal and horizontal averages. In figure 2.7, we compare values of the Nusselt number for varying Rayleigh numbers at $Pr = 0.71$ to the results of the Galerkin method of Clever and Busse (1974).

In both tests we have used Ma=10^{-3} with Δx_{lb} such that $\nu_{lb} * N > 1$. This choice then sets $\Delta t_{lb} = \Delta x_{lb}/(c_s \cdot Ma)$. It is important to note that at lower Rayleigh numbers (and thus lower Reynolds number) we have a larger error as in the low Re cylinder case of §2.6.1. For $Ra \geq 2000$, we have excellent agreement in both setups and are ready to apply the code developed herein to our thesis work with a typical error of $\approx 1\%$.

2.7 Summary

The LBM is an effective, and simple means of simulating fluid flows. With wide success in simulating a wide variety of fluids problems (Chopard et al., 2002; Artoli

et al., 2006; Peters et al., 2009; Jahanshaloo et al., 2013; Martinez et al., 1994; Mishra and Roy, 2007; He and Luo, 1997), the LBM offers a novel computational approach to the under-ice boundary layer. The primary advantages for our implementation are the ease of development, as well as the ability to directly compute momentum and scalar fluxes at the boundaries as in (2.19, 2.31). The code developed here has been benchmarked against several common problems to validate the implementation of the LBGK form presented in §2.1.1 as well as the relevant boundary conditions and inclusion of scalar fields and buoyancy fluxes as outlined in §2.3. We will now proceed to apply the computational infrastructure developed here to the first research question of the thesis: how do sea ice generated internal waves alter the heat and momentum flux at the ice-ocean interface?

Chapter 3

Sea ice generated internal waves: effects on ice-ocean heat and momentum balance

The seasonal evolution of the polar oceans can be well characterized by periods of ice formation and ice melt. In fall and winter, large scale ice formation releases dense salty brine into the surface boundary layer which can destabilize the upper ocean and give rise to buoyancy driven convection. In the summer and spring, ice melt deposits a layer of fresh and comparatively buoyant melt water at the surface thus stabilizing the upper ocean (Thomas and Dieckmann, 2010).

This stable stratification, when coupled with rough sea ice, can impact the dynamics of the ice-ocean boundary layer through generation of internal waves (McPhee and Kantha, 1989; Skyllingstad et al., 2003; Cole et al., 2018; Iakovlev, 2018). Within this chapter, I will investigate the role of internal wave generation in an idealized setting of a ridged ice floe moving over a stably stratified ocean, with a focus on ice-ocean exchanges of heat and momentum. For this problem we will use the computational infrastructure for the LBM developed and tested in the previous chapter.

The structure of this chapter is as follows: §3.1 serves to introduce the concept of stratified shear flow over topography. Here we review the historical development of relevant theory, and results in the literature from work on the atmosphere, ocean bottom, and under rough sea ice. Following this, we outline the geophysical setup to be used in §3.2 for stably stratified shear flow beneath a ridged ice floe. The mathematical formulation of the problem and an estimate of the relevant parameter values are presented in §3.2.2. The process for verifying computational convergence is outlined in §3.2.3. Following this we examine the results of these simulations in §3.3. In §3.3.1 and §3.3.2 I discuss the qualitative flow field and measured momentum

exchange and compare it to previous theory and results. I then investigate properties of heat exchange at the ice-ocean interface in §3.3.3, followed by a sensitivity study of the simulations in §3.3.4. A final discussion of key results and future work occurs in §3.4.

3.1 Stratified shear flow over topography (SSFOT)

Stratified shear flow over topography (SSFOT) is a fundamental aspect of the climate system. This type of flow appears both in the atmosphere with winds blowing over mountain ranges (dubbed orographic gravity waves) (Palmer et al., 1986), and in the ocean via flow over bottom topography (Zhang et al., 2017; Mashayek et al., 2017) or ocean flow beneath rough sea ice (McPhee and Kantha, 1989; Skyllingstad et al., 2003; Fer and Sundfjord, 2007; Cole et al., 2018). In the atmosphere, orographic gravity wave drag directly effects the angular momentum budget of the atmosphere and stratospheric temperatures (Teixeira, 2014). In the ocean, flow over bathymetry contributes to nutrient transport in coral reefs (Reid et al., 2019), diapycnal mixing in the deep ocean (Mashayek et al., 2017), and upper ocean flow past ice topography impacts sea ice drift and ice-ocean fluxes of heat and momentum (McPhee and Kantha, 1989; Cole et al., 2014; Skyllingstad et al., 2003)

The review of the foundations and geophysical applications of SSFOT presented here will be split up into four parts. In §3.1.1 we review the theoretical background for SSFOT. In §3.1.2 we review the relevant results from atmospheric flows over topography and in §3.1.3 we examine the relevant literature of SSFOT at the ocean bottom. Lastly, in §3.1.4 we examine the theoretical and observational work on generation of internal waves due to flow past sea ice.

3.1.1 Theoretical developments of SSFOT

Throughout this section we will focus on incompressible fluids such that $D\rho/Dt = 0$ implying that the conservation of mass equation becomes

$$\nabla \cdot \mathbf{u} = 0. \tag{3.1}$$

One of the fundamental quantities for continuously stratified fluids is the buoyancy (Brunt–Väisälä) frequency, N given by

$$N^2 = -\frac{g}{\rho}\frac{d\rho}{dz} \tag{3.2}$$

for an incompressible fluid (Vallis, 2017). The buoyancy frequency represents the response of a fluid parcel to unforced vertical oscillations and is the fastest frequency buoyancy driven fluctuations can achieve. This parameter is commonly derived by examining a parcel of fluid displaced vertically in a continuously stratified flow (Vallis, 2017). After this initial displacement, the fluid parcel experiences a restoring force due to buoyancy. This restoring force sets up an oscillation with frequency given by (3.2). This oscillation has the potential to create a travelling wave through a pycnocline within the media, known as an internal wave.

We can examine a simplified case to gather an initial understanding of internal waves before proceeding to a more detailed examination. As in Vallis (2017), for a linearly stratified Boussinesq fluid on an f-plane, the dispersion relation for plane wave disturbances proportional to $\exp(ik_x x + ik_y y + ik_z z - i\omega t)$ about a state of rest is given by

$$\omega^2 = \frac{N^2(k_x^2 + k_y^2) + f^2 k_z^2}{k_x^2 + k_y^2 + k_z^2} \tag{3.3}$$

for wave number $\mathbf{k} = (k_x, k_y, k_z)$, Coriolis parameter f and angular frequency ω. Looking at the numerator, if $N^2(k_x^2 + k_y^2) >> f^2 k_z^2$, the impact of Coriolis forces on these internal waves can be neglected. We will focus primarily on this limit of negligible Coriolis effects below.

In the geophysical system, a common mechanism to generate the initial displacement is due to flow over topography such as mountains or sea mounts. In these instances, values of N are typically $\mathrm{O}(10^{-2}-10^{-4})(\mathrm{s}^{-1})$ with N^{-1} the response timescale of stratification. This timescale is often shorter than many in the Earth system and so SSF work often takes the approach of expressing the motion as perturbations to a basic state in hydrostatic equilibrium (Baines, 1998).

The theoretical history of SSFOT has focused primarily on two different approaches: The Taylor-Goldstein Equation and Long's model.

3.1.1.1 The Taylor-Goldstein equation

The Taylor-Goldstein Equation is a linearized form of the inviscid Navier stokes equations under the Boussinesq approximation (see Vallis (2017)) as derived independently by G.I. Taylor (Taylor, 1931), S. Goldstein (Goldstein, 1931), and B. Haurwitz (Haurwitz, 1931). It is given here assuming a Fourier decomposition in x and y as in Lam (2013),

$$\frac{\mathrm{d}^2\hat{\omega}}{\mathrm{d}z^2} + \left[\frac{N^2(k_x^2+k_y^2)}{\Omega^2} + \frac{U''k_x + V''k_y}{\Omega} - (k_x^2+k_y^2)\right]\hat{\omega} = 0. \tag{3.4}$$

Here $\Omega = \omega - \mathbf{U}\cdot\mathbf{k}$ is the Doppler shifted-intrinsic frequency of the wave, k_x and k_y are the horizontal wave numbers, $\hat{\omega}$ is the Fourier transform of the vertical velocity, U'' and V'' are the second derivatives of U and V with respect to z, and $\mathbf{k}$ is the wave vector $\mathbf{k} = (k_x, k_y, k_z)$.

Applications of the Taylor-Goldstein equation to SSFOT often utilize a boundary geometry prescribed by the so called "witch of Agnesi" profile given by Agnesi (1748)

$$y(x) = \frac{ha^2}{x^2+a^2} \tag{3.5}$$

where h is the maximum height of the curve and a its characteristic half-width. The use of the witch of Agnesi is ubiquitous primarily due to its simple decomposition into Fourier space which, when coupled with (3.4), allows for a much more tractable problem compared to other more complex boundary geometries (Lam, 2013). In the geophysical system, topography often has more complex geometry with jagged edges. These edges may permit boundary layer separation as the characteristic length scale goes to 0 at the edge (Sutherland et al., 2013), but this flow feature is not permissible in the theoretical work reviewed in this section.

We can determine some key governing parameters of SSFOT by examining the 2D steady state form of this equation as given by

$$\hat{w}''(z) + [l(z)^2 - k^2]\hat{w}(z) = 0 \tag{3.6}$$

where the function $l(z)$ is the Scorer parameter

$$l^2(z) = \frac{N^2}{U(z)^2} - \frac{U''(z)}{U(z)}. \tag{3.7}$$

If U is a constant background wind profile, and we have static stability with N a constant, then $l(z)$ is a real valued constant in time, and one can solve (3.6) assuming a lower boundary condition of no normal-flow. As in Lam (2013), under these assumptions (3.6) has solutions

$$\hat{w}(z) = \hat{w}(0)e^{i\sqrt{l^2-k^2}z} \text{ if } l^2 > k^2 \tag{3.8}$$

$$\hat{w}(z) = \hat{w}(0)e^{-\sqrt{l^2-k^2}z} \text{ if } l^2 < k^2. \tag{3.9}$$

These solutions correspond to different characteristic wave behaviours. In (3.8), if $l^2 > k^2$, the solution is characterized by oscillatory waves. In (3.9) the solution is instead a decaying exponential implying that waves are evanescent. Under the earlier assumptions, $l^2 = N^2/U^2$, and so we can relate this to a transition between the two solutions occurring at $N^2/(k^2U^2) = 1$. A physical justification of this regime shift is given in Nappo (2012) and is presented here. We can rewrite this transition criterion as $N^2/(k^2U^2) = N^2/(1/t_{adv})^2$ where t_{adv} is the time for the flow to complete an oscillation by advection. This rewriting then suggests that an oscillatory wave can only exist when $l^2/k^2 > 1$. This in turn implies that the advection time t_{adv} of the wave has to be larger than the period of oscillation given by N. Reworded, if the oscillation speed of the generated wave is faster than the advective speed of the flow, the wave may propagate upstream. If this criterion cannot be met, then the wave is swept away before an oscillation can occur leading to evanescent (exponentially decaying) waves characterized by (3.9).

Performing an inverse Fourier transform of the solutions of (3.8) and (3.9), we can derive a solution for $w'(z)$, the vertical velocity as

$$w'(x,z) = 2Re\left[\int_0^l iUk\hat{h}(k)e^{i\sqrt{l^2-k^2}z}e^{ikx}dk + \int_l^\infty iUk\hat{h}(k)e^{-\sqrt{k^2-l^2}z}e^{ikx}dk\right]. \quad (3.10)$$

where $\hat{h}(k)$ is the Fourier transform of the topography. From (3.10), with a particular wave number k, the contribution of k is weighted by $k\hat{h}(k)$. If the contribution of the topography to the flow primarily occurs at $k < l$, the first integral dominates the solution. This limit is known as the hydrostatic limit and can be shown to be described by the condition $Na/U >> 1$ (Lam, 2013) where we recall that a is the characteristic horizontal length scale. Within this limit, solutions can be sought that neglect the second integral in (3.10) and thus simplify the problem. Due to the simplicity of the equations in the hydrostatic limit, much of the theoretical work using the Taylor-Goldstein equation takes place in this regime (Teixeira and Argain, 2020; Teixeira and Yu, 2014). Though some work has been done using computational approaches to solve the Taylor-Goldstein equation for systems in the non-hydrostatic regime, the Taylor-Goldstein equation is still linear (Wurtele et al., 1987; Iwasaki et al., 1989; Seo et al., 2018). In the non-linear regime, Long's model offers a promising alternative.

3.1.1.2 Long's model

Long's model is another analytical approach to stratified flow over topography that permits non-linearity in 2D problems (Long, 1953). Long's model is constructed with

a few assumptions: the boundary geometry is prescribed as being on a streamline consistent with the boundary being impermeable, the fluid is inviscid, and there is no disturbance of streamlines in the upstream direction. Instead of re-deriving the model here as done in Baines (1998), we here present the result and requisite boundary conditions.

Long's model yields

$$\nabla^2\delta + \kappa^2\delta = 0 \tag{3.11}$$

where

$$\kappa^2 = N(z_0)^2/U(z_0)^2 = -g\frac{\mathrm{d}\rho_0}{\mathrm{d}z_0}/2q, \tag{3.12}$$

with $q = \rho_0(z_0)U(z_0)^2/2$ and the variable $\delta(x,z) = z - z_0$ where z_0 is the vertical position of a streamline far upstream. κ is constant if $\mathrm{d}\rho_0/\mathrm{d}z_0$ is constant and q is commonly specified via $\mathrm{d}q/\mathrm{d}z = 0$ in most work (Baines, 1998). This restriction on q implies the flow is not sheared, but useful for building insight. Equations (3.11) and (3.12) are used alongside enforcing $\delta \to 0$ as $x \to -\infty$, and no upstream reflection of waves from the obstacle as in Miles and Huppert (1968). These conditions also imply that boundary layer separation is prohibited.

Early work using Long's model looked at cylindrical (Miles and Huppert, 1968) or generalized semi elliptical obstacle shapes (Huppert and Miles, 1969). These ellipses were characterized by an aspect ratio $\gamma = h/a$ with h the obstacle height and a the obstacle full width at half maximum similar to the witch of Agnesi shape of (3.5). The studies using Long's model primarily focus on the value of Nh/U, sometimes referred to as Long's number (Sutherland et al., 2013) or more simply as a vertical Froude number, as opposed to Na/U as in the Taylor-Goldstein equation. The latter parameter is still relevant for indicating the strength of hydrostatic effects and is implicitly adjusted by altering γ in these studies. Both of these studies examined a range of values for Nh/U, with those of Huppert and Miles (1969) shown in figure 3.1. From these calculations a few key processes are easily seen in the streamlines of figure 3.1. Firstly, it is clear that internal waves in this setup radiate diagonally away from the obstacle which is qualitatively consistent with the diagonal energy propagation indicated by the group velocity calculated from the classical linear wave problem (Vallis, 2017). This vertical propagation is an important factor for non-local wave breaking in the atmosphere and ocean as we will discuss later. Secondly, the tilting of the wave front increases with increasing Nh/U in figure 3.1 (b-c) beyond the critical point of $Nh/U = 0.5$ shown in 3.1 (a). The exact value of this critical point may

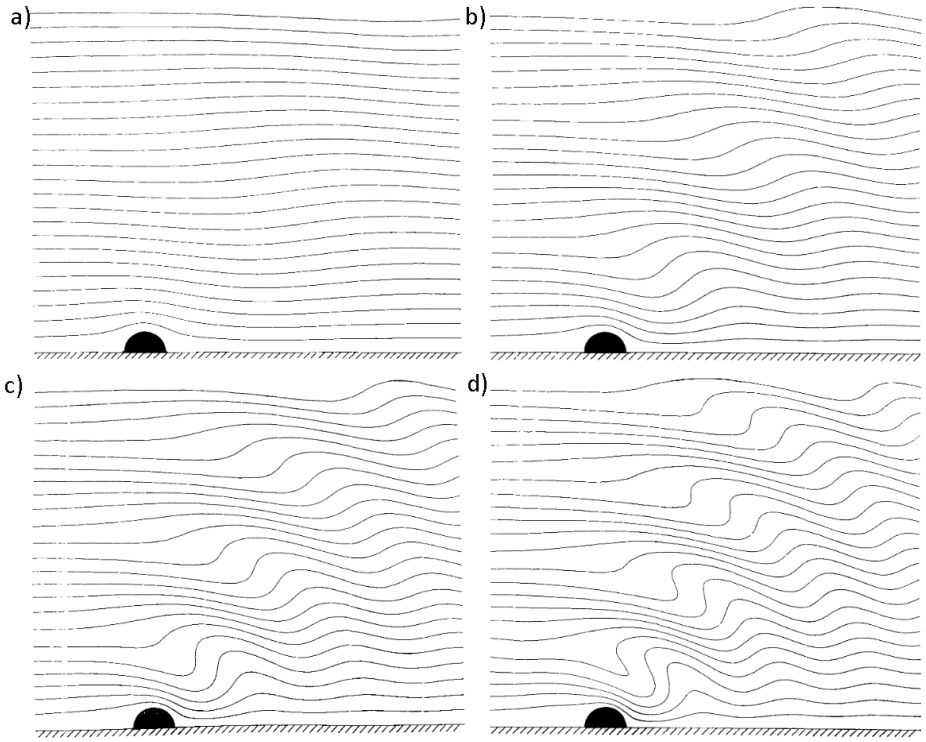


Figure 3.1: Streamlines showing Long's model solutions for uniform upstream flow over a semi circle a) $Nh/U = 0.5$, b) $Nh/U = 1.0$, c) $Nh/U = 1.27$, d) $Nh/U = 1.5$. Figures reproduced from figures A1-A4 of Miles and Huppert (1968).

vary due to a number of effects such as asymmetry of the topography, rotation, or 3d effects as discussed in Baines (1998). The critical point established here is analogous to the critical point in the solutions of the Taylor-Goldstein equation of (3.8) and (3.9) as the obstacle height can be associated with the wave number condition of $N^2/(k^2U^2)$ (see Aguilar and Sutherland, 2006).

In the calculations of Miles and Huppert (1968), these visual alterations to the flow field were accompanied by a significant change in the drag exerted upon the boundary. For ellipses where $0 \leq \gamma \leq 1$, the drag exerted on the boundary was proportional to $(Nh/U)^3$. However, if the flow was hydrostatic with $\gamma >> 1$ and $Na/U >> 1$ (similar to the limit found by work using the Taylor-Goldstein equation) the drag approximately scales proportional to Nh/U (Baines, 1998; Teixeira and Yu, 2014). In another study using Long's model, the drag was found to vary as $(Nh/U)^2$ for the quasi-linear regime, $(Nh/U)^n$ with $n \geq 2$ for the high-drag regime, and as $(Nh/U)^{1.3}$ for the blocked regime (Stein, 1992). This variation in the drag is potentially significant for a variety of atmospheric and oceanic processes discussed in §3.1.2 and §3.1.3 and will be a central facet of our investigation as it applies to sea

ice in §3.2.

3.1.2 Atmospheric development of SSFOT

In the atmosphere, SSFOT manifests due to flow over mountain ranges and gives rise to so-called 'orographic gravity wave drag' (Palmer et al., 1986). In this setting, the flow of the stably stratified surface layer of the atmosphere over hills and mountains can create internal waves through the processes outlined in the previous section. If these internal waves are not evanescent and thus able to propagate energy, and momentum, away from their sources, then they must exert a drag force on the mountains that generate them via Newton's third law. On large scales, this drag exerted by waves on mountains serves to slow down the overall atmospheric circulation (Teixeira, 2014) which through thermal wind balance effects stratospheric temperatures at high latitudes after the flow has adjusted to a geostrophically balanced state (McFarlane, 15 Jul. 1987).

Another important impact is the non-local breaking of internal waves in the atmosphere (Kim and Mahrt, 1992). As internal wave propagation has a vertical component seen in figure 3.1, orographic gravity waves are able to propagate upwards through the atmosphere until the waves break or reach a critical level due to variations in the Scorer parameter, (3.7), with height. Two processes have been identified to explain this non-local wave breaking. As the density of the atmosphere decreases with height, the amplitude of the internal wave may increase until it reaches a point where the amplitude becomes limited due to saturation effects and breaks (Lindzen, 1988). Variable wind profiles with height have also been known to influence this process through the formation of critical levels (Booker and Bretherton, 1967). A total critical level is defined by the level where the second term of the Scorer parameter of (3.7) has a singularity. In 2D flow this is reached if $U = 0$. Vertical flux of momentum due to wave breaking is also determined by 'partial critical levels' where the same singularity occurs, but for only some wavenumbers (Grimshaw, 1975).

The resultant non-local wave breaking has an appreciable effect on the mean atmospheric flow (Teixeira, 2014) through variable deposition of turbulence throughout the atmosphere as observed in Kim and Mahrt (1992). Unfortunately the scales of internal wave generation are often smaller than the resolution of global climate models and thus the aforementioned processes need to be parameterized (Palmer et al., 1986). These parameterizations are often developed by using results from idealized theoretical work (Gregory et al., 1998; Grimshaw, 1975; Lindzen, 1988; Xu et al., 2012). A number of incremental additions to existing parameterization schemes have

emerged to include new treatments of topography (Koo et al., 2018), non-linear effects (Miles and Huppert, 1968), non-hydrostatic effects (Keller, 01 Jul. 1994; Seo et al., 2018), f-plane and β-plane approximations (Jones, 1967; Janowitz, 1977), and more as covered in Teixeira (2014).

The limits within which parameterizations are developed in the atmospheric case are not immediately portable to other geophysical applications such as the ocean. For example, a key feature of the atmosphere is the significant density variation with increasing altitude. Density variations on the same scale are absent from the Earth's oceans (Vallis, 2017). Furthermore, the current atmospheric work also focuses on specific limits of the quantities for Nh/U and Na/U and typically proceeds in the hydrostatic limit of (3.4) (Teixeira, 2014; Lam, 2013). Though work done on wind shear, non-linear, and non-hydrostatic effects still exists (Lam, 2013; Eckermann et al., 2010; Grimshaw, 1975) and will prove valuable in both the oceanic and under ice settings, a number of knowledge gaps remain.

3.1.3 Oceanic SSFOT

Oceanic instances of SSFOT occur primarily in the deep ocean around large topographical features such as sea mounts or ridges (see review by Legg, 2021). Internal waves are also generated at the open ocean surface via wind and wave interactions though we omit discussion of this topic here with the exception of comparison to the under ice case in §3.1.4.

A significant body of existing work on SSFOT at the ocean bottom focuses on the impact of the generated internal wave spectra on diapycnal mixing (Mashayek et al., 2017), nutrient upwelling (Reid et al., 2019), and large scale oceanic overturning rate (Trossman et al., 2016). Around large oceanic topography, the limiting factor for the formation of persistent internal waves via the criteria discussed within §3.1.1 is most often the oceanic bottom velocity (Legg, 2021). The main mechanisms for providing significant bottom velocity have been tidally driven flow (Alford et al., 2014; Grimshaw and Helfrich, 2018), geostrophic flow (MacKinnon et al., 2017) and mesoscale eddies (Ferrari and Wunsch, 2009). A key development in the oceanic literature that is largely absent from the atmospheric case is the study of non-linear effects on the flow.

Non-linear effects on stratified flow have been observed to result in upstream blocking of flow and the creation of hydraulic jets (Winters and Armi, 2012; Klymak and Legg, 2010; Klymak, 2018). Upstream blocking of flow creates a region of stagnant fluid which effectively alters both the height and the width of the topography. This

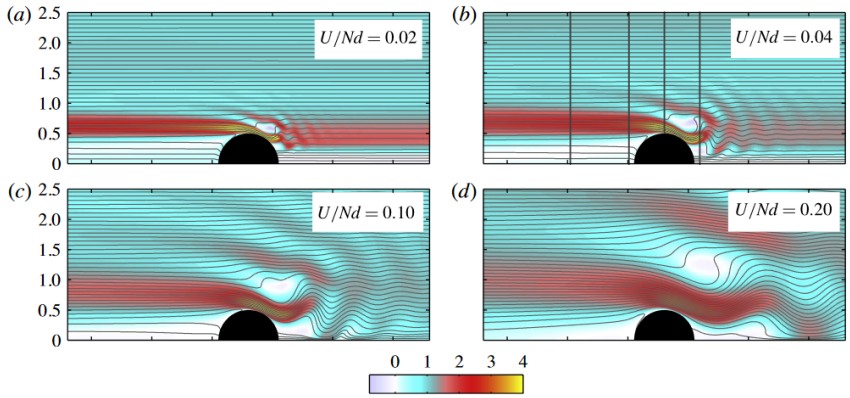


Figure 3.2: Figure 1 from Winters and Armi (2012) where a 2D Spectral method was used to simulate stratified flow above a half cylinder with diameter d ($2h$) and $Re = 91$. At these low values of Nh/U strong upstream blocking is apparent and has a corresponding down stream jet of width U/N. In this picture, the blocked fluid and the jet become dynamically uncoupled.

change in effective topography then alters effective values of Nh/U and Na/U, as described in Aguilar and Sutherland (2006). When blocking occurs, the flow develops a jet of height U/N above the topography, as in figure 3.2 (Winters and Armi, 2012). This jet of high flow velocity can, in turn, create a localized region of turbulence and in some cases the local value of Nh/U may change from super-critical to sub-critical via a hydraulic jump (Winters, 2016). These results have been numerically and experimentally verified at a modest Reynolds number of $Re = 91$, though variation in Re remains to be examined (Winters and Armi, 2012).

Experimental work has shown that non-linear effects may also lead to boundary layer separation (Aguilar and Sutherland, 2006). In the event of boundary layer separation, observed amplitudes of internal waves are smaller than those predicted by linear theory. This feature also corresponded with an observed increase of the resulting wave-induced drag compared to the expected values of linear theory.

In the deep ocean, internal wave generation serves to extract momentum from the background flow to create internal waves which may then break locally or non-locally and accelerate the expected energy cascade (Legg, 2021). In the ocean, this energy loss from the mean flow and the drag force due to topographical effects has been found to scale proportional to U^3 for $Nh/U << 1$ (Klymak and Legg, 2010). This result is similar to that of Miles and Huppert (1968) for 'squat semi-ellipses' discussed in §3.1.1 for constant N and h, and is recognizable as the linear limit identified in Long's model. For $Nh/U > 1$ however, blocking of the flow below the height of the obstacle

occurs (Lott et al., 2021) and the drag scales as U^2 (Klymak, 2018). The difference in scalings from the earlier values predicted in §3.1.1.2 may be due to the nonlinear effects such as blocking which is permitted in Klymak (2018) and is known to affect the properties of generated waves due to the stagnant flow essentially modifying the topography shape (Aguilar and Sutherland, 2006).

Many of the results discussed here and previously in §3.1.2 will serve to inform the interpretation of SSFOT as it pertains to the under ice boundary layer. The studies examined here predominantly deal with flows with uniform background flow as opposed to shear, though the physics are strongly related with sheared flow effects being represented by the full Scorer parameter (3.7). Many fundamental questions of interest are under studied within the literature in either setting. Fluxes of heat and salt at the ice-ocean interface for example, are hitherto unexamined but essential for understanding the role of sea ice in the climate system now and in the future.

3.1.4 Under ice internal wave generation

The internal wave field in the polar oceans is influenced on daily to seasonal time scales by variations in ice roughness, ice concentration, and wind forcing (Cole et al., 2018). Understanding the impacts of the sea ice generated wave field on vertical mixing in the Arctic, ice-ocean fluxes of heat, salt, and momentum, as well as ice drift are essential for making accurate predictions for a changing ice cover. Compared to lower latitudes where wind and waves are more readily able to generate internal waves at the ocean surface, the internal wave field in the Arctic is quite weak (D'Asaro and Morehead, 1991).

From in situ observations, variations in sea ice generation of internal waves are primarily determined by wind-driven accelerations of the ice (Fer, 2014), changes in mixed layer depth (and thus the surface stratification strength) (Halle and Pinkel, 2003), and pressure ridges (McPhee and Kantha, 1989) as observed in Cole et al. (2018, 2014). Each of these processes represents one of the fundamental quantities introduced in §3.1.1 for the governing parameters Nh/U and Na/U.

Within Cole et al. (2014), ice tethered profilers equipped with velocity sensors were used to estimate turbulent vertical heat, salt, and momentum fluxes just below the ice-ocean interface. From these measurements, locally generated internal waves were observed to correspond to elevated momentum flux. Internal wave activity was also seen to be associated with increased stratification within the mixed layer in the December-January period, with a positive upward salt flux, and little change in upward heat flux. In the periods of February-March and October-November, periods

of positive heat fluxes were observed indicating a dependence on the strength of the vertical gradient of temperature for correlation of internal wave activity and increased upwards heat flux. In the more recent study of Cole et al. (2018), internal wave activity was observed to depend on both ice concentration and ice roughness with newer, smoother ice, being associated with a reduced internal wave generation, and enhanced internal wave dissipation at the ice-ocean surface.

The effects of surface generated internal waves in the Arctic were first reported as the infamous 'dead water phenomena' observed by Nansen (1897) and then studied in the laboratory by Ekman (1904). In stratified fluids, bodies moving at the surface may generate internal waves which may result in a higher drag on the body than in a homogeneous fluid (Fourdrinoy et al., 2020). In the voyage of Nansen's Fram, this resulted in an exceptional reduction in speed. It has also been postulated that this phenomenon is responsible for the defeat of Antony and Cleopatra at the naval battle of Actium in 31 BC as the bulk of their reinforcements were slowed down by dead water within the Mediterranean sea (Fourdrinoy et al., 2019).

The first detailed study of internal wave generation due to sea ice is that of McPhee and Kantha (1989). This study was motivated by novel observations positing the impact of internal wave drag on ice motion taken during the 1984 Marginal Ice Zone Experiment (Morison et al., 1987). The observations reported in Morison et al. (1987) for velocity and temperature were measured at 2m, 4m, and 7m below the ice-ocean interface and within the marginal ice zone off the coast of Greenland. It was noticed that when the ocean surface was sufficiently stratified, the derived drag coefficient was 2-3 times the mean. Furthermore, the generation of internal waves during periods of strong stratification corresponded with reduced heat and mass transfer at the ice-ocean interface, a feature that was demonstrated within lab experiments by Linden (1975). The role of heat transfer due to internal waves is of unique interest for this setting and an understudied process in the existing literature.

Within McPhee and Kantha (1989), a linearized form of the inviscid Boussinesq equations is utilized to examine the role of internal wave generation on the ice-ocean drag coefficient in a setup as shown in figure 3.3. Key results of this work were relations of wave drag to a number of parameters such as upper ocean stratification, mixed layer depth, and buoyancy jump at the mixed layer pycnocline. For a sinusoidal ice boundary with single wavenumber k_x moving at speed, U, the relation for the drag coefficient given by McPhee and Kantha (1989) with $H = 0$ and $\Delta b = 0$ in figure 3.3, is

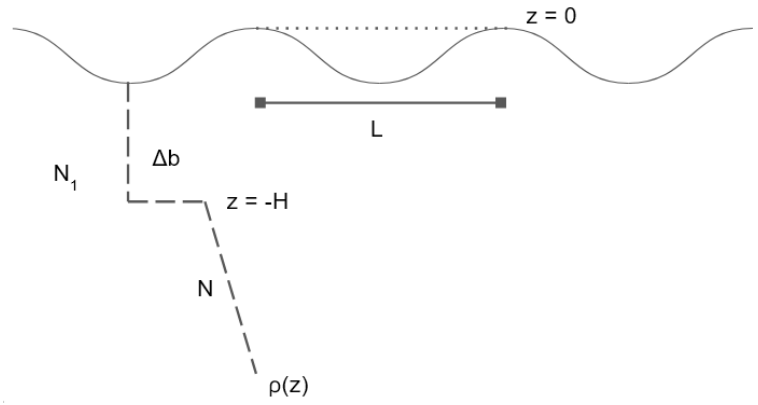


Figure 3.3: Schematic of idealized two layer system based on figure 1 of McPhee and Kantha (1989) with small buoyancy frequency N_1 in an upper layer and lower layer buoyancy frequency N separated by a discontinuous buoyancy jump Δb at $z = -H$. The surface is characterized by a sinusoidal relief with wave number $k = 2\pi/L$ and amplitude h_0

$$\frac{c_{wd}}{(k_c h_0)^2} = \frac{\nu}{2}(1-\nu^2)^{1/2} \tag{3.13}$$

where C_{wd} is the total drag coefficient, $k_c = N/U$ is the critical wave number, h_0 is the roughness scale of the ice, and $\nu = k_x/k_c$ is the ratio of a chosen wave number to the critical wave number. A broader relationship is also established for $\Delta b \neq 0$, $H \neq 0$. For a specific value of ν this results in a prediction of drag scaling proportional to $(Nh/U)^2$, which is slightly different to those relations previously mentioned in §1.3.2 and §3.1.1.2. Alternatively, (3.13) scales proportional to Nh/U for fixed k_x with $k_x << k_c$ ($Uk_x/N << 1$) with k_x being given by the lateral scale of a topographical feature such as a pressure ridge.

Using these results, a perturbation for ice-ocean drag was introduced into a simple one dimensional upper ocean model and used to examine modifications to the heat and momentum fluxes. Within the model, wave drag was included as a perturbation to the surface boundary momentum forcing which may effect heat exchange by varying the Reynolds fluxes into the boundary layer. The resulting numerical models with and without internal wave drag were then compared to those observed by Morison et al. (1987) as shown in figure 3.4.

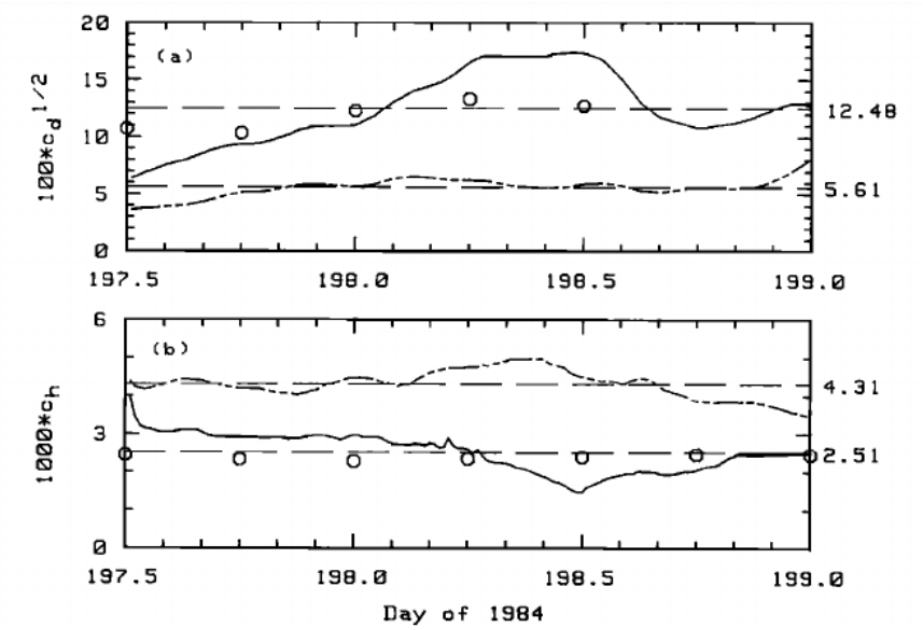


Figure 3.4: Time series of drag coefficient (a), and heat flux coefficient (b), for two model runs within McPhee and Kantha (1989). The broken lines are model runs without the internal wave drag parameterization, solid lines are model runs with internal wave drag effects, and open circles are the MIZEX data of Morison et al. (1987). Long dashed lines indicate averages of model runs. Images presented here are those of figure 13 from McPhee and Kantha (1989)

In this study, the inclusion of internal wave drag reduced the modelled heat exchange by about 60% compared to a control run with just form and skin drag. Furthermore, the increased energy extracted from internal wave formation predicted a reduction in mixing and mixed layer deepening potentially inhibiting upwelling of warmer waters at depth. The wave drag results for calculated exchange coefficients were also closer to the values observed in Morison et al. (1987). In the wave drag runs, a wider variation in momentum and heat exchange is also seen, suggesting increased heterogeneity of mass and momentum exchanges. Compared to modern approaches, such as the Large Eddy Simulation approach, the idealized one dimensional model of McPhee and Kantha (1989) neglects many higher order processes such as 2D and 3D turbulence.

The impact of pressure ridges on heat and momentum transport has also been examined more recently using Large Eddy Simulations (LES) (Skyllingstad et al., 2003). The primary focus of the study was to recreate heat and momentum fluxes observed in the Surface Heat Budget of the Arctic Ocean field campaign and reported in Perovich et al. (2003). In Skyllingstad et al. (2003), two cases were simulated, a large 10m deep keel in a winter mixed layer of depth 20m, and the effects of shallower

keels (1m, 0.5m) on mixing in a summertime layer with a warm, fresh surface water layer of 0.5m depth.

During the period recreated by Skyllingstad et al. (2003), a strong wind event was observed causing a period of increased turbulence and heat flux to the ice-ocean interface. At first, this appears to contradict the earlier results of McPhee and Kantha (1989) which observed increased wave drag in this regime with a corresponding reduction in heat exchange, though McPhee and Kantha (1989) did not account for turbulence. However, prior to the observed wind event, bottom ablation rates measured by ice gauges did not balance the measured incoming solar flux (Perovich et al., 2003). This suggests that a strongly stratified melt water layer served to insulate the ice-ocean interface from the heat of the underlying ocean. Density profiles and stratification within the Arctic Ocean are strongly dominated by salinity (Timmermans et al., 2008). As both models calculated heat flux using the Reynolds fluxes of §1.3.1.1, it is possible that the increased temperature gradient in Skyllingstad et al. (2003) contributed to this difference. Furthermore, the comparatively simple model of McPhee and Kantha (1989) omitted any treatment of 3D turbulence.

3.1.5 Summary of SSFOT background

Across the geophysical system, SSFOT plays an important role in determining the large scale characteristics of climate (Palmer et al., 1986; Baines, 1998; Legg, 2021; Teixeira and Yu, 2014; Cole et al., 2018). From early theoretical developments, we know that the general form of the flow depends on the parameters Na/U and Nh/U (Baines, 1998; Aguilar and Sutherland, 2006; Lam, 2013; Miles and Huppert, 1968). The first parameter characterises the importance of non-hydrostatic effects via simplifications to the Taylor-Goldstein equation in §3.1.1.1 with $Na/U << 1$ in the hydrostatic limit (Lam, 2013). The second parameter, Nh/U, was determined in work using Long's model, as discussed in §3.1.1.2, to be an indicator of non-linear effects (Miles and Huppert, 1968; Baines, 1998). Furthermore, a critical point for Nh/U was determined via both approaches with a sub-critical flow yielding evanescent waves and super-critical flow resulting in persistent oscillatory waves (Lam, 2013; Baines, 1998). In the super critical case, the wavelength scales with the quantity Nh/U as does the drag force (i.e momentum extracted from the boundary) (Aguilar and Sutherland, 2006; Baines, 1998; Miles and Huppert, 1968; Klymak, 2018). These results suggest that the dependence of the drag on topography followed an asymptotic power law relation $C_d \propto (Nh/U)^n$ with different values of n in different flow regimes (Miles and Huppert, 1968).

These theoretical results have been found to be applicable to geophysical settings in the atmosphere and ocean. As discussed in §3.1.2, the primary impacts of internal waves generated at the atmospheric boundary layer are reduction in atmospheric circulation (Teixeira, 2014), and vertically heterogeneous turbulence as a result of non-local wave breaking (Kim and Mahrt, 1992). Though this body of work is still relevant to the ocean and the under-ice boundary layer, differences in approach/assumptions and parameter values leave key gaps which require more detailed study for the relevant settings.

At the ocean bottom, flow over topography impacts vertical mixing of water-masses (Mashayek et al., 2017) and nutrient transport (Reid et al., 2019) as well as the large scale overturning rate (Trossman et al., 2016). Non-linear effects have been shown to manifest as upstream blocking of flow (Klymak, 2018), hydraulic jumps (Winters and Armi, 2012), or weakly radiating boundary layer turbulence (Aguilar and Sutherland, 2006). These regions are an important energy pathway linking large scale ocean circulation to small scale turbulence (Musgrave et al., 2016).

In each of the above settings, a discussion of scalar fluxes such as heat or salt, has been understandably absent from the literature. However, in the setting of sea ice this is a key focus. The first detailed study of sea ice generated internal waves and the corresponding impact on heat flux is that of McPhee and Kantha (1989) and aimed to explain the observations of Morison et al. (1987). Notably that observations reflected a period of increased ice-ocean drag correlated with reduced ice-ocean heat flux. More recent work on this topic includes observations of the SHEBA experiment (Perovich et al., 2003) and subsequent modelling studies such as Skyllingstad et al. (2003) as well as observations from ITPs and seagliders as in Cole et al. (2018). In the results of Skyllingstad et al. (2003), it was found that in similar density stratification to that of McPhee and Kantha (1989), internal waves could increase the heat flux at the ice-ocean surface. This result comes from a scenario where strong thermal stratification was present at depth and within a model that permits 2D and 3D turbulence; both features are missing from McPhee and Kantha (1989).

The full story of SSFOT will motivate and inform our approach to the thesis topic in §3.2. The primary goals of this work will be to investigate the effects of stratified ocean flow beneath a pressure ridge on the flow structure, drag coefficient, as well as the net and spatial patterns of heat exchange at the ice-ocean boundary. For this, we use the computational infrastructure developed in chapter 2 to span the relevant parameter space for Nh/U and Na/U. In the Arctic, the range of these parameters is approximately given by $Nh/U \in [0.01, 2.5]$ and $Na/U \in [0.1, 25]$ as we

will establish in §3.2.2. This range varies from linear to non-linear, and hydrostatic to non-hydrostatic. This affords us the opportunity to more completely characterise the parameter space relevant to the under ice boundary layer. Similarly, the ability to calculate fluxes directly at the ice-ocean interface allows us to investigate the under-ice boundary layer directly, at fine spatial scales, and not via approximations made within the deeper ocean.

3.2 Internal wave generation under a ridged summer ice floe

With the above literature review of stratified shear flow over topography and the computational framework developed in chapter 2, we are in a position to ask: how do variations in the parameters Nh/U and Na/U impact sea ice generated internal waves in the ice-ocean boundary layer? To address this, I apply the LBM code developed in chapter 2 to an idealized picture of a ridged ice floe moving atop a continuously stratified ocean.

This section will proceed as follows. In §3.2.1 we establish the model of stratified ocean flow past a pressure ridge to be solved including the assumptions made as well as choices for the flow initialization and boundary conditions. In §3.2.2 we develop the mathematical formulation of the problem and identify the Froude number and Reynolds number as key dimensionless parameters. We then discuss the calibration of the sponge region in §3.2.3. A discussion of results follows in §3.3.

3.2.1 Schematic

The physical system to be examined herein is that of a ridged first year ice floe moving over a stagnant ocean that is continuously stably stratified in temperature and salinity. For the sea ice boundary we consider an otherwise flat ice floe with a single triangular ridge of height, h, and base width, $4h$. This ridge geometry is informed primarily by the median properties reported in Wadhams et al. (2012) for first year ice with a triangular ridge of angle $\theta \approx 26.6$ degrees. In the real-world system both the ice and the ocean are moving relative to each other due to a number of forcing mechanisms such as geostrophic flow, mesoscale or submesoscale eddies, and forcing of the ice floe from wind and storm events (Tsamados et al., 2014; McPhee, 2008; Armitage et al., 2016). For our purposes we neglect the acceleration of the ice floe, and exploit a Galilean shift to examine the problem where the water moves with

a uniform velocity relative to the stationary sea ice upper boundary. The simulation schematic is depicted in figure 3.5.

The ice-ocean interface is cold and fresh compared to the underlying ocean. The ocean flowing in underneath the floe is continuously stratified in temperature T and salinity S with a constant buoyancy frequency N. Density variations are dominated by the salinity stratification. Initially we will proceed with a stable stratification in both S and T such that the ocean is warm and fresh at the surface and cold and salty at depth. During ice melt, in between ice floes the exposed ocean is able to warm at the surface from radiative heating. As a result the exposed ocean surrounding the ice floe may become stably stratified in temperature. This warm ocean water may then flow underneath ice floes or have ice floes be transported above it. The temperature profile of figure 3.5 is an approximation to this picture with a temperature maximum near the ice-ocean interface and a continuous stratification with depth. This initially sets the temperature profile as being discontinuous with the specified ice-ocean boundary condition which would create an adjustment region of the boundary layer downstream of the inlet. We will later examine some of the sensitivity to this process by examining cases where the ridge is placed further away from the inlet.

In §3.3.3, we also invert the temperature profile for the inflow so that the underlying ocean is stably stratified in S and ρ, but unstably in T so that the temperature is continuous with the boundary condition. In both cases the initial stratification is used for the inflow on the left side of the domain. These two cases resemble two different regimes of ice melt. The original set up may more closely resemble a cold fresh ice floe flowing over warm ocean water previously in a lead which would allow for the surface ocean to become warmer than the underlying mixed layer. In this perspective our inverted temperature simulations may more closely resemble a configuration where the lead is strongly influenced by upstream ice melt within the ice pack or the scenario in which upwelling oceanic heat contributes most strongly to melt.

The inflow velocity is set to a uniform velocity u_0 to mirror a Galilean shift of the the ice floe moving over a stagnant ocean. At the start of the sponge, the velocity inflow is also discontinuous to the boundary and so this setup mirrors the experimental setups where an obstacle is dragged through an initially stationary stably stratified fluid (Aguilar and Sutherland, 2006; Sutherland et al., 2013, 1999).

A number of idealizations have been made to make this problem numerically tractable. In regards to the ice roughness, small scale, and periodic roughness as well as the dendritic structure of the ice-ocean interface have been neglected in favour of

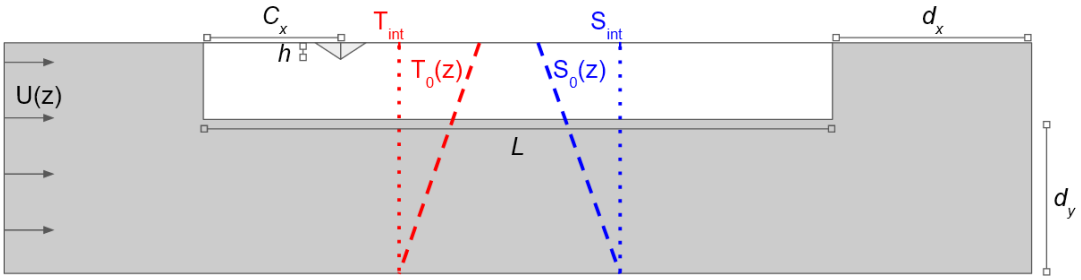


Figure 3.5: We consider a system of a flat ice floe with a ridge of height h and base width $w = 4h$ ($\theta \approx 26.6$ degrees) informed by Wadhams et al. (2012). The center of the ridge is placed a distance $C_x = L/3$ into the computational domain. On the left side, a uniform horizontal inlet velocity of $u = u_0$,$v = 0$, is applied with both T and S stably stratified as shown with $T = T_0(z)$, $S = S_0(z)$. This configuration is used to set the target distribution f_a of (2.33). A sponge region itself extends a horizontal distance $d_x = 2w$ and vertical distance $d_y = 2w$ around the computational domain as indicated by the shaded region. The upper surface boundary conditions are no-slip and no penetration, isothermal, and isohaline with temperature T_{int} and salinity S_{int} in non-dimensional units. .

a computationally tractable no-slip no-penetration boundary condition with a piecewise planar boundary. Similarly we assume the ice-ocean interface is isothermal and isohaline, rather than using more complex flux-based boundary conditions given by the three equation formulation as discussed in §1.2. If the turbulent heat and salt flux are spatially uniform, the three equation formulation discussed in §1.3.3 would yield isothermal and isohaline boundary conditions. In this representation we are effectively neglecting spatial and temporal variations in the interfacial temperature and salinity that may arise from variations in the fluxes. The mass flux from melting and evolution of a free boundary is also neglected. Implementation of more complex boundary conditions is possible within the LBM, however is left for future work and we focus here on building insight with the simpler case.

It is also an approximation to assume that the pressure ridge is entirely solid. Pressure ridges are formed through the mechanical fracture of converging sea ice resulting in a pile of broken ice above and below the waterline with corresponding heights/depths set by hydrostatic equilibrium. As a result of this pile up, pressure ridges are highly channelized potentially impacting the alteration of the flow field below (Nuber et al., 2013). For example, when calculating the ice-ocean drag components the pressure drag, set via the pressure difference at the upstream and downstream sides of the obstacle, may be overestimated in the numerical setup illustrated in figure 3.5 if in the real-world system much of the flow is not deflected around the

obstacle but instead goes through it. The accuracy of the simulations in this work thus improve for low porosity which would limit the mass flux through the ridge. Furthermore, in this 2D example we have implicitly assumed that the geometry of the ridge is effectively infinite along the direction parallel to the ridge whereas variations in the ridge shape may have significant variance in this third dimension.

3.2.2 Mathematical setting

Within the ocean, the relevant equations are the Navier-Stokes equations for mass and momentum, as well as conservation of heat and salt. In all equations, $\mathbf{u}$ is the ocean velocity, t is time, and p is pressure. Subscripts o and int indicate properties of the ocean or the ice-ocean interface respectively. subscript d in this section indicates dimensionless quantities. Conservation of heat is given by

$$\rho_o c_o \left[\frac{\partial T}{\partial t} + \mathbf{u} \cdot \nabla T\right] = \nabla \cdot [k_o \nabla T] + A_R \tag{3.14}$$

where ρ_o is the density of ocean water, c_o is the specific heat of the ocean, T is temperature, k_o is the thermal conductivity of the ocean and A_R is radiative heating. We here neglect radiative heating setting $A_R = 0$. Conservation of salt, with salinity S, yields

$$\rho_o \left[\frac{\partial S}{\partial t} + \mathbf{u} \cdot \nabla S\right] = \nabla \cdot (\rho_o \mathcal{D}_o \nabla S), \tag{3.15}$$

where $\mathcal{D}_o$ is the diffusivity of salt. The ocean can usually be treated as incompressible so that conservation of mass is given by

$$\nabla \cdot \mathbf{u} = 0 \tag{3.16}$$

Lastly, using the Boussinesq approximation the momentum equation in a rotating reference frame is given by:

$$\frac{\partial \mathbf{u}}{\partial t} + (\mathbf{u} \cdot \nabla)\mathbf{u} = \frac{-\nabla p}{\rho_o} - \mathbf{\Omega} \times (\mathbf{\Omega} \times \mathbf{r}) - 2\mathbf{\Omega} \times \mathbf{u} + \nu \nabla^2 \mathbf{u} - g\frac{\Delta\rho}{\rho_o}\hat{\mathbf{k}} \tag{3.17}$$

where we denote the planetary angular velocity by $\mathbf{\Omega}$, the kinematic viscosity $\nu = \mu_o/\rho_o$, $\Delta\rho = \rho - \rho_\infty$ where ρ_∞ is the reference density at the base of the mixed layer and $\hat{\mathbf{k}}$ is a vertical unit vector.

We use a linearized equation of state for density $\rho = \rho_\infty[1-\alpha(T-T_\infty)+\beta(S-S_\infty)]$ where the subscript ∞ denotes the value of the quantity at the bottom boundary, α the thermal expansion coefficient and β the haline contraction coefficient. The Rossby number is $Ro = U/fL \sim 5 > 1$ as estimated at 75 degrees north, with $U = 0.1m/s$,

and typical domain length $L = 150m$, and larger still on the 20m horizontal scale of the pressure ridge. In this work we assume that the Rossby number is sufficiently large to neglect rotational effects, though there is potential for submesoscale processes to play a role in the physical picture as for sufficiently small velocities the Rossby number may approach 1.

Identifying characteristic scales for the ice-ocean relative velocity, U, a summer mixed layer depth H, the magnitude of the temperature and salinity differences between the ice properties and the maximum value of the inflow ΔT and ΔS, as well as the salinity and temperature at the ice-ocean interface, S_{int} and T_{int} respectively, we can introduce the following non-dimensional scaling:

$$P_d = \frac{P}{\rho_0 U^2}, \qquad z_d = \frac{z}{H}, \qquad \mathbf{u}_d = \frac{\mathbf{u}}{U}, \qquad S_d = \frac{S - S_{\text{int}}}{\Delta S},$$
$$T_d = \frac{T - T_{\text{int}}}{\Delta T}, \qquad t_d = \frac{t}{H/U}, \qquad \nabla_d = H\nabla$$

Substituting these into (3.14) through (3.17) the non-dimensional momentum equation becomes

$$\frac{\partial \mathbf{u}_d}{\partial t_d} + \mathbf{u}_d \cdot \nabla_d \mathbf{u}_d = \frac{1}{Re}\nabla_d^2 \mathbf{u}_d - \frac{1}{Fr^2}(S_d - R_\rho T_d)\hat{\mathbf{k}} - \nabla_d P_d, \tag{3.18}$$

where $Re = HU/\nu$ is the Reynolds number describing the ratio of inertial to viscous effects on the flow, $R_\rho = \alpha\Delta T/\beta\Delta S$ is the ratio of density changes due to temperature and salinity, the Froude number, $Fr = U/\sqrt{Hg\beta\Delta S}$ compares the strength of the mean flow to the haline buoyancy forces, and is proportional to $(Nh/U)^{-1}$ in this setting from the previous chapter if salinity differences dominate the buoyancy force.

The non-dimensional heat equation is

$$\frac{\partial T_d}{\partial t_d} + \mathbf{u}_d \cdot \nabla_d T_d = \frac{1}{Re \cdot Pr}\nabla_d^2 T_d, \tag{3.19}$$

where $Pr = (\nu c_o \rho_o)/k_o = \nu/\kappa_o$ is the Prandtl number comparing the momentum diffusivity to thermal diffusivity, κ_o.

The non-dimensional salt equation is

$$\frac{\partial S_d}{\partial t_d} + \mathbf{u}_d \cdot \nabla_d S_d = \frac{1}{Sc \cdot Re}\nabla_d^2 S_d, \tag{3.20}$$

where $Sc = \nu/D_o$ is the Schmidt number comparing the momentum diffusivity to chemical diffusivity of salt and $Q_{d,salt}$ represents the nondimensional salt fluxes in the same manner as $Q_{d,heat}$.

$H = 20$ m	$U = 10^{-1}$ m s^{-1}	$\Delta T \sim 2$ K
$\Delta S \sim 7$ psu	$\nu = 1.89 \times 10^{-6}$ m^{2}s^{-1}	$k_w = 0.570$ W m^{-1} K^{-1}
$\rho_o = 1028$ kg m^{-3}	$c_o = 3971$ J K kg^{-1}	$D = 6.8 \times 10^{-10}$ m^2 s^{-1}
$\beta = 7.8 \times 10^{-4}$ psu^{-1}	$\alpha = 5.82 \times 10^{-5}$ K^{-1}	$g = 9.81$ m s^{-2}
$h = 5$ m	$\theta_{ridge} \approx 26.6°$	

Table 3.1: Relevant scales to be used for the non-dimensionalization process.

We can estimate the values of the dimensionless parameters using the characteristic scales shown in table 3.1 where ΔT represents the change in temperature between the cold ice and the maximum inflow temperature and ΔS is the salinity change over the surface 20m approximated from September profiles from ITP observations as reported in Toole et al. (2010). The values for ν, k_o, ρ_o and c_o are from Sharqawy et al. (2010), D_o from Notz and Worster (2009), β from Vallis (2017), α from Unesco and SCOR (1981) and the gravitational constant g is well known. h is a median value of keel depth from Wadhams et al. (2012), and U is an approximate ice drift velocity on the same order as the mean ice velocity reported by Lund et al. (2018). Approximate values of the non-dimensional parameters used in (3.18)-(3.20) can then be determined as in table 3.2

$Pr = (\nu c_o \rho_o)/k_o = 13.5,$	$Sc = \nu/D = 2780,$
$Re = \frac{HU}{\nu} = 1.05 \times 10^6,$	$Fr = \sqrt{\frac{U^2}{Hg\beta\Delta S}} = 0.096,$
$R_\rho = \frac{\alpha \Delta T}{\beta \Delta S} = 0.021$	$Fr_h = \sqrt{\frac{U^2}{hg\beta\Delta S}} = 0.19$

Table 3.2: Approximate values of non-dimensional parameters using the scales of table 3.1, using molecular viscosity and diffusivity

We have defined Fr_h as the Froude number using the obstacle height instead of the mixed layer height. This value is more readily comparable to non-dimensional quantities in the literature, and so we will continue our discussion with this value. We can relate Fr, and Fr_h, to the parameter Nh/U from the SSFOT literature, discussed in §3.1.1. Given the chosen ratio $h/H = 1/4$ and $N^2 = g\beta\Delta S/H$ we can write

$$\frac{Nh}{U} = \frac{h}{H}\frac{\sqrt{g\beta\Delta SH}}{U}$$

so that $(Nh/U) \approx (4Fr)^{-1} = (Fr_h)^{-1}$.

The values calculated in table 3.2 are indicative, and can vary between locations. For example, the characteristic height of a pressure ridge may vary between 2-15

meters in first year ice (Wadhams et al., 2012) and larger in multi year ice. Additionally, depending on location and forcing, the ice-ocean relative velocity may vary from 1 cm/s to 50 cm/s in storm events (Armitage et al., 2016). Similarly, the upper ocean stratification can vary from a strong thin melt layer overlying salty ocean to a completely mixed layer such that $\Delta S = \Delta T = 0$. Within this work we will focus on the impact of these parameters as characterized by a range of Reynolds and Froude numbers.

For the simulations in §3.3 we use $Re = 100, 250, 500$, $Pr = Sc = 1$, $R_\rho = 0.02$ and a range of Froude numbers $Fr_h \in [0.2, 25]$. As we hold the obstacle aspect ratio the same for all simulations we will be implicitly varying Na/U as well. This range of Fr_h with constant ridge geometry corresponds to a range of $Nh/U \in [0.04, 5]$ and $Na/U \in [0.08, 10]$ and so we span from linear to nonlinear regimes and hydrostatic to non-hydrostatic regimes. A fixed ratio h/H is maintained in the simulations, which is rationalised by the use of an absorbing boundary condition in the sponge region to numerically represent the truncation of a physical domain much deeper than H (i.e. This approximates the solution for a semi-infinite domain in the vertical).

The artificially low Reynolds number is due to computational limitations, though previous work has suggested low Reynolds number simulations still capture most of the flow characteristics (Winters and Armi, 2012). We might however expect the quantitative values of drag and heat flux to scale with Re. A lower Reynolds number may be seen as consistent with an enhanced turbulent diffusivity and viscosity, rather than the molecular values. In this same sense, we equate the Prandtl and Schmidt numbers. This suggests the completely turbulent limit of the problem where the molecular diffusivity is negligible. Under this assumption we are neglecting double diffusive effects which may play a role in the real-world system. Understanding the role of double diffusive effects in this problem is left as potential future work.

For implementation into the LBM we take these parameters and apply the discretization method as in §2.2. Before proceeding to the simulations, we must still calibrate the absorbing boundary condition method introduced in §2.3.4.

3.2.3 Simulation calibration

Before we analyse simulations, we need to infer whether the simulation reaches a steady state. I do this by considering how the drag coefficient C_d varies over time as shown for a few values of Froude number in figure 3.6 for $Re = 100$. For the Reynolds numbers used in this work, we have found that the simulations converge to a steady state with respect to the flow field and drag coefficient (temporal evolution for

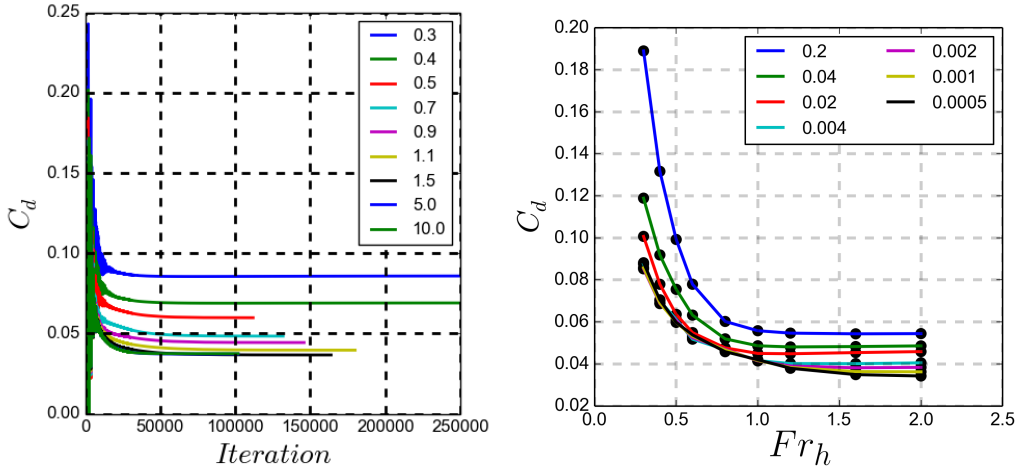


Figure 3.6: (left) Evolution of the drag coefficient for $Re = 100$ with simulation iteration for the various values of Fr_h in the legend, and (right) drag coefficient as a function of Fr_h for varying damping coefficients σ_m as indicated in the legend. All flows converge to a steady state as reflected in C_d (left). For values of σ_m below those shown numerical instabilities are encountered.

$Re = 250, 500$ is not shown here). For the simulations in this section we will thus run until the drag coefficient converges as determined by a threshold of $\Delta C_d/\Delta t < 10^{-8}$.

We now must also address the calibration of our absorbing boundary condition 'sponge' region outlined in §2.3.4. As shown in the schematic of figure 3.5, the computational domain is surrounded with a sponge region that is twice the computational height such that $d_x = d_y = 2w = 8h$. Using this sponge I tested a range of damping coefficients, σ_m of (2.33), shown in figure 3.6 for $Re = 100$. For this geometry it was determined that the steady state drag coefficient converges for values of σ_m within the range $.004 - .001$. Higher values of σ_m produced inflated values for C_d as the wave is partially reflected if damping grows too sharply in space, whereas lower values resulted in numerical instability from the interaction of waves with the boundary. These results for C_d are shown in figure 3.6. This result was found to hold for $Re \leq 500$.

We can also do a qualitative check to look for any numerical anomalies by examining flow structure across the full computational domain as in figure 3.7. In the vertical component of the velocity field, we clearly see wave formation, and in the horizontal, though less clear, we see some indications of flow at or beneath the depth of the obstacle height being blocked. Outside of the computational domain, we see the waves propagating into the sponge region and dissipating as they approach the

bottom and lateral boundaries. The wave fronts curve slightly both within the computational domain as in the sponge. This appears in other studies as shown in figures 3.2 and 3.1, so is most likely a feature of the flow caused by the diagonal propagation of energy in the system varying across the Fourier spectrum of wavenumbers that represent this obstacle. In the later sections we will show only the computational domain not covered by the sponge region in order to focus on the details of interest.

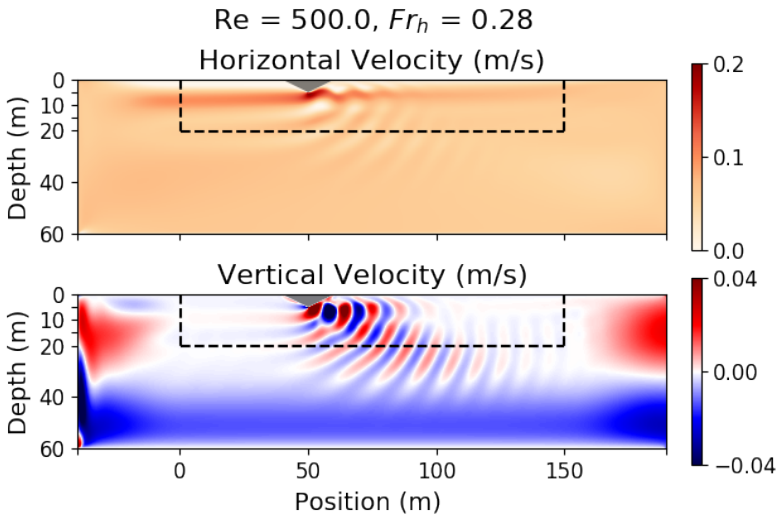


Figure 3.7: Components of velocity for $Fr_h = 0.28$ and $Re = 500$ using the simulation setup as shown in figure 3.5. The dashed line indicates the boundary of the computational domain and the start of the sponge region. The colour bar gives the component velocity in m/s with all domain height and position in meters.

Using the information gained from this calibration test, I decided on a value of $\sigma_m = 0.001$ for the absorption coefficient. We first examine the qualitative flow structure and see how it compares to the existing work overviewed in §3.1.

3.3 Results

The simulations in this study all use a Mach number $Ma = 0.01$ and Δx_{lb} determined by enforcing $\nu_{lb}/\Delta x_{lb} > 1$ which is the aforementioned ad hoc method used to ensure simulation stability. This condition then sets $\Delta t_{lb} = Ma\Delta x_{lb}/\sqrt{3}$. I first consider the flow field and characteristic wavelength for simulations spanning linear and nonlinear, hydrostatic and nonhydrostatic parameter spaces with low Reynolds number, and compare to the theoretical work reviewed in Baines (1998) for the inviscid, hydrostatic

and nonlinear limit described by Long's model as discussed in §3.1.1.2. Next I examine the effect of sea ice generated internal waves on the drag coefficient and inspect how the observed behaviour scales with Fr_h and Re. With some understanding of how simulations in the present configuration compare to past work, I then examine any impacts on the interfacial heat flux and compare the results to those predicted by Reynolds flux parameterizations outlined in §1.3.1.1 and observations of §1.3.3. Lastly, I run some sensitivity tests to investigate the potential impact of varying ridge geometry.

3.3.1 Simulation flow field

From the existing literature on SSFOT overviewed in §3.1, we expect a few key features of flow may also be relevant in the current configuration. First, we know there exists a critical point around $Nh/U = 0.5$, which corresponds to $Fr_h = 2.0$. The internal waves are evanescent and decay for $Fr_h > 2$ and are persistent with upstream and downstream propagation for $Fr_h < 2$. Furthermore, there exist regimes at low Fr_h where upstream blocking of the flow may occur as shown earlier in figure 3.2. In general, for $Fr_h < 2$ we expect the wavelengths of generated internal waves to decrease proportional to changes in the principal wave number given by N/U (Baines, 1998). To check the existence of these features within our simulation we will first look at the velocity components with $Re = 500$ and a variety of Froude numbers as shown in figures 3.8 through 3.11. The simulations solve the dimensionless configuration given by (3.18) - (3.20), with dimensionless quantities then converted into dimensional quantities using the length and velocity scales of table 3.2 to illustrate characteristic scales for a particular case study. However, due to dynamical similarity, these simulations are also applicable to other configurations with the same Re and Fr_h though with different U and H which will yield rescaled flow amplitude and lengthscales.

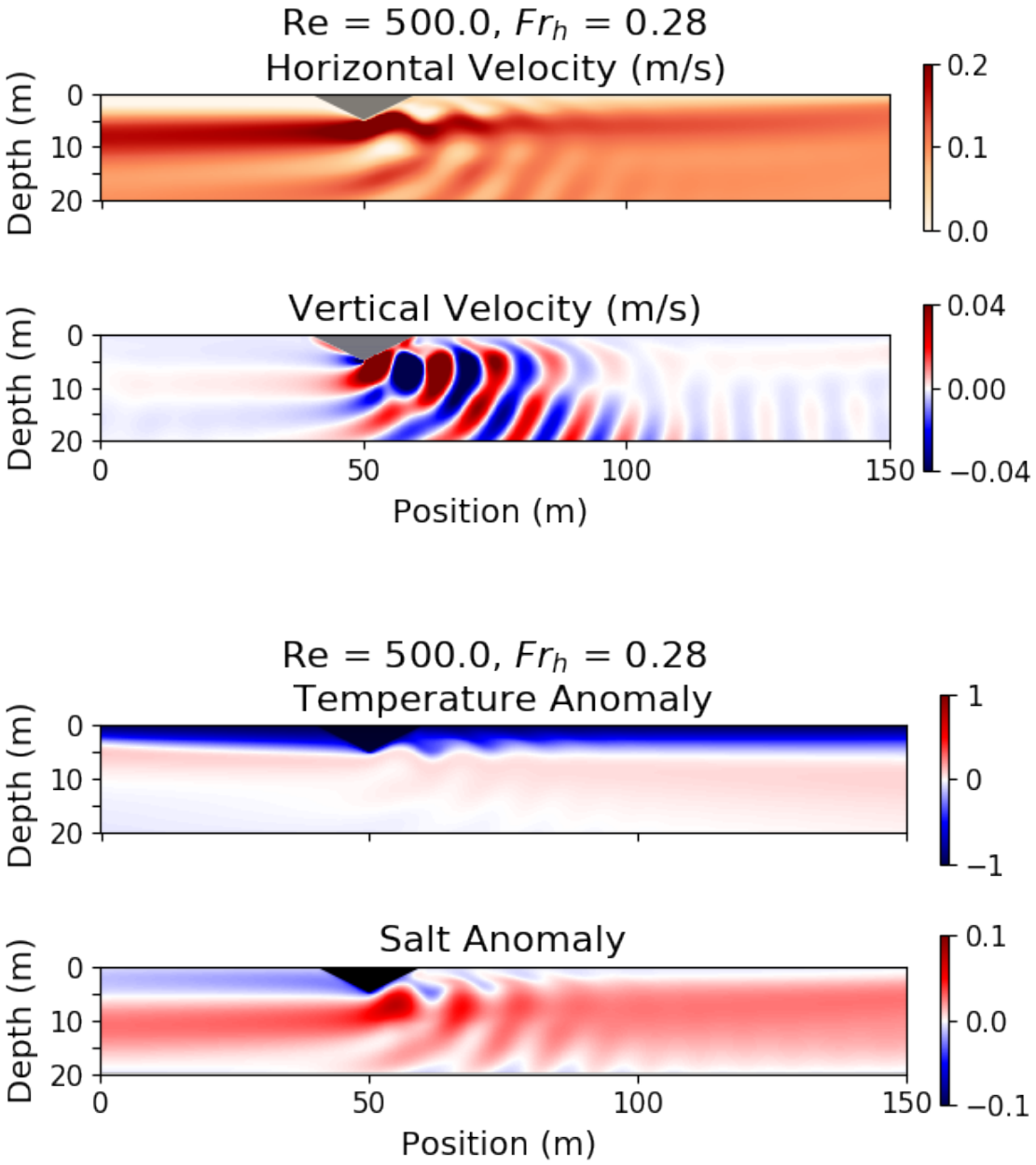


Figure 3.8: Components of velocity for $Fr_h = 0.28$ and the non dimensionalized temperature and salinity anomalies calculated using the simulation setup as shown in figure 3.5. The anomalies are calculated by subtracting the inflow profiles of $T_0(z)$ and $S_0(z)$ respectively. In both components of the velocity we clearly see wave formation with a more pronounced pattern in the vertical velocity. Additionally we see upstream flow blocking similar to the behaviour of figure 3.2 for a cylindrical obstacle and a comparable value of Fr_h. An intense, narrow near surface jet can be seen. These same features can be seen in the dimensionless temperature and salinity fields alongside a pronounced near surface cooler and fresher layer. Quantities dimensionalized using U, h of table 3.2

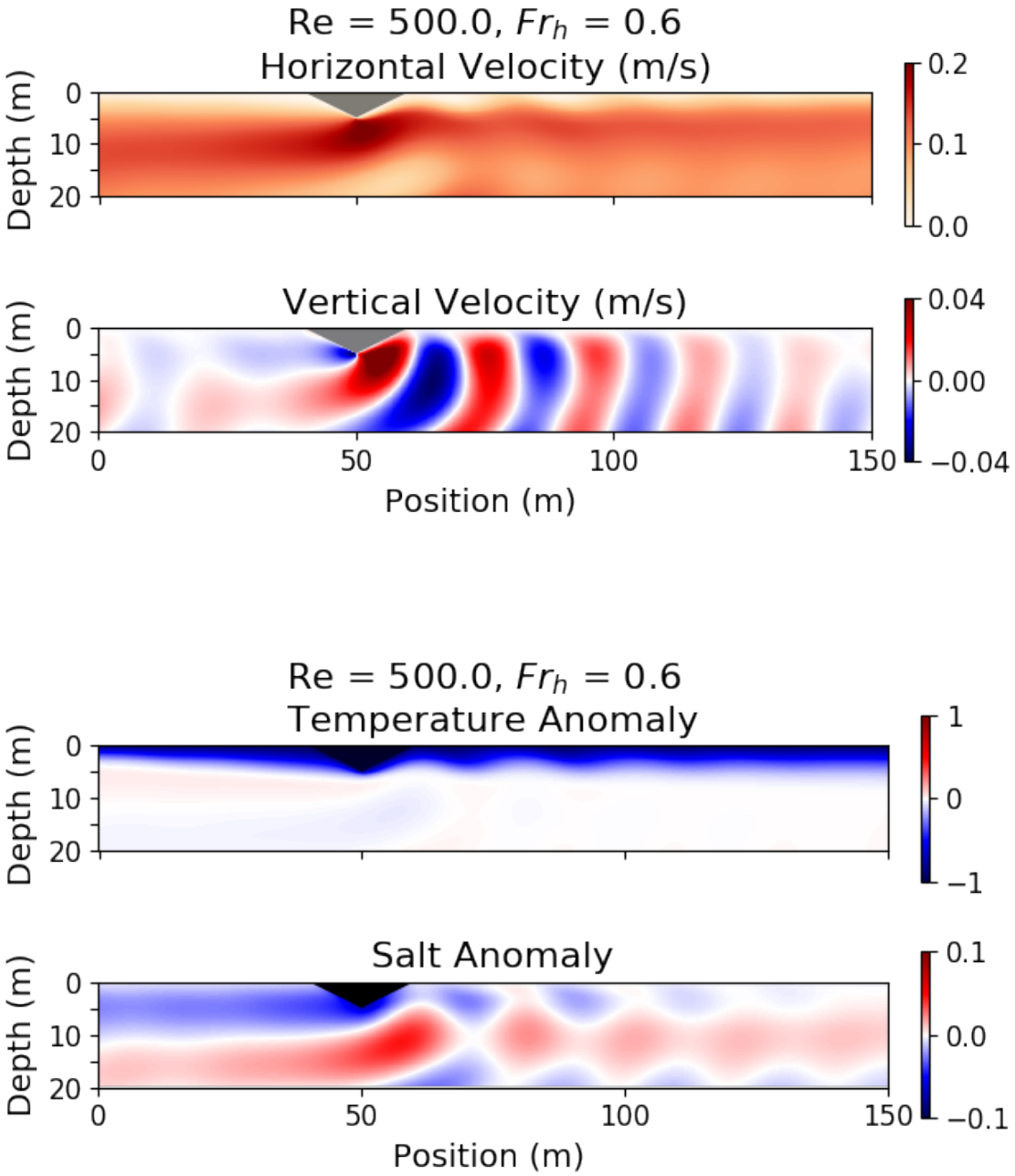


Figure 3.9: Same as figure 3.8 but for $Fr_h = 0.6$, above the threshold for blocking regimes observed in Winters and Armi (2012), or predicted from the atmospheric case as in Lott et al. (2021). A small region of upstream stagnant flow exists in qualitative agreement with a transition to flow blocking expected at $Fr_h \approx 0.5$ from Baines and Guest (1988). Comparing to figure 3.8 we see the wavelengths of the waves growing longer with decreasing stratification (I.e. Larger Fr_h). Similarly the intensity of the near surface jet has diminished in both magnitude and width. Quantities dimensionalized using U, h of table 3.2

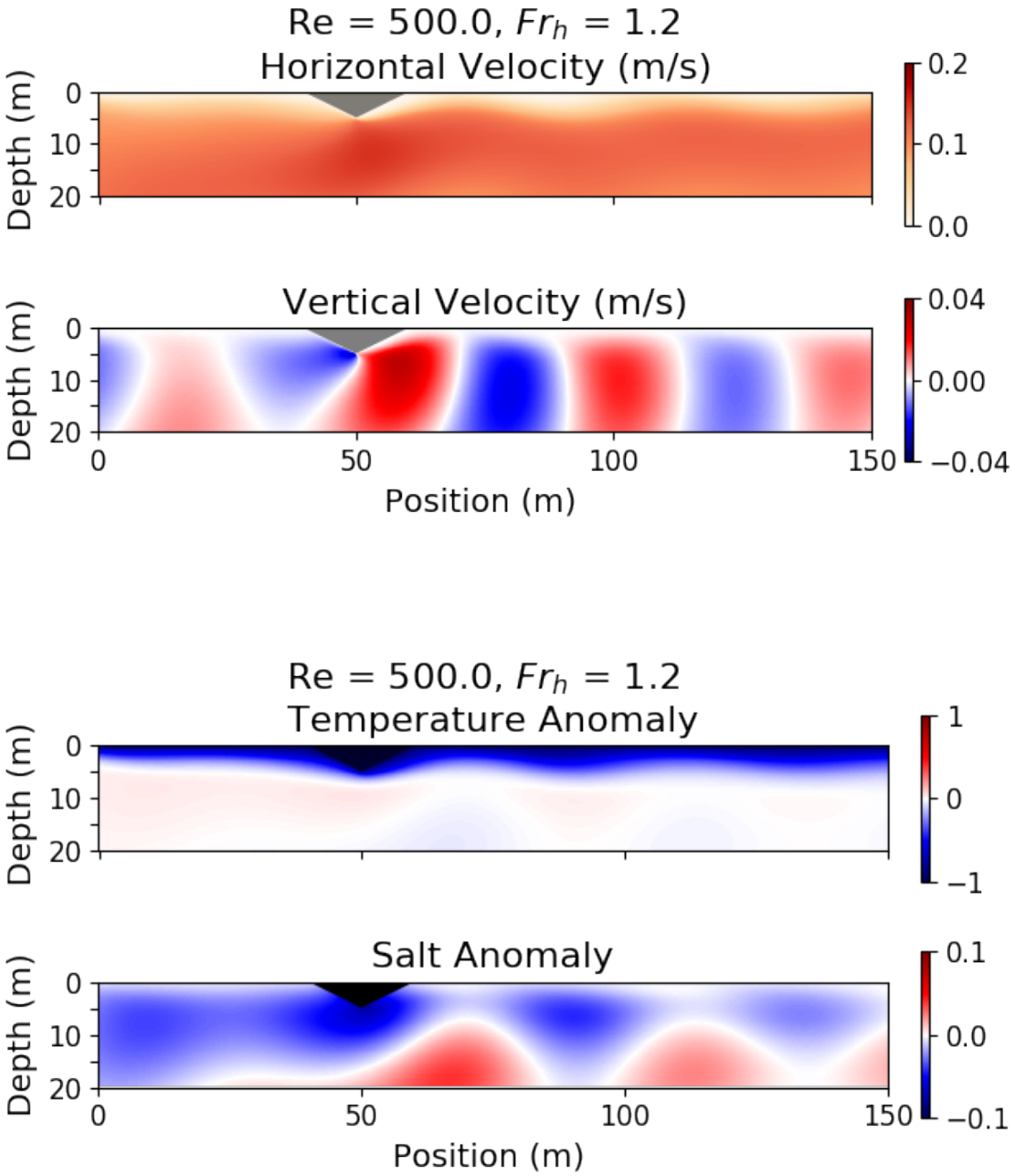


Figure 3.10: Same as figure 3.8 but for $Fr_h = 1.2$. We observe much the same features as in figure 3.9. Compared to the lower values of Fr_h in figures 3.8 and 3.9, the wavelengths of the generated internal waves are longer. Quantities dimensionalized using U, h of table 3.2

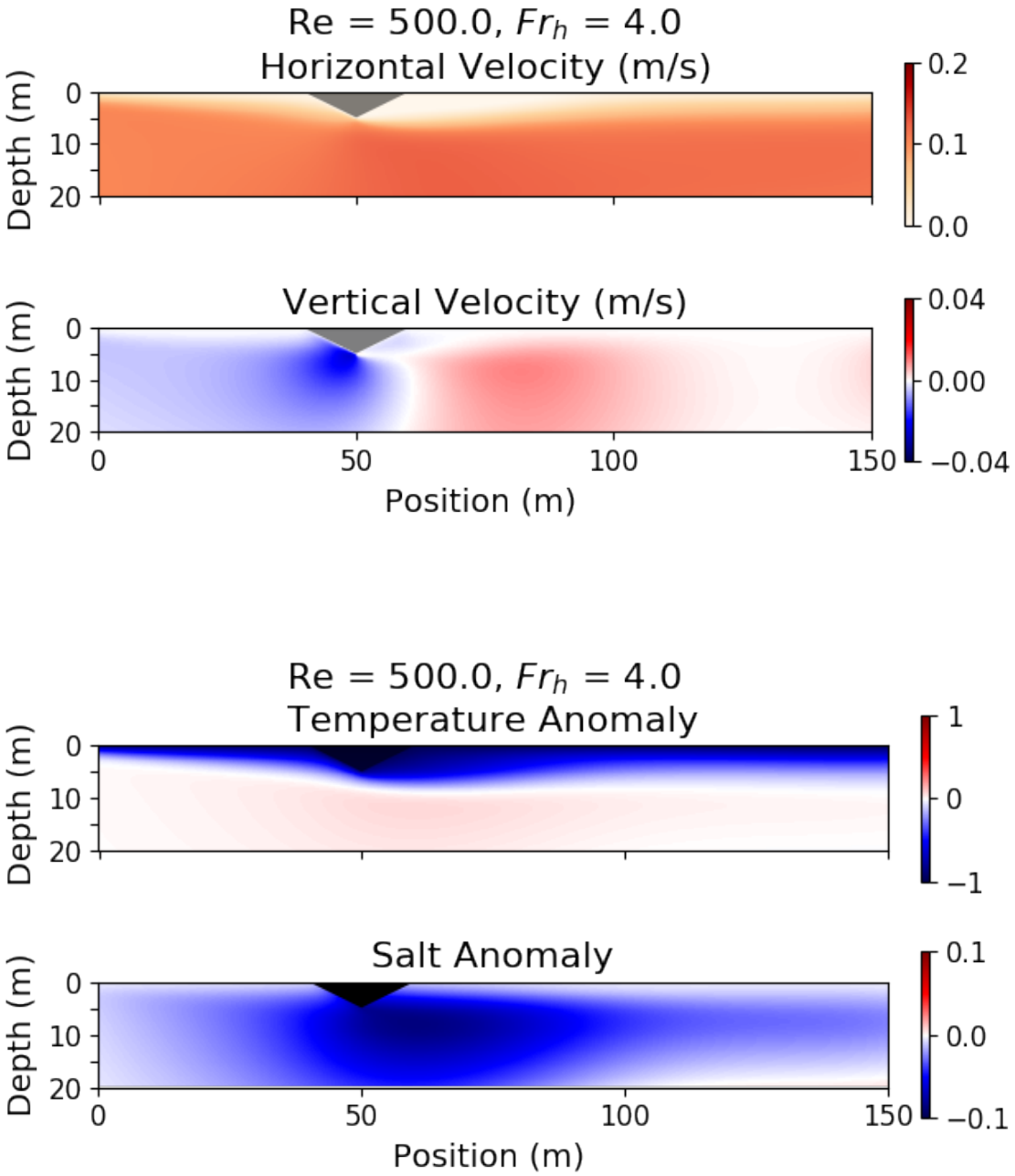


Figure 3.11: Same as figure 3.8 but for $Fr_h = 4.0$. This flow is the first super-critical flow shown. None of the aforementioned processes of internal wave generation or flow blocking are observed. Instead, the main feature is an apparent recirculation bubble on the downwind side of the obstacle as the boundary layer separates at the tip. Quantities dimensionalized using U, h of table 3.2

Inspecting the output in figures 3.8 - 3.11, we observe that the qualitative behaviour is consistent with the predictions of §3.1.1. Flow that is sub-critical with $Fr_h < 2$ ($Nh/U > 0.5$) (figures 3.8, 3.9, 3.10), has persistent internal wave formation as predicted in §3.1.1.1 and §3.1.1.2. Furthermore, we observe upstream blocking of the flow at low values of Fr_h as in figure 3.8. We also see the width and strength of the subsurface jet shrinks and intensifies with decreasing Fr_h as expected from Winters and Armi (2012). The non-blocking subcritical flow of figures 3.9 and 3.10 resembles the large eddy simulation calculations of Skyllingstad et al. (2003) for small amplitude keels in a simulated summer regime where internal waves are generated due to the enhanced velocity over the ridge. In that study, the salinity variations from sea ice generated internal waves were observed to generate lateral variations in the freezing point depression in the lee of the pressure ridge. The model results of Skyllingstad et al. (2003) indicate that this freezing point depression had a significant effect on ice bottom melting rates. Qualitatively we can see a similar behaviour by looking at the anomalies of the dimensionless temperature and salinity fields in figures 3.8 - 3.11 where the internal waves create patterns in the vertical temperature gradient, and salinity fields near the boundary. This heterogeneity in the heat flux due to internal waves may alter the characteristic roughness of sea ice and potentially further alter the characteristic internal wave field. We will examine this feature further in §3.3.3.

As Fr_h increases beyond the critical point of $Fr_h = 2$, instead of persistent internal waves or upstream blocking, waves are evanescent as was predicted in §3.1.1.1. In this regime, the flow begins to separate downstream of the ridge peak. The boundary layer separation allows for the formation of a weakly recirculating region in the shadow of the obstacle separated from the flow over the pressure ridge. This nearly stagnant region of 'melt water' may insulate the region from exchange of heat and salt with surrounding waters. Figure 3.11 indicates relatively sharp temperature gradients near the edge of this region of separated flow, with cold 'melt water' within the stagnant region, although it is hard to unambiguously distinguish this from the thermal boundary layer thickness seen at other Fr_h in figures 3.8- 3.10.

We next compare the wavelength of the generated internal waves to the theoretical results outlined in Baines (1998). Up until the expected critical value of $Fr_h = 2$, the wavelengths of stationary internal waves in a mean flow are predicted to increase with increasing Fr_h (Baines, 1998), with wave number $k = N/U$ from (3.12). We can re-express this to yield the wavelength as a function of Froude number $\lambda = 2\pi U/N = 2\pi h Fr_h$ for a fixed ridge height, h. For $Re = 100, 250, 500$ we calculate horizontal wavelengths by looking at the vertical velocity field at 5m depth and calculating

the average peak to trough distance, $\lambda/2$ down wind of the obstacle. Here we have looked downstream only to avoid considerations of complications from upstream flow characteristics such as blocking. The averaged values are compared to the expected value from Long's model results in figure 3.12.

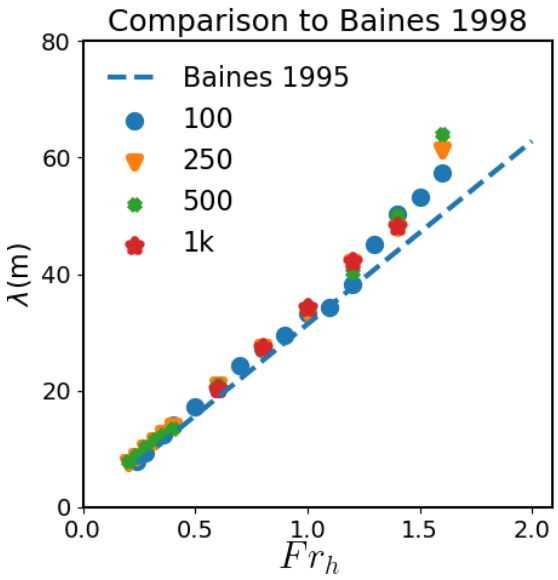


Figure 3.12: Comparison of horizontal wavelengths, λ, predicted from Long's model (Baines and Hoinka, 1985) (dashed line), and the present idealized pressure ridge simulations (symbol colour indicates Reynolds number). The simulations selected for comparison span both the Reynolds number and Froude number ranges of the study. For the simulations, the wavelength is calculated by looking for turning points in the vertical velocity field to calculate the average value of the half wavelengths on the downstream side of the obstacle. These results are specific to a particular N/U

This comparison illustrates a general lack of sensitivity of the wavelength to the Reynolds number. A deviation of the wavelengths from the scaling using Long's model occurs at $Fr_h \approx 1.8$. This could be due to simply the low number of peaks/troughs within the domain for these Froude numbers, leading to larger uncertainty in the statistics for the average value. For example at $Fr_h \approx 1.5$, $\lambda \approx 50$m so we only have two full wavelengths in the domain. Furthermore the slight variation could be attributed to the numerous additional processes included in these simulations versus the theoretical predictions from §3.1.1.2, such as viscosity, no-slip boundary conditions, non-hydrostatic effects, etc. The range of departure is also close to the transition point of $Fr = 2$. In more complicated models the exact value of this point has been known to vary due to the effects just listed (Lott et al., 2021; Legg, 2021). Nevertheless, the scaling from Long's model appears to capture the leading order

behaviour reasonably well for $Fr_h < 1.8$. With these initial comparisons finished, we next examine the effect of wave generation on the ice-ocean momentum flux via the drag coefficient.

3.3.2 Drag results

To diagnose the drag force and the corresponding drag coefficient, we use the methods outlined above in §2.3, specifically (2.19). We then calculate the drag coefficient as in §2.6.1. From existing work on the topic, we expect to see an increase of the drag coefficient with increasing stratification (Miles and Huppert, 1968; Baines, 1998; Teixeira, 2014). The general form of this scaling from observations, theoretical work, and numerical results suggests a power law scaling $C_d \propto (Nh/U)^n$ or equivalently $C_d \propto Fr_h^{-n}$ for $Fr_h < 2$. The exact value of n has been shown to be dependent on a variety of processes including boundary geometry and various non-linear/non-hydrostatic processes (Teixeira, 2014; Baines, 1998; Legg, 2021; Miles and Huppert, 1968; Klymak and Legg, 2010; Klymak, 2018; Lott et al., 2021) as outlined in §3.1, but are commonly found to be in the range $-3 \leq n \leq -1$. This power law scaling is known to only occur in the subcritical regime where internal waves are generated (Legg, 2021; Lott et al., 2021; Baines, 1998), but both sub and supercritical regimes are relevant to flow past pressure ridges. Furthermore, due to the range of Froude numbers possible in this setting which span linear to nonlinear and hydrostatic to non-hydrostatic, it is not clear which of the aforementioned scalings might apply to sea ice pressure ridges. We first consider a sweep of simulations for $Re = 100$ and Fr_h in the range $0.2 < Fr_h < 100$ ($0.01 < Nh/U < 5$).

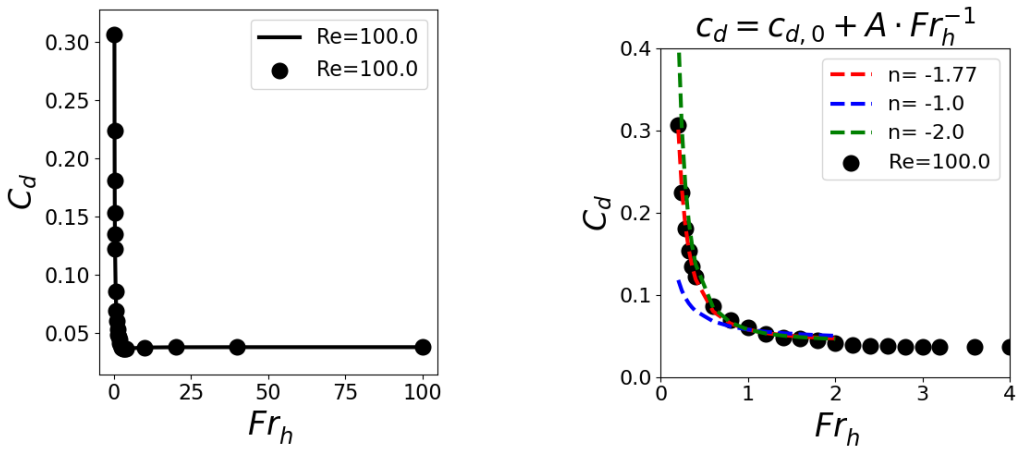


Figure 3.13: Plot of drag coefficient, C_d, as a function of Fr_h for all values of Fr_h (left) and Fr_h about the transition region near $Fr_h = 2$ (right). In the left plot we see that at large Fr_h the drag is constant indicating the absence of wave drag. In the right panel we plot a power law fit $C_d = C_{d,0} + A(Fr_h)^{-n}$ for the sub-critical data ($Fr_h < 2$) using a nonlinear least squares method. The values for this fit and confidence intervals are $C_{d,0} = 0.043 \pm 0.0026$, $A = 0.015 \pm 0.0017$, $n = -1.77 \pm 0.069$ with $R^2 = 0.99$. We also plot the same power law relationship fixing $n = -1, -2$ and fitting a new A, $C_{d,0}$ to the data to see similarity to integer powers with $n = -1$ giving $C_{d,0} = 0.053 \pm 0.0029$, $A = 0.0036 \pm 0.0077$ with $R^2 = 0.96$, and $n = -2$ giving $C_{d,0} = 0.010 \pm 0.00022$, $A = 0.049 \pm 0.0022$ with $R^2 = 0.99$.

As can be seen in the plots of figure 3.13, the transition in behaviour matches up with the expected critical point of $Nh/U = 0.5$ ($Fr_h = 2$) from Baines and Hoinka (1985). In the super-critical regime ($Fr_h > 2.0$), the drag coefficient adjusts to a constant signifying the absence of internal wave drag when the waves become evanescent. We will now focus primarily on the sub-critical regime ($Fr_h < 2$).

In this sub-critical regime shown in figure 3.13, C_d varies by an order of magnitude from $C_d \approx 0.036$ at $Fr_h = 2.0$ to $C_d \approx 0.3$ at $Fr_h = 0.1$. This is quite an appreciable variation, that could arise in practice as the Froude number varies with different ocean stratification, or relative velocity between ice and the upper ocean. That said, variations of the ice-ocean drag of this magnitude and larger have been observed and predicted in the range $4 \times 10^{-4} < C_d < 2 \times 10^{-2}$ (Tsamados et al., 2014; Heorton et al., 2019; McPhee et al., 1987). In the full system, such a wide variation is due to a host of factors including variations in wind and ocean currents, turning angles, sea ice concentration, wave driven effects and other processes as discussed in Tsamados et al. (2014). This same study also suggests that internal wave drag is also an important contributing factor for the ice-ocean drag coefficient, a result reflected in the results of our simulations. The values of drag shown in figure 3.13 are one to two orders

of magnitude higher than the averaged observed value. It is possible that the larger magnitude of the drag is due to the artificially low Reynolds number of $Re = 100$, and so we explore sensitivity to the Reynolds number later.

The literature discussed in §3.1 also suggests a power law scaling $C_d \propto Fr_h^{-n}$ for $Fr_h < 2$. To verify the strength of this scaling, I used the curve_fit function from the Scipy.optimize package for Python 3 which uses a non-linear least squares approach to fit a prescribed function to data. The function chosen for this purpose is $C_d = C_{d,0} + AFr_h^n$ which results in a best fit ($R^2 = 0.99$) being found for $n \approx -1.77$ for $Re = 100$ as shown in figure 3.13. In this power law fit, $c_{d,0}$ corresponds to the drag in neutral stratification and A is an adjustment parameter that likely includes physical processes such as sheltering due to ridge spacing and orientation. Letting $n = -1, -2$ and fitting for new values of A and $C_{d,0}$ provides for a comparison to established scaling laws from theoretical studies such as McPhee and Kantha (1989) and Miles and Huppert (1968).

The exponent n as determined by this functional fit is within the range discussed in the literature as presented in §3.1. However, it is closer to the lower bound $C_d \propto Fr_h^{-1}$ and $C_d \propto Fr_h^{-2}$ reported for purely hydrostatic flow as in Miles and Huppert (1968). For the setup used in this work, the obstacle half width is $a \approx 2h$ and so $Na/U \approx 2Nh/U = 2(Fr_h^{-1})$. In our simulations, for the regime where persistent internal waves are generated, and the drag varies, we have $Na/U \geq 1$. From §3.1.1.1 this indicates a regime where both nonlinear and non-hydrostatic effects may be relevant. As Fr_h decreases, the generated internal waves exert a stronger drag force upon the obstacle and the regime becomes increasingly non-linear though at the same time the flow becomes increasingly hydrostatic. It is unlikely that this is the only factor resulting in the low value of n as $Na/U \approx 1$ for much of the nonlinear regime with $Fr_h < 2$ and so the flow is in the transition between hydrostatic and non-hydrostatic regimes. It is possible that viscosity is affecting the measured exponent. To test this we examine the power law scaling for $Re = 100, 250, 500$ shown in figure 3.14.

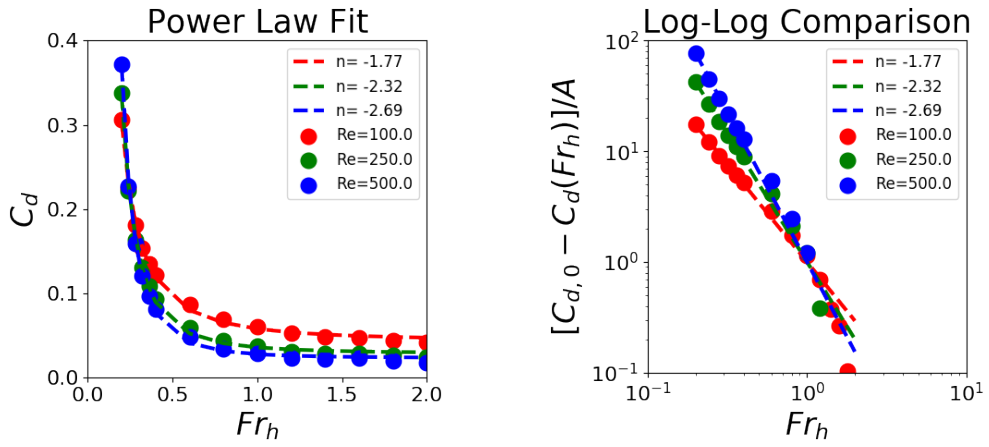


Figure 3.14: Drag coefficient as a function of Froude number (left) and a log-log compensated plot of the same data (right) to evaluate the differences between the power law scaling for $Fr_h \leq 2$ from the LBM computation (dots) and fit to a power law (dashed lines) for $Re = 500$ (blue), $Re = 250$ (green), and $Re = 100$. Each fit has an R^2 of 0.99 with values and confidence intervals for $Re = 500$ given by $C_{d,0} = 0.023 \pm 0.002$, $A = 0.004 \pm 0.0005$, $n = -2.69 \pm 0.07$ for $Re = 250$ given by $C_{d,0} = 0.028 \pm 0.002$, $A = 0.007 \pm 0.0008$, $n = -2.32 \pm 0.07$ and for $Re = 100$ given by $C_{d,0} = 0.043 \pm 0.0026$, $A = 0.015 \pm 0.0017$, $n = -1.77 \pm 0.069$

Here we observe that the increased Reynolds numbers result in a number of changes to the drag coefficient. First, the neutrally stratified drag decreases with increasing Re. For $Re = 100$, $C_{d,0} = 0.043$ as opposed to $C_{d,0} = 0.023$ for $Re = 500$. This is still higher than the observed values of C_d, though again the simulated Reynolds number is much lower. Secondly, the value of n increases with increasing Re. This increase is still within the range of values predicted in the literature though now shifted more towards the scaling predicted by Miles and Huppert (1968) for non-hydrostatic flow of $(Nh/U)^3$. For larger Re, we would still expect to have $-3 < n < -1$ according to the literature for inviscid theories overviewed earlier in §3.1, though $C_{d,0}$ and A may vary from those predicted here. For the low values of Re examined, it is expected that the homogeneous drag coefficient, $C_{d,0}$ will scale in the manner usually attributed to Blausius for viscous boundary layer flow as $C_{d,0} \propto Re^{-1/4}$ (Blasius, 1913; Goldenfeld, 2006; Schlichting and Gersten, 2016). In figure 3.15, we compare the values of n, A and $C_{d,0}$ for $Re = 100, 250, 500$ as determined in figure 3.14. For $C_{d,0}$ we plot vs $Re^{-1/4}$ to examine if the parameter scales linearly and thus indicates agreement with the Blausius scaling.

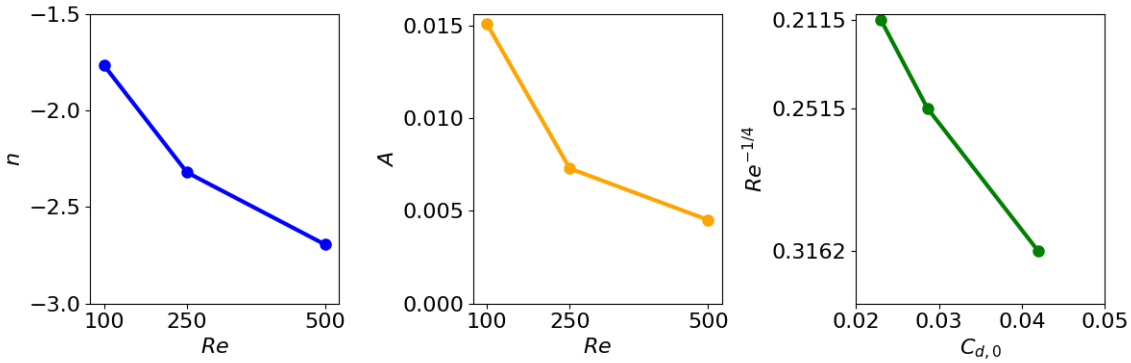


Figure 3.15: Plot of parameters determined by the power law fit of figure 3.13 with increasing Re, from left to right, n, A and $C_{d,0}$. For $C_{d,0}$ (rightmost) we plot $C_{d,0}$ vs $Re^{-1/4}$ to check for linear relationship as the expected Blausius scaling for low Reynolds number ($C_{d,0} \propto Re^{-1/4}$).

In figure 3.15, the few data points appear to scale nearly linear suggesting some agreement with the expected scaling $C_{d,0} \propto Re^{-1/4}$ of Blasius (1913). Examining the scaling of $C_{d,0}$ for $Re < 100,000$ as in Goldenfeld (2006) for Nikuradze's famous experiments for flow through a smooth pipe (Nikuradse, 1933) suggests that the geophysical values of Re may be in the asymptotic regime where $C_{d,0}$ becomes insensitive to changes in Re. So then by using observed coefficients to constrain $C_{d,0}$, it may be possible to establish a physically relevant scaling from these low Re calculations of our work if one can establish correct values of n and A.

The dependence of n and A on the Reynolds number is unfortunately more difficult to establish. It is possible that the wave drag parameters are primarily inertial, and asymptote to Re independent values for large Reynolds number. In this case it would be possible to deduce geophysically relevant values of A and n that, when accompanied by a geophysical value of $C_{d,0}$, could be used to provide a physically relevant scaling. The trends from the available data are suggestive that n is decreasing towards -3 with increasing Re, with a corresponding decrease in A. But the data does not extend to high enough Re to unequivocally determine an asymptote. Establishing a confident scaling would likely require further investigation of larger Reynolds numbers than were able to be considered in this work, and so we are unable to provide this result here. It is also possible that with higher Re the sponge region would need to be expanded due to the increased energetics thus entailing a further computational cost. Therefore we leave this for future work.

The simulations analyzed here predict neutrally stratified drag coefficients an order of magnitude larger than those observed in the polar regions (Tsamados et al., 2014;

Heorton et al., 2019; McPhee et al., 1987). As just discussed, this appears to be due to the artificially low Reynolds number. At low Fr_h these results indicate an increase of approximately an order of magnitude from this neutrally stratified value. One is then prompted to ask how much of this increase over the range of Fr_h is also attributable to assumptions of the model. Examining the plots of figure (3.14) suggests that the amplitude of this change is robust as we vary Re. Furthermore, recalling established results from the literature discussed in §3.1, the resultant power law scalings within this work are found to be within the expected range. These reasons suggest that unless a transition to turbulence significantly modifies the drag in a way that opposes this trend, the variation of drag with Fr_h examined here is likely to occur in the real-world system.

With this established relationship of the ice-ocean momentum exchange in good agreement with the broad theory of SSFOT, we have established a plausible scale for the variation of the ice-ocean drag coefficient due to the inclusion of internal wave drag. The power law scaling lies within the range of scalings predicted by the general SSFOT literature discussed in §3.1 and in the ice-ocean boundary layer studies such as that of McPhee and Kantha (1989). Within these works, both studies also reported either an increase or decrease in heat flux associated with increased drag due to dynamics of SSFOT. With the boundary conditions outlined in §2.1.2 we can examine the effects of sea ice generated internal waves and the corresponding change in ice-ocean momentum flux on the net, and spatial variability of the, ice-ocean heat flux.

3.3.3 Ice-ocean heat flux

A commonly used approximation for calculating the heat flux is that the heat transfer will scale as $Q = \rho_o c_p \gamma_T u_*(\Delta T)$. Here Q is the net heat flux from the ocean to the ice-ocean interface, the friction velocity u_* is defined in terms of the shear stress τ via $u_*^2 = \tau/\rho_o = C_d \mathbf{u}|\mathbf{u}|$ and γ_T is a constant heat transfer coefficient (Tsamados et al., 2015). This approximately predicts that $Q = \rho_o c_p \gamma_T \sqrt{C_d}|\mathbf{u}|\Delta T$ with a heat flux proportional to $\sqrt{C_d}$. This commonly used scaling assumes that shear driven boundary layer turbulence transports both heat and momentum with the same eddy velocity scale u_* (Schlichting and Gersten, 2016). In §3.3.2 it was shown that wave momentum fluxes have a significant impact on the ice-ocean momentum flux, and so we might expect deviations to this scaling law for the heat flux as well. Figure 3.16 shows the area-averaged heat flux as calculated via (2.31) and averaged over the ice-ocean boundary.

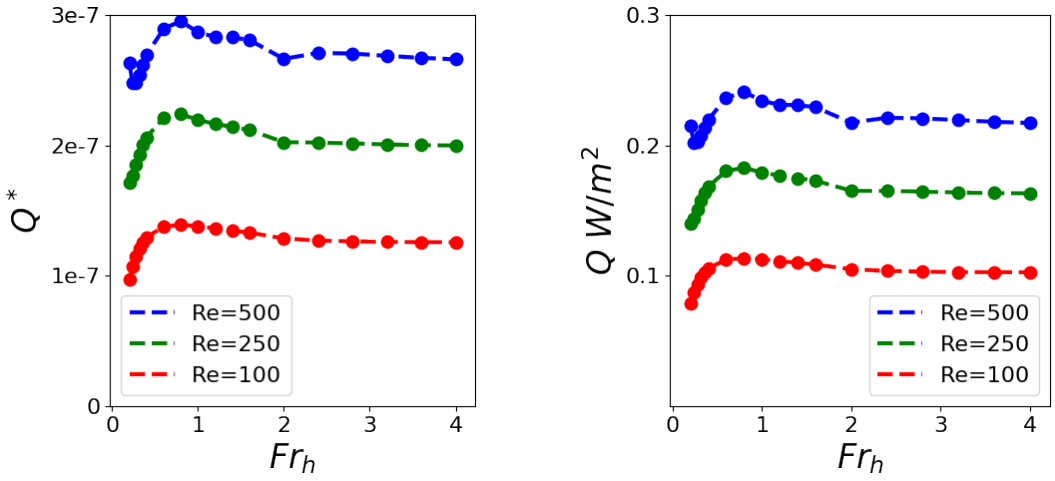


Figure 3.16: Plot of the dimensionless area-averaged heat flux $Q^* = Q/\rho_o c_p U \Delta T$, (left) and dimensionalized heat flux, Q, (right) with $U = 0.1$ m s^{-1} and $\Delta T = 2$ K, for $Re = 500$ (blue), $Re = 250$ (green), and $Re = 100$ (red) for a variety of Fr_h.

For each Reynolds number, the simulated heat flux has a local maximum near $Fr_h \approx 0.8$. For $Fr_h > 0.8$ the general trend is for the heat flux to decrease with increasing Fr_h (neglecting a small oscillation near the sub-to-supercritical transition point $Fr_h = 2$ for $Re - 500$). Below $Fr_h \approx 0.8$, a significant reduction in the heat flux to the ice is observed. In contrast, the drag coefficient decreases with increasing Fr_h for the full range of sub-critical Fr_h tested. Noting that $Q^* = Q/\rho_o c_p U \Delta T$ we see that a model with heat flux $Q = \rho_o c_p \gamma_T \sqrt{C_d}|\mathbf{u}|\Delta T$ is therefore qualitatively inconsistent with these simulation data. At the most extreme points, the non-dimensional heat flux varies by nearly 15% compared to the heatflux at supercritical values of Fr_h.

A potential mechanism for this reduction may be found in alterations to the upstream flow field at low Fr_h, with the blocking regime transition predicted for $Fr_h < 0.5$ by linear theory (Baines and Guest, 1988) and suggested in figure 3.2 from Winters and Armi (2012). This blocking flow field is illustrated clearly in our own simulations for $Fr = 0.28$ in figure 3.8. Here we observe a region of slow flow and relatively cold temperature/low salinity upstream of the ridge. In between $Fr_h = 0.8$ and this critical value, the heat transfer may be impacted by the apparent transition and partial blocking region as in figure 3.9. It is possible that this phenomenon may serve to insulate the upstream portion of the floe and create the low Fr_h behaviour of figure 3.16. Additionally, variations in the temperature gradient normal to the ice floe due to internal waves may alter the downstream heat flux as observed in the model results of Skyllingstad et al. (2003). To investigate this, we examine a number of vertical cross sections of temperature as in figure 3.17.

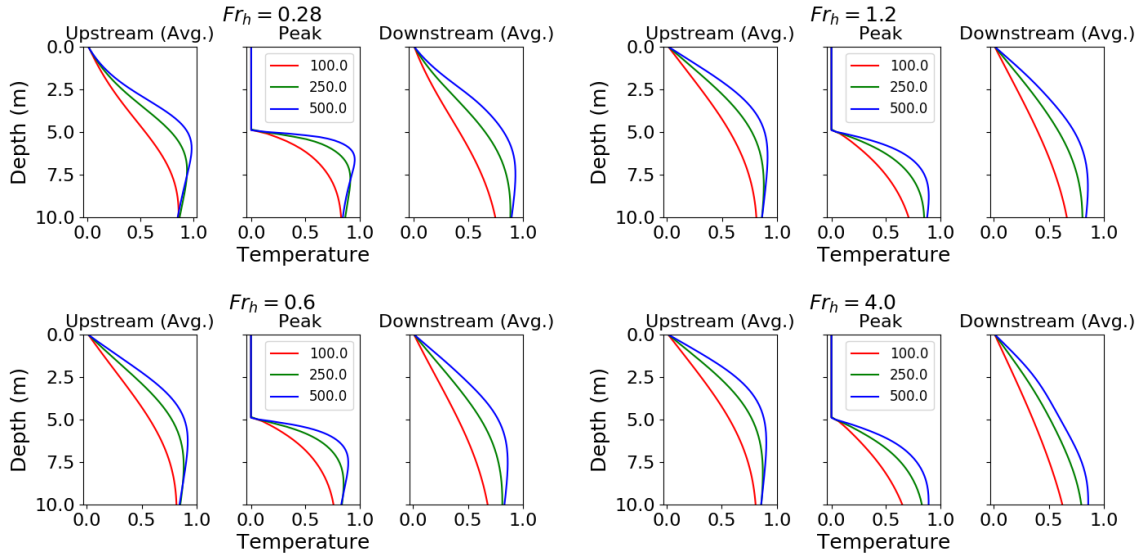


Figure 3.17: Vertical profiles of dimensionless temperature in the surface 10 meters for the average upstream, ridge peak, and average downstream. Here the averaged upstream and downstream are calculated to avoid bias when selecting a location upstream or down stream which may be affected by the generated waves. These are calculated by summing the temperatures for each column element-wise before the start of the ridge or after the ridge and then dividing by the number of columns in that region. The Fr_h values correspond to those shown previously in figures 3.8 - 3.11

From the vertical cross sections of temperature we observe that the primary effect of increasing the Reynolds number in this picture is the decreasing boundary layer thickness. This is qualitatively consistent with boundary layer theory as the lower viscosity reduces the extent of viscous diffusion of vorticity away from the boundary (Schlichting and Gersten, 2016). This shrinking boundary layer allows for a larger vertical temperature gradient closer to the boundary, and thus increased heat flux. At $Fr_h = 0.28$, in the upstream averaged temperature profile of figure 3.17, some concavity close to the interface can be seen that is missing in the larger values of $Fr_h = 0.6, 1.2, 4.0$ displayed. This is indicative of upstream blocking of the flow allowing for a stagnant cold and fresh pool to form. The downstream temperature profiles also appear to have some concavity for low Fr_h, though it is less significant than the blocking region upstream.

We can examine the corresponding spatial variations in the heat flux linked to these varying vertical temperature gradients by plotting the local heat flux and the integrated heat flux throughout the domain as in figure 3.18. The integrated heat flux is here normalized by the domain length and given by

$$\frac{\int_0^x Q(x)dx}{L} \tag{3.21}$$

where x is the length into the computational domain from the inlet. This quantity is useful for inferring trends for the heat flux variation with the length of the floe. Figure 3.18, shows evidence of a developing boundary layer upstream of the ridge, responding to the discontinuous temperature inlet. This may suggest sensitivity to the position of the ridge in relation to the inlet for our results. The boundary layer development seems weaker for $Fr_h = 0.28$, consistent with significant blocking of the flow.

A spike in heat transfer occurs over the ridge with a stronger signal in lower values of Fr_h. The integrated heat flux plot of figure 3.18 (lower panel) shows this heat flux spike is sufficient for the accumulated heat flux at lower $Fr_h = 0.28$ to have overtaken the heat flux at $Fr_h = 4$ by the end of the ridge, despite initially smaller upstream heat fluxes. Hence the lower downstream heat fluxes must also contribute to the lower dimensionless heat fluxes seen at lower Fr_h.

Downstream of the ridge, there is a roughly linear increase in the integrated heat flux with distance into the domain, with superimposed oscillations near the ridge for subcritical Fr_h indicating the effect of internal waves on the interfacial heat exchange. The middle panel of figure 3.18 zooms in on the spatial oscillations in heat flux and suggests that internal waves may drive variation in melting rates (though melting is

not included in the present model). The strongly enhanced melting of the ridge would also tend to shallow the ridge over time and remove the sharp peak.

The roughly linear scaling of this downstream integrated heat flux suggests the sensitivity of this component is not fundamentally altered by the domain size. The same can not necessarily be said about the upstream flow for subcritical Fr_h and the sensitivity to this is investigated briefly later on in §3.3.4.

To further visualize how heat flux is partitioned with changing Fr_h in figure 3.19 we examine the fractional contributions to the heat flux of the upstream, ridge, or downstream regions for a selection of Fr_h. For $Re = 500$, in the blocking regime with $Fr_h < 0.5$, the heat flux over the ridge begins to increase significantly with decreasing Fr_h as shown in figures 3.18 and 3.19. With an increase in the Froude number, the peak in heat flux at the keel drops off slightly and the upstream and downstream partitions of the floe absorb a greater fraction of the heat. As seen in figure 3.18, for $Fr_h < 2.0$ the downstream heat flux has an oscillatory pattern to it corresponding to the principal wavelengths determined by N/U. In the super-critical regime, $Fr_h > 2$, where we witnessed a downstream stagnant layer in the shadow of the obstacle in figure 3.11, we see a slight reduction in the downstream heat flux with increasing Fr_h correlated with an increased fraction of the heat flux occurring on the upstream side of the obstacle.

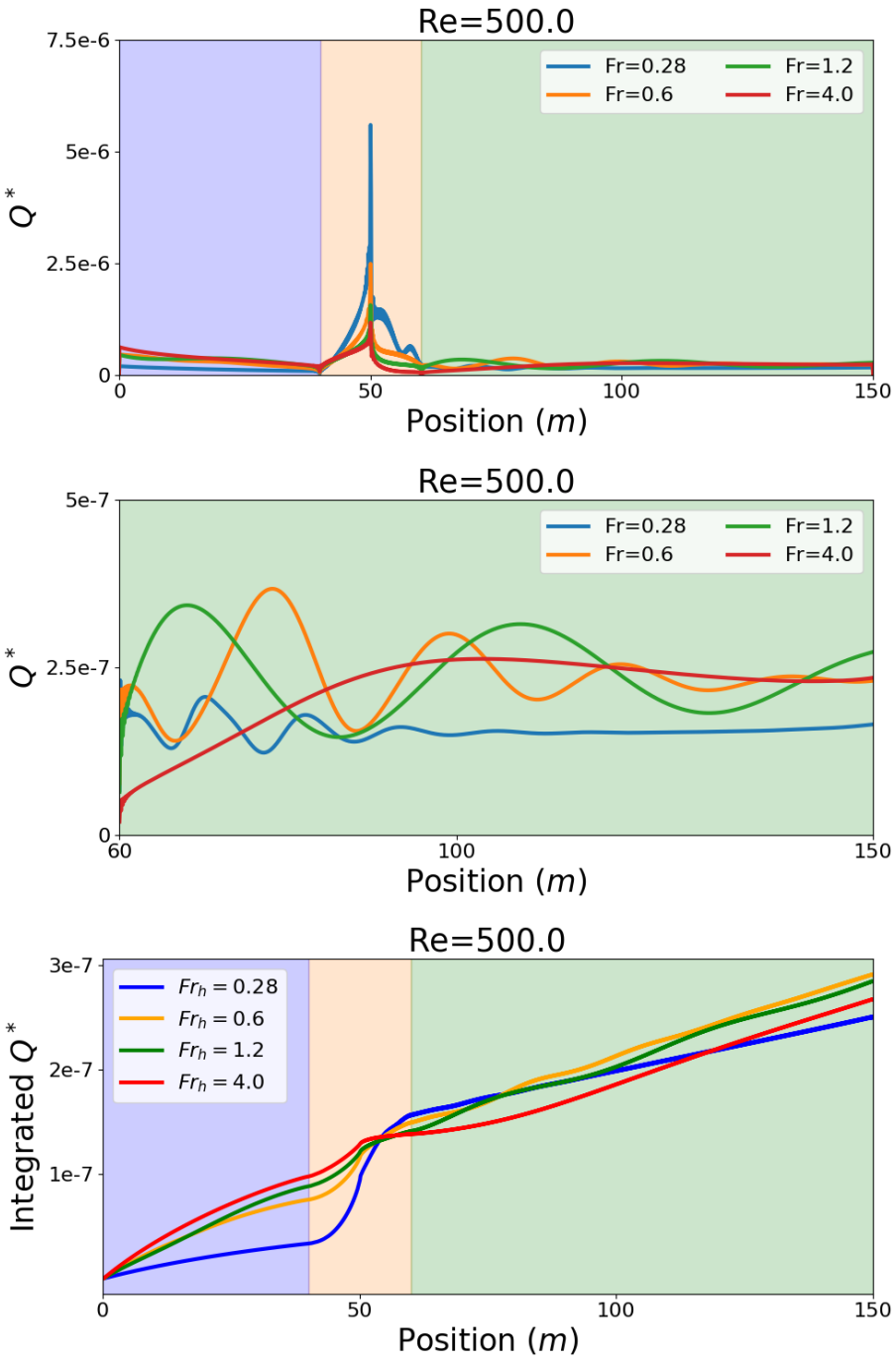


Figure 3.18: Local dimensionless heat flux across the ice-ocean interface for a variety of Froude numbers (top), a subsequent zoom on the downstream oscillatory behaviour (middle), and then the total area integrated heat flux in the computational domain (bottom). In the topmost plot, a clear peak in the local heat flux is observed over the ridge. The middle plot zooms in on the downstream behaviour of this plot to examine the oscillatory behaviour of the downstream heat flux. The bottom plot illustrates that the integrated heat flux is roughly linear with downstream extent, but the upstream development appears affected by the evolving boundary layer. Shading illustrates upstream (blue), ridge (orange), and downstream (green) regions.

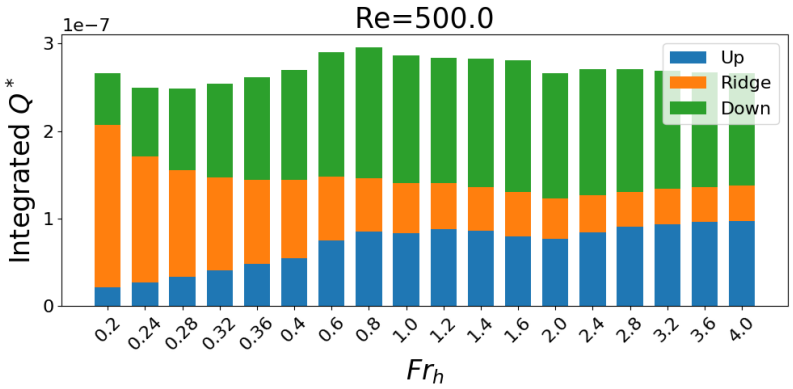


Figure 3.19: Area integrated dimensionless heat flux within each region of the domain for a variety of Fr_h and $Re = 500$: upstream (blue), ridge (orange), and downstream (green).

The results of these simulations as shown in figures 3.13 and 3.16 indicate that below a certain value of Fr_h, the ice-ocean drag coefficient increases while the ice-ocean heat flux decreases. This is similar to the result predicted by McPhee and Kantha (1989) and observed in Morison et al. (1987). This result was not seen in the more recent study using LES computations of Skyllingstad et al. (2003). It is possible in our design of the problem as depicted in figure 3.5 that the discontinuous temperature between the inflow and ice-ocean boundary conditions sets the variation of heat exchange as seen in figures 3.16, 3.18, and 3.19. This discontinuity leads to the evolution of a boundary layer at the inlet and into the start of our domain as the flow adjusts to the boundary temperature. One way to test this is to invert the temperature profile in the initial condition, the inlet and the ABC method, so that the temperature near the interface is at the freezing point and increases to some far field warm water temperature. Geophysically this might correspond to a setting where pooling of melt water leads to a relatively cold fresh region near the ocean surface between ice floes, which is close to the melting temperature. We will use the same non-dimensionalization except with ΔT given as $T_{ML} - T_{int}$ where T_{ML} is the temperature at the bottom of the computational domain. In these simulations as in §3.2.2 the other parameters are given by table 3.1. As the temperature has minimal impact on the buoyancy due to the small density ratio, R_ρ, we expect the momentum exchange to behave as discussed above in §3.3.2.

We verify the approximate dynamic similarity of these new simulations in figure 3.20, by comparing the calculated drag coefficients for a sweep of Froude numbers, to the previously established power law fits determined in figure 3.14. In this case with

unstably stratified temperature, the calculated drag coefficients match the power law fits of §3.3.2 with an R^2 of 0.99 in each case.

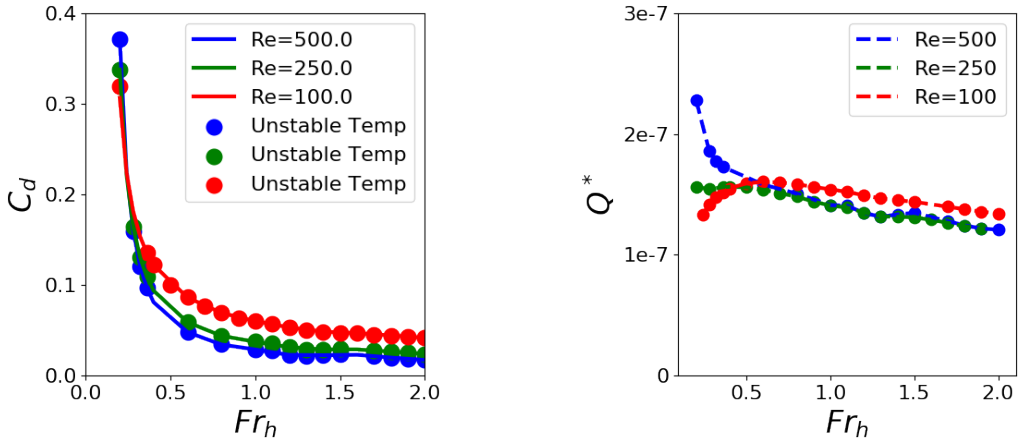


Figure 3.20: Drag coefficient (left) and area integrated heat flux (right) vs Fr_h for $Re = 100$ (red), 250 (green), 500 (blue), with the unstable temperature stratification. On the left, the previously identified power law fits (solid lines) are compared to the new simulation data points (dots). The stably stratified temperature simulations match the previous fit with an $R^2 = .99$ for each Re

We now examine the area-averaged heat flux as a function of Fr_h for the unstable temperature configuration in figure 3.20. The heat flux with this unstable temperature profile is more uniform with Reynolds number in contrast with the sensitivity to Re seen in the previous stable temperature profile. The exception to this observation is the diverging behaviours for $Fr_h \lesssim 0.6$, where the $Re = 500$ curve indicates increased heat flux with decreasing Fr_h, and $Re = 100$ shows the opposite. For the intermediary case of $Re = 250$ the temperature varies little with Fr_h. For $Re = 500$, we then have increased heat flux with increased drag coefficient which is qualitatively similar to the observations of Perovich et al. (2003) and model results using said observations in Skyllingstad et al. (2003). Compared to the previous simulations with $Re = 500$ and differing thermal stratification, the area-averaged heat flux is reduced by order 40%. This suggests that the temperature gradient resulting from the chosen inlet profile above has a modest influence on the interfacial heat flux.

Examining the vertical temperature profiles for the averaged upstream and downstream temperature profiles, and at the ridge peak (figure 3.21) we see a different pattern from the previous equivalent setups in figure 3.17. In this unstable thermal stratification, the temperature gradients are much more closely aligned with a very

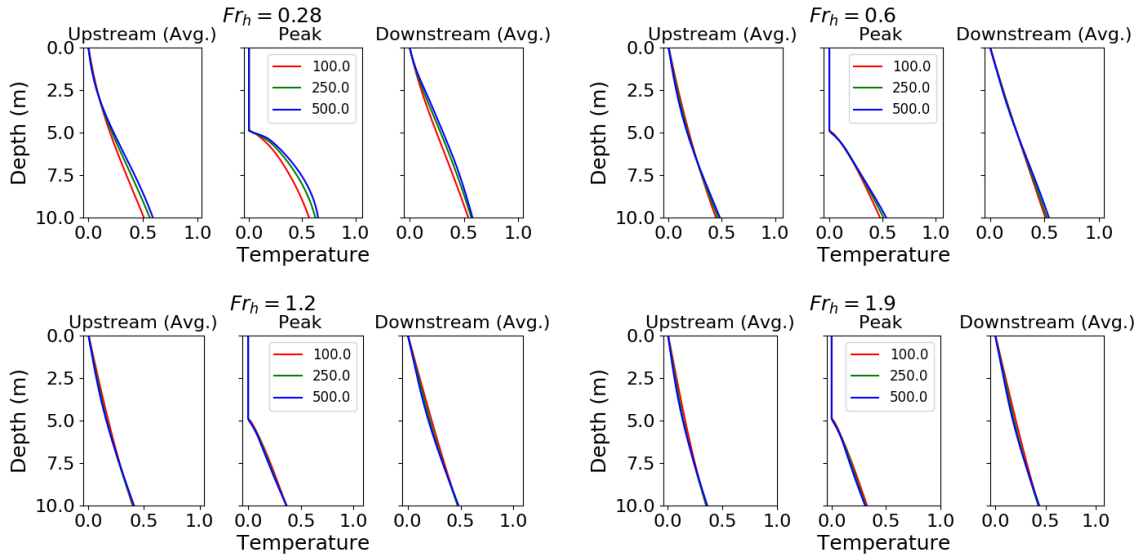


Figure 3.21: Vertical temperature profiles in the surface 10 meters for the average upstream, ridge peak, and average downstream. The same Fr values as shown previously but instead of $Fr_h = 4$ we have $Fr = 1.9$ as only $Fr_h < 2$ were examined for this comparison

slight difference in the case of $Fr_h = 0.28$. For $Fr_h = 0.28$, the $Re = 100$ simulation has a smaller temperature gradient than the higher Re simulations close to the boundary in all three profiles, with a more appreciable difference in the ridge peak and average downstream plots. A probable cause of this is the variation in the viscous boundary layer thicknesses due to the increasing Reynolds numbers. In line with boundary layer theory, a larger Reynolds number would generate a smaller viscous boundary layer. As this boundary layer is diverted and flows over the ridge, it modifies the heat transfer there and may generate a stronger temperature gradient near the ice-ocean interface. We can try to understand this scaling of heat flux with Reynolds number in a similar manner to the previous case by looking at the spatially integrated heat flux, as well as the partitioning of the area-integrated heat flux for the unstable temperature profile as in figure 3.22 for $Re = 500$.

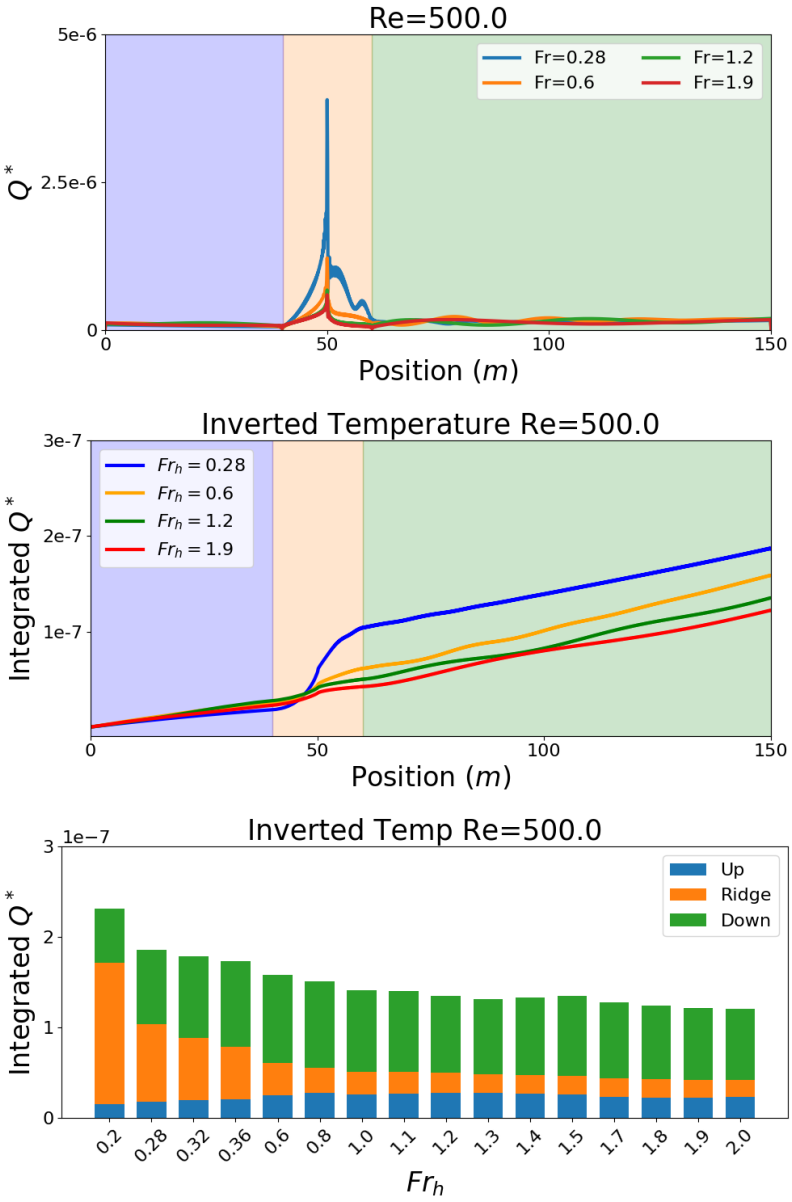


Figure 3.22: Local heat flux (top), integrated heat flux (middle) and the regional contributions to the area-averaged heat flux of each region (bottom) for a variety of Froude numbers with stable temperature stratification and $Re = 500$. The $Fr = 0.28$ line appears wider around the ridge due to increased noise likely due to the stair-casing of the obstacle boundary in the simulation domain. The shaded regions correspond to different regions of the domain: upwind (blue), ridge (orange), and downwind (green).

Compared to the stable thermal stratification in figure 3.18, the lateral variation of heat exchange for $Re = 500$ shows a similar broad pattern though the magnitude is reduced. The upstream region appears to be missing the signs of thermal boundary layer adjustment present in the earlier configuration resulting in a decreased up stream

heat flux. A spike in heat flux is observed over the ridge whose magnitude decreases with increased Fr_h. This spike in heat flux is amplified at low Fr_h as in the stable temperature configuration examined previously, because there is upstream blocking of the flow (as in figure 3.8). The downstream oscillations in heat flux due to internal waves observed previously are also present in figure 3.22.

As opposed to the previous simulations, the upstream and downstream heat flux appears largely similar for all Fr_h, varying less than 5% across the full range of Fr_h. This suggests the heat flux over the ridge plays a primary role in setting the area-averaged heat flux at the floe scale. We would thus expect an increase in the Reynolds number to increase the heat flux to the ridge. Similarly, a decrease in Reynolds number would be expected to see a corresponding decrease in heat flux. To confirm this inference, we can examine the same array of figures just discussed but with $Re = 100$ as in figure 3.23.

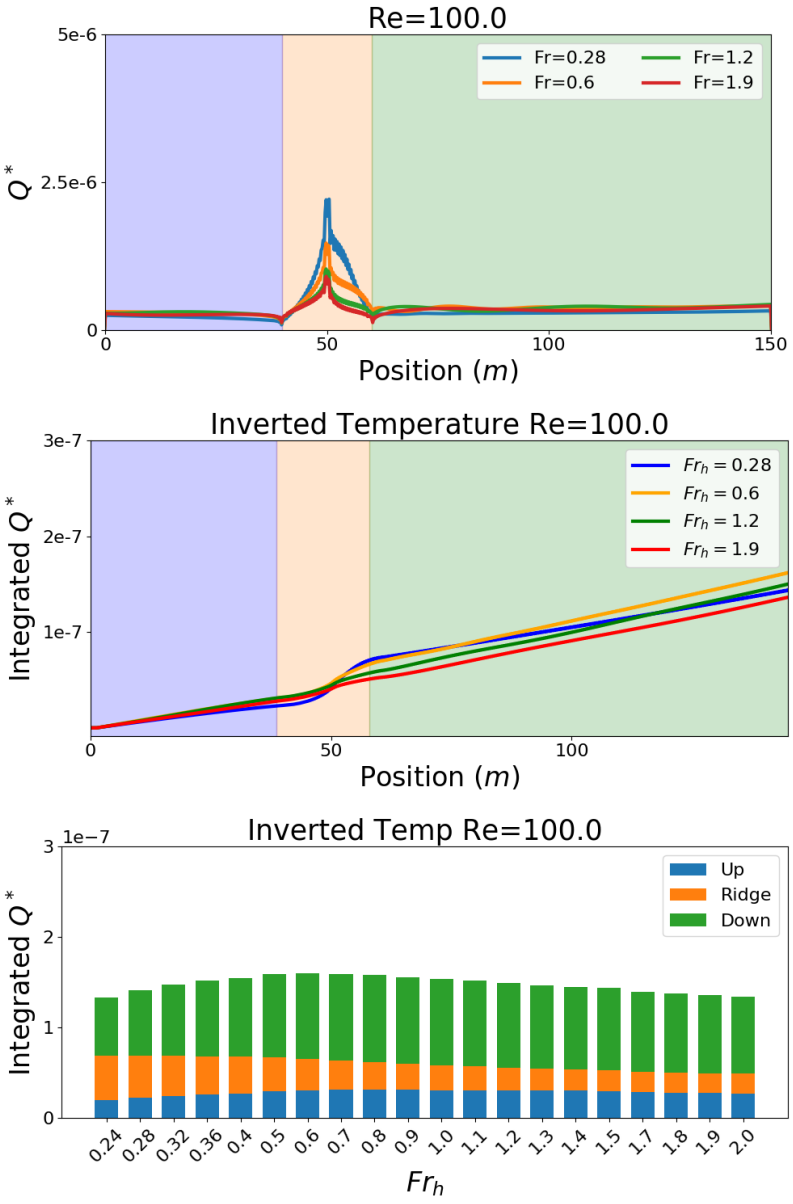


Figure 3.23: Local heat flux (top), integrated heat flux (middle) and the regional contribution to the area-averaged heat flux of each region (bottom) for a variety of Froude numbers with stable temperature stratification and $Re = 100$. The shaded regions correspond to different regions of the domain: upwind (blue), ridge (orange), and downwind (green). For $Fr = 0.28$ the line within the top panel appears thicker likely due to the increased signal to noise ratio due to the obstacle stair-casing in the stable temperature case.

Comparing the spatial heat flux data for $Re = 500$ in figure 3.22 and $Re = 100$ in figure 3.23 we see that the reduction in Reynolds number is accompanied by

a significant decrease in the heat flux over the ridge. Though there is still some increase in heat flux over the ridge as can be seen in the top panel of figure 3.23, the marked increase observed earlier accompanying flow blocking for $Fr_h < 0.5$ is absent. For $Re = 100$, the net heat flux instead appears to be largely controlled by the downstream heat flux as seen most clearly in the bottom panel of figure 3.23. This pattern of reduced downstream heat flux with decreasing Fr_h was seen in the original configuration as well. A consequence of decreasing Fr_h, is to increase the stability of the stratification which may make it more difficult for fluid at depth to advect and mix upwards. In the current configuration where the heat content of the fluid increases with depth, this can create a stronger insulation of the surface boundary. As we reduce Fr_h, we also reduce the kinetic energy of the flow reducing the scale of the potential energy barrier that can be overcome. Changes in Reynolds number with Fr_h fixed alters the boundary layer dynamics with larger values of Re generating smaller boundary layers which allows for an increase in intensity of the subsurface jet (see figures 3.8, 3.9).

The primary conclusion of this comparison between stratification profiles is that internal wave activity leads to variations in the magnitude and spatial variation of the heat flux. For the stable temperature profile, flow blocking inhibited heat flux in the downstream and upstream regions but enhanced it over the ridge with a strongly amplified near surface jet over the ridge. The net effect of this in a stable temperature stratification was a net decrease in the area-averaged heat flux with decreasing Fr_h as reflected in the downward turn at $Fr_h \lesssim 0.8$ in figure 3.16. It is possible that the enhancement of heat flux around the ridge at even lower Fr_h may eventually outweigh the reduction in heat flux downstream and upstream. This result may explain the increase in heat flux observed at $Fr_h = 0.2$ compared to $Fr_h = 0.24$ as shown in the bottom panel of figure 3.19, though a robust prediction would need more data points at lower Fr_h.

Generation of internal waves were observed to cause downstream oscillations in the local heat flux which may further alter the sea ice roughness. In the regime of $Fr_h < 2$ the amplified velocity near the ridge peak was also observed to have high local heat flux. With decreasing Fr_h, the contribution of the heat flux over the ridge became the dominant component of the area-averaged heat flux. These phenomena suggest the importance of ridges for heat flux in strong stratification. Over time, the strong heat fluxes over the ridge would lead to preferential melting peaked near the ridge tip, so that ridge amplitude and steepness may naturally reduce over time. It was also seen that upstream of the obstacle, the evolution of the boundary layer due

to the discontinuity between the inflow profile and the ice boundary conditions for temperature and velocity appeared to affect the heat flux. We examine the sensitivity of these results to this process, and the obstacle geometry now.

3.3.4 Sensitivity to ridge geometry and position

As previously mentioned, there is a discontinuity between the inflow velocity (and temperature for the stable stratification case) and the ice-ocean boundary, which results in an adjusting boundary layer from the leading edge of the ice floe and creates a sensitivity to the observed metrics on domain size. To investigate this, in figure 3.24 we compare the integrated heat flux for a select number of runs with $Re = 100$ and $Fr_h = 0.28, 0.6, 1.2, 4.0$ where the obstacle is centered about $C_x = 100$m, as well as $C_x = 50m$ as in figure 3.5.

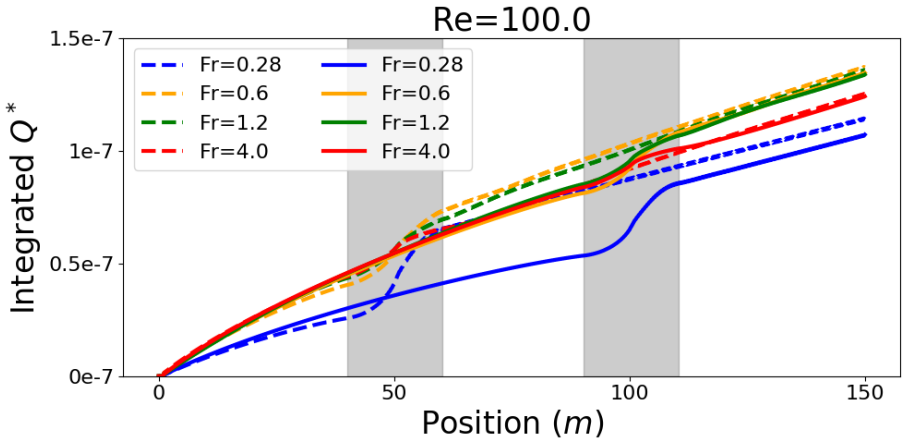


Figure 3.24: Integrated heat flux for a variety of Froude numbers with stable temperature stratification and $Re = 100$ with $C_x = 50m$ (dashed lines) and $C_x = 100m$ (solid lines). The shaded regions around 50m and 100m indicate the ridge positions for the corresponding simulations.

For $Fr_h \geq 0.6$ the heat flux upstream of the ridge shows a consistent evolution of the boundary layer, until the ridge is encountered. The response of the flow over the ridge differs depending on the value of Fr_h with a larger spike in heat flux occurring at low values of Fr_h. The downstream behaviour of the integrated heat flux appears approximately linear. Interestingly, the integrated heat fluxes for a given $Fr_h \geq 0.6$ appear to converge downstream of the obstacle, indicating that the total heat flux is almost independent of the location of the ridge. The ridge location has greater impact on the strength of melting over the ridge for the case $Fr_h = 0.28$ with strong blocking. Nevertheless, heat fluxes downstream of the ridge only differ by approximately 10%

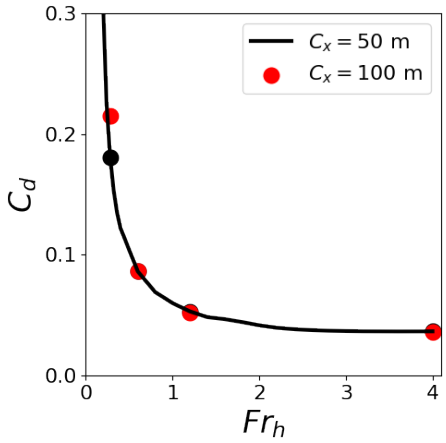


Figure 3.25: Drag coefficient comparison between the previous simulations shown with $C_x = 50m$ (Black dots and line) and a selection of runs with $C_x = 100m$ (red dots) for $Re = 100$ and $Fr = 0.28, 0.3, 0.6, 4.0$. Note that the three black dots with highest Froude number for $C_x = 50m$ are hard to distinguish from the red dots for $C_x = 100m$.

with a doubling of distance of the ridge from the inflow. These results indicate that whilst the pattern of the heat flux upstream, and over the ridges is partially influenced by the ridge location, the change in total heat flux averaged over the floe remains modest. We see a similar behaviour when comparing the calculated drag coefficients for these simulations in figure 3.25, with drag coefficient showing negligible dependence on ridge location for $Fr_h \geq 0.6$, but modest variation of order 20% for $Fr_h = 0.28$.

It is also possible that the specific ridge geometry may influence heat and momentum exchange at the boundary. As noted in §3.2.1, the morphology of a pressure ridge is not always as simple as the form implemented here. To examine potential alterations to the previous results, we examine a selection of simulations with a varied ridge geometry. We here examine the cases of a smooth (flat) ice floe and the 'witch of Agnesi' profile more thoroughly studied in the theoretical literature (Baines, 1998; Lam, 2013). For the witch of Agnesi shape, we use the formulation of (3.5) with $a = 2h$. For this comparison we look at a variety of Fr_h with $Re = 100$ and compare to the previous results using the original setup depicted in figure 3.5.

As we see in figure 3.26, the general pattern of increased drag with decreased Froude number holds, though the associated power law exponent varies slightly, as well as a minor variation in the unstratified drag coefficient. Comparing specific geometries we can infer that the Lorentzian "witch of Agnesi" shape yields drag coefficients that are fairly similar to the triangular ridge. With a triangle ridge we

have an instance where the length scale goes to 0 at the point of the triangle, whereas the Lorentzian ridge has a smooth transition. This has been known to have potential impacts on the separation of the boundary layer from the interface resulting in weaker internal wave spectra and localized turbulence (Sutherland et al., 2013). Such effects seem to have limited impact on the drag coefficient here, perhaps because they are inhibited in this comparison due to the modest Reynolds number. The scenario with a flat ice floe has a lower unstratified drag coefficient due to the absence of any roughness and so is purely skin drag rather than wave or form drag. The drag coefficient decreases slightly with increasing Fr_h, although the fitted power law exponent is much lower due to the absence of wave drag.

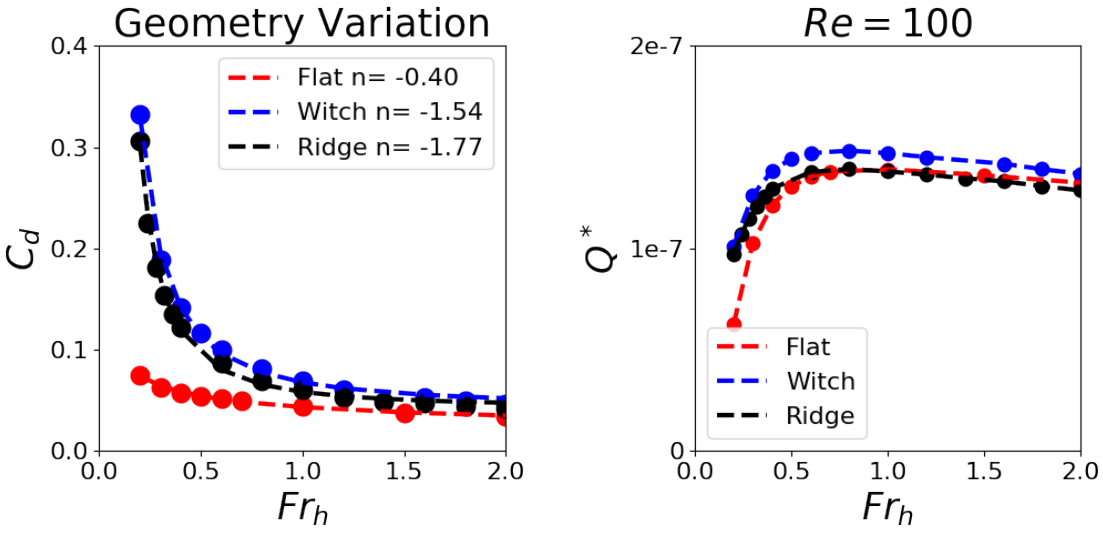


Figure 3.26: Drag coefficient (left) and area-averaged heat flux (right) as a function of Froude number for varying floe geometries. The drag coefficient data is shown with n determined by a nonlinear least squares power law fit as in previous figures. The geometry was varied as a smooth flat floe (red) with ($n = -0.40 \pm 0.07$, $C_d = 0.035 \pm 0.007$, $A = 0.008 \pm 0.007$) witch of Agnesi profile from §3.1.1.1 (blue) with ($n = -1.54 \pm 0.06$, $C_d = 0.024 \pm 0.002$, $A = 0.044 \pm 0.004$), and the triangular ridge of figure 3.5 for comparison (black) given by $C_{d,0} = 0.043 \pm 0.0026$, $A = 0.015 \pm 0.0017$, $n = -1.77 \pm 0.069$.

The area-averaged heat flux shown in figure 3.26 for the different obstacle geometries appears to have less variation than in the drag coefficient. The reduced value of the area-averaged heat flux for a flat ice floe at low Froude number suggests the heat flux over topography is an important component in this metric. This conclusion is further established by the earlier plots of the partitioning of the integrated heat flux as in 3.18. This suggests that larger and rougher MYI ridges under the same

scenarios may cause a localized increase in heat flux in comparison to smoother FYI. However as both of these ice types have differing values of roughness and thus h, the occurrence of blocking may complicate the area-averaged picture.

3.4 Summary and future work

The results discussed in this chapter strongly indicate that the generation of internal waves due to ice-ocean processes play an important role in the under-ice fluxes of heat and momentum. As shown in §3.3.1, flow under a ridged ice floe experiences the characteristic regimes predicted for stratified flow over topography, as characterised by the Froude number Fr_h. For sub-critical flow with $Fr_h < 2$, we observe internal wave generation with wavelengths controlled by the mean flow and stratification as $\lambda \propto U/N$ in agreement with theoretical predictions (Baines, 1998). At $Fr_h \lesssim 0.8$ and below, we also see the blocking of upstream flow across the depth of the ridge accompanied by a near surface jet at the depth of the ridge tip. For super-critical flow, the persistent waves become evanescent and the boundary layer appears to separate from the floe beyond the ridge tip creating a region of stagnant pool of 'meltwater' in the shadow of the pressure ridge.

Beyond the qualitative flow properties, we demonstrated that within a geophysically motivated range of Fr_h, the drag coefficient experiences a significant variation. This variation indicates the importance of wave drag for determining the turbulent momentum exchange at the ice-ocean boundary. Within the Reynolds numbers tested, we found the scaling of the drag coefficient with Fr_h to be well characterized by $C_d = C_{d,0} + AFr_h^n$. Focusing on the predicted values of n, our simulations predicted values between $-1.77 \leq n \leq -2.69$ for $Re = 100$ to $Re = 500$ respectively. The broader literature of stratified shear flow over topography has a variety of proposed scalings dependent on a number of processes and regime changes as reviewed in §3.1. Our results here are for a modest Reynolds number case and we have assumed a uniform turbulent eddy viscosity and diffusivities which generated relatively laminar patterns for the resulting flow. Comparing to inviscid models using the nonlinear Long's model, our results for $Re = 500$ show closest agreement to the non-hydrostatic scaling of Miles and Huppert (1968) with $n = -3$. However it is unclear if the scaling of n with Reynolds number would asymptotically approach this value, or exceed it. It has been suggested that an alternate scaling in the blocking regime of $Fr_h < 0.5$ might occur (Baines and Guest, 1988) but we see no clear evidence of this in this work. This is potentially due to the artificially low Reynolds number, or an insufficient number of

data points in this regime. Despite these limitations, this work provided a spanning of Fr_h space (and implicitly Nh/U and Na/U) with the inclusion of a multitude of mechanisms such as nonlinear effects, boundary layer separation, viscosity, and non-hydrostatic effects. Previously such a generalized examination was largely the realm of experimental work such as Sutherland et al. (1999), Aguilar and Sutherland (2006) and Baines (1998) and even then for a handful of parameter values. The primary conclusions of these studies is focused on the generation mechanisms of the waves themselves and identification of the flow regimes for blocking, wave generation and evanescent waves. Similar to the results tested in §3.3.4 for the triangular ridge and Lorentzian witch of Agnesi profile, Aguilar and Sutherland (2006) note close agreement in all metrics between triangular and sinusoidal hills which, though not the exact profile, have many similar properties. They further test a rectangular hill and note substantial differences. Though this is not tested here, MYI ridges can often be characterized as a sort of rubble pile (Wadhams et al., 2012) and so may suggest stark differences in their properties from those observed in our work.

The observed effect of the Froude number on momentum exchange at the boundary raises the question of whether there is a corresponding impact on heat exchange. In the observational record of the under-ice boundary layer, the ice-ocean heat flux is typically characterized by the ice-ocean velocity, roughness, and stratification as detailed in §3.1.4. In model studies (McPhee and Kantha, 1989; Skyllingstad et al., 2003) and observational records (Morison et al., 1987; Perovich et al., 2003) contrasting trends in wave drag and heat flux was observed depending on the underlying thermal stratification.

In this work, with a stable temperature stratification, we find there is a maximum heat flux at $Fr_h \approx 0.8$. The heat flux decays to a uniform value at large Froude number. For $Fr_h < 0.8$, the heat flux increases with Froude number whilst the drag coefficient decays. This indicates that the usual scaling for heat fluxes proportional to friction velocity, and thus proportional to $\sqrt{C_d}$, is not always appropriate when there is significant internal wave drag. When the in-flowing stratification has temperature increasing with depth, and surface temperature continuous with the ice-ocean boundary condition, there is a qualitative change in the behaviour at low Fr_h between different Reynolds numbers, with heat flux initially increasing with Froude number at low Reynolds number, but heat flux decreasing with increasing Fr_h for higher Re. The behaviour is more consistent at large Fr_h, with heat flux decaying slightly with Fr_h. At the lowest value of $Fr_h = 0.2$ for the $Re = 500$ case there appears to be in

additional change in the heat flux curve, though it has not been possible to find a satisfactory explanation for this.

Dimensionalizing the heat flux with a scaling of $U = 0.1$ m s^{-1} and $\Delta T = 2$ for the $Re = 500$ runs with a stable temperature profile, we measure a heat flux of $Q \approx 0.22$ W m^{-2} at large Fr_h. Compared to this value, the peak heat flux at $Fr_h \approx 0.8$ shows an increase in heat flux of order 10%. The minimum heat flux calculated in figure 3.16 indicates a decrease of the same order.

The dimensional heat flux calculated in this work for all configurations is far lower than changes in heat fluxes associated with the inclusion of internal wave drag of other studies. In McPhee and Kantha (1989), a 60% reduction in heat flux was attributed to the inclusion of internal wave drag in a one-dimensional turbulence closure model with $Re \approx 250$ calculated using an approximate value of their eddy viscosity near the ice ocean interface. This study did have real-world values of eddy viscosity and eddy diffusivities which may account for some of this difference. To put this magnitude of heat flux in context, we note that the equilibrium ice state of the Arctic ocean shows significant sensitivity to the basal heat flux with an increase of 1 to 2 W m^{-2} predicted to result in a thinning of the equilibrium ice state by O(1) m yr^{-1} (Kwok and Untersteiner, 2011). The mean value of heat flux here would thin ice by approximately 0.02m/year. The 10% variation in the total heat flux due to stratified flow is an even smaller 0.002m/year, and thus is not a direct leading order impact using the values simulated here. It is possible that, the simulations examined thus far may underpredict the variation due to the artificially large constant turbulent viscosity and diffusivities, the assumption of $Pr = Sc = 1$, and the simplified isothermal/isohaline boundary conditions. Each of these effects could be examined using the existing infrastructure developed here given suitable computational resources, although are left as potential future work.

In spite of the modest impact on the area-averaged energy budget, the pressure ridges do however have a significant impact on the spatial distribution of melting across an ice floe. In each simulation, it is apparent that the heat flux at the ice-ocean interface is spatially heterogeneous. For subcritical Froude numbers, $Fr_h < 2$, the heat flux at a point is in part dependent on the internal wave field (e.g. see figure 3.18). This poses a potential consideration for field observations in the case of measuring turbulent heat fluxes close to the ice-ocean interface which may vary downstream of the ridge and not be characteristic of the ridge as a whole.

Whilst the governing parameters were fixed in this work, they may evolve over time in the geophysical system. For example, the oscillatory heat flux patterns observed for

subcritical flow in figure 3.18 would preferentially melt certain areas of the sea ice and thus alter the ice roughness. This would then evolve the ice face, and thus change the generated internal wave spectra and subsequently the heat flux. From figures 3.18 and 3.22, we expect this to preferentially alter the ridge height and shape thus changing the governing parameters and the aspect ratio of the ridge. The wavelike patterns of heat flux downstream of the ridge will also shape the ice-ocean interface. The wavelength of these oscillations is controlled by U/N with waves initialized relative to the ridge location. If both the ice-ocean relative velocity and stratification remain constant for extended periods then we might expect the persistency of the pattern of melting to generate corrugations in the ice-ocean interface downstream of the ridge. Temporal variations of the ocean conditions could imprint a spectrum of wavelengths.

The transient response to changing environmental conditions has also been neglected in this study. Natural adjustment timescales for the flow include the advective timescale L/U, which will be of order an hour for a 150m floe and 0.1m/s ice-ocean velocity difference. The timescale for adjustment of propagating internal waves is important for strongly subcritical flow, but is then by definition faster than the advective adjustment because $U/Nh << 1$. We might expect the results to apply in a quasi-steady fashion whenever the environmental conditions adjust slower than the above flow adjustment timescales. Rotational effects may alter the cross keel flow on larger floe lengths, potentially affecting the expected drag, heat, and internal wave spectra predicted within this work, or set up critical layers as in the atmospheric case, as a result of shifting velocity with depth as in the Ekman spiral solutions discussed in §3.1. Additionally, the stratification profiles here were assumed to be linear. Stratification in the polar oceans evolves on daily, seasonally, and longer timescales. From the results of this work, one may expect that with a change in the upper ocean stratification a corresponding change would appear in the ice-ocean drag, and heat flux.

A key question raised by this work is what, if any, the impact of this modified wave drag would be at larger scales. In the ice-covered oceans, a number of properties affect the internal wave field. At the ice interface alone, variations in roughness, stratification, ice concentration, or 3D effects neglected in this work may alter the predictions raised here. Additionally, when the ice-ocean velocity and keel are not perpendicular, we might expect a leading order approximation to use the component of ice-ocean velocity normal to the ridge in place of U, but the effects of tangential flow remain uncertain. Compared to the study of Skyllingstad et al. (2003), we do not account for 3D turbulence. It is possible that the 3D nature of pressure ridges allows

for flow around the deepest part of the ridge as observed in some model studies of atmospheric flow over mountains (Xu et al., 2012). In the study of Xu et al. (2012), the key phenomena seen in our work are still present but, due to the ability for some of the flow to go around the obstacle, a reduction in the amplitude of internal wave spectra and momentum flux was predicted. In this setting, these 2D results may overestimate internal wave activity as well as the heat and momentum fluxes. However, in the case that the ridge extends suitably far in the lateral directions the physical picture would be captured by the results just discussed.

A potential avenue of exploration of this work would be to take the general power law scaling and apply it to an idealized model. This would provide an initial estimate of the importance of this process and its potential role in determining the large scale properties of the ice-covered oceans. In the next chapter of this thesis we will pursue this to estimate the impact of the modified wave drag demonstrated here.

Chapter 4

The effects of internal wave drag and ice rheology on an ice-covered gyre

The Arctic Ocean, Earth's smallest ocean, is centered over the North Pole and surrounded almost completely by land. In the winter, the Arctic Ocean becomes entirely covered by a layer of sea ice formed by the freezing of salty ocean water (as discussed in §1.2). In summer, much of this ice melts away. The state of the Arctic Ocean, as well as its influence on the broader climate system, is deeply influenced by the Arctic Ocean freshwater budget (Carmack et al., 2015). In this discussion, the liquid freshwater content of an ocean layer is defined as

$$FWC = \int_{z_2}^{z_1} \frac{S_{ref} - S(z)}{S_{ref}} dz, \tag{4.1}$$

where the z axis is positive upwards and the ocean surface is set at $z = 0$, S_{ref} is a reference salinity commonly taken to be 34.8 PSU, and $S(z)$ is the salinity of the ocean at depth z.

This variation in salinity sets many of the characteristic properties of the Arctic Ocean. For example, the vertical density stratification of the Arctic Ocean is controlled predominantly by variations in salinity as opposed to the dominant role of temperature variations at mid latitudes (Carmack, 2007). This salinity control of stratification allows for buoyant, fresh surface water to insulate sea ice from warm North Atlantic water at depth, thus enabling ice-growth and preventing massive sea ice melt (Rippeth et al., 2015; Carmack et al., 2015). Understanding the destiny of freshwater in the Arctic Ocean is thus essential for understanding past and future ice-states.

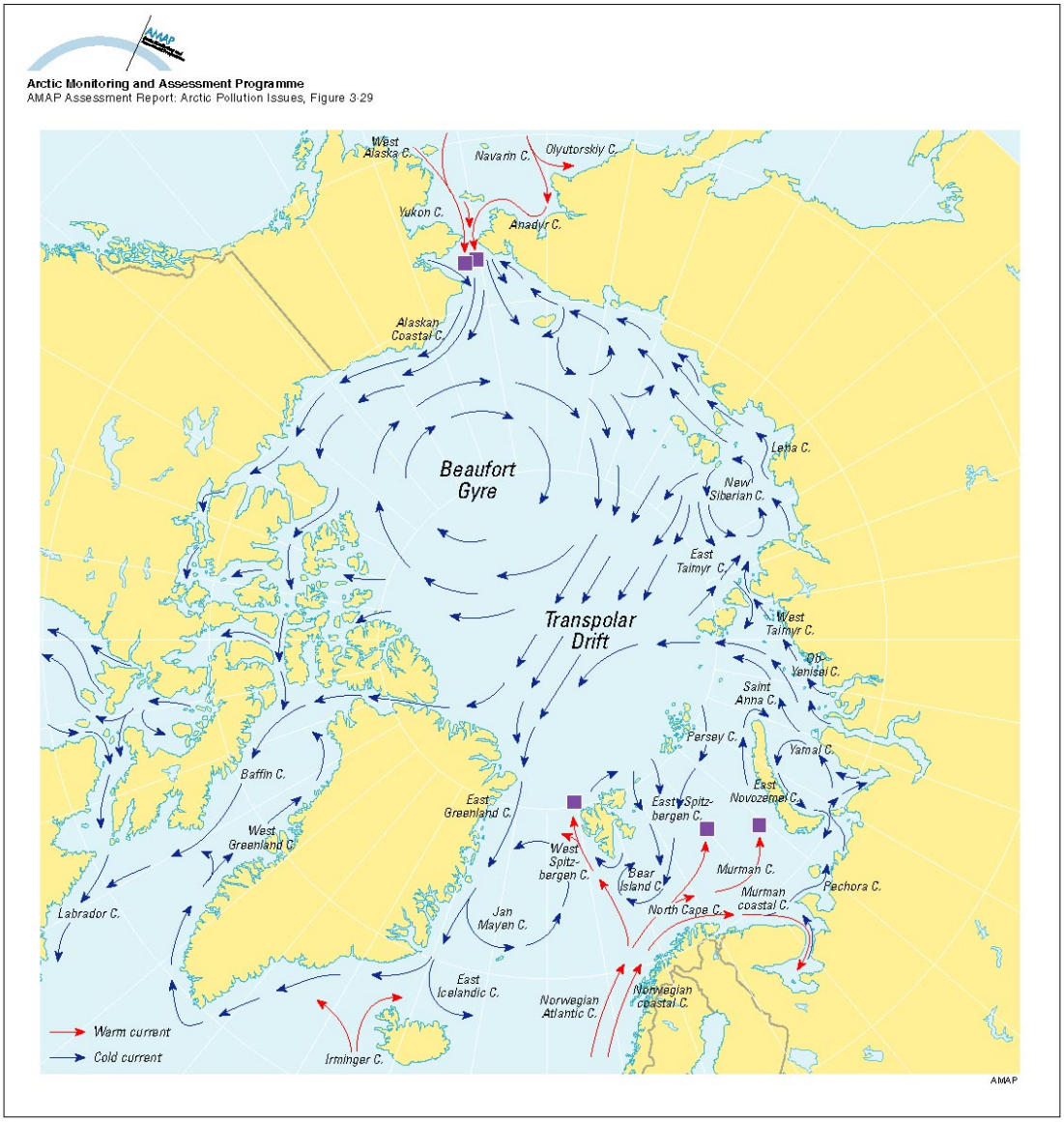


Figure 4.1: Surface currents in the Arctic region. Square boxes indicate that the denser inflowing (Atlantic and Pacific) waters are submerging under the Polar Surface Water. Image courtesy of the Arctic Monitoring & Assessment Programme

The surface freshwater budget of the Arctic Ocean is strongly constrained by the surrounding land boundary as seen in figure 4.1. The pathways for exchange with other water masses are thus restricted to inflow from Siberian/North American rivers, the Chukchi Sea and the North Atlantic, outflow via the Canadian Archipelago and around Greenland, or local fluxes from evaporation, precipitation, and sea ice growth/melt which deposit fresh water at the surface. Due in part to this defining bathymetry, the Arctic Ocean is sometimes referred to as the Arctic Mediterranean and some studies even model the Arctic using estuarine models (as discussed in Timmermans and Marshall, 2020). These defining pathways of exchange with the broader oceans, along with forcing from the atmosphere, define the two primary structures of the Arctic Ocean circulation depicted in figure 4.1: the Transpolar drift, and the Beaufort Gyre.

The Transpolar drift was first observed by Nansen's voyage of the Fram as reported in Nansen (1897). In this work, Nansen refers to the predominant cross-Arctic transportation of sea ice from the Bering Strait to the North Atlantic. The Beaufort Gyre is a region of persistent anticyclonic ice-ocean stress which drives the accumulation of surface freshwater in the Canada Basin. This region is the largest reservoir of freshwater within the Arctic and thus an essential component of the Arctic Ocean freshwater budget (Proshutinsky et al., 2019). Of these two features, the Beaufort Gyre is the most well studied (Timmermans and Marshall, 2020) and the one we will focus on in this work. Within this chapter, we will investigate how variations in the ice-ocean drag coefficient, such as those due to sea ice generation of internal waves, might impact the structure of the Beaufort Gyre and its freshwater content.

In chapter 3.1, we demonstrated the potential variability of ice-ocean momentum fluxes due to interactions between ice-roughness in the form of pressure ridges, drift, and the surface ocean state. Though in our simulations the values of roughness, buoyancy frequency and ice-ocean relative velocity were fixed, the physical values vary spatially and temporally in the polar oceans and are subject to change under a changing Arctic ice state. Here we aim to apply the predicted scaling of ice-ocean drag coefficient due to internal waves derived in chapter 3 in an idealized model of the ice-ocean system. The aim is to understand the potential impact of wave drag on the upper ocean structure over regional length scales. The ice-ocean stress results from an interplay of driving wind stress, mechanical stresses in the ice controlled by sea ice rheology, and their impact on ice velocity relative to the ocean velocity (Feltham, 2008)

The structure of the chapter is as follows. We will start with a broad overview of existing work on the Beaufort Gyre in §4.1 including a description of its structure, influence on the Arctic Ocean freshwater budget, and a summary of past research. This is then followed by a review of sea ice rheology in §4.2. Next, we will develop the mathematical model of the ocean to be utilized in §4.3, with modifications to include a parameterization of wave drag in §4.4. This model adapts the idealized ocean gyre model of Manucharyan et al. (2016) to explore the impact of variable ice-ocean drag on the gyre structure. Results of sensitivity studies to modified drag are examined in §4.4.1. In §4.5.1 the model is extended to include an idealised treatment of varying ice stress using a simple Newtonian viscous sea ice rheology. The computational approach for this formulation is also outlined in the same section. This rheological model allows us to explore the impact of varying ice-ocean drag when there is a non trivial balance of the atmospheric wind stress and ice-ocean stress. In this case there may be redistribution of stress via internal stresses within the ice. The sensitivity of the ice-ocean stress predicted by this simple sea ice rheology to variations in atmospheric, oceanic, and rheological parameters is examined in §4.5.6. Finally we summarize the key results of this chapter, its limitations, and potential future work in §4.6.

An attempt at coupling these models to examine an equilibrium gyre state including the effects of surface ocean currents was made. Unfortunately the numerical model was unable to consistently converge. The approach, and progress made thus far, is set out in an appendix of this chapter in §4.A.

4.1 The Beaufort Gyre

The Beaufort Gyre is a region of persistent anticyclonic ice-ocean circulation in the Canada basin driven by the Beaufort Sea high pressure system (Serreze and Barrett, 2011). The ice-velocity in this region is shown in figure 4.2. Over time, the persistent ice-ocean stress drives lateral Ekman flow at the ocean surface thereby creating a region of accumulated low-salinity surface water (see reviews by Proshutinsky et al., 2009b, 2019; Timmermans and Marshall, 2020). This accumulation of freshwater in the Beaufort Gyre has made it the largest reservoir of fresh water in the Arctic Ocean and thus a fundamental aspect of the Arctic Ocean freshwater budget (Proshutinsky et al., 2019).

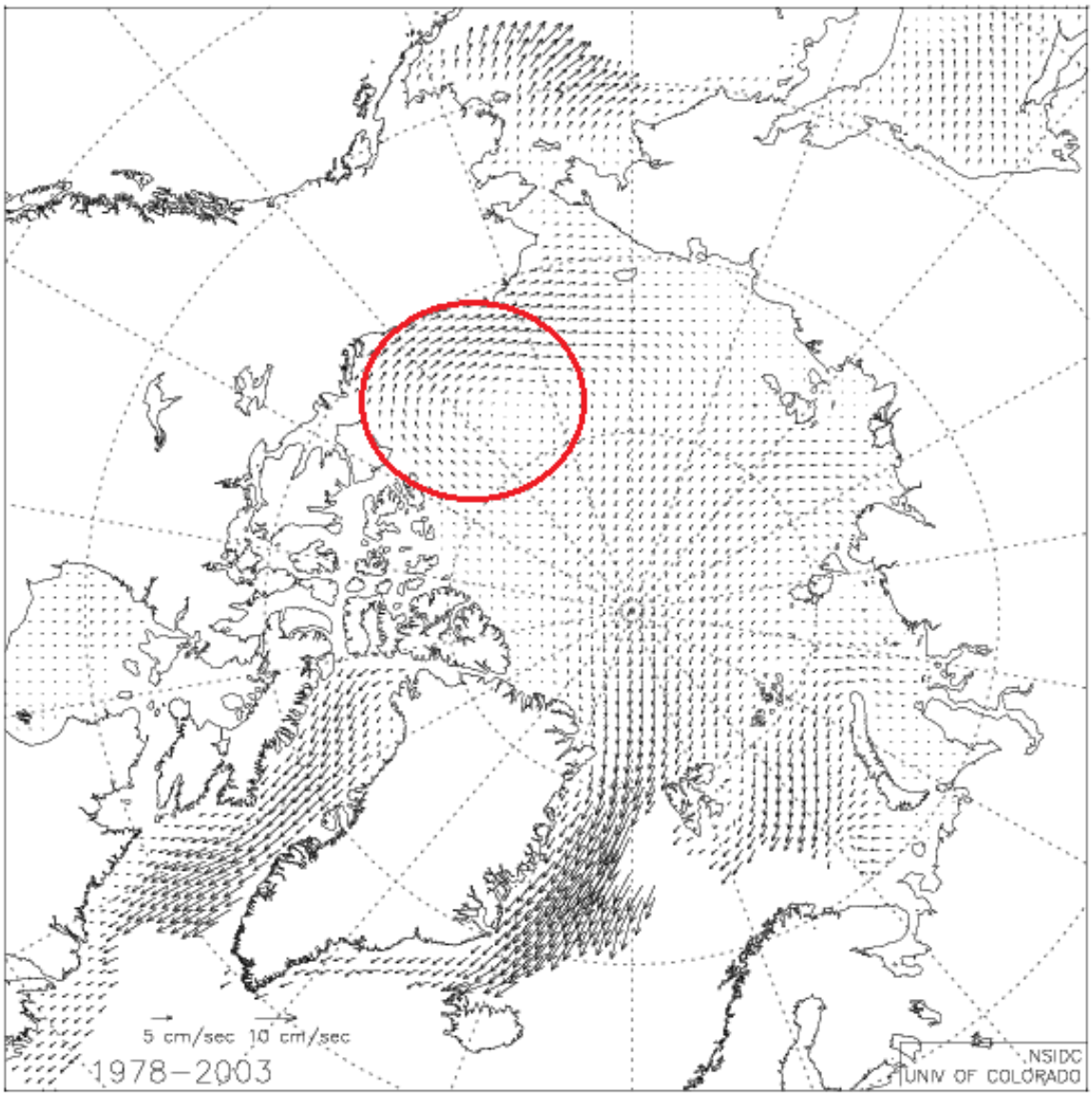


Figure 4.2: Plot showing mean (average) Arctic ice motion from 1978 to 2003. Arrows show the direction and velocity of the ice, with longer arrows representing higher velocities. The red circle indicates the general region of study. Image courtesy of the National Snow and Ice Data Center, University of Colorado, Boulder, CO

For the period of 2000-2010, the liquid freshwater content of the gyre has increased by more than 8,000 km^3 (Proshutinsky et al., 2020; Giles et al., 2012). For this same time period, the solid freshwater content from sea ice fell by $\approx$ 2,700 km^3 (Haine et al., 2015) accompanying a dramatic change in sea ice type and thickness (Kwok, 2018). Therefore $\approx$ 5,300 km^3 must have come from other sources (as discussed in Proshutinsky et al., 2019; Wang et al., 2018, 2019b). It is important to note that the uncertainties of current estimates of freshwater content are still significant,

though a persistent trend in freshwater content and an identification of the governing mechanisms has been established in these studies. Improvement of these uncertainties, or a fuller representation of gyre mechanics is necessary to understand the strength and scale on which the gyre impacts the Arctic Ocean freshwater budget and the broader climate system (see Carmack et al., 2016).

The rate of freshwater accumulation in the Beaufort Gyre depends on the particular atmospheric forcing (Proshutinsky et al., 2019). On nearly decadal timescales, the atmospheric forcing over the gyre has been proposed to oscillate between regimes of anticyclonic, or cyclonic atmospheric forcing. This oscillation corresponds to the strength of the Beaufort High, a high pressure system centered around the Beaufort Sea, or the Icelandic Low pressure system (Proshutinsky and Johnson, 1997). On seasonal timescales, strong anticyclonic wind speeds in the winter drive the ice covered ocean to accumulate freshwater whereas the summer is characterized by relatively weak cyclonic atmospheric stress. This reduction in surface stress allows for the release of freshwater into the surface ocean due to a reduction in the lateral Ekman transport (Proshutinsky et al., 2002, 2009a,b, 2019; Timmermans et al., 2011).

In addition to the variability in atmospheric forcing, accumulation of freshwater during periods of anticyclonic ocean stress only occurs if there is freshwater at the surface to be transported (Proshutinsky et al., 2002, 2009b). Estimates of freshwater contributions based on geochemical methods demonstrate that the Beaufort Gyre contains fresh water from a myriad of sources including meteoric, Eurasian and North American rivers, the Pacific Ocean, and sea ice melt (Yamamoto-Kawai et al., 2005, 2008, 2009; Prowse et al., 2015). The local contribution of ice melt water over the period 2003-2018 represents less than 8% of the total freshwater content change of the gyre. This suggests that most of the freshwater flux is of non-local origin.

The increased accumulation of freshwater in the Beaufort Gyre prompts the question, what happens if it is released? At the surface, release of freshwater is important for sea ice production due to its impact on stratification (Aagaard and Carmack, 1989). As the Arctic Ocean stratification is predominantly controlled by salinity, the surface freshwater can inhibit upward heat transport from depth, therefore reducing the ice-ocean heat flux. Hence surface freshening can promote increased sea ice area and ice thickness (Kellogg, 1975; Aagaard and Carmack, 1989; Toole et al., 2010). This surface release of freshwater can occur due to variations in the surface ocean stress field (Proshutinsky et al., 2019) but a full description of the processes involved in fresh water release from the gyre is still an open question. As mentioned above, the release of surface freshwater occurs on seasonal cycles due to seasonal variations

in the atmospheric patterns or on longer timescales depending on the strength of the Beaufort High and Icelandic Low pressure systems.

As freshwater is accumulated in the gyre, isopycnals at depth are depressed and tilted accompanied by an increase in sea surface height. In this work, we will characterize the gyre structure via the shape of an individual isopycnal chosen to be representative of the main pycnocline. In the Beaufort Gyre system, characterizations of the vertical structure depend on the average behaviour of the halocline: the strongly salinity stratified region between the surface ocean and deeper warm water (Manucharyan and Spall, 2016). To characterize the halocline via a single isopycnal curve we will proceed assuming that the eddy diffusivity is depth independent and so isopycnals are parallel throughout the halocline. This is a simplification to the real system for which the exact structure and variability of the halocline is fundamental for the evolution of the heat and freshwater budgets of the region (Kenigson et al., 2021). However, this approach has been used with great success for studies of the primary mechanisms of the Beaufort Gyre (Manucharyan and Spall, 2016; Meneghello et al., 2018b; Doddridge et al., 2019).

This sloping of isopycnals throughout the halocline generates the conditions for baroclinic instability to occur, allowing for the release of freshwater at depth (Manucharyan and Spall, 2016; Manucharyan et al., 2016). Freshwater release at depth has been proposed to explain observed "Great Salinity Anomalies" (Proshutinsky et al., 2002; Carmack et al., 2008). These salinity anomalies are observed as a major pulse of freshwater travelling at depth around the Arctic basin which may then effect deepwater formation and thus the larger climate system (Dickson et al., 1988).

Understanding the dynamics behind the Beaufort Gyre is thus fundamental for an understanding of the broader Arctic Ocean, and its impacts on the climate system. Two primary mechanisms governing the Beaufort Gyre structure have been proposed. One considers the reduction of Ekman pumping due to accelerated geostrophic ocean flow, and thus lower sea ice–ocean surface stress (Meneghello et al., 2018b; Doddridge et al., 2019; Meneghello et al., 2020). Another mechanism considers enhanced mesoscale eddy activity at depth due to sloping isopycanls (Manucharyan et al., 2016; Manucharyan and Spall, 2016; Armitage et al., 2020).

The first method for gyre equilibration, dubbed the "ice ocean governor" (Meneghello et al., 2018a), suggests that the increased freshwater content and corresponding increase in geostrophic flow speed results in a reduced ice-ocean shear. Modelling studies indicate that this induced geostrophic flow has been increasing in recent years (2003-2014) and has been much stronger than the Ekman velocities at the surface (Zhong

et al., 2018). The smaller ice-ocean relative velocity thus decreases the ice-ocean stress (Meneghello et al., 2018b; Doddridge et al., 2019; Meneghello et al., 2020). The geostrophic flow can change the magnitude and sign of vertical Ekman transport (Timmermans and Marshall, 2020). In Meneghello et al. (2020) it was found that a model including the effects of this governor predicted the Beaufort Gyre freshwater content to be half the amount predicted by a comparison model equilibrated only by mesoscale eddies. This result suggests that spin-up of the ocean currents is potentially a stronger balancing mechanism than baroclinic instabilities at depth. A variant on this idea considers that if the ice is sufficiently stiff, the velocity of the ice-pack in the gyre may be set by the ice rotation beyond the gyre boundary. In this picture, the ocean velocity may exceed that of the ice velocity in the gyre creating a flywheel effect (Proshutinsky et al., 2002).

The second proposed mechanism postulates that the accumulation of surface freshwater due to lateral Ekman transport is primarily balanced by mesoscale eddies (Manucharyan et al., 2016; Manucharyan and Spall, 2016; Armitage et al., 2020). In this picture, the accumulation of freshwater slopes isopycnals so that the depth of the isopycnal in the gyre center is greater than at its edge. The sloping of isopycnals provides a source of available potential energy, which can promote baroclinic instabilities. This results in mesoscale eddy generation that may release freshwater at depth.

This eddy feedback has a typical adjustment timescale of ≈ 6 years for changes in sea surface height and halocline slope (Manucharyan and Spall, 2016). This is much longer than the 1-2 year equilibration timescale of the ice ocean governor (Doddridge et al., 2019). The predicted halocline slope as a function of the gyre radius is much shallower, and closer to observational values, in models with the ice-ocean governor (Meneghello et al., 2020). That said, recent work has suggested the eddy activity is likely to increase as the gyre progresses towards an ice free state (Armitage et al., 2020) and therefore become a more important component of the freshwater circulation within the Arctic Ocean.

Each of these mechanisms is sensitive to changes in the Arctic Ocean stress field. In a changing Arctic, ice roughness, concentration, and efficiency of ice-ocean momentum transfer are subject to change (Martin et al., 2014, 2016; Tsamados et al., 2014). This changing surface stress in turn has the potential to intensify the Beaufort Gyre, and drive increased accumulation of freshwater as suggested in Davis et al. (2014) and Lique et al. (2015). This is potentially further altered by the changing ice concentration of the Arctic Ocean, and specifically the Beaufort Gyre Region (Martin

et al., 2014; Armitage et al., 2020). In Martin et al. (2014) it was inferred that the ice-ocean stress is strongest for an ice concentration between 70-80%. In addition to alteration of the ice coverage, atmospheric forcings such as that of the Arctic Oscillation strength also influence the ice-ocean stress and thus the Arctic freshwater content (Cornish et al., 2020). Changes to mechanical properties of the ice, or atmospheric forcing are further complicated by their effects on the ice internal stresses in the gyre region (Wang et al., 2019a; Dewey et al., 2018; Zhong et al., 2018).

In Wang et al. (2019a) a global ice-ocean model with the elastic-viscous-plastic rheology of Hunke (2001) is used to examine the role of ice internal stresses in modifying the sea ice velocity, which in turn changes the ice-ocean relative velocity and the ice-ocean stress. The key result of Wang et al. (2019a) is that seasonal cycles in ice concentration and ice thickness cause changing regimes of ice internal stress which may reduce the freshwater accumulation of the gyre by $\approx 25\%$. The seasonal cycles can be characterized as 1) a winter ice pack with high concentration, thick ice, and an increase in ice internal stresses which reduce the ice velocity and 2) a summer ice pack approximately in free drift. These internal stress regimes offer an additional seasonal feedback that may operate in conjunction with the ice ocean governor of Meneghello et al. (2018b). In the winter when ice internal stresses are high, the difference between ice and ocean velocities is reduced dramatically, and may even change sign giving rise to seasonal upwelling as observed in Meneghello et al. (2018a). It was predicted in Wang et al. (2019a) that this feedback should weaken as the Arctic ice thins, areal coverage shrinks, and internal stresses become negligible. Understanding the details of sea ice rheology could be important for determining the strength of this feedback as well as more completely capturing the pathways for sea ice to influence the conventional balance of Ekman transport, baroclinic eddies, and geostrophic velocity feedbacks that set the Beaufort Gyre state.

4.2 Sea ice rheology

All mediums respond differently to external stress. For fluids like air or the ocean, this is commonly represented by viscous effects. For other mediums like magma, plastic, rubber bands or sea ice, a more complex representation of the stress is needed to understand how the material deforms and flows. The field of study pertaining to this is known as rheology and the particular formulation of a material's relationship between flow, stress, and strain rate is often called the material's rheology. We limit the discussion of this review to the basic elements of rheological models and some

particular developments of sea ice rheology as informed by reviews such as Feltham (2008), Schoof and Hewitt (2013) and Zhang (2021).

The underlying assumption behind the rheological study of sea ice is that it can be well represented by continuum mechanics. Here we will examine a depth-integrated form of the ice rheology on an f-plane. In this view, the equation for the horizontal momentum balance for sea ice is given by

$$\frac{D(m\mathbf{u})}{Dt} = -mf\mathbf{k} \times \mathbf{u} + \tau_{\mathbf{a}} + \tau_{\mathbf{o}} - m\hat{g}\nabla H + \nabla\tau - \nabla P. \tag{4.2}$$

where m is the ice mass per unit area, f is the Coriolis parameter, $\mathbf{k}$ is the vertical unit vector, $\tau_{\mathbf{a}}$ and $\tau_{\mathbf{o}}$ are the atmosphere-ice and ocean-ice stresses, $\hat{g}$ is the gravitational acceleration vector, ∇H is the sea surface tilt, and $\nabla\tau$ is the ice interaction force given by the divergence of the sea ice deviatoric stress tensor, τ, neglecting hydrostatic stress (Feltham, 2008). The ice mass per unit area is determined by

$$m = \rho_i \int_0^\infty g(h)hdh, \tag{4.3}$$

where $g(h)$ is the ice thickness distribution function for ice thickness h and ρ_i is the ice density. The exact formulation of this distribution is most commonly given as in Thorndike et al. (1975), though more sophisticated methodologies for evolution of the thickness distribution have been developed in recent years as in Toppaladoddi and Wettlaufer (2017).

The primary aim of sea ice rheology is then to establish the particular form of the deviatoric stress (internal stress of the ice) based on sea ice processes. This is known as the constitutive law, or flow law. To develop the constitutive law, we seek a relationship between stress, τ_{ij}, and the strain rate

$$\dot{\epsilon}_{ij} = \frac{1}{2}\left(\frac{\partial u_i}{\partial x_j} + \frac{\partial u_j}{\partial x_i}\right), \tag{4.4}$$

where $\dot{\epsilon}_{ij}$ is the shear strain and u_i denote the velocity components within the medium. In this form, we are considering viscous rheologies as opposed to purely elastic behaviour where stress instead depends on the accumulated strain, ϵ_{ij}. Assuming that sea ice is isotropic, a general form of this relationship for a viscous-plastic sea ice rheology is given by a tensorial relationship between the two as in Feltham (2008),

$$\tau_{ij} = 2\eta\dot{\epsilon}_{ij} + [\zeta - \eta]\,\dot{\epsilon_{kk}}\delta_{ij} \tag{4.5}$$

where ζ is the bulk viscosity and is commonly related to η, the shear viscosity, using a yield curve. This yields

$$\frac{\partial \tau_{ij}}{\partial x_j} = \frac{\partial}{\partial x_j}\left[\eta\left(\frac{\partial u_i}{\partial x_j} + \frac{\partial u_j}{\partial x_i}\right)\right] + \frac{\partial}{\partial x_i}\left[(\zeta - \eta)\nabla \cdot \mathbf{u}\right]. \tag{4.6}$$

For a Newtonian rheology with η constant and if the flow is incompressible, then this reduces to

$$\frac{\partial \tau_{ij}}{\partial x_j} = \eta \frac{\partial^2 u_i}{\partial x_j^2}. \tag{4.7}$$

This is the simplest form of sea ice rheology, the viscous rheology (often referred to as Newton's rheology). This rheology is the form used by early studies of sea ice rheology as in Ruzin (1959) and Reed and Campbell (1960) and resembles the rheology of an ideal fluid. Viscous rheology treats interactions between ice floes equivalently to a constant eddy viscosity. In early rheological models, such as the viscous, compressible model of Ruzin (1959), convergence of sea ice through the thickness distribution, $g(h)$, was unbalanced. Because of this, these early sea ice models predicted an unrealistic convergence of sea ice, and so an unrealistic predicted ice thickness, in the Beaufort Sea. This issue was remedied in later work by adding an additional pressure term to prevent unrealistic sea ice thickness as in Rothrock (1970) and Solomon (1970). This pressure can be specified via an equation of state dependant on ice-thickness and concentration as in Hibler (1979) or if the ice is treated as incompressible, the pressure can be determined to ensure the incompressibility condition is met.

In contrast to the viscous rheology, an ideal solid is sometimes represented by so-called elastic behaviour, commonly called Hooke's rheology after Hooke's law. In this case the shear stress τ and shear ϵ satisfy

$$\tau = G\epsilon, \tag{4.8}$$

where G is the elastic modulus. The elastic modulus represents the resistance to deformation of the medium. For an ideal elastic rheology, G has no time dependence. Therefore, when a stress is applied, an immediate strain is observed and when the stress is removed, the strain immediately disappears. Many materials demonstrate both viscous and elastic behaviours and are thus classified as having visco-elastic rheologies (Roylance, 2001). The resulting behaviour of visco-elastic materials is that the application of stress may cause temporary deformation if the stress is quickly removed, but permanent deformation if it is maintained for long time periods (Roylance, 2001). One example of a visco-elastic model is the Maxwell model given by

$$\dot{\epsilon}_{ij} = \frac{\tau_{ij}}{\eta} + \frac{\dot{\tau}_{ij}}{G}. \tag{4.9}$$

Many characteristic processes of sea ice are not captured by viscous or elastic mechanisms. For example, sea ice often undergoes sporadic and irreversible mechanical deformations of ice floes through processes such as ridging, or lead formation as discussed in §1.2 and in Feltham (2008). These processes are characteristic of so-called plastic rheologies (Roylance, 2001). Within a plastic rheology, mechanical deformation can occur after some critical stress state has been reached. Rheologies implementing plastic behaviour have been implemented for sea ice successfully as in Parmerter and Coon (1972); Coon et al. (1974) and Rothrock (1975). The most popular model of sea ice is the viscous-plastic rheology of Hibler (1979). This model combines a viscous response for low strain rates, with plastic behaviour and a yield surface for high strain rates. Rallabandi et al. (2017) argued that a further viscous regularization to the Hibler rheology, at even higher strain rate, typically included for computational purposes, actually provides an essential physical control on sheared flow near boundaries. The model of Hibler (1979) was more recently modified to include a form of elasticity to improve computational efficiency as in Hunke and Dukowicz (1997) (Feltham, 2008; Toyoda et al., 2019; Zhang, 2021).

More modern work on improving these early parameterizations have focused on anisotropy of the sea ice (Wilchinsky and Feltham, 2006), brittle behaviour (Boutin et al., 2021), and the limitations of the model of Hunke and Dukowicz (1997) in high resolution models (Hutter et al., 2018). A specific concern is to examine the scales at which the continuum model of sea ice rheology breaks down (Blockley et al., 2020).

In §4.5, we will take a first look at the potential impacts of sea ice rheology on the underlying ocean state as part of our idealized model of the Beaufort Gyre. In doing so, we will assume isotropic sea ice and implement a Newtonian viscous rheology as given by substituting (4.7) into (4.2). From the above discussion, we know that this approach will neglect many physical properties of sea ice such as the evolution of the thickness distribution and floe fracturing along with plastic deformation. This simplistic version was chosen primarily to keep the problem tractable while still providing insight into the potential role of ice-internal stresses in redistributing the spatial distribution of ice-ocean stress. Importantly, the simple viscous rheology provides a method that allows for internal stresses within the ice to redistribute and absorb some interfacial surface stress; over large length scales this may influence the ocean structure of the gyre, as discussed in detail below.

4.3 Idealized model of Beaufort Gyre structure

In this section we will adapt the approach used within Manucharyan et al. (2016) and Manucharyan and Spall (2016), employing a Transformed Eulerian Mean framework (see Plumb and Ferrari, 2005). The model looks at the Beaufort Gyre as a balance between surface accumulation of freshwater due to Ekman transport, in competition with isopycnal slumping driven by mesoscale eddies. The eddies are created from baroclinic instabilities due to sloping isopycnals. In this idealized gyre, we will hold the gyre radius fixed. In the real-world system the gyre radius is limited primarily by the bathymetry of the Canada basin. Recent work has identified a number of impacts due to the presence of bathymetry (Regan et al., 2020; Manucharyan and Isachsen, 2019), but we neglect these here as we aim to use a simple tractable model to examine the impact of variable surface drag.

As opposed to the approach used by Manucharyan et al. (2016) where the surface stress is prescribed, we will instead prescribe the ice-ocean relative velocity as a function of gyre radius, in an axisymmetric gyre set up shown in figure 4.3. These velocities will be used to calculate the drag force with the inclusion of wave drag effects motivated by §3.3.2, and then the subsequent ice-ocean drag in an ice covered gyre. We first use this to understand the consequences of variable ice-ocean drag in an ocean only model. In §4.5 we will consider the modification of this problem where the ice-ocean velocity is predicted from the response of ice internal stresses to specified atmospheric and oceanic forcing.

In §4.3.1 we develop the mathematical formulation of our idealized gyre using the framework of Manucharyan et al. (2016). In §4.4 we introduce the particular form of the ice-ocean stress to be used, inspired by the wave drag results of §3.3.2. The predictions and sensitivities of this preliminary steady state model are examined in §4.4.1. We will seek to modify this model to include the effects of a simple sea ice rheology in §4.5.

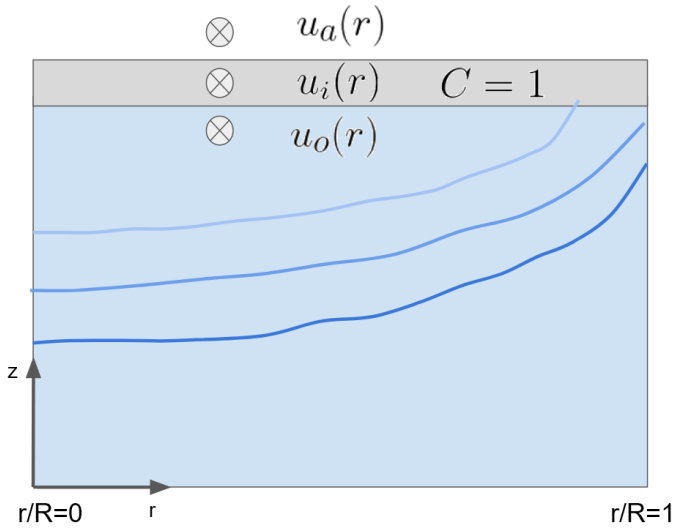


Figure 4.3: Sketch of radial cross section through an axisymmetric gyre to be examined in §4.4.1, §4.5.6. The atmospheric (u_a), ice (u_i), and ocean velocity (u_o) are all in the same azimuthal direction in the gyre, though magnitudes vary. In §4.4.1 we will impose $u_{rel} = u_i - u_o$ and in §4.5.6 we impose u_a and u_o to calculate u_i. R denotes the outer radius and r/R a scaled radius. In this section all models will use an ice concentration of $C = 1$ as well as a fixed ice thickness.

4.3.1 Transformed Eulerian mean framework

The transformed Eulerian mean (TEM) framework has been widely used to look at the effects of mesoscale eddies on mean flow in geophysical turbulence (see Plumb and Ferrari, 2005; Vallis, 2017). In Manucharyan et al. (2016) and Manucharyan and Spall (2016) this approach was applied in a conceptual model of the Beaufort Gyre. The basic idea is to deconstruct the ensemble averaged flow into components representing the mean, and mesoscale eddy induced flow represented via the residual terms. This is done in the quasi-geostrophic limit. Here we review the derivation of the model in cylindrical coordinates following the approach of Manucharyan et al. (2016) and drawing on theory outlined in Vallis (2017).

The Reynolds averaged buoyancy equation in cylindrical coordinates is given by

$$\overline{b}_t + \overline{v}\overline{b}_r + \overline{w}\overline{b}_z + \overline{(v'b'_r)} + \overline{(w'b'_z)} = \overline{S}, \tag{4.10}$$

where $b = g(\rho_0 - \rho)/\rho_0$ is the buoyancy, $b_z = \partial b/\partial z$, $b_r = \partial b/\partial r$, $\overline{v}$ and $\overline{w}$ are the mean Eulerian radial and vertical velocities respectively, and $\overline{S}$ denotes the sum of all buoyancy sources and sinks. Over bars indicate an average in the azimuthal direction with $'$ indicating deviations from the azimuthal mean.

With this equation we will assume the adiabatic limit where buoyancy fluxes are assumed to be predominantly aligned with isopycnals in the interior of the ocean (Vallis, 2017). This is a fairly good approximation in the deep ocean, but clearly breaks down in the surface mixed layer due to enhanced mixing and surface fluxes. We therefore treat the surface mixed layer as providing a boundary condition for the deep ocean circulation.

By averaging the incompressibility relation and subtracting from the un-averaged form, one finds that the velocity fluctuations are also incompressible

$$\frac{1}{r}\frac{\partial}{\partial r}\left(rv'\right) + \frac{\partial w'}{\partial z} = 0, \tag{4.11}$$

which can then be used to rewrite (4.10) as

$$\bar{b}_t + \overline{v}\bar{b}_r + \overline{w}\bar{b}_z + \frac{1}{r}\frac{\partial\left[r\overline{(v'b')}\right]}{\partial r} + \frac{\partial\overline{(w'b')}}{\partial z} = \overline{S} \tag{4.12}$$

We can define the eddy advection velocities from the eddy induced mass flux as in Vallis (2017), defining an eddy streamfunction

$$\psi^* = \frac{\overline{v'b'}}{\bar{b}_z}, \tag{4.13}$$

with effective eddy-induced transport velocities

$$v^* = -\psi^*_z, \quad w^* = \frac{1}{r}(r\psi^*)_r. \tag{4.14}$$

Following Marshall and Radko (2003), if there is no buoyancy flux across an isopycnal, then the normal component of eddy induced fluxes is zero implying

$$\frac{\overline{v'b'}}{\bar{b}_z} = -\frac{\overline{w'b'}}{\bar{b}_r}. \tag{4.15}$$

This can be derived by noting that an isopycnal has $b(r,z)$ =constant, and normal $\mathbf{n} = \nabla b$, then setting the normal component of the flux to zero.

Using all of the above, we can then represent the eddy flux divergences via an additional advection of mean gradients in buoyancy by the eddy streamfunction via

$$\bar{b}_t + (\overline{v} + v^*)\bar{b}_r + (\overline{w} + w^*)\bar{b}_z = \overline{S}. \tag{4.16}$$

With this we can represent the advection of the mean buoyancy through a single residual streamfunction, $\widetilde{\psi} = \overline{\psi} + \psi^*$ that balances the sources and sinks. In the interior of the ocean, where buoyancy sources are small we can let $\overline{S} = 0$ and at

steady state we must have $\widetilde{\psi} = 0$ (Marshall and Radko, 2003). To use this, first we must identify the form of $\overline{\psi}$.

Following the arguments within Manucharyan et al. (2016) we assume that Reynolds stresses are negligible in the momentum equation for large scale flows and that the inertial term can be neglected for time scales larger than f^{-1}. Lastly the azimuthal pressure gradient term vanishes by symmetry and we get

$$f\overline{v} = -\overline{\tau}_z/\rho_0, \tag{4.17}$$

where τ is the azimuthal stress and ρ_0 is the Boussinesq reference density. In the ocean interior, the vertical shear stress is negligible so we can integrate the above to any depth below the surface Ekman layer to get

$$\overline{\psi} = \frac{\tau}{\rho_0 f}, \tag{4.18}$$

where the stress, τ, is elevated at the ocean surface, and we recall that

$$\overline{v} = -\overline{\psi}_z, \quad \overline{w} = \frac{1}{r}(r\overline{\psi})_r. \tag{4.19}$$

(4.18) is the contribution of the Ekman transport with $\overline{\psi}$ being depth integrated radial transport. It is important to note that in addition to the adiabatic assumption, this formulation neglects any potential effects of ocean bathymetry on the problem.

For a steady state gyre, with no residual circulation, we obtain

$$\widetilde{\psi} = \overline{\psi} + \psi^* = \frac{\tau}{\rho_0 f} + \frac{\overline{v'b'}}{\overline{b}_z} = 0. \tag{4.20}$$

We can further reduce this through the use of a mesoscale eddy parameterization for the eddy fluxes such as the Gent-McWilliams parameterization (Gent and Mcwilliams, 1990). This approach assumes a down-gradient nature for the eddy buoyancy fluxes (or equivalently layer thickness fluxes in a layered model) :

$$\overline{v'b'} = -K\overline{b}_r \tag{4.21}$$

where the eddy diffusivity $K = K(s)$ depends on the magnitude of the isopycnal slope $s = |\overline{b}_r/\overline{b}_z|$. Following Manucharyan et al. (2016) we will use a general power law dependence on the slope for K giving

$$\psi^* = -K\overline{s} = -k\overline{s}^m \tag{4.22}$$

where k is a constant (units $m^2\ s^{-1}$) referred to as the eddy efficiency. The value of k can be seen as an indicator for how efficient eddies are at flattening sloping isopycnals. The reference value for k to be used in this work is $k = 3 \times 10^6\ m^2\ s^{-1}$ from Manucharyan et al. (2016). In the geophysical system, k is spatially and temporally heterogeneous. Furthermore values of k depend on the surface forcing up to the eddy saturation limit[1]. The Beaufort Gyre is far from this limit, and so significant variability of this parameter may be possible under transient forcing (Manucharyan and Spall, 2016).

With these approximations the steady state isopycnals must satisfy

$$\widetilde{\psi} = \frac{\tau}{\rho_0 f} - k\left(\frac{\overline{b}_r}{\overline{b}_z}\right)^m = 0. \tag{4.23}$$

From this result, Manucharyan et al. (2016) solved for pycnocline depths given an assumed surface stress τ. In the next section we will instead use the results of §3.3.2 to provide an initial exploration of the impact of the modified wave drag on the Beaufort Gyre vertical structure, and understand the potential magnitude and pattern of influence before proceeding to the fully coupled model.

4.4 The steady state gyre

In the steady state case given by (4.23) we can identify $\overline{b}_r/\overline{b}_z = \partial z/\partial r$, and solve for the isopycnal height, z, by a simple separation of variables. In this formulation, m is typically set to values of 2 or 3, and a simple imposed function for the surface stress τ can be prescribed to study the structure of the gyre as in Manucharyan et al. (2016). However in contrast to previous analysis by Manucharyan et al. (2016), we seek to include some perturbation to the surface stress dependent on the Froude number for the near surface flow. Therefore $\tau(r)$ depends on the buoyancy frequency N, the ice-ocean relative speed $u_{rel}(r)$ and the ice roughness at the ocean surface, h.

Motivated by the results of chapter 3, we let the drag coefficient be given by

$$C_d = C_{d,io} + A\left[\frac{u_{rel}}{Nh}\right]^n \tag{4.24}$$

where $C_{d,io}$ is the unmodified ice-ocean drag and u_{rel} is the magnitude of the ice-ocean relative velocity. The parameters n and A can be constrained by the power law fits of §3.3.2. In general, A likely depends on the frequency and spacing of ridges

[1] "Eddy saturation" is the regime in which the total time-mean volume transport of an oceanic current is relatively insensitive to the wind stress forcing

as well as the orientation of the ridge to the mean flow. In this work, we start with $A = 0.001$ which is the same order of magnitude as in the $Re = 500$ computations of §3.3.2. This factor was determined with approximate ridge spacing of 150m, and ridge height $h = 5m$. Comparing to the climatological values of these parameters presented in Tsamados et al. (2014) for September ice characteristics over the period (1990-2012) we observe that for the Beaufort Gyre region, a typical value is $h \approx 8$m and the spacing between ridges is $D_s \approx 100$m. These values differ slightly from the simulation parameters used to constrain the value of A, but are of the same order of magnitude. We therefore proceed with $A = 0.001$ for the default configuration, though we test the sensitivity of the model to this parameter in §4.4.1. The value of $C_{d,io}$ chosen here is the canonical value of $C_{d,io} = 5.5 \times 10^{-3}$.

For the power law exponent, n, we will use $n = -2$ for the default model configuration which is within the range of exponents predicted by our study and by the broader literature. Similar to A, the sensitivity of the model to this exponent is examined in §4.4.1. For values of the surface stratification N, and the roughness scale h, we use $N^2 = 10^{-5}$ s^{-2} ($N \approx 0.003$ s^{-1}) and the obstacle height of our previous work $h = 5$m. The chosen value of $N^2 = 10^{-5}$ implies a change in density $\Delta\rho \approx 0.02$kg m^{-3} over a depth of 20m, the mixed layer depth of the previous chapter. The value of $\Delta\rho \approx 0.02$kg m^{-3} is similar to the value of $\Delta\rho \approx 0.03$kg m^{-3} sometimes used to diagnose an ocean mixed layer depth (de Boyer Montégut et al., 2004). We proceed with this parameter value for now and test sensitivity to both N and h in §4.4.1.

The ice-ocean forcing in the Beaufort Gyre is primarily anticyclonic, In this chapter we let this be the positive direction and so $\tau > 0$. With this, τ is given by

$$\tau = \rho_0 \left(C_{d,io} + A \left[\frac{u_{rel}}{Nh} \right]^n \right) u_{rel}^2, \tag{4.25}$$

where u_{rel} is a function of r, and therefore so too is τ. In the real-world system, the other parameters may also vary spatially and temporally though here we treat them as constant. Plugging (4.25) into (4.23) and $\overline{b}_r/\overline{b}_z = -\partial z/\partial r$ we arrive at

$$\frac{\partial z}{\partial r} = \left[\frac{C_{d,io} u_{rel}^2}{fk} + \frac{A u_{rel}^2}{fk} \left(\frac{u_{rel}}{Nh} \right)^n \right]^{1/m} \tag{4.26}$$

which describes the structure of an isopycnal accounting for the modified wave drag when given u_{rel}. We can then solve (4.26) given an initial value of the isopycnal depth, z_0, at the gyre edge with varying parameter values and functional forms of u_{rel}. Here we will use $z_0 = -20$m or the mixed layer depth above as the adiabatic assumption used to develop the TEM model breaks down in the active mixing layer (Plumb and

Ferrari, 2005). Imposing u_{rel} is clearly a simplification of the full force balance in the geophysical system, where the ice and ocean velocities respond to atmospheric wind stress, but is pursued here to understand the model sensitivity.

If $n < -2$, (4.26) is singular for $u_{rel} = 0$ as a result of the extrapolation of our power law fit. Physically, the internal wave drag will reach a maximum value rather than diverging towards infinity (McPhee and Kantha, 1989; Baines, 1998; Miles and Huppert, 1968). In this work we replace the Froude number $Fr_h = u_{rel}/Nh$ used in (4.26) by $Fr_h = max(u_{rel}/Nh, Fr_{h,0})$ which limits the drag coefficient for $Fr_h \leq Fr_{h,0}$. Our initial choice of this value is the limit of our simulation study of the previous chapter, $Fr_{h,0} = 0.2$. This choice of limit is somewhat ad hoc, so we explore the sensitivity to the threshold value of $Fr_{h,0}$ in §4.4.1. If the restriction on the drag coefficient is not imposed the stress diverges, and the isopycnal depth goes to negative infinity. This infinitely deep isopycnal is only an issue if $n < -2$, with $n \geq -2$ still having artificially high drag, but not infinite.

4.4.1 Effects of internal wave drag and sensitivity

Here we seek to build an understanding of the role the proposed parameterization of wave drag may have on the gyre structure. We first need to identify potential functional forms of u_{rel}. We will seek to build a more sophisticated approach to this relationship in later sections, but here we fix u_{rel} initially to explore the impacts of wave drag and build an understanding of the parametric uncertainties. The default configuration parameters are given in table 4.1.

We begin this investigation by assuming a linear function of $u_{rel} = u_0(r/R)$ where we have chosen $u_0 = 0.01$ m s^{-1} as the value of the relative velocity at the gyre edge. We note that this is similar to the strategy used in Manucharyan and Spall (2016) of letting $\tau(r) = \hat{\tau}r/R$ and specifying $\hat{\tau}$. The value of u_0 is chosen to be small, though on the same order of observed ice and geostrophic currents as presented in (Meneghello et al., 2018a). Physically u_0 indicates the difference between the ice and ocean velocities which have similar spatial distributions in the observations. This linear velocity profile can be seen as the ice cover rotating within the gyre according to a solid body rotation. We will use this velocity profile to first compare a reference case of constant ice-ocean drag with the modified form of (4.26) for varying values of n. Following this, we examine the sensitivity of the isopycnal depth profile to an additional functional form of u_{rel}.

The reference value of $A = 0.001$ is close to the value obtained for the power law fit of the $Re = 500$ data of §3.3.2 and is likely an overestimate for the real-world

system due to variations in the orientation of the ridge with the relative ice-ocean velocity and other 3D effects but is used here to build insight.

$h = 5$ m	$N^2 = 1 \times 10^{-5}$ s^{-2}	$u_0 = 0.01$ m s^{-1}
$m = 2$	$k = 3 \times 10^6$ m^2 s^{-1}	$C_{d,io} = 5.5 \times 10^{-3}$
$z_0 = 20$ m	$A = 0.001$	$n = -2$
$f = 1.4 \times 10^{-4}$ s^{-1}		

Table 4.1: Default values for parameters to be used in this standalone ocean model.

To develop a qualitative understanding of potential changes to the gyre state, we examine a proxy for the freshwater content of the gyre, based on the volume between the isopycnal curve and the ocean surface at $z = 0$, rotated about the axis $r = 0$. In this manner we can define a reference volume V_0, and compare variations in parameters via the ratio V/V_0. This is analogous to comparing the volume between the sea-surface height, and a selected isopycnal in a continuously varying stratification.

Using the simple linear profile for $u_{rel} = u_0(r/R)$ and the default values of parameters shown in figure 4.4 for exponent $n = -1, -2, -3$ we see that this wave drag parameterization has the potential for modest impact on the gyre liquid freshwater content. Compared to simulations without wave drag, the fractional volume change with $n = -1$ is quite small ($\approx 3\%$), though for $n = -3$ the change is more pronounced ($\approx 13\%$). In chapter 3, the exponent of $n = -1$ was reported as a feature of the hydrostatic regime, with $n = -3$ being more typical of non-hydrostatic flow (Miles and Huppert, 1968). Similarly, in the computational work of chapter 3, values of $n < -1$ were observed with n decreasing towards $n = -3$ with increasing Reynolds number. In addition to the changes in freshwater content, changing n changes the isopycnal slope which may have a significant impact on geostrophic flow which is proportional to the isopycnal slope rather than the depth.

With $n = -1$, if we assume this change in isopycnal depth is reflective of the total change of freshwater in the gyre then the 3% change in volume for the $n = -1$ case would imply an increase in the freshwater content of ≈ 705 km^3 using values for the 2000-2010 estimate of Beaufort Gyre liquid freshwater content (Haine et al., 2015). As a point of comparison, this hypothetical increase is approximately 11% of the observed increase of 6,400km^3 from 2003 to 2018 (Proshutinsky et al., 2019). For $n = -3$, these numbers are inflated to a change of 13% in the BG freshwater content, implying a volumetric change of 3055 km^3 which is equivalent to 48% of the observed increase from 2003 to 2018.

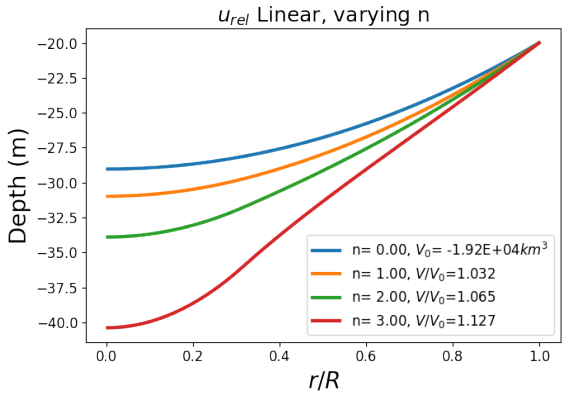


Figure 4.4: Comparison of isopycnal shape calculated for constant drag coefficient (blue) with wave drag parameterizations using $n = -1, -2, -3$ (orange, green, red). For n=0, we set A=0 and so $C_d = C_{d,io}$. The volume V_0 of the constant drag case is used as a reference to which the volumes of the wave drag cases are compared as V/V_0.

Though this is a useful illustrative case, in this model we have fixed the relative ice-ocean velocity while adjusting the drag coefficient and therefore increased the total ice-ocean stress. In figure 4.5 we plot the calculated variation in drag coefficient for $A = 0$ with $n = 0$, and $A = 0.001$ with $n = -1, -2, -3$, to investigate how strong these variations are. From these figures, we observe that the drag reaches a maximum at the low Froude number cut off, when the velocity is low near the center of the gyre. In the real-world system with an imposed atmospheric stress this increased drag would be compensated by changes in the ice and ocean velocities or other processes and not necessarily transmitted as increased ocean stress.

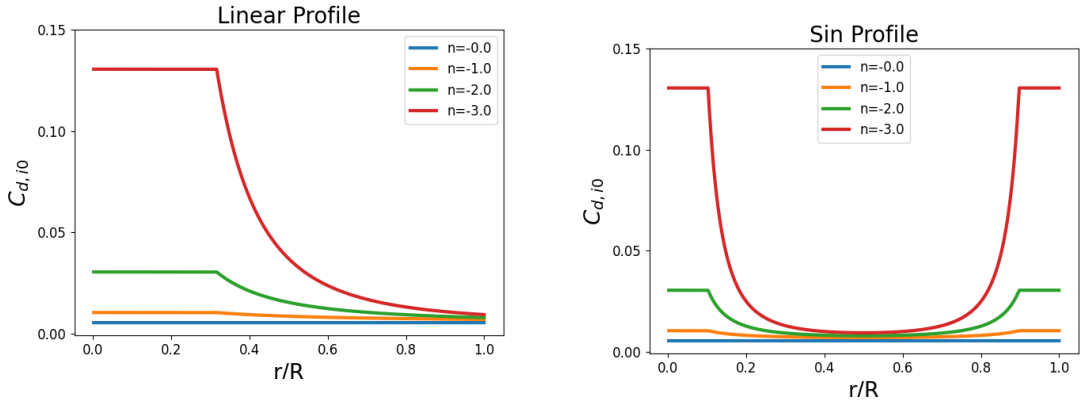


Figure 4.5: Plot of the drag coefficient calculated using (4.24) for the parameter values of table 4.1 and the velocity profiles of (4.28) (left) and (4.29) (right) for $n = 0$ with $A = 0$ (blue), $n = -1$ (orange), $n = -2$ (green), $n = -3$ (red).

We can explore the impact of this adjustment to the ice-ocean stress by calculating the net torque in each computation and re-normalize with u_0 adjusted so that the torque matches the torque set in the constant drag run. To do this we calculate the torque, Γ, as

$$\Gamma = \int_0^R \tau(r)\, r dr \tag{4.27}$$

where the stress is calculated for each case as in (4.25). Because the torque is proportional to stress, (4.23) shows that we can normalise the torque from Γ_n to Γ_0 by rescaling the isopycnal depth of $z - z_0$ by $(\Gamma_0/\Gamma_n)^{1/m}$ for $n = -1, -2, -3$ as shown in the left plot of 4.6. With this normalized torque the differences in the fractional volume are $\leq 1\%$ but some difference in the shape of the isopycnal curve remains. This is an expected result as we expect Fr_h to increase in the gyre interior for the linear velocity profile as shown in figure 4.5. This varied shape has implications for enhanced mesoscale eddy transport of water at depth due to the changing slope as well as for the distribution of geostrophic velocity.

The function for relative velocity used in figure 4.4 is chosen primarily due to simplicity. We can easily examine any number of functions for $u_{rel}(r)$. As mentioned above, the linear profile approximates solid body rotation in absence of ocean velocity. We can similarly examine the case where the surrounding pack ice imposes a no-slip condition on the ice velocity. If the geostrophic velocity is also negligible at the gyre edge then $u_{rel}(R) = 0$ and $u_{rel}(0) = 0$. A simple function satisfying these boundary conditions is $u_{rel} = u_0 sin[(r\pi)/R]$. The two velocity profiles examined in this section are then

$$u_{rel}(r) = u_0(r/R), \tag{4.28}$$

$$u_{rel}(r) = u_0 sin\left(\frac{r\pi}{R}\right) \tag{4.29}$$

We can use (4.27) together with the selected velocity profiles and (4.25) to solve for the respective torques and normalize u_0 in (4.29) so that the total torque is the same as the linear case. Using the reference parameters of table 4.1 we can compare the resultant isopycnal profiles as in the right panel of figure 4.6. In contrast with the linear profile, the sinusoidal velocity profile of (4.29) shows an additional point of concavity towards the gyre edge, and steepened isopycnal slope in the middle of the gyre. This altered profile may modify both the geostrophic and the eddy induced flow which is set by the isopycnal slope. Regions of steeper slope have higher available potential energy and, through the generation of baroclinic eddies, can

control the freshwater exchange below the surface. Such eddies will also transport other physiochemical tracers such as heat and salinity. The variation in the volume prescribed by these curves indicates the importance of the ice-ocean relative velocity in fixing the isopycnal profile. Furthermore, this result indicates that with equivalent torque, the distribution of stress across the gyre surface has an appreciable impact on the gyre freshwater content. Therefore quantities affecting the ice-ocean relative velocity such as ocean currents or ice rheology may influence the gyre structure. As noted earlier, one such feedback affecting the ocean surface velocity is the ice-ocean-governor mechanism of Meneghello et al. (2018b) whereby the accumulation of freshwater may drive a change in surface geostrophic velocity, in turn adjusting the ice-ocean stress.

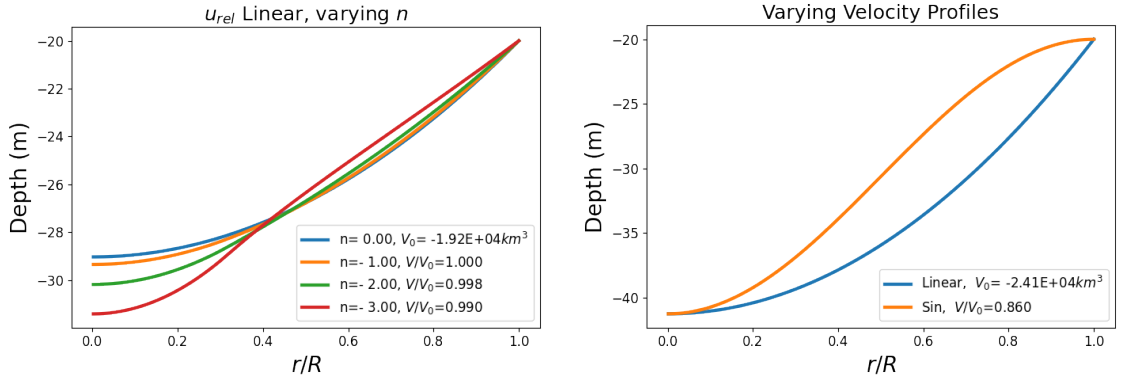


Figure 4.6: Plots of Isopycnal depth for the torque normalized runs of figure 4.4 (left) and the torque normalized velocity profiles for linear relative velocity of (4.28) (blue) and the sinusoidal profile of (4.29) (orange) with the parameter values of table 4.1 (right)

We can conduct an uncertainty estimate by spanning geophysically relevant ranges of the parameters within table 4.1 and plotting the fractional freshwater change V/V_0 for varying parameter values. This is shown without normalization of the ice-ocean torque for the linear velocity profile (4.28) in figure 4.7. We note that the governing parameter for the magnitude of the wave drag impact is Nh/U and so changes to N, h, or $u = u_{rel}$ can alter the value of the drag coefficient. For this reason, we have plotted the uncertainty estimate with two ocean stratifications in figure 4.7: $N^2 = 10^{-5}$ s^{-2} as in table 4.1, and the stratification values of chapter 3 for a summer case of $N^2 = 10^{-3}$ s^{-2}. We take V_0 to be given by a model run using the default configuration of table 4.1 with either $N^2 = 10^{-5}$ or $N^2 = 10^{-3}$ s^{-2}.

Among the parameters examined in figure 4.7, the reference value of u_{rel} showed the strongest influence over the isopycnal volume. This is expected, as any increase

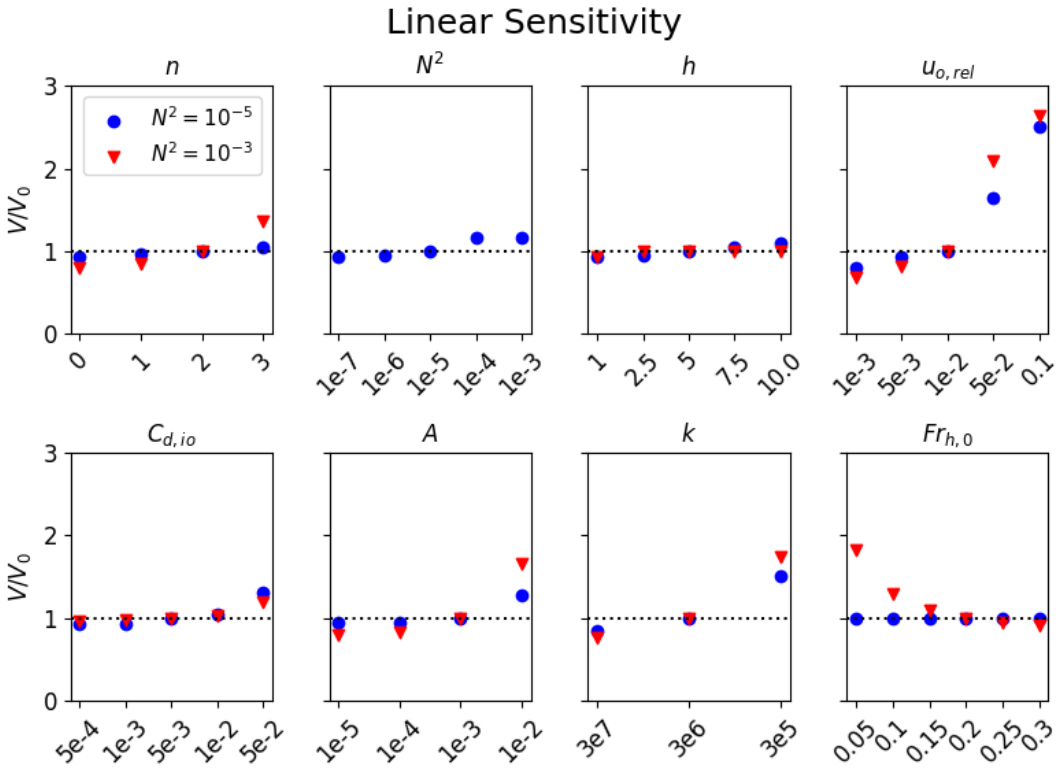


Figure 4.7: Sensitivity of the freshwater content of the gyre to a number of parameters as indicated by the change in fractional volume V/V_0 with V_0 determined by calculation using the reference values of table 4.1. In the top right panel the magnitude of $u_{0,rel}$ is used. Inverted red triangles indicate computations done with $N^2 = 10^{-3}$ s^{-2} motivated by the summer mixed layer of chapter 3. Blue circles indicate the reduced mixed layer value of $N^2 = 10^{-5}$ s^{-2}

in u_{rel} directly increases the magnitude of the surface stress. Only the mesoscale eddy parameter, k, demonstrated comparably strong influence for both values of N^2. The eddy efficiency parameter k, signifies the efficiency of mesoscale eddies in flattening isopycnals, therefore we expect that a reduction in this efficiency results in a deeper isopycnal with steeper slope and therefore larger volume. The response of increasing the eddy efficiency similarly would result in a shallower pycnocline.

The wave drag parameters n, A, and $Fr_{h,0}$ demonstrated sensitivity comparable to changes in k or u_{rel} for the strongly stratified $N^2 = 10^{-3}$ s^{-2} case, but only modest changes for the reduced value of N^2. For the case of $N^2 = 10^{-3}$ s^{-2}, as $Fr_{h,0}$ increases, V/V_0 decreases to a nearly constant value. This is indicative of the wave drag reaching the maximum value, set by the aforementioned restrictions on $Fr_{h,0}$, for the majority of the domain so that C_d essentially becomes constant. We expect that the sensitivity to $Fr_{h,0}$ with a large change in ridge height would have a similar effect. In the case where $N^2 = 10^{-3}$ s^{-2}, for $2.5 < h < 10$ the fraction V/V_0 is approximately unity as can be seen in figure 4.7. This insensitivity to increasing ridge height is due to the entirety of the domain being at the limiting value of $Fr_{h,0}$ and so any increase in h keeps Fr_h below the cut off and no longer causes variations in the drag coefficient. For a reduced stratification, a larger change in V/V_0 is seen for changes in h, although still relatively modest. In the real-world system changes in h would drive contributions to changing form drag as well (Tsamados et al., 2014). In the present model, the impacts of differing form drag changes are represented by changing $C_{d,i0}$ which demonstrates modest sensitivity.

The value of A exhibits modest sensitivity for $N^2 = 10^{-5}$ s^{-2} and slightly enhanced sensitivity for $N^2 = 10^{-3}$ s^{-2}. This is unsurprising as increasing A directly increases the contribution of wave drag effects relative to the form and skin drag effects included in $C_{d,io}$ in (4.25). As $A \to 0$ the drag goes to the expected neutrally stratified behaviour.

The sensitivity of isopycnal volume to varying $Fr_{h,0}$ was negligible for $N^2 = 10^{-5}$ s^{-2}. However under increased stratification, changes in $Fr_{h,0}$ lead to impact comparable to changing eddy efficiency and relative velocity maximum. The gyre volume increases as the cut-off Froude number, $Fr_{h,0}$ decreases. The increased sensitivity of the wave drag parameters with increased stratification suggests any observed impact on gyre structure may vary on seasonal timescales as the upper ocean changes regimes from deep winter mixed layers to shallow mixed layers and melt water lenses in summer.

In the Beaufort Gyre, the relative velocity and thus the ice-ocean stress is determined by the ocean surface velocity, including the geostrophic velocity, and the ice velocity. The former of these is the heart of the ice-ocean governor. The latter is determined by a balance of atmospheric, oceanic stresses on the ice at the respective interfaces, and internal stresses within the ice. We will now seek to develop a rudimentary model of the ice rheology which we will later couple to the ocean model just examined.

4.5 Rheological model

In this section, we use a simplified Newtonian viscous ice-rheology to investigate the effects of ice rheology on the ocean surface stress. This rheology neglects the potential for plastic mechanical deformation of the sea ice, but still allows for development of a tractable model where sea ice is able to support some of the applied wind stress via ice internal stresses. By the axisymmetry of the current problem, these stresses would be shear stresses which are captured here using a Newtonian viscous rheology. Viscoplastic models such as the regularized Hibler model described in Rallabandi et al. (2017) typically incorporate Newtonian viscous behaviour at low stresses and for large deformation rate, but allow for plastic deformation when stress reaches a yield criterion. These plastic responses are neglected here; we discuss the consequences of this later on in §4.5.6.

We first derive the model in §4.5.1 where we derive the full equation for sea ice motion with a viscous rheology. The physical justification for the boundary conditions is examined in §4.5.2 and the parameter values to be used in the application of the model are introduced in §4.5.3. Following this, a linear version of the model is examined in §4.5.4 to build initial insight. The method for solving the nonlinear model is then established in §4.5.5 with results and sensitivities discussed in §4.5.6

4.5.1 Model derivation

In this section u_r and u_θ refer to the ice velocity which are assumed to only depend on r due to axisymmetry. In general the mass conservation of ice with some fractional ice coverage, C, is given by

$$\frac{\partial C}{\partial t} + \nabla \cdot (\mathbf{u}C) = 0. \tag{4.30}$$

For $C < 1$, if we assume the concentration in the region is not changing with time and assuming symmetry about the axis $r = 0$, all $\partial/\partial\theta$ terms are 0. Then in cylindrical coordinates (4.30) is given as

$$\frac{1}{r}\frac{\partial(ru_rC)}{\partial r} = 0 \tag{4.31}$$

which implies that $ru_rC = 0$. Provided u_r is bounded at the origin, if $C \neq 0$ then $u_r = 0$ everywhere. Note that this also means we recover the standard incompressibility relation

$$\nabla \cdot \mathbf{u} = \frac{1}{r}\frac{\partial(ru_r)}{\partial r} + \frac{1}{r}\frac{\partial u_\theta}{\partial \theta} = 0. \tag{4.32}$$

We will also here assume that the continuum average of the sea ice lid has uniform thickness such that h_i is constant and individual ice floes are rigid. This still allows for microscopic ice thickness changes in pressure ridges, but assumes a spatially uniform statistical distribution of ice thickness when averaged over many floes as a continuum model. In an isotropic Newtonian viscous rheology with ice of a uniform thickness we have, from §4.2, the depth-integrated momentum equation for sea ice

$$m\frac{D\mathbf{u}}{Dt} = -mf_c\mathbf{e}_z \times \mathbf{u} - mg\nabla H - \nabla P + \eta\nabla^2\mathbf{u} + \tau_a + \tau_o. \tag{4.33}$$

Converting (4.33) to cylindrical coordinates, and noting that terms with u_r and $\partial/\partial\theta$ are zero, we arrive at the following equations for the radial and azimuthal components

$$-m\frac{u_\theta^2}{r} = -mf_cu_\theta - mg\nabla H - \frac{\partial P}{\partial r} + (\tau_a)_r + (\tau_o)_r \tag{4.34}$$

and

$$0 = \eta\left(\frac{1}{r}\frac{\partial}{\partial r}\left[r\frac{\partial u_\theta}{\partial r}\right] - \frac{u_\theta}{r^2}\right) + (\tau_a)_\theta + (\tau_o)_\theta. \tag{4.35}$$

Our primary interest is in the azimuthal momentum balance to determine u_θ (the radial momentum balance can be satisfied via an adjustment of the radial pressure gradient). For brevity we will use τ_o and τ_a for the azimuthal components from now on. We can rearrange (4.35) as

$$r^2\frac{\partial^2 u_\theta}{\partial r^2} + r\frac{\partial u_\theta}{\partial r} - u_\theta = -r^2\frac{\tau_a}{\eta} - r^2\frac{\tau_o}{\eta}. \tag{4.36}$$

Equation (4.36) is then a 2nd order nonlinear ODE which one may solve for the ice velocity given τ_a and τ_o and specified boundary conditions. The stress terms of (4.36), τ_a and τ_o, are commonly implemented as a quadratic function of the velocities

$$\tau_a(r) = \rho_aC_{d,ai}u_a(r)|u_a(r)|, \qquad \tau_o(r) = -\rho_oC_{d,io}u_{rel}(r)|u_{rel}(r)|. \tag{4.37}$$

In this system, $u_{rel} = u_\theta - u_{ocean}$ is a function of ice velocity, u_θ, as well as the geostrophic velocity and surface currents, u_{ocean}. The atmospheric stress in principle depends on u_{ice}, though because $|u_{ice}| << |u_a|$ we neglect it.

For our work we use the boundary conditions given by

$$u_\theta(0) = 0 \qquad \text{and} \qquad a u_\theta(R) - bRu'_\theta(R) = 0. \tag{4.38}$$

The first is an imposition on the velocity at the origin to avoid a stress singularity as $r \to 0$, and the latter is a Robin boundary condition. The choices of a and b in the Robin boundary condition are tied to the stress tensor.

4.5.2 Robin boundary condition physical interpretation

The Robin boundary condition of (4.38) can be implemented with a variety of choices for a and b. We here discuss the physical interpretation by examining the Navier Stokes stress tensor in cylindrical coordinates. Noting that terms involving u_r and $\partial/\partial\theta$ are all zero as above, we write

$$\sigma_{r,\theta} = \eta \left(\frac{\partial u_\theta}{\partial r} - \frac{u_\theta}{r} \right) = -\Upsilon u_\theta \tag{4.39}$$

where the second equality represents an assumed linear dependence between stress and ice velocity. This is a partial slip condition on the gyre velocity where Υ controls the slip. Rewriting this we have

$$u_\theta - \frac{1}{1 - \frac{\Upsilon R}{\eta}} R \frac{\partial u_\theta}{\partial r} = 0 \tag{4.40}$$

and so $a = 1$ and $b = (1 - \Upsilon R/\eta)^{-1}$. Hence, $a = b = 1$ corresponds to no stress at the outer boundary ($\Upsilon = 0$), and $a = 1$, $b = 0$ represents no slip at the gyre edge ($\Upsilon \to \infty$). We can rewrite Υ in terms of b as

$$\Upsilon = \frac{\eta}{R} \left(1 - \frac{1}{b} \right). \tag{4.41}$$

For partial slip cases, $0 < \Upsilon < \infty$ and $b > 1$ or $b < 0$. The primary cases of no-slip ($\Upsilon \to \infty$) can be motivated by the basin conditions where land fast ice or pack ice at the gyre edge impose sufficient stress to slow the ice within the gyre to rest. The stress free limit ($\Upsilon = 0$), represents weak or negligible resistance at the edge of the gyre. This weak resistance may occur if there were no sea ice beyond the gyre edge, or if ice at the gyre edge were to be in free drift.

With this insight, we will primarily focus on the two cases of the no-slip, and stress free boundaries. These cases can be seen as analogous to the regimes established in Wang et al. (2019a) for the winter, and summer ice internal stress regimes. We also examine a number of values for $\Upsilon \in (0, 10^7)$ for sensitivity as the frictional slip case is potentially relevant in the geophysical picture. The model developed in §4.5 describes an axisymmetric gyre, but there is an asymmetric set of boundary conditions in reality. Ice conditions at the gyre edge may vary strongly between the Alaskan coast, the Bering strait, and the interior Arctic ice pack. For example, the observed ice velocities as in figure 4.2 indicate a profile that is increasing towards the gyre edge with a maximum being seen near the Alaskan coast which would be resembled more closely by the free-stress case. The partial slip conditions can be seen as a transitionary case that might be qualitatively representative of the average of the conditions around the gyre.

4.5.3 Parameter values for rheological model

In addition to the parameters previously used for the ocean model developed in §4.3.1 and §4.4 as set out in table 4.1, we have the atmospheric parameters $C_{d,ia}$ the air-ice drag coefficient, ρ_a the density of the atmosphere near the ice surface , and $u_{a,R}$ the wind speed at the outer edge of the gyre. Instead of a relative velocity we specify a characteristic value of the ocean velocity $u_{0,ocean} = 0.01$. Lastly we have the ice viscosity η whose value is taken within the range of sea ice viscosities examined in Hibler and Tucker (1977), but we check sensitivity to this parameter for a range of η in the linear model of §4.5.4 and in the nonlinear model within §4.5.6. In this work we will use a linear form of the atmospheric velocity $u_a(r) = u_{a,R} r/R$ throughout.

$n = 2$	$h = 5$ m	$N^2 = 1 \times 10^{-5}$ s^{-2}	$A = 0.001$
$\rho_a = 1.25$ kg m^{-3}	$C_{d,ia} = 1.25 \times 10^{-3}$	$\rho_o = 1028$ kg m^{-3}	$C_{d,io} = 5.5 \times 10^{-3}$
$u_{0,ocean} = 0.01$ m s^{-1}	$u_{a,R} = 5$ m s^{-1}	$\eta = 1 \times 10^{10}$ m^2 s^{-1}	$R = 500,000$ m

Table 4.2: Default values for parameters to be used in this standalone rheology model.

4.5.4 Rheology model with linear drag

To build insight we first examine a simplified form of the system which we are able to solve analytically. Here we assume a simplified linear dependence on u_{rel} and u_a for oceanic and atmospheric stresses. Furthermore we assume the wind speed and ocean current speed are given by linear functions of the distance from the gyre center ($u(r) = u_0 r/R$) so that

$$\tau_a = u_{a,R}\frac{r}{R}\rho_a C^*_{d,ai} \tag{4.42}$$

and

$$\tau_o = (u_o\frac{r}{R} - u_\theta)\rho_o C^*_{d,io}. \tag{4.43}$$

where $C^*_{d,ai}$ and $C^*_{d,io}$ are linear drag coefficients with units ms^{-1}, and $u_{a,R}$ is the value of the near surface wind speed at the gyre edge.

Plugging these relations into (4.36) and doing some algebraic rearrangement provides

$$r^2\frac{\partial^2 u_\theta}{\partial r^2} + r\frac{\partial u_\theta}{\partial r} - u_\theta\left(1 + \frac{\rho_o C_{d,io}}{\eta}r^2\right) = -\frac{u_{a,R}\rho_a C_{d,ai}}{\eta R}r^3 - \frac{u_o\rho_o C_{d,io}}{\eta R}r^3 \tag{4.44}$$

To simplify we make the following substitutions

$$A_0 = \sqrt{(\rho_o C_{d,io})/\eta}, \tag{4.45}$$

$$A_1 = \frac{u_{a,R}\rho_a C_{d,ai}}{\eta R}, \tag{4.46}$$

$$A_2 = \frac{u_o\rho_o C_{d,io}}{\eta R}, \tag{4.47}$$

and let $r_s = rA_0$ so that (4.44) becomes

$$r_s^2\frac{\partial^2 u_\theta}{\partial r_s^2} + r_s\frac{\partial u_\theta}{\partial r_s} - u_\theta\left(r_s^2 + 1\right) = -\left(A_1 + A_2\right)A_0^{-3}r_s^3 \tag{4.48}$$

which is recognizable as a non-homogeneous form of the well known modified Bessel's equation (Watson, 1995). The solutions to the homogeneous equation are given by a linear combination of the modified Bessel functions of the first and second kind, $I_1(r_s)$ and $K_1(r_s)$ respectively. $K_1(r_s)$ is singular at the origin, so we set the coefficient for $K_1(r_s)$ to 0, so that the homogeneous solution $H(r_s)$ is $H(r_s) = \alpha_0 I_1(r_s)$ for a yet to be determined α_0. A particular solution of (4.48) can be obtained by assuming a polynomial of degree 3 such that

$$P(r_s) = \gamma_3 r_s^3 + \gamma_2 r_s^2 + \gamma_1 r_s + \gamma_0. \tag{4.49}$$

Substituting this into (4.48) and matching coefficients we find $\gamma_3 = \gamma_2 = \gamma_0 = 0$ and $\gamma_1 = (A_1 + A_2)A_0^{-3}$ so that the particular solution is

$$P(r_s) = (A_1 + A_2)A_0^{-3}r_s \tag{4.50}$$

and so we have

$$u_\theta(r_s) = H(r_s) + P(r_s) = \alpha_0 I_1(r_s) + (A_1 + A_2)\, A_0^{-3} r_s. \tag{4.51}$$

It now remains to determine α_0. Applying the Robin boundary condition (4.38) at $r = R$ to (4.51) we find

$$\alpha_0 = \frac{(A_1 + A_2)\, A_0^{-3} R_s (b - a)}{[a I_1(R_s) - b R_s I_1'(R_s)]}. \tag{4.52}$$

where $R_s = A_0 R = \sqrt{(\rho_0 C_{d,io} R^2/\eta)}$ and so the full analytical solution for u_θ is given by

$$u_\theta = \left(u_o + u_{a,R} \frac{\rho_a C_{d,a}}{\rho_o C_{d,io}}\right) \left[\frac{r_s}{R_s} - \frac{(a-b) I_1(r_s)}{a I_1(R_s) - b R_s I_1'(R_s)}\right] \tag{4.53}$$

With this result we observe that the ice velocity has a linear response to the ocean and atmospheric velocity. Given the linear drag laws, this implies a linear response to atmospheric stress. Furthermore, the viscosity is only present within the rescaling of the radius $r_s = r A_0$ and so changing viscosity simply stretches the length scale and changes the horizontal shape with a boundary layer forming at the outer boundary for small viscosity. If $a = 1$, $b = 0$, the viscosity also affects the peak magnitude of the sea ice velocity. These behaviours are shown in figure 4.8. In the free stress case where $a = b = 1$, the terms from the homogeneous solution disappear and the ice velocity depends linearly on the stress terms yielding a solid body rotation. The effect of the ice viscosity on the ice velocity could allow for increased ice-ocean stress in a winter ice state with low strength as suggested in Wang et al. (2019a).

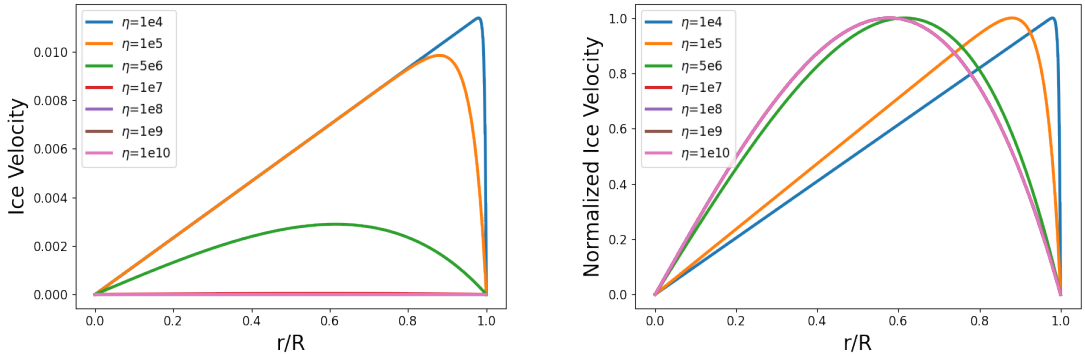


Figure 4.8: Ice velocity (left) and normalized ice velocity (right) as a function of scaled gyre radius r/R for a wide range of viscosity with units $\mathrm{m}^2\ \mathrm{s}^{-1}$ for no slip boundary conditions. Ice velocities were calculated from (4.53) using the parameter values of table 4.2. For this illustrative case we have used $C^*_{d,ai}$ and $C^*_{d,io}$ as having the same magnitude as $C_{d,ai}$ and $C_{d,io}$.

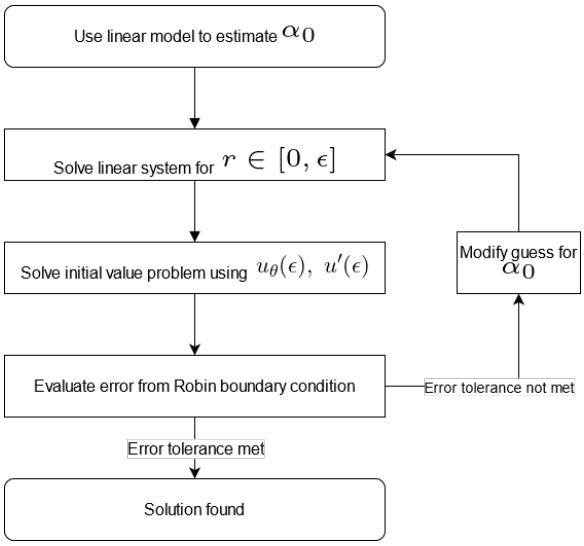


Figure 4.9: Flow chart indicating the algorithm used to implement the shooting method for bypassing the singular point at $r = 0$, where the numerical solution of the initial value problem proceeds on $\epsilon < r < R$

4.5.5 Rheological model with quadratic drag

Initial attempts at numerical solution of (4.36) with quadratic drag failed to immediately converge. This is potentially due to numerical solvers struggling near the origin where the modified Bessel function, K_1, cancelled in the analysis of §4.5.4, is singular. To sidestep this singularity, we can use the analytical solution of the linear drag model to calculate values of $u_\theta(\epsilon)$ and $u'_\theta(\epsilon)$ for some $\epsilon << R_{gyre}$. We then solve (4.36) as an initial value problem using these terms. The values of $u_\theta(\epsilon)$ and $u'_\theta(\epsilon)$ first determined may lead to a solution that does not satisfy the Robin boundary condition of (4.38) for the nonlinear problem. So we instead calculate the coefficient α_0 in (4.52) which we may use to calculate $u_\theta(\epsilon)$ and $u'_\theta(\epsilon)$ from (4.51) and it's derivative. We can then alter this guess for α_0 to adjust the initial conditions via a shooting method as diagrammed in figure 4.9. Through this method we can determine the value of α_0 that minimizes the error of the Robin boundary condition from (4.38). We note that the analytical solution (4.51) assumes linear drag laws, rather than the quadratic drag of the full problem. However, the drag is relatively small near to the origin due to the small velocities and approaches zero as $r \to 0$. Therefore, this approximation introduces only a small error, and yields a reasonable approximation to the solution for small ϵ.

Unfortunately even with the shooting method, solutions were not immediately able to converge with the quadratic ocean drag, though the full system with linear

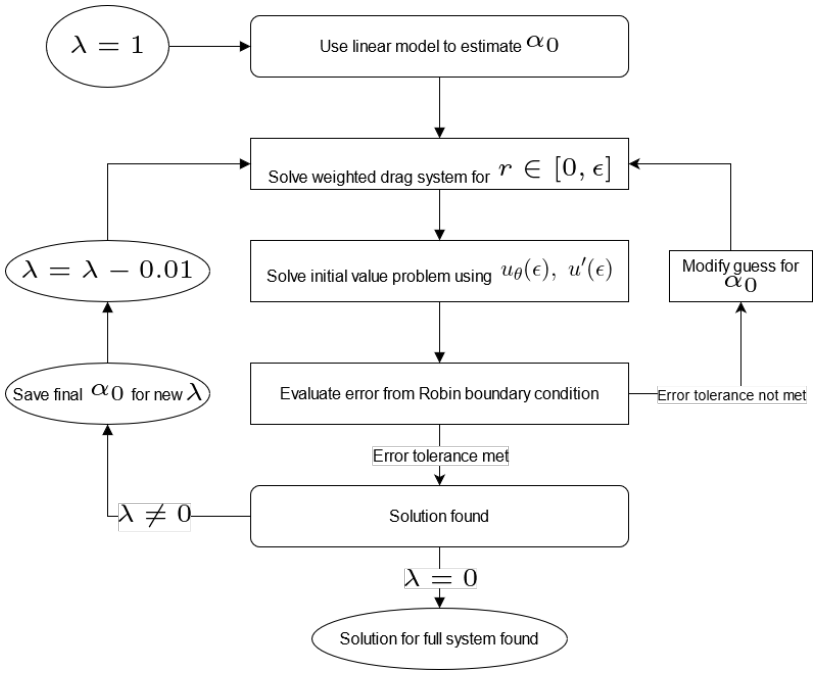


Figure 4.10: Flow chart indicating the algorithm used to implement the continuation method alongside the shooting method to completely solve (4.36) with quadratic ice-ocean stress by iteratively solving (4.54).

ocean drag and quadratic atmospheric drag was solvable numerically via the shooting method. To remedy this we employed a continuation method alongside the shooting method as shown in the flow chart of figure 4.10. This continuation method iteratively solved a version of (4.36), involving weighting of linear and quadratic drag.

$$r^2\frac{\partial^2 u_\theta}{\partial r^2} + r\frac{\partial u_\theta}{\partial r} - u_\theta = -r^2\frac{\tau_a^{quad}}{\eta} - \lambda r^2\frac{\tau_o^{lin}}{\eta} - (1-\lambda)r^2\frac{\tau_o^{quad}}{\eta} \tag{4.54}$$

where τ_o^{lin} indicates the linear stress relation of (4.43), τ_o^{quad} and τ_a^{quad} are the ocean and atmospheric stress using the quadratic form of (4.37), and $\lambda \in [0, 1]$ is a continuation parameter with $\lambda = 1$ corresponding to linear drag. Following each iteration, the determined value of α_0 is saved. In the next iteration, λ is decreased by some value (here 0.01 was found to work) and the saved value of α_0 is used as the updated initial guess. This process is repeated until $\lambda = 0$, representing the solution of (4.36) with quadratic oceanic and atmospheric stress. This incremental continuation procedure has the advantage of assuring that the initial starting guess for each iteration does not stray too far from the eventual solution to that iteration, aiding convergence of the nonlinear solver used in the shooting method.

4.5.6 Sensitivity of idealized rheological model.

Here we examine the sensitivity of the ice floe and its coupling to the ocean to variations in $C_{d,io}$, η, $u_{a,R}$, and the oceanic velocity u_o. We use the velocity profiles of (4.28) and (4.29) for ocean velocity instead of relative velocity. We also test a number of boundary conditions at $r = R$ by varying the coefficients in the Robin boundary condition as discussed previously. As in §4.4.1, we will examine the effects of wave drag by comparing against a case with constant drag coefficient. As with the ocean only model, we will also show cases with $N^2 = 10^{-3}$ s^{-2} as used for the summer stratification in chapter 3. Because N enters the calculation via the Froude number U/Nh, similar results occur by holding N constant and increasing h thus allowing us to indirectly infer the potential role of changing ice roughness as well. Each of these quantities are known to vary on seasonal timescales with greater fractions of thicker, rougher multiyear ice in the winter alongside a well mixed upper ocean, and thinner ice over a more strongly stratified ocean in summer. These pathways present a potential modification to the typical picture of ice internal stresses in the Beaufort Gyre. Unless specified, plots shown will use $N^2 = 10^{-5}$ s^{-2}. The default values of all rheological model parameters are those earlier presented in table 4.2.

Figure 4.11 shows example profiles of the ice velocity, and resultant ice-ocean stress assuming a linear profile of $u_{ocean} = u_{0,ocean}(r/R)$, with both wave drag and a constant drag coefficient $C_{d,io}$. The left column uses the stress-free boundary conditions and the right column no-slip boundary conditions while the rows represent the stratification strength $N^2 = 10^{-5}$ s^{-2} and $N^2 = 10^{-3}$ s^{-2}. For $N^2 = 10^{-5}$ s^{-2} in the top panel of figure 4.11, the effect of wave drag on the system is negligible. For the free slip condition in the top left, the boundary exerts no viscous stress on the ice yielding an ice velocity close to solid body rotation. In this case the viscous stresses (first equality of equation 4.39) are exactly zero for solid body rotation with $u_\theta \propto r$, and so the disk of ice spins at a speed that balances the local atmospheric and ice-ocean stresses. The ice and ocean velocities both vary approximately linearly with radius, and since the drag varies quadratic with relative velocity yielding approximately quadratic variation with r. For no slip, the ice is slowed by viscous drag at the gyre edge, leading to non-monotonic variation of ice velocity and ice ocean stress. The ice ocean stress has smaller amplitude, as some of the atmospheric stress is balanced by viscous ice stresses at the gyre boundary.

For $N^2 = 10^{-3}$ s^{-2} in figure 4.11, a number of significant deviations are observed. For the stress free condition with $N^2 = 10^{-3}$ s^{-2}, the ice velocity experiences a significant reduction with the inclusion of wave drag, with $u_{ice}(R)$ reduced to approximately

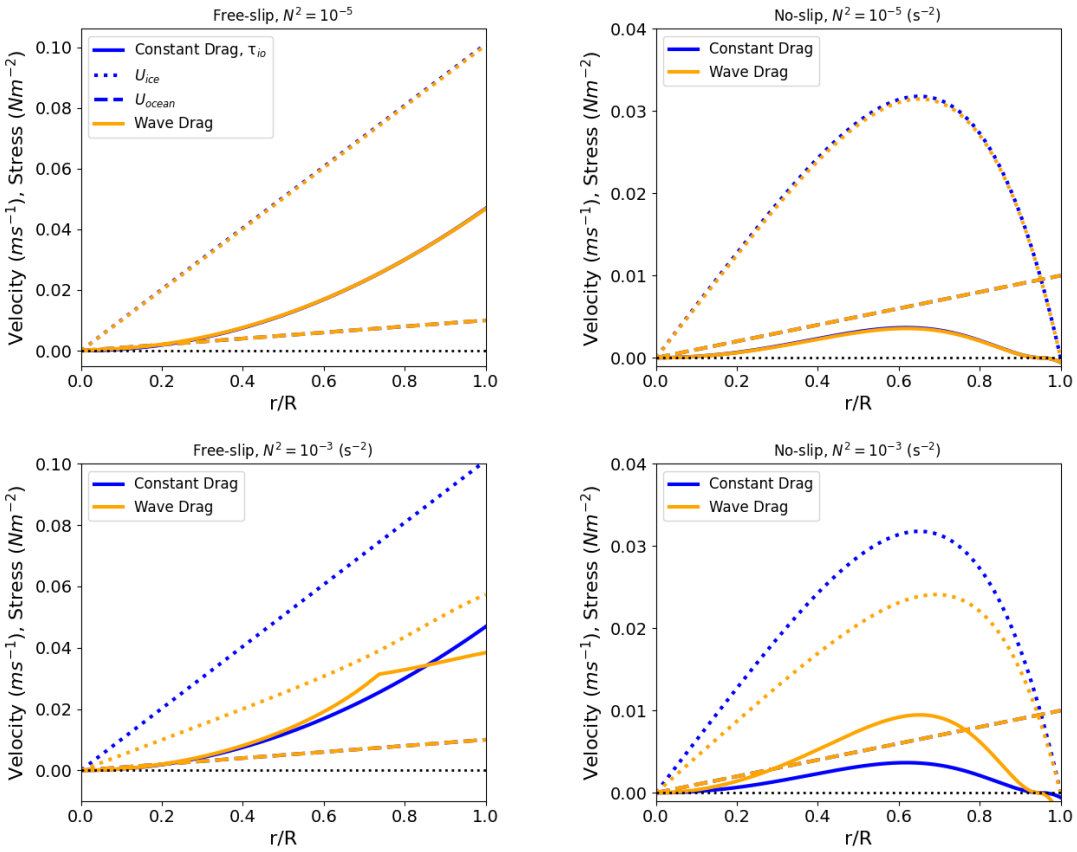


Figure 4.11: Radial variation for the magnitudes of ice velocity (dotted lines), ocean velocity (dashed lines) and ice-ocean stress (solid line) for constant drag coefficient (orange) and with wave drag (blue). The top row displays model results for $N^2 = 10^{-5}$ s^{-2} for free-slip (left), and no-slip (right) boundary conditions. The bottom row displays the same model results for $N^2 = 10^{-3}$ s^{-2}. The black dotted line indicates zero level.

half of the value when using constant drag coefficient. For constant drag coefficient, both the free slip and no slip cases see similar patterns of spatial variation for both high and low stratifications. However, with wave drag the strongly-stratified free stress case (orange lines, lower left panel) sees some spatial variation in the response of ice velocity and ice-ocean stress due to spatially varying wave drag. The response differs from a simple uniform change of amplitude. From $r/R = 0$ until $r/R \approx 0.75$ the shape of the ice-ocean stress is similar to that of the constant drag case, but with slightly increased amplitude. At $r/R \approx 0.75$ the drag changes from the nearly quadratic shape and becomes approximately linear despite no observable change in the shape of u_{ice} or u_{ocean}. Figure 4.12 shows the radial variation of C_d as determined by (4.24). For $N^2 = 10^{-3}$ s^{-2}, in the range $0 < r/R \lesssim 0.75$, the drag coefficient is at the maximum value permitted in the model and then decreases for larger r as the ice-ocean relative velocity grows and so $Fr_h > Fr_{h,0}$. For the no-slip case and summer stratification value, the wave drag is at the maximum value for $0 < r/R < 1$ and so the behaviour is similar to that of an increased constant drag coefficient. The enhanced wave drag also reduces ice velocity versus the case with constant drag coefficient. However the net effect of increased drag coefficient and reduced ice velocity is still an increase in ice-ocean drag. Because the viscous ice drag at the gyre edge exerts some torque on the ice, this allows the ice-ocean stress to vary more substantially while still satisfying the net torque balance on the ice. Each of the no-slip profiles in 4.11 predict negative ice-ocean stress at the outer radius of the gyre predicting a region of Ekman down-welling.

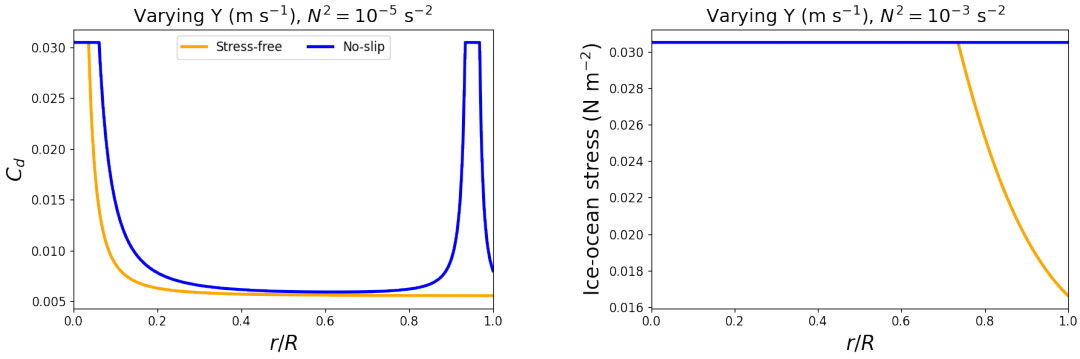


Figure 4.12: Plot of Drag coefficient as a function of r/R calculated using (4.24) for the free slip and no-slip conditions shown in figure 4.11 for $N^2 = 10^{-5}$ s^{-2} (left) and $N^2 = 10^{-3}$ s^{-2} (right)

For the weak stratification profile used in the top row of figure 4.11, we saw no appreciable variation in any of the ice properties. In figure 4.12, we investigate the

drag coefficient for these model outputs and see that for each stratification, both the free-slip and no-slip case possessed regions with appreciable increase in drag coefficient. For the low stratification case, these regions are only a small fraction and so their impact on the gyre is reduced. Though variations in the weak stratification have negligible effect on the large scale ice motion, they may potentially be important for local mixing processes. Furthermore, in a more complex rheology these regions may be more susceptible to plastic deformation due to the locally increased stress.

The profiles of ice velocity in the free-slip and no-slip cases of figure 4.11 are reminiscent of those prescribed by the studies of Manucharyan and Spall (2016), and in Meneghello et al. (2018a) respectively. In Manucharyan and Spall (2016) a linear function of surface ocean stress is applied. In Meneghello et al. (2018a) instead of an ice-ocean stress, an ice velocity profile was prescribed with $u_{ice}(0) = u_{ice}(R) = 0$, on top of a stagnant ocean which was then allowed to evolve and alter the ocean velocity. Each of these can be seen to impose conditions on the sea ice motion which, from figure 4.11, approximately line up with the two ice conditions, free slip and no slip, and may explain some of the differences in isopycnal slopes determined in each of these studies. Meneghello et al. (2018b) also allowed for the spinning up of the ocean geostrophic velocity which can strongly mediate the ice-ocean relative velocity and thus the ice-ocean stress. The study of Wang et al. (2019b) which included ice rheology found summer and winter states that are qualitatively similar to the properties of the simulated ice velocity with free-slip and no-slip boundary conditions shown in figure 4.11. The modifications to the ice velocity and ice-ocean stress seen in strong stratification suggests that the wave drag may qualitatively alter the ice-ocean feedback on the gyre. In the geophysical system, the boundary condition is potentially in between the free-slip and no-slip cases illustrated here, which motivates consideration of partial slip boundary conditions.

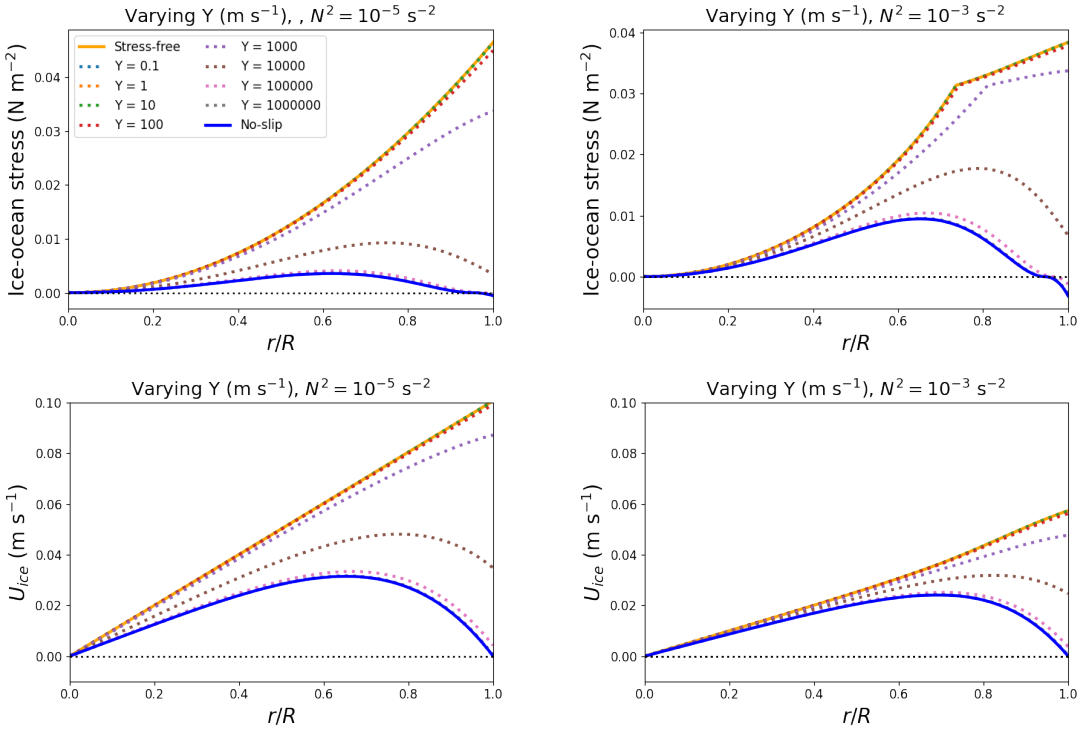


Figure 4.13: Radial variation of ice ocean stress (top) and ice velocity (bottom) with $N^2 = 10^{-5}$ s^{-2} (left) and $N^2 = 10^{-3}$ s^{-2} (right) for varying values of the partial slip friction coefficient $\Upsilon = Y$. The dashed black line indicates the zero level.

In figure 4.13, we examine the response of the model to intermediary values of the lateral friction coefficient Υ for the two cases $N^2 = 10^{-5}$ s^{-2}, $N^2 = 10^{-3}$ s^{-2}. In both stratifications, for values of Υ in the range 0 m s^{-1} $< \Upsilon <$ 10^7 m s^{-1} the ice-ocean stress shifts between the expected limits with an intermediary state appearing for 10^3m s^{-1} $\lesssim \Upsilon \lesssim 10^5$(m s^{-1}). With increasing Υ, the viscous drag on ice at the gyre edge increases, and the slip velocity progressively reduces with increasing viscous shear at the outer boundary. The ice velocity similarly transitions between the characteristic solid body rotation at small Υ to a no slip limit whereby the ice velocity is 0 at the gyre edge. This reduction in ice velocity with increasing Υ also reduces the relative ice-ocean velocity, first forcing the Froude number below cut off at the gyre edge and removing the break in slope of the ice-ocean stresses. Wang et al. (2019a) found that seasonal variations in Ekman pumping were primarily controlled by seasonal changes in ice speed which may be represented by different lateral frictional slip conditions in this model. At the largest values of Υ the ice at the gyre edge moves slower than the ocean, resulting in a small region of reversed ice-ocean stress at the gyre edge.

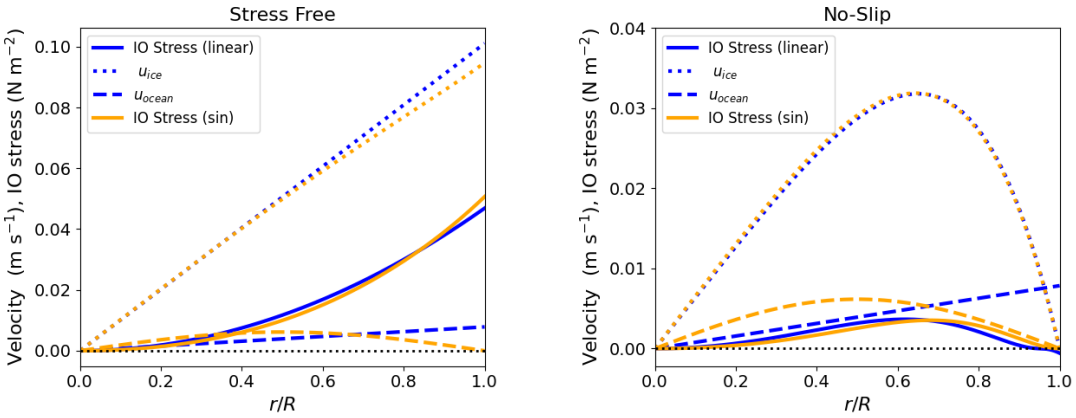


Figure 4.14: Comparison of calculations done with varying ocean velocities for stress-free (left) and no-slip (right) boundary conditions. Curves shown are of ice velocity (dotted), ice-ocean stress (solid) and ocean velocity (dashed). Different colours indicate the different velocity profiles of the ocean velocity using the linear form (4.28) (blue) and the sin form of (4.29) (orange)

As done in §4.4.1 for the relative velocity, we can investigate the impact of our choice in ocean velocity profile on the results so far discussed. We use the default parameters of table 4.2 with the wave drag parameterization turned off, and varying the ocean velocity form using (4.28) and (4.29). These results are shown for the stress-free and no-slip conditions in figure 4.14. The overall effect of the variation in ocean velocity profiles on the ice-ocean stress and velocity is modest, and less than the differences for the summer stratification seen in figure 4.11. In the real system the ocean geostrophic velocity depends on the isopycnal slope. We later examine the effects of this geostrophic velocity, but here use the linear velocity profile to determine the model's sensitivity to uncertainty in the chosen parameters.

We look at the torque, Γ, for a broad comparison of all parameters. The atmospheric torque, Γ_a, and ice-ocean torque, Γ_o, can be calculated as

$$\Gamma_a = \int_0^R \tau_a (2\pi r) dr, \qquad \Gamma_o = \int_0^R \tau_o (2\pi r) dr. \tag{4.55}$$

By net torque balance, the torque arising from the internal stresses within the ice is the difference of these torques $\Gamma_{net} = \Gamma_a - \Gamma_o$, and is plotted in figure 4.15 for a range of Υ with both $N^2 = 10^{-5}$ s^{-2} and $N^2 = 10^{-3}$ s^{-2}. It is also informative to examine just the quantity Γ_o to glimpse the potential impacts on the underlying structure of the gyre and thus potential importance on the Beaufort Gyre freshwater. As seen earlier in (4.13) the varying slip parameter Υ controls a regime shift from the stress free limit near $\Upsilon = 0$ to the no-slip limit of large Υ. Figure 4.15 shows that nearly all

of the atmospheric torque is transmitted to the ocean for small Υ for both values of N^2, where small Υ is close to the free slip limit. The transition to the no-slip regime at large Υ corresponds to a region where the internal stresses balance an increasing fraction of the atmospheric torque with only a portion being transmitted to the ocean. For $\Upsilon \geq 10^4$ m s^{-1} we observe a divergence in the net and ocean torques between the two values of N^2. Here a stronger stratification profile is observed to result in reduced net torque, signifying a decrease in the ice internal stresses. This is similarly seen as an increase in the torque exerted on the ice by the ocean.

The regime change for varying Υ shown in figure 4.13 can be seen to loosely resemble changes in the ice internal stresses as a result of changing sea ice concentration at the gyre edge. In this picture, $\Upsilon = 0$ leads to approximate solid body rotation and hence negligible lateral viscous stresses through the ice. This represents sea ice in free drift with no shear stress at the gyre edge. Meanwhile, increasing Υ signifies increasing boundary friction which might be consistent with increasing ice concentration and mechanical interactions at the gyre edge. Sea ice in the Beaufort Gyre region is known to vary between these regimes on a seasonal cycle (Timmermans and Marshall, 2020; Meneghello et al., 2018a; Wang et al., 2019a; Dewey et al., 2018). Though we do not seek to characterize the temporal variability of the system, understanding the response of the ice dynamics to variations in slip condition is potentially useful for understanding how the gyre ice cover may respond under changing sea ice states. For example, in figure 4.13 we see that for large Υ the weaker stratification of $N^2 = 10^{-5}$ (s^{-2}) yielded larger ice internal stresses and a reduced ice-ocean torque. Comparing this to the model output for the summer stratification value of $N^2 = 10^{-3}$ (s^{-2}), we observe that the strong summer stratification results in a 27% decrease in the ice internal stresses corresponding with an increase in the ice ocean torque in the no-slip limit. Hence, the effects of stratification may play an appreciable role on varying the response of the gyre in a regime where significant ice stresses occur at the gyre edge. In the work of Wang et al. (2019a), the increased internal stresses resulting from the winter ice pack are observed to play a key role in limiting the freshwater content of the gyre by seasonal down-welling. The results here suggests that wave drag effects may alter the strength of this feedback by allowing for more efficient momentum transfer at the ice-ocean boundary.

Figures 4.16 and 4.17 examine the sensitivity of the model torques to variations in parameter values. In these figures, Γ_{net} indicates the absorption of atmospheric and oceanic stresses on the ice by ice internal stresses with increasing Γ_{net} indicating increasing absorption of ice-internal stresses.

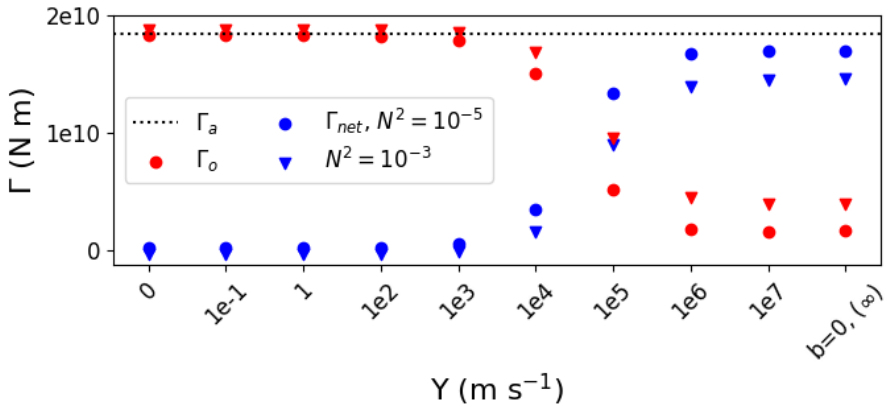


Figure 4.15: Plot of net torque Γ_{net} (blue), ocean torque Γ_o (red), and atmospheric torque Γ_a (dotted line) for varying values of $\Upsilon = Y$ m s^{-1} with $N^2 = 10^{-5}$ s^{-2} (circles), and $N^2 = 10^{-3}$ (s^{-2}) (crosses).

In the stress free case we expect to see $\Gamma_{net} = 0$ and $\Gamma_o = \Gamma_a$ indicating a balance between the ice and ocean stresses with no ice internal stresses. A cursory investigation of figures 4.16 and 4.17 shows that this picture broadly holds.

For the no-slip case, it is clear that within this model Γ_{net} shows strongest sensitivity to $u_{a,R}$. This parameter and $u_{0,ocean}$ control the total stress on the ice so this is not unexpected. In the top panel of figure 4.16 we see that the strength of the sensitivity to these parameters is altered in the different stratification regimes. For $u_{a,r}$, the increased stratification results in a decreased response to changing wind speed with a net torque for the strongly stratified case reduced by 16% for $u_a = 10$ m s^{-1}. As Γ_a is unaffected by changing ice-ocean drag, this suggests a decrease in the ice internal stresses, in turn implying more efficient momentum transfer at the ice-ocean interface. This is verified by examining the corresponding plots in figure 4.17 where we see increasing ice-ocean stress with increasing $u_{a,R}$.

Increasing the value of $u_{0,ocean}$ in the no-slip case shows a corresponding increase in Γ_{net} indicating increased ice internal stresses. In this case however, Γ_o decreases and changes sign giving negative ice-ocean torque for increasing $u_{0,ocean}$. In the no-slip case, with the ice velocity bound at both the gyre center and outer radius, increasing $u_{0,ocean}$ is not matched by an increase in u_{ice} and so the ice-ocean stress becomes negative (see top right panel of figure 4.13). This is analogous to the model results of Wang et al. (2019a) whereby a winter ice pack was seen to fix the ice velocity while the geostrophic velocity was unperturbed. Here a reduction in ice velocity occurred over a stable ocean velocity to change the sign of the stress resulting in seasonal

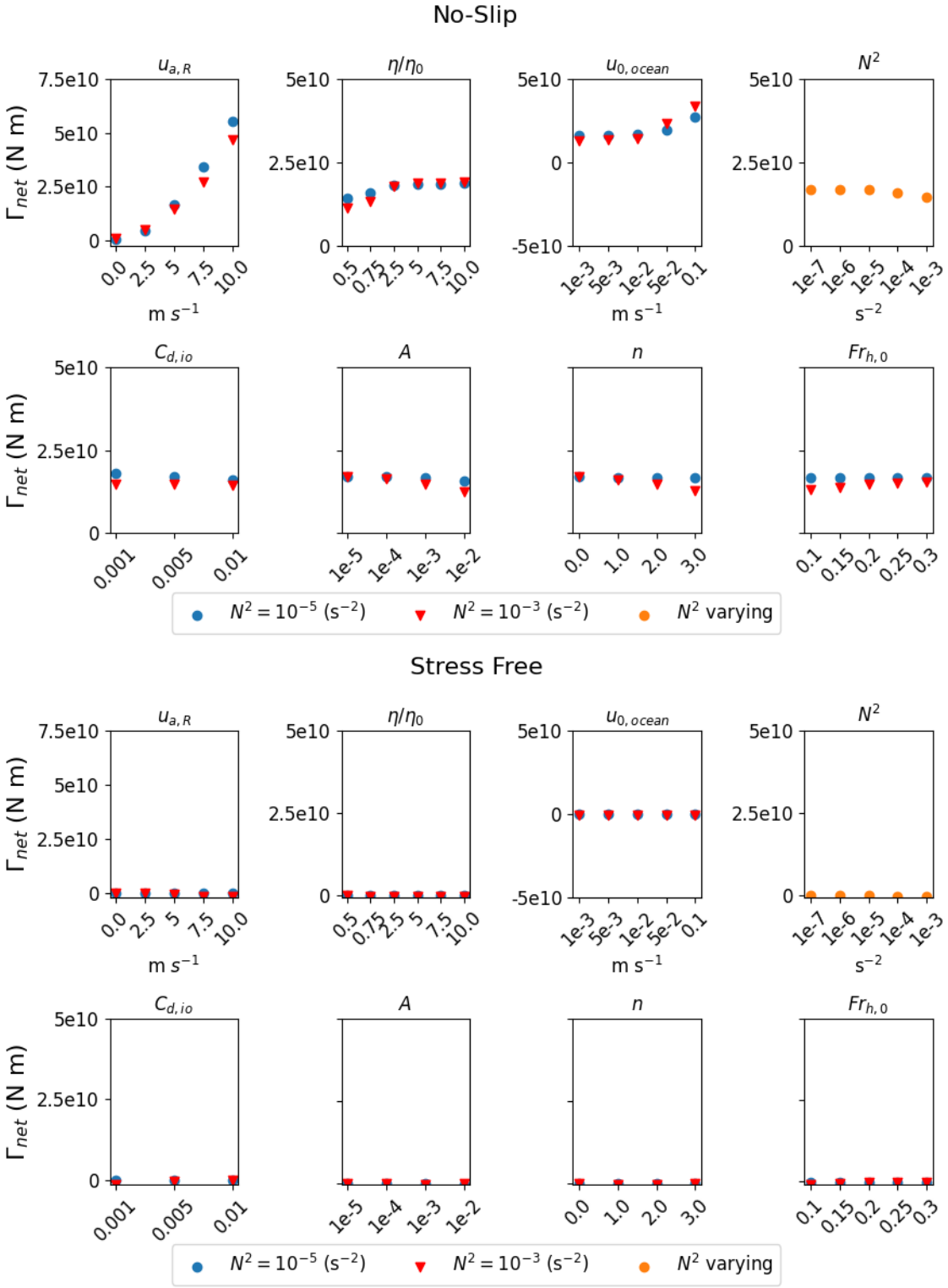


Figure 4.16: Sensitivity of $\Gamma_a - \Gamma_o$ to varying parameter values for the no-slip case (top) and the free slip case (bottom). The stress scale for atmospheric velocity is larger than for the other parameters so as to make sensitivity in the other parameters easier to observe.

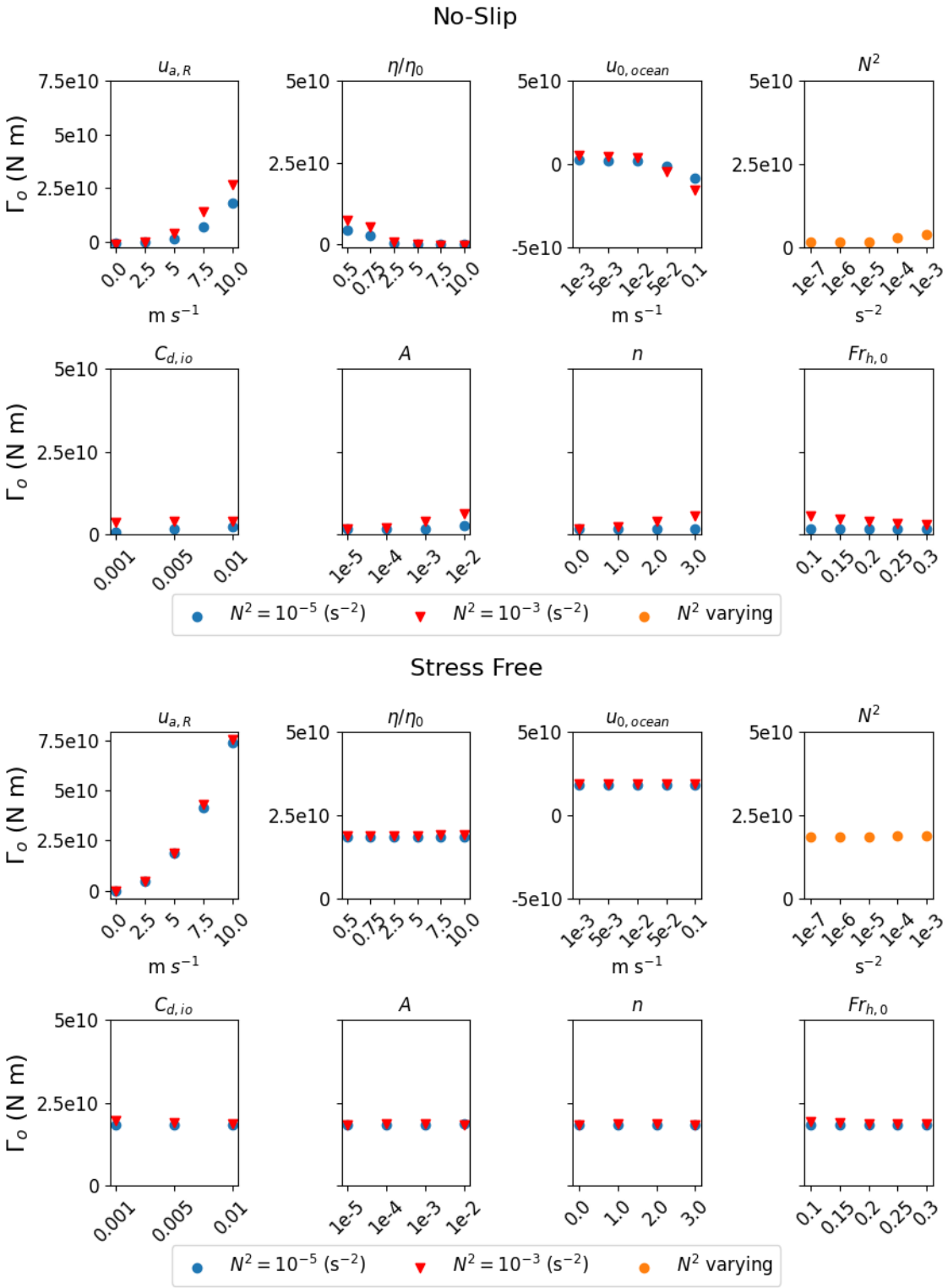


Figure 4.17: Sensitivity of Γ_o to varying parameter values for the no-slip case (top) and the free slip case (bottom). Here the ocean velocity has a negative torque so we also show it on a unique y axis.

upwelling which has been observed as in Meneghello et al. (2018a). Contrary to the case of changing $u_{a,R}$, the strong summer stratification enhanced the variation in Γ_{net} and Γ_o for changing $u_{0,ocean}$.

For the no-slip boundary condition and with the weakly stratified N^2, the torques are insensitive to changes in wave drag, though a decrease in Γ_{net} is seen for increasing $C_{d,io}$ corresponding to increased ice-ocean torque. In the case with increased stratification strength, changes in the wave drag parameters A, n, and $Fr_{h,0}$ provide modest changes in Γ_{net}. For each of these parameters, an increase in the strength of the wave drag appears to increase the transmission of atmospheric torque to the ocean. This is seen as a decrease in Γ_{net} compared to the weakly stratified case for increasing A (maximum reduction of -20%) and n (maximum reduction of-25%) and for decreasing $Fr_{h.0}$ (maximum reduction of -20%). This suggest that an increased ice-ocean drag in regimes of strong stratification result in more efficient transfer of atmospheric stress to the ice-ocean boundary for fixed profiles of $u_{a,R}$ and $u_{0,ocean}$.

A sensitivity comparable to changes in the wave drag parameters is observed for the shear viscosity, η, for which we plot the ice velocities for both stratifications in figure 4.18. With increasing viscosity, the net torque increases by giving the expected result that weaker sea ice is more readily able to transmit atmospheric stress to the ocean (Dewey et al., 2018). This also suggests a reduced role of thinner (weaker) ice in modulating the oceanic response to atmospheric forcing. With a strong stratification this response appeared muted with a reduction in the ice velocity observed. It is possible that with reduced viscosity, a reduction in the seasonal Ekman upwelling could occur due to increased ice mobility as predicted in (Wang et al., 2019a).

We initially sought to characterize the behaviour of lower values of the shear viscosity, η, however numerical issues arose if η was too small. In the no-slip case, this is potentially explained by the thinning of the viscous boundary layer as $r \to R$ as observed earlier in the linear model in figure 4.8. This can also be seen in the model with quadratic ocean drag as shown in figure 4.18 where reductions in η cause the peak velocity location to grow in amplitude and move closer to the gyre edge, in qualitative agreement with the linear result in figure 4.8.

The surface ice-ocean stress field predicted by the rheological model would drive changes in the lateral Ekman transport and thus changes in the gyre freshwater content. This in turn, will drive changes in the isopycnal slope/depth as in §4.4.1. We investigate the predicted isopycnal curves from our simulations with varying Υ by imposing the calculated ice-ocean stresses shown in figure 4.11 and solving (4.23). This approach is not yet fully coupled, as the ocean velocity assumed for calculating

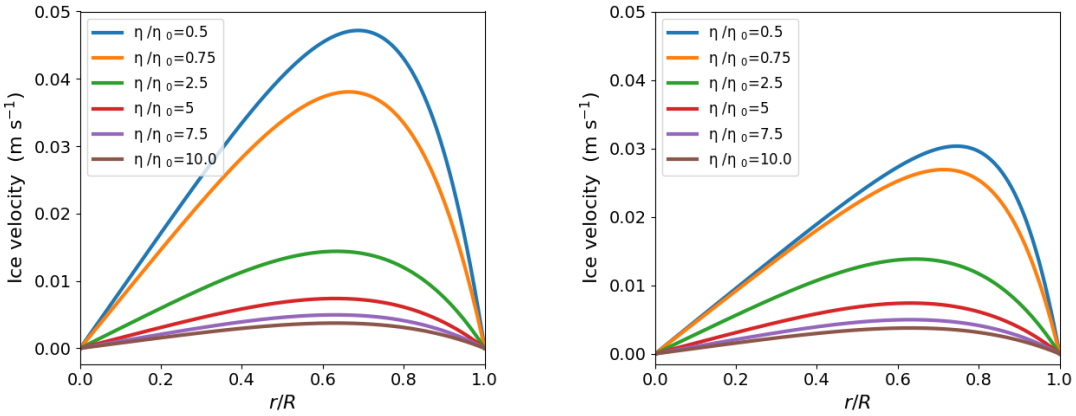


Figure 4.18: Profiles of ice-ocean velocity for $N^2 = 10^{-5}$(left) and $N^2 = 10^{-3}$ (right) for varying viscosity with no-slip boundary conditions. With decreasing ice viscosity, the peak ice velocity shifts outward to the gyre edge of $r = R$ indicative of a viscous boundary layer.

ice velocity will not in general equal the geostrophic velocity for the isopycnal slope. Additionally, the profiles from figure 4.13 predict negative ice ocean stress near to the gyre edge, which physically corresponds to outward Ekman flow. The construction of the TEM theory assumes inward Ekman flow drives freshwater accumulation and the depression of isopycnals in the gyre interior, which is compensated by baroclinic eddy driven flow to achieve a steady state. However, this balance breaks down with outward Ekman flow, which simply exports freshwater from the domain rather than the freshwater accumulation and eddy compensation in the gyre centre. Hence the current TEM formulation is no longer appropriate in the regions of negative ice ocean stress. A full physical resolution of this issue would need a time dependent model, but for simplicity we here set the isopycnal slope to zero in regions of negative ice-ocean stress. This effectively moves the gyre edge inward to the region of positive ice-ocean stress, with the freshwater halocline matching the mixed-layer depth outside this. The isopycnal curves calculated from the stress profiles of figure 4.13 for varying Υ are shown in the top row of 4.19 for each stratification profile.

From these isopycnal curves, if we assume a level of no motion below the specified isopycnal (similar to a reduced gravity model) the azimuthal component of the geostrophic flow can be approximated by

$$u_{\theta,geo}(r) = \frac{g'}{f}\frac{\partial h}{\partial r} \tag{4.56}$$

where g' is the reduced gravity across the isopycnal and we here use the value for the halocline from Doddridge et al. (2019) of $g' = 6.22 \times 10^{-2}$. Using the isopycnal curves

of figure 4.19 we can then calculate geostrophic velocities for these profiles as shown in figure 4.19.

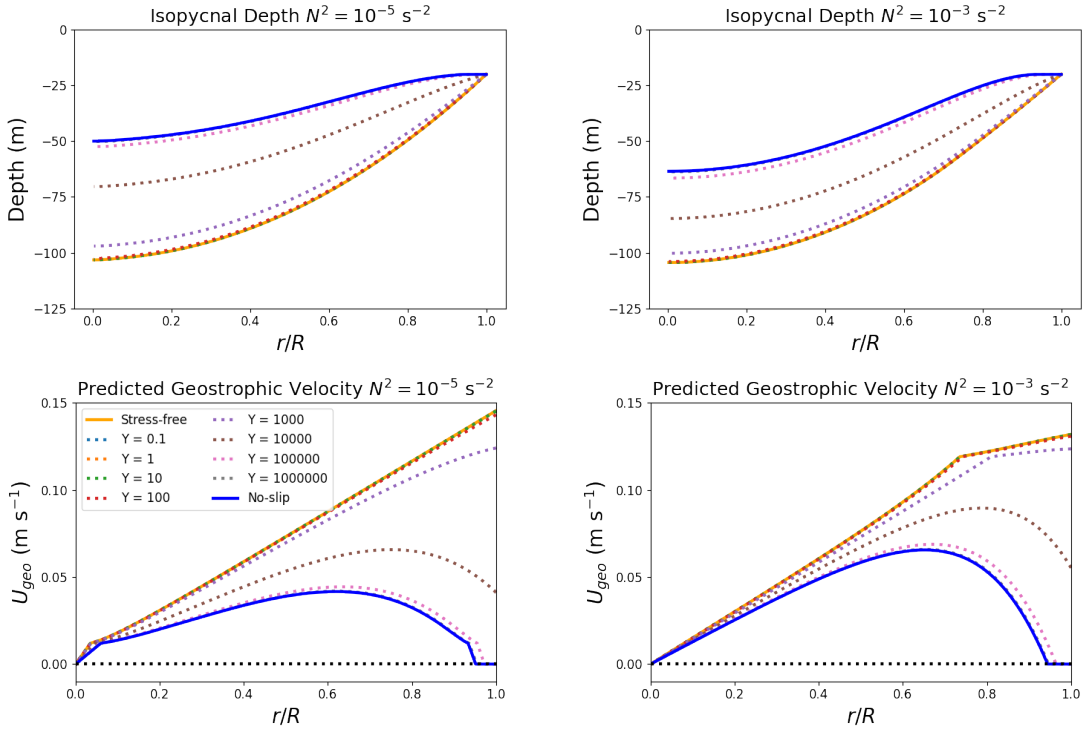


Figure 4.19: Isopycnal depth (top row) and geostrophic velocities (bottom row) calculated for the no-slip (blue solid line) and free-slip (orange solid line) conditions as well as a selection of Υ (m s^{-1}) with $N^2 = 10^{-5}$ s^{-2} (left column) and $N^2 = 10^{-3}$ s^{-2} (right column). Isopycnal depth was calculated by taking the calculated stress profiles from the rheology model and using (4.23) but with dz/dr set to zero in regions of negative ice-ocean stress (see main text). Geostrophic velocities calculated using (4.56) and the isopycnal profiles from the top panel of each column.

The no-slip case most closely resembles the sin profile of figure 4.6 in shape, with the other profiles resembling the standard linear case. The no-slip case is noticeably shallower than the calculations with $10^6 \lesssim \Upsilon$ which can be seen to be predicted from the patterns of ice-ocean torque in figure 4.15 where small Υ corresponded with low internal stresses and nearly all of the torque being transmitted to the ocean. As Υ increases and we approach the no-slip limit, the ice internal stresses rise dramatically and only a small amount of the imposed air-ice torque is transmitted to the ice-ocean boundary.

The isopycnal curves calculated from the ice stresses of figure 4.13 shown in the top row of figure 4.19 are largely similar in structure for the two different stratifications, with an increase in the isopycnal depth seen for larger N^2 and large Υ.

For the isopycnals calculated from the no-slip case, a slightly increased region of minimum permissible depth, determined by the initial depth z_0, is seen at $r/R \approx 0.8$ for $N^2 = 10^-3$ in the top right plot of figure 4.19. This can be seen slightly more clearly in the point at which the calculated geostrophic velocity is 0 in the second row of figures, though it is small. Furthermore, as we decrease Υ, the isopycnal depth deepens and the geostrophic velocity becomes linear a small distance away from the origin. This boundary for $r \approx 0$ is set by the increased drag arising from the wave drag effects seen in figure 4.12 and is seen for all Υ in the weakly stratified case. In contrast with the small Υ behaviour, as $\Upsilon \to \infty$, the geostrophic velocity increases with r until $r \approx 0.6$ and then decreases to 0 with the maximum geostrophic velocity only approximately 1/3 of the stress-free case. For the strong stratification of $N^2 = 10^{-5}$ s^{-2}, the wave drag for the no-slip case is saturated as seen in figure 4.12 so the features resulting from changing drag coefficient are absent. As $\Upsilon \to 0$, the geostrophic velocity adjust to the stress-free limit with a transition period between $10,000\text{m s}^{-1} < \Upsilon < 1,000\text{m s}^{-1}$ where the wave drag is no longer constant throughout the domain. This feature was illustrated earlier as in the stress free case by the wave drag variation shown in the left panel of figure 4.12.

In some of these cases such as the no-slip case, and $\Upsilon \geq 10,000\text{m s}^{-2}$, the resulting geostrophic velocity differs significantly from the prescribed linear ocean velocity. If this new ocean velocity were to be fed back into the model, a further change to the stress, and therefore the gyre structure, may occur. An initial attempt to fully couple these models was made, but convergence issues were encountered. These results are covered as part of an appendix to this section §4.A.

4.6 Summary

In this chapter, a hierarchy of models was developed to examine the potential impacts of internal wave drag on the liquid freshwater content and vertical structure of the Beaufort Gyre. In the ocean model developed in §4.3 and the sea ice rheology model of §4.5, we examined the individual sensitivities of the ocean and ice to a parameterization for internal wave drag. We found that varying drag coefficients due to sea ice generation of internal waves can have a significant impact on isopycnal depths and ice velocity in regimes where the Froude number $Fr_h \lesssim 1$ over a significant part of the domain. We note that in this chapter we specifically examined the role of internal waves on modifying the ice-ocean drag coefficient and thereby altering the gyre state.

However in the geophysical setting, the ice-ocean drag coefficient (as well as the air-ice drag coefficient) vary spatially and temporally due to a number of processes (as in Tsamados et al., 2014). The results of this work are thus indicative of the potential need to better account for variable ice-ocean drag in general in order to accurately characterize the mechanics of the Beaufort Gyre.

For the first model of this chapter, in §4.3, we modified the idealized model of the Beaufort Gyre presented in Manucharyan and Spall (2016) to incorporate the effects of the variable ice-ocean drag coefficient derived in chapter 3. This transformed Eulerian mean model characterizes the Beaufort Gyre as a balance between lateral Ekman inflow at the surface, and baroclinic eddy induced outflow at depth. In §4.4, we modified the Ekman transport by introducing a power law relationship for the internal wave drag as $C_d = C_{d,io} + A\,[u_{rel}/Nh]^n$ and utilizing this drag coefficient in a quadratic stress relationship for the ocean surface stress.

Using this, we investigated the sensitivity of the halocline depth to the exponent of the wave drag relationship, n. Here we observed modest changes (13%-3%) in the predicted freshwater content of the Beaufort Gyre for $-3 < n < -1$. Using the average Beaufort Gyre liquid freshwater content from Haine et al. (2015), this implies potential changes in freshwater content of approximately 705km^3 to 3055 km^3. The primary driver of this change in isopycnal volume was seen to arise from changes to the ice-ocean drag coefficients by an order of magnitude (see figure 4.5) which amplifies the surface stress and inward Ekman transport. To build insight into cases where the ice experiences a net balance between atmosphere and ocean torques, we examined the setting where the total ice-ocean torque was held fixed, but the value of the drag coefficient was allowed to vary changing the spatial distribution of ice-ocean stress. In this torque normalized picture, the observed change in the freshwater content was small and $< 1\%$ for all values of n tested. Although the freshwater content proved insensitive to the wave drag changes, we still observed varying isopycnal depths and thus varying isopycnal slopes across the gyre radius. In the geophysical system, changes to the spatial structure of the isopycnal slope would drive changes in both the geostrophic velocity as well as the eddy induced flow at depth. Hence, while the overall gyre freshwater content may be insensitive to the wave drag parameterization, local rates of freshwater import and export and eddy-driven mixing may show variation due to enhanced wave drag. The model used in §4.4 however, does not directly resolve this oceanic response, to varying ice-ocean drag, because it neglects the feedback on the geostrophic velocity.

To examine the importance of the form of the ice-ocean relative velocity used in this model, we compared the linear relative velocity of (4.28) with a torque normalized version of the sinusoidal profile (4.29). Physically, these two velocity profiles can be seen as the geophysical case of ice in free drift (because viscous ice stresses are identically zero for a solid body rotation), or ice experiencing significant stress at the gyre edge. Comparing model configurations using both velocity profiles we observed a change in liquid freshwater content of 14% for $n = -2$.

Each of the model implementations so far assumed a relatively weak stratification of $N^2 = 10^{-5}$ s^{-2}. However the work of chapter 3 where the wave drag was established had a much stronger summer stratification of $O(10^{-3})$. To capture the effects of seasonal variations in stratification we examined the sensitivity of the model to uncertainty in the parameter choices for two values of N^2.

The impact of ocean stratification was considered for cases representative of winter ($N^2 = 10^{-5}$ s^{-2}) and summer ($N^2 = 10^{-3}$ s^{-2}) stratification. Here it was found that without normalization of the torque, strong stratification significantly amplified the effects of wave drag because it allowed the ice-ocean velocity to attain Froude numbers of order $Fr \lesssim 1$. Notably, in a sensitivity study the magnitude of changes from wave drag parameters in the strong stratification were comparable to leading order sensitivities from $u_{0,rel}$ and the eddy efficiency parameter k. The substantial sensitivity to the ice-ocean relative velocity of this model is in agreement with the established importance of ocean currents on the gyre structure (Meneghello et al., 2018b,a, 2020; Doddridge et al., 2019; Wang et al., 2019a). Similarly, the strong sensitivity to changing eddy parameterization illustrates the importance of eddy effects as discussed in Manucharyan and Spall (2016). In the present model both of these responses have been simplified. For example, recent studies have proposed that the influence of depth-dependent eddy diffusivity could be important for accurate characterization of the isopycnal slope with depth (Kenigson et al., 2021). To characterize the halocline via a single isopycnal curve we have assumed that the eddy diffusivity is depth independent and so isopycnals are parallel throughout the halocline. Similarly, by prescribing a relative velocity we have artificially fixed the response of the ice and ocean velocities, which in reality would adjust so that the ocean velocity is given by a geostrophic balance from the isopycnal slope and the ice velocity is in dynamical balance.

I built upon the results of the ocean model by investigating the ice response thus providing complimentary insight to the body of work studying the effects of geostrophic velocity in the Beaufort Gyre (Meneghello et al., 2018b,a, 2020; Dewey

et al., 2018; Doddridge et al., 2019). Here I applied a simplified viscous sea ice rheology in §4.5 to an axisymmetric model of ice flow. The primary advantage of this approach compared to a more detailed regional climate model is in the ability to investigate the role of specific processes. A disadvantage is that we neglect some of the geophysical and rheological complexity, such as plastic deformation.

A key component of this model was the choice of boundary condition at the gyre radius. Here we assumed a linear dependence between viscous stress and ice velocity, corresponding to a variable slip condition with slip parameter Υ. The limit $\Upsilon \to 0$ leads to a stress-free or free-slip boundary condition, while $\Upsilon \to \infty$, corresponds to a no-slip regime with $u = 0$ at the outer boundary. These can be seen to represent the geophysical setting whereby ice at the gyre edge is in free drift for the free slip case, or where the ice pack surrounding the gyre exhibits substantial stress at the outer edge of the gyre and so fixes the velocity (such as landfast ice).

In 4.5.1, we derived an analytical solution, (4.53) for a simplified case of (4.36) by assuming linear dependence of the atmosphere and ocean stress on relative velocities as well as linear radial variation of the atmospheric and oceanic velocities. The analytical solution (4.53) demonstrated that reduced ice viscosity yields a narrower boundary layer at the gyre edge, and enhanced ice velocity throughout the domain. These results are qualitatively reminiscent of the model study of Wang et al. (2019a) which found that a reduction of sea ice strength resulted in increased momentum transfer from the atmosphere through the ice. In the stress free case, the influence of viscosity disappeared with the ice velocity only depending linearly on the ocean and atmospheric velocity, yielding a state of solid body rotation.

For stress relations that vary quadratically with velocity numerical solutions of (4.36) were developed using a continuation method. We examined the same two stratification cases as in the previous work: a weakly stratified case with $N^2 = 10^{-5}$ s^{-2} and a 'summer stratification' case motivated by the scales of chapter 3 with $N^2 = 10^{-3}$ s^{-2}. For both of these cases we examined the free-slip and no-slip limits. It was found that the wave drag parameterization only demonstrated any significant effects for the strong stratification cases. In the free-slip case with wave drag, the ice still exhibited solid body rotation, but with slower ice velocity than the constant drag case. This is due to variation of the drag coefficient, which also leads to variation of the ice-ocean stress. Stress started off approximately quadratic as in the constant drag case, but with Fr_h decreasing below the threshold, $Fr_{h,0}$, near the gyre edge. As a result, the ice-ocean drag coefficient began to decrease quadratically with u_{rel}. This quadratic decrease of the drag coefficient along with a quadratic increase in stress

with u_{rel} resulted in a transition to a linearly increasing ice-ocean stress as $r \to R$ (see figures 4.11 and 4.24). The no-slip case exhibited a maximally increased drag coefficient throughout the domain ($Fr_h < Fr_{h,0}\ \forall r \leq R$). The resulting profile of ice velocity saw a reduction in the peak ice velocity by approximately 1/3, though with the ice-ocean stress increased by approximately a factor of 3 due to the increased value of C_d from 5.5×10^{-3}, to $\approx 3 \times 10^{-2}$.

A similar examination of the ice velocity and ice-ocean stress was conducted for the partial slip condition with $0\text{m s}^{-1} < \Upsilon < 10^7\text{m s}^{-1}$ for both stratification cases. For the weakly stratified case, no signs of wave drag impact were observed with the partial slip condition appearing to quite cleanly transition from the stress-free to no slip limit over the range $10^3\text{m s}^{-1} < \Upsilon < 10^7\text{m s}^{-1}$. In the no slip limit, slight negative stress at the gyre edge was observed, which implies outward Ekman pumping at the edge of the gyre.

For varying Υ, with the wave drag implementation, we observed increased negative stress at the gyre edge for large Υ. During the transition $10^3\text{m s}^{-1} < \Upsilon < 10^7\text{m s}^{-1}$ we observed that as Υ decreased, the transition below the maximal Froude number ($Fr_h < Fr_{h,0}$) was able to occur within the domain for $\Upsilon \leq 10^4\text{m s}^{-1}$. The exact value of when this phenomena occurs was not calculated but can be seen to be between $10^4\text{m s}^{-1} < \Upsilon < 10^5\text{m s}^{-1}$. When this transition occurs, the ice-ocean stress changes from a quadratic to a linear increase with r.

Examining the net and ice-ocean torques arising from varying the boundary friction coefficient Υ (figure 4.13) we found a shift from a regime with full transmission of the atmospheric torque to the ocean surface to one where sea ice internal stresses were significant and reduced the momentum transfer from the atmosphere to the ocean. Comparing the weakly stratified case with the strong summer stratification we observed that with larger N^2 there was increased transmission of atmospheric torque to the ocean surface for large Υ. Increased surface stratification enhances the ice-ocean surface stress and also increases the lateral Ekman transport into the gyre.

Similar to §4.3, we examined the sensitivity of the model to the choice of parameters (figures 4.16 and 4.17). In the no-slip case, increasing the stratification was seen to increase the effects of the wave drag, resulting in increased momentum transfer through the ice cover (reflected as a reduced Γ_{net}). Increasing the ocean velocity resulted in increased ice internal stresses for each case, and was similarly amplified in the strongly stratified scenario. In the stress free case, the net torque was approximately zero in every case, corresponding to no ice internal stress and so the atmospheric torque is transferred directly to the ocean.

We then sought to crudely couple the ice and ocean system by applying the surface stresses output by the ice-only model, to the previous ocean model. In this picture we found that the increased stratification gave rise to deeper isopycnals with a stronger geostrophic velocity. The geostrophic velocities calculated far exceeded the ocean velocity used for this model. This indicates that the geostrophic velocity would respond to this increased stress via an acceleration of the ocean which would decrease the stress and hence the isopycnal depth. This would be consistent with the physics of the ice-ocean governor mechanism Meneghello et al. (2018b).

It was found that in both the ocean-only and the ice-only models that the inclusion of wave drag, in regimes of strong stratification, significantly impacted the gyre structure. In the ocean only model of §4.4 we found that the addition of wave drag, strongly affected the predicted gyre freshwater content. Within the ice-only model, it was shown that wave drag effects could generate modest ($\approx 20\%$) changes in the ice-ocean torque in the gyre compared to model runs with a constant drag treatment with potential implications for the seasonal variability of Ekman upwelling in the gyre. Applying the predicted stress to the ocean only model to approximate an ocean response, we found that the inclusion of wave drag increased the response of the ocean via increased isopycnal depth in the no-slip limit. This increased isopycnal depth also manifested as an increased geostrophic velocity compared to the constant drag configuration potentially suggesting that spatial variations in the drag coefficient may have appreciable effects on the typical response of the ice-ocean governor.

The ice model developed here neglected several processes and made a number of assumptions: ocean geostrophic velocities, assumption of an axisymmetric gyre, a viscous rheology, constant ice thickness and roughness, and a fixed upper ocean stratification. In the real-world system, the spin up of geostrophic velocity may dampen the increased stress resulting from the modified wave drag parameterizations. However, this reduction in stress is a result of a reduction in the ice-ocean velocity, which would also enhance the role of the modified wave drag in the gyre and possibly offset the above effect. The neglect of spatial variations in azimuthal gyre structure, N^2, and imposed ice stresses at the gyre edge prevents a direct quantitative application of this model as the Beaufort Gyre exhibits azimuthal variation between coastal regions and the central Arctic. However, the model is still useful for developing conceptual insight. The sensitivities determined here still serve to inform potential qualitative impacts of wave drag specifically and more broadly variations in drag coefficients arising from a number of effects. One such case is modification of form drag due to sea ice roughness. The treatment of rheology was simplistic to aid tractability

whilst capturing the basic effect of transmission of lateral stresses. In our model we neglected plastic deformation or any adjustment to the sea ice thickness distribution. In plastic yielding regions the stress state stays at the yield criteria, implying uniform transmission of ice stresses in the yielded region. This would somewhat modify the variation of shear in ice velocity across the gyre, although is still likely to lead to significant stress accommodation by the ice, and might be interesting to include in future work. Notably Rallabandi et al. (2017) observed that viscous shear layers are needed to satisfy no slip or frictional boundary conditions, so some aspects of the viscous rheology considered here are also likely to be relevant for calculating ice stresses at the gyre edge. Given spatial variations in ice roughness or say variations in ice coverage of the ocean between MYI and FYI, one might setup gradients in the ice-ocean drag coefficient and thus the surface stress not dissimilar to the process just examined here for internal wave drag. The observed significant impact of ice boundary effects and the rheological response on the ice-ocean drag in the idealised model suggests these extra effects could also have a prominent role.

The results of these two standalone models motivated an attempted coupling outlined in §4.A. Unfortunately this coupled model demonstrated poor convergence for cases where the drag coefficient was significantly modified by wave drag effects. An oscillation between states was observed which triggered a limitation of the TEM model applied here. Namely, that this formulation was unable to treat negative stress in the steady state formulation.

A natural further development of this problem would be to use the key insights here within the confines of a time dependent model. The key limitations found were that of the ocean response to the changing ice-surface stress. This ocean response via geostrophic velocity is well established and a key feature of the system. The attempt at a simplistic coupling outlined in §4.A suggested the importance of this time dependent response in the wave drag case. Drawing on the primary conclusions of §4.3, and §4.5, a future approach for the time dependent system would be able to outline the role of wave drag in gyre state and variability. A possible pilot of these results for regional models would be to examine the sensitivity of the Beaufort Gyre to the chosen ice-ocean drag coefficient. In regional scale models focusing on sea ice, the drag coefficient is often treated as a constant with the canonical value of $C_{d,io} = 5.5 \times 10^{-3}$. It is straightforward to propose that the variation seen in this value within this chapter could alter surface gradients of ice-ocean stress thereby affecting the strength and pattern of lateral Ekman transport which is the fundamental process for setting the Beaufort gyre state.

4.A Coupled ice-ocean model

With an ocean model developed in §4.4 and an ice model in §4.5 we now seek to couple these models to produce radial profiles of ice-ocean stress, ice and ocean velocities, and isopycnal depth at an equilibrium state. We first overview the algorithm used to couple these models in §4.A.1 and discuss a number of model runs in §4.A.2.

4.A.1 Description of coupled model Algorithm

The TEM model of §4.4 requires a surface stress, or relative velocity to calculate isopycnal depth. From this isopycnal depth, a geostrophic velocity can be calculated. Our Rheological model developed in §4.5 requires ocean velocity and atmospheric velocity to calculate ice stress. We could apply these models in an iterative fashion whereby an initial guess of an isopycnal depth is given to determine ocean velocity which is then used in the rheology model to determine a resulting ice stress, and then applied back to the ocean to derive a new isopycnal shape. As we are currently neglecting the time dependence of the system in both the ocean and rheology models this approach only has the ability to provide qualitative insight regarding effects of specific isopycnal profiles. We instead here seek to determine an equilibrium state of the gyre using these two models. We can determine an equilibrium state of the ice-ocean system with a prescribed atmospheric wind stress by finding a state where iterative application of these models yields little or no change in the isopycnal depth. The algorithm design is shown in the flow chart of figure 4.20.

The algorithm is initialized using an isopycnal profile with an ocean velocity that is linear in r as in (4.26). Using this profile a new ocean velocity is calculated from (4.56), which is then used in the continuation method outlined in figure 4.10 to determine the ice velocity. A relative velocity is then calculated using these ice and ocean velocities. Next, this relative velocity is used in (4.26) to calculate a new isopycnal curve. The RMS deviation between the initial and final isopycnal profiles are calculated at 20 evenly spaced points in the domain. The numerical solver thus alters the polynomial coefficients used to represent the isopycnal domain in an attempt to minimize this RMS deviation.

Coupling these models is thus an optimization problem where the difference in isopycnal depth after one iteration is the metric for minimization. Within the algorithm, the approximation of isopycnal curves by polynomials enabled increased computational efficiency for the calculation of the geostrophic velocity as opposed to

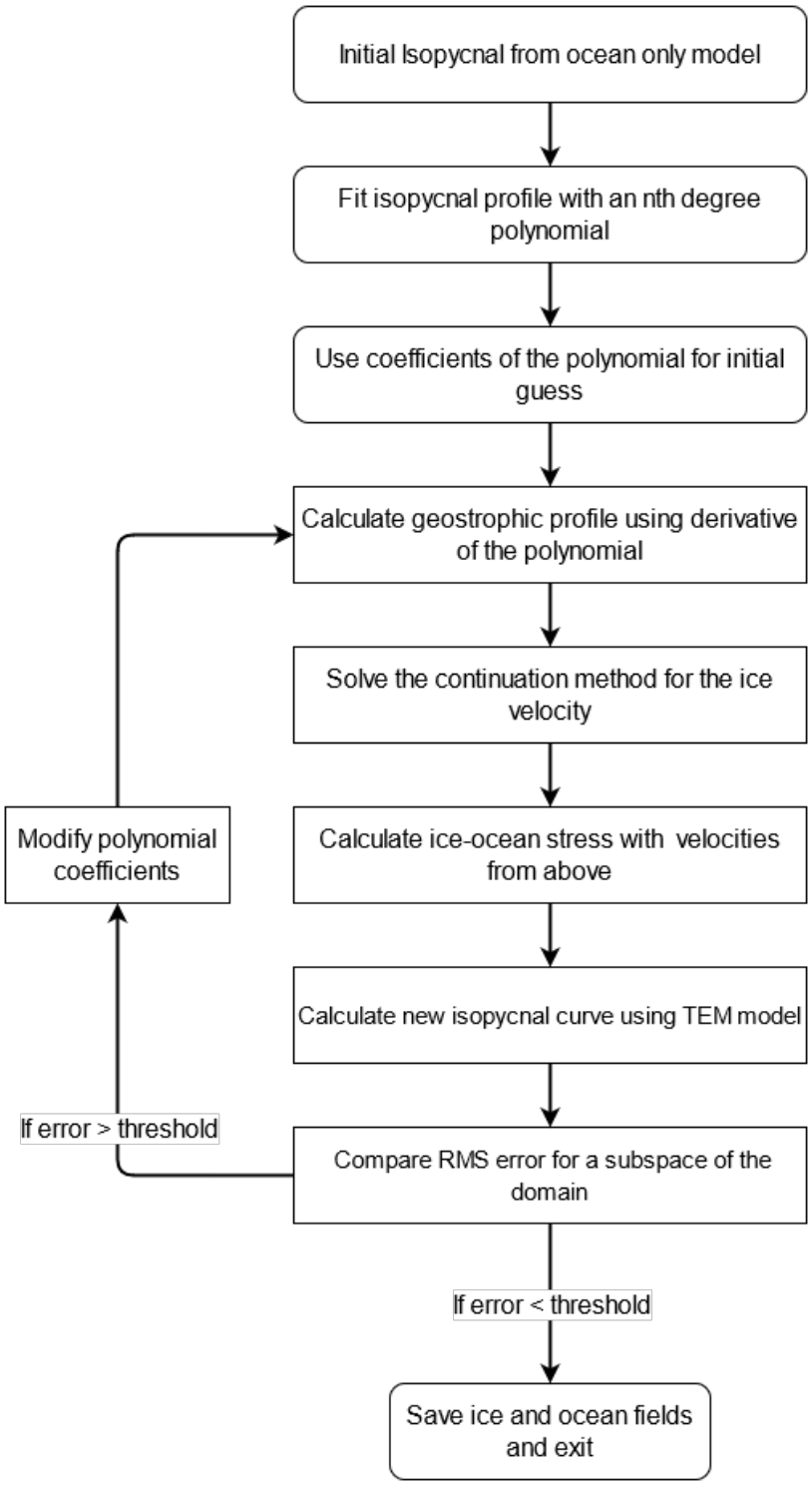


Figure 4.20: Description of the coupled model algorithm used to determine an equilibrium state of the gyre. This algorithm serves as a wrapper around the continuation method illustrated in figure 4.10 to determine an equilibrium gyre state.

calculating the full numerical derivative across the domain each iteration. Furthermore, the numerical solver used, fmin from the scipy.optimize package for Python 3 (here we used the default values for xtol=ftol=$1e-4$), requires variables to adjust in order to adjust the gyre state. The use of a polynomial to specify the isopycnal shape provided a computationally feasible parameter space for a solver to iterate through. For this test case we set the degree of the polynomial be 7. A drawback of this approach is slight error introduced due to the turns in the polynomial resultant from the many inflection points. Any concavity in the isopycnal guess propagates to the geostrophic velocities and so on to every other field. In our system we seek to provide qualitative insight into the potential importance of wave drag on the Beaufort Gyre structure, not quantitative predictions of changes in freshwater content.

4.A.2 Coupled ice-ocean model results.

Using the method of coupling just established we here present a test case for both the stress free and no-slip boundary conditions, with and without wave drag. In this section we examine a model configuration using the weak stratification profile of $N^2 = 10^{-5}\ \mathrm{s}^{-2}$. In §4.5.6 we saw that this stratification corresponds to a regime where wave drag is not a major influence on the system because the Froude number U/Nh was relatively large for the given ocean velocity profile. We evaluate whether this conclusion is robust when the ocean velocity varies in response to the ocean stress.

Before examining results we note that for the geostrophic velocity shown, some anomalies arise as a result of the polynomial fit of the isopycnal used. As mentioned in §4.A.1 (figure 4.20), the use of a polynomial allows a numerical optimization algorithm to vary a modest number of parameters to determine an equilibrium shape of the isopycnal. Unfortunately this produces characteristic undulations of polynomial fits which may be non physical. Additionally, this error is propagated through the system as the geostrophic velocity, relative velocity, and ice-ocean stress are calculated using the derivative of the polynomial fit. Hence the results should be interpreted with caution, and aim to provide some initial qualitative insights rather than quantitative predictions. The initial results of the coupled model runs for these configurations is shown in figure 4.21.

For the stress free case shown in the right column of figure 4.21, we observe that both of the configurations with constant drag coefficient, and with the wave drag parameterization yield essentially the same results for each field. A small exception is at $r/R \approx 0$ where each field besides the ice velocity see small differences near $r/R = 0$. In the ice-velocity, a small deviation is observed at $r/R = 1$. These slight

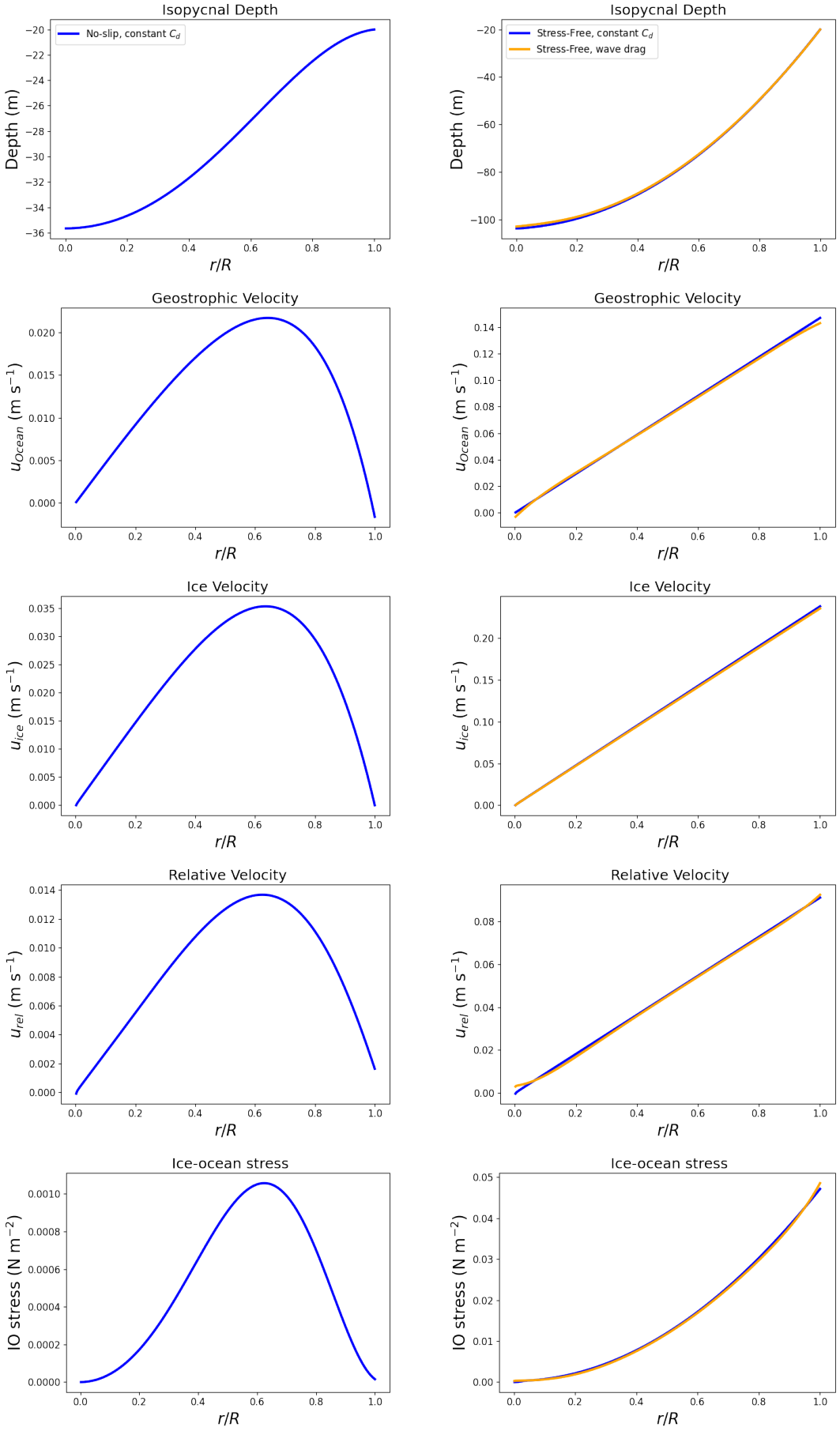


Figure 4.21: Coupled model runs for No-slip (left) and stress-free (right) boundary conditions. In each panel we compare model output with constant drag coefficient (blue) and our wave drag parameterization (orange). For the no-slip case, the wave drag model was unable to converged and is discussed in the text and in figure 4.22.

deviations are likely due to small errors resulting from the use of a polynomial to fit the isopycnal as discussed above. Despite this small error, the solutions recreate the relationship seen in the stress free case for small N shown in the ice-rheology model §4.5.6, indicating negligible impact of the wave drag.

In the no-slip case shown in the left column of figure 4.21, only the constant drag case was able to converge. It was found that within the model, the numerical optimization scheme oscillated between two states. This variability is illustrated in figure 4.22 by plotting the final returned isopycnal and velocity states at termination, alongside the state by taking the isopycnal given and using it as an initial condition for a single iteration of the scheme diagrammed in figure 4.20. Subsequent iterations continue to oscillate, to good approximation, between the two states. An average of the two states was also used as a new guess, but the system quickly diverged back to these states (not shown). Model configurations with increased wind speed and varied Υ were also attempted, with no convergence obtained. Runs with no-slip boundary conditions tended towards oscillatory states with larger variation between the observed states for larger wind speed.

A potential reason for this oscillation of the iteration is that there is actually no steady state and the system is instead implicitly time dependent. This could further be exacerbated by variations in the drag coefficient in response to changing ice-ocean relative velocity. In the 'second state' of the model (green curve of figure 4.22), the ice-ocean stress is negative at the gyre center and outer edge. As discussed previously, negative stress results in outward Ekman pumping. This may lead to implicitly time dependent dynamics, as there is no longer a steady balance between inward Ekman flow, isopycnal downwelling, and outward eddy driven transport from isopycnal slumping. This was numerically represented by a region of 0 isopycnal slope. A future approach using the ice and ocean models here developed would be to examine the time dependent case which may allow for transient adjustment not possible here.

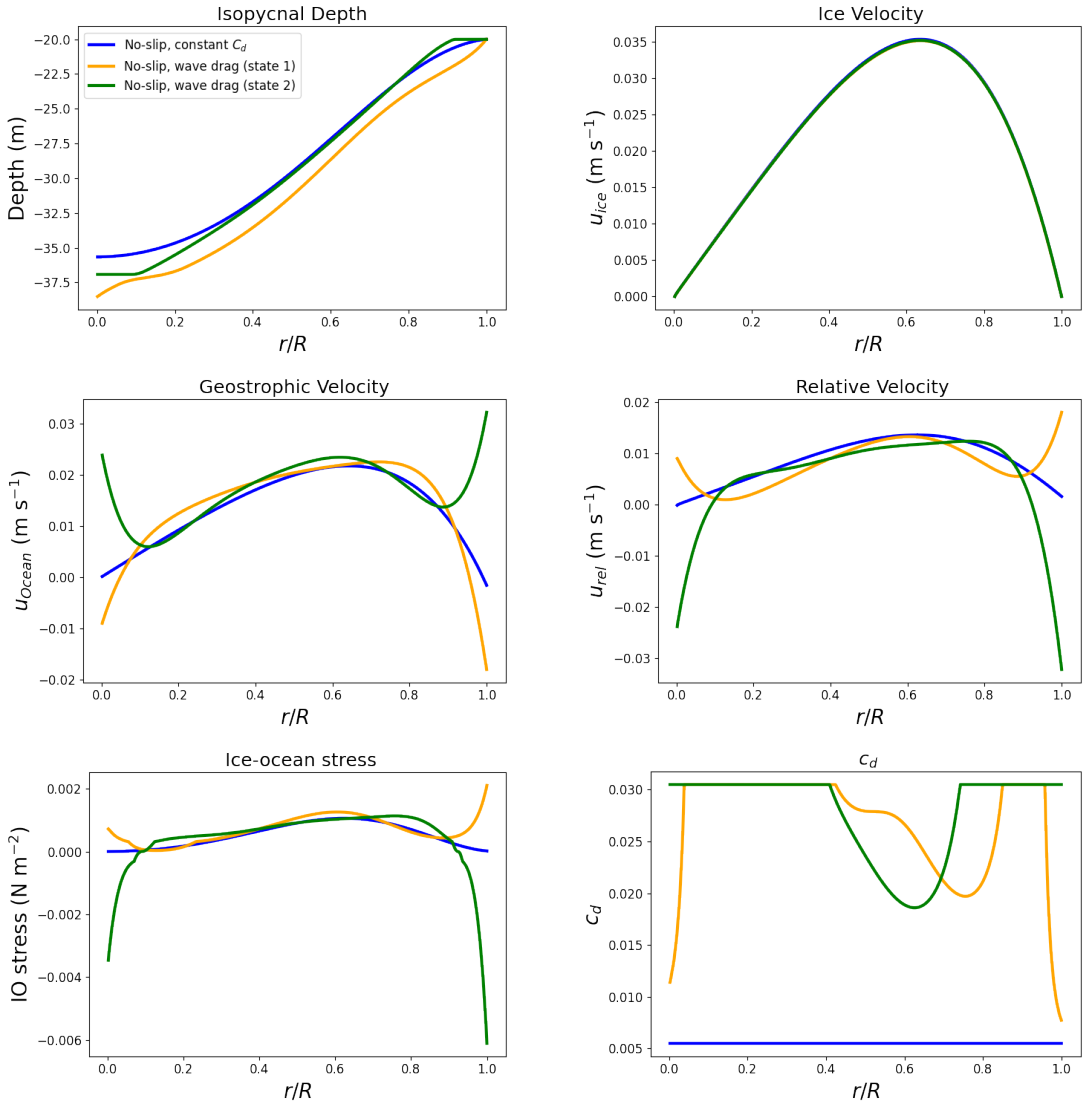


Figure 4.22: Coupled model output for the no-slip boundary condition of figure 4.21 with constant drag (blue) and then the oscillating states of the wave drag configuration (orange, green).

Chapter 5

Seasonal evolution of upper ocean water masses in the Antarctic seasonal ice zone

The content of this chapter is the product of work initiated while a Fulbright fellow at the University of Gothenburg, Sweden within the polar gliders group and continued on return to Oxford. The advisors on this work were Dr. Louise Biddle and Dr. Sebastiaan Swart alongside my DPhil supervisor at Oxford, Dr. Andrew Wells. The work borrows ideas developed by Dr. Biddle published in Biddle et al. (2017), of a One-dimensional (1D) mixed layer model. Dr. Swart provided early guidance on the project direction and Dr. Biddle provided guidance on the methodology and model design. The original model developed by Dr. Biddle in MATLAB was used as a starting point for my own model, developed within Python. I further integrated a number of treatments of additional processes for sea ice formation and evolution. All of the analysis was done by me with advisory input from Dr. Swart, Dr. Biddle, and Dr. Marcel Du Plessis at the University of Gothenburg and Dr. Wells of Oxford. I have also written this chapter and accompanying paper draft with feedback provided by Dr. Biddle, Dr. Du Plessis and Dr. Wells.

5.1 Introduction

Since the start of the satellite record, Antarctic winter sea ice extent experienced a period of continual increase (Parkinson and Cavalieri, 2012) until a sudden reversal of this trend in 2014 (Parkinson, 2019) with a 40-year minimum winter ice extent occurring in 2017. The rate of decrease in winter ice extent since 2014 far exceeds rates seen in the Arctic (Parkinson, 2019). Neither the positive trend in winter ice

extent, or the recent reversal, have been fully characterized by global climate models (Turner et al., 2013; Roach et al., 2020). These trends in Antarctic sea ice extent occur alongside a substantial seasonal variation in the so-called Seasonal Ice Zone (SIZ).

The SIZ is formally defined as the area between the minimum and maximum seasonal ice limits, plus the region of the adjacent ocean that is significantly affected by sea ice processes (Wadhams, 1986). In the Antarctic, the sea ice extent ranges from around 19 million km^2 at its maximum in September to around 3-4 million km^2 at its minimum in February (Comiso and Nishio, 2008; Parkinson, 2019). This seasonal change in ice cover plays an essential role in global climate via alterations to the surface fluxes in heat, salt, and momentum (Tsamados et al., 2014) as well as water mass transformation (Abernathey et al., 2016). Within this study, we will use a simple 1D ice-ocean model and comparison to ocean observations to examine the role of Ekman pumping and other ice-ocean processes on the evolution of upper ocean water masses in the SIZ.

This chapter will proceed as follows. A brief overview of 1D ocean models and some relevant applications within the ice covered regions is presented in §5.1.1, followed by a description of the water masses that define the Southern Ocean and SIZ structure in §5.1.2. Following this literature review, in §5.2 I present the primary observational data and atmospheric forcing to be used with a discussion of the observed seasonal evolution of the study region in §5.3. I then outline the details of the model used for this study in §5.4. The model results are analyzed in §5.5, followed by an investigation of the model sensitivity to perturbations of the model parameters in §5.5.1. I end the chapter with a summary of key results and implications for future work in §5.6.

5.1.1 1D ocean models

A number of 1D ocean model schemes exist, though all generally fall into one of three categories depending on the implemented vertical mixing scheme: turbulence closure schemes (TC Models) (e.g. McPhee et al., 1987; Kantha and Clayson, 1994; Harcourt, 2015; Mellor and Yamada, 1982), K-profile parameterizations (KPP) (Large et al., 1994; Van Roekel et al., 2018), and bulk mixed layer models (Price et al., 1986; Kraus and Turner, 1967; Gaspar, 1988; Niller, 1977). Turbulence closure scheme models use eddy diffusivities to parameterize small scale turbulence within a mixing layer at the ocean surface. In these models, turbulent fluxes are often treated as local such that turbulent fluxes only exist in the presence of vertical gradients of the mean values (Van Roekel et al., 2018). So-called KPP models expand the ideas of TC models to

allow for non-local influences on the vertical distribution of eddy diffusivities (O'Brien, 1970). Both of these models are slightly more computationally expensive due to the additional calculations needed to determine the turbulent fluxes. In this work, we take the simpler approach provided by bulk mixed layer models.

Bulk mixed layer models are the simplest of the 1D boundary layer parameterizations and treat the surface ocean as a uniform 'slab' with homogeneous water properties (Price et al., 1986; Kraus and Turner, 1967; Gaspar, 1988; Niller, 1977). The physical picture of mixing in the upper ocean boundary layer is much more complicated, but this key simplification makes these models more straightforward to implement as well as computationally more efficient. Typically, these models also neglect turbulent mixing below the mixed layer (Price et al., 1986; Kraus and Turner, 1967). The 1D ocean model scheme used in this study is a hybridization of Price et al. (1986), and Kraus and Turner (1967) as set out in Biddle et al. (2017). For our work we modify the model of Biddle et al. (2017) further to include a more sophisticated treatment of sea ice processes. We outline this model in detail in §5.4 and here instead focus on past applications of these bulk-mixed layer models to the ice-covered oceans.

Though the original formulations of 1D ocean models were targeted at applications for mid-latitudes (Price et al., 1986; Kraus and Turner, 1967), a number of studies have modified these models to study the ice covered regions (Wilson et al., 2019; Petty et al., 2013; Frew et al., 2019; Biddle et al., 2017; Martinson, 1990; Martinson and Iannuzzi, 1998). A primary focus of such models has been an accurate representation of the coupling between the seasonal evolution of ice thickness and mixed layer characteristics (as in Wilson et al., 2019; Martinson, 1990; Martinson and Iannuzzi, 1998).

One of the key studies of one-dimensional models in the ice-covered oceans is that of Martinson (1990) which applied a bulk mixed layer model. In this study a negative feed back between ice growth and entrainment of warm water into the mixed layer was identified of relevance to Antarctic ocean conditions. In the winter, ice formation may drive mixed layer deepening as a result of convective instability arising due to brine rejection (Thomas and Dieckmann, 2010). Depending on the background gradients in temperature, this mixed layer deepening may entrain warm waters at depth which can provide a basal heat flux to the ice, thus suppressing further ice growth. The understanding of this feedback established within Martinson (1990) was applied using the bulk mixed layer model of Price et al. (1986) in Wilson et al. (2019) with a rudimentary sea ice cover in the Weddell Sea. This explained the resilience of

a very weakly density stratified halocline. In Wilson et al. (2019), it was established that strong atmospheric forcing events such as storms, could cause a destabilization of the balance achieved by the heat-entrainment feedback leading to substantial ice melt. This in turn suggests important regional sensitivity to the feedback mechanism established within Martinson (1990).

Petty et al. (2013) adapted the bulk mixed layer model of Kraus and Turner (1967), adding a thermodynamic ice growth scheme to examine the impact of changes in atmospheric forcing on the vertical structure of the Amundsen and Weddell Seas. It was found that regional differences in atmospheric forcings alone could account for the differences in vertical structure. This study was then expanded on by Frew et al. (2019) to examine the role of evolving snow cover on ice for modulating the response of the mixed layer to atmospheric forcings. Biddle et al. (2017) combined the models of Kraus and Turner (1967) and Price et al. (1986) to examine the impact of glacial meltwater on the evolution of water masses in the Amundsen Sea.

These simple but easily constructed and controlled models allow for explicit inclusion/exclusion of a wide variety of physical processes. Being able to cleanly separate each physical process, or include/exclude processes at will, allows for a focused examination of the impacts of said processes. In this study we make use of this flexibility to examine the role of sea ice processes in the evolution of both the Upper Circumpolar Deep Water (UCDW) and Winter Water (WW) layers at a particular region in the SIZ. Specifically we will show that in the seasonal ice zone at 60°S and 0°E, vertical transport due to Ekman pumping is a leading order effect on the transformation of UCDW and WW layers on seasonal timescales.

5.1.2 Water masses of the Antarctic seasonal ice zone

The global ocean can be divided into a number of water masses defined by their distinct physiochemical properties (in particular their temperature and salinity) as determined by their origin (Pauthenet et al., 2019). Tracking the position of these water masses as well as their evolution has been used to understand large scale ocean circulation and climate variability (Emery and Meincke, 1986; Walin, 1982). For our work, we focus on the transformation of key water masses in the Southern Ocean as a result of upper ocean processes. In this sense, a broader perspective of the role of these water masses is useful to determine the potential impacts of the results to be examined later on.

In general, when represented in depth-latitude space, the meridional circulation of the Southern Ocean can be represented as a Deacon cell shown in figure 5.1 from

Speer et al. (2000). The cause of the split of the meridional overturning circulation into an upper branch and a lower branch, is attributed to water-mass transformation by surface fluxes of heat and freshwater (Speer et al., 2000; Marshall and Speer, 2012). For the lower branch of the circulation depicted in figure 5.1, sea ice is thought to contribute via effects on bottom water formation (Jacobs, 2004). In this process, sea ice formation close to the Antarctic continent contributes to the formation of high-salinity shelf water which is tied to the production of Antarctic Bottom Water (Jacobs, 2004).

More recently, the role of sea ice in the upper branch has been examined in Abernathey et al. (2016). In this study, the preferential deposition of sea ice melt water, and transport of snow by sea ice northward sets up meridional buoyancy gradients at the ocean surface. As a result, the ocean surface waters at lower latitudes are lightened. Coupling this lightening of the surface ocean layer with mixing and thus entrainment of the underlying CDW water was seen to result in an enhanced transformation of CDW to lighter waters and thus accelerate the upper branch of the meridional overturning circulation. The study of Abernathey et al. (2016) thus suggests that increased wind driven export of sea-ice, as well as enhanced entrainment of CDW, could cause an acceleration of the upper branch of the meridional overturning circulation. Understanding the seasonal evolution of the CDW layer, and the buoyancy fluxes at the surface are thus important for a complete understanding of this mechanism.

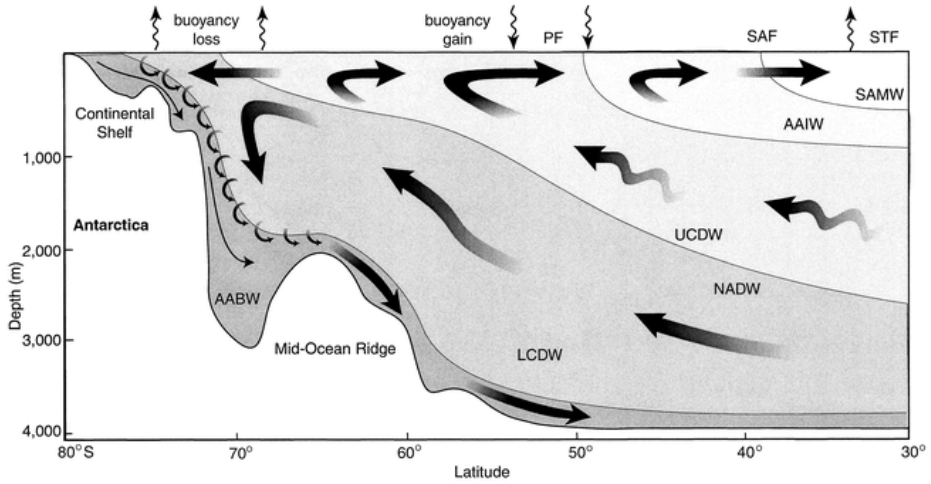


Figure 5.1: Typical representation of the Southern Ocean meridional circulation from figure 8 of Speer et al. (2000). The circulation can be split up between an upper cell driven by northward Ekman transport, southward eddy transport in the UCDW layer, and sea ice processes (Abernathey et al., 2016), and a lower cell driven by dense water formation near the continent. Water masses depicted are Antarctic Bottom Water (AABW), Lower Circumpolar Deep Water(LCDW), North Atlantic Deep Water (NADW), Upper Circumpolar Deep Water (UCDW), Antarctic Intermediate Water (AAIW), and Sub-Antarctic Mode Water (SAMW)

On seasonal time scales, the dynamics of the upper ocean in the SIZ are strongly influenced by ice-ocean processes such as ice melt and growth, surface driven mixing, the ice-albedo effect as well as evaporation and precipitation (Abernathey et al., 2016). The memory of the system to the history of these processes lies primarily in the winter mixed layer and the formation of its characteristic Winter Water (WW) (Pellichero et al., 2017). In the summer, a warm and fresh summer mixed layer (SML) forms atop the WW layer due to ice melt and increased heat exchange at the surface. The presence of the WW layer influences the heat and salt content of the SML due to entrainment thus setting the surface ocean properties for subsequent ice-growth seasons (Pellichero et al., 2017). Additionally, the WW layer is primarily responsible for insulating the ocean surface from the vast heat content of the Upper Circumpolar Deep Water (UCDW) below (Abernathey et al., 2016). Potential ventilation of the warm UCDW has implications for Antarctic sea ice formation in subsequent years (Jacobs and Comiso, 1997; Martinson, 1990). Understanding the primary drivers of WW formation and persistence, as well as transformation of the underlying UCDW, are thus essential to representing the Antarctic SIZ on timescales longer than seasonal.

Historically, observations of the under ice regions have been sparse with a bias towards the logistically simpler ice free summer months (Swart et al., 2019). This

observational gap has limited the work attempting to more completely characterize this seasonally ice covered region. In recent years, autonomous instrumentation such as gliders, seal tags and float programs, including ARGO and SOCCOM (Southern Ocean Carbon and Climate Observations and Modeling) floats, have started to fill this observational gap (Swart et al., 2019; Saenz and Arrigo, 2014; Roquet et al., 2013). In this study, we will make use of this increased in situ data to outline the water-mass evolution of the SIZ before attempting to characterize the relative importance of surface processes in the observed evolution in §5.5.

5.2 Data acquisition and processing

Here we introduce the data from observations and reanalysis to be used in this study. For the implementation of our model we use an initial profile of the ocean, which we will take from a SOCCOM (Southern Ocean Carbon and Climate Observations and Modeling project) float, and atmospheric forcing, to be taken from reanalysis products. We can then compare the time evolution of our model to a time series of observed ocean profiles from the SOCCOM float. Furthermore, we will make use of satellite based sea ice concentration data as a check on the sea ice evolution calculated by the model.

5.2.1 SOCCOM Floats

The primary oceanic observations to be used in this analysis are Conductivity, Temperature, and Depth (CTD) Profiles from SOCCOM floats. SOCCOM float data were collected and made freely available by the Southern Ocean Carbon and Climate Observations and Modeling (SOCCOM) Project (http://www.argo.ucsd.edu).

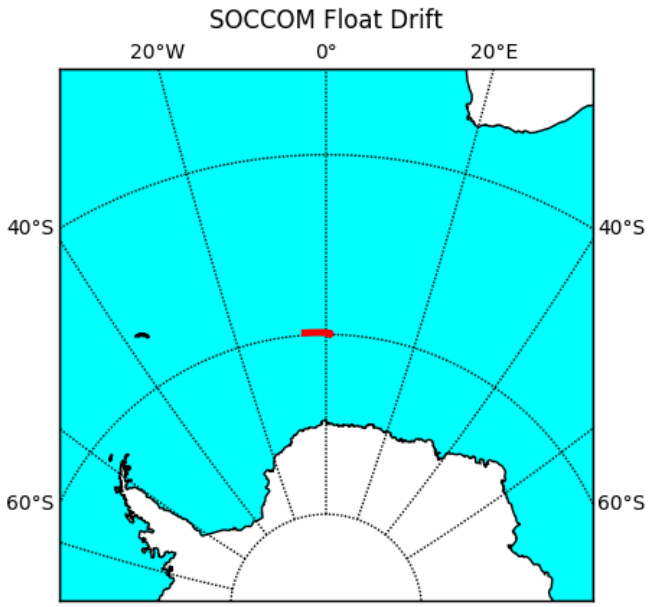


Figure 5.2: Drift of SOCCOM float(Red line) over the study period.

The SOCCOM float data used in this study covers the period from the 22nd of July 2018 until the 6th of March 2019. This time series corresponds to observations starting late in the sea ice growth period until well after the summer melt out. SOCCOM floats move with the ocean currents at the float's current residence depth integrated over time, and the drift of this float is shown in figure 5.2. We initiate our model using the adjusted data which have been modified for known bias (Cabanes et al., 2016). The profiling pattern of the SOCCOM float is given in figure 5.3.

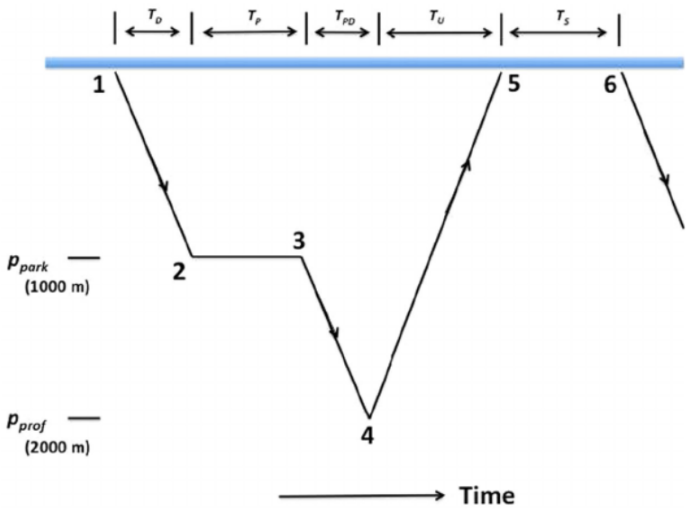


Figure 5.3: Profiling pattern of SOCCOM floats over one profile interval from figure 3 of Riser et al. (2018b). Characteristic values of the times for each profiling step are given by $T_D = 3$ hours, $T_P = 7$ days, $T_PD = 3$ hours, $T_U = 6$ hours, $T_S = 6$ hours.

CTD profiles were taken approximately every 10 days. Over the course of this observational period the float surfaced as far west as 59.78S, 4.71W in July before the ice detection scheme stopped surface maneuvers. The last surfacing of the float before it was covered by sea ice occurred on August 2nd, 2018 04:25:15 at 59.7S, 4.4W, the float then surfaced 144 days later on December 23rd, 2018 13:35:42 once the ice retreated at 59.78S, 0.297W. Its location during this time is estimated by linear interpolation between its last surfacing before ice cover and first surface after ice melt. The path of the float throughout the study time period with the ice covered portion determined with this interpolation is shown in figure 5.2.

5.2.2 Ice concentration

Satellite based ice concentration data is used in this study to initialize the model ice concentration and to serve as a comparison to the model ice concentration time-series. We use the daily AMSR2 data for ice concentration provided by the University of Bremen's Sea Ice Remote Sensing Group Data Archive (Spreen et al., 2008). For this product, the calibrated brightness temperature data from satellite observations are used to create a sea ice concentration product with a resolution of 3125 × 3125 meters.

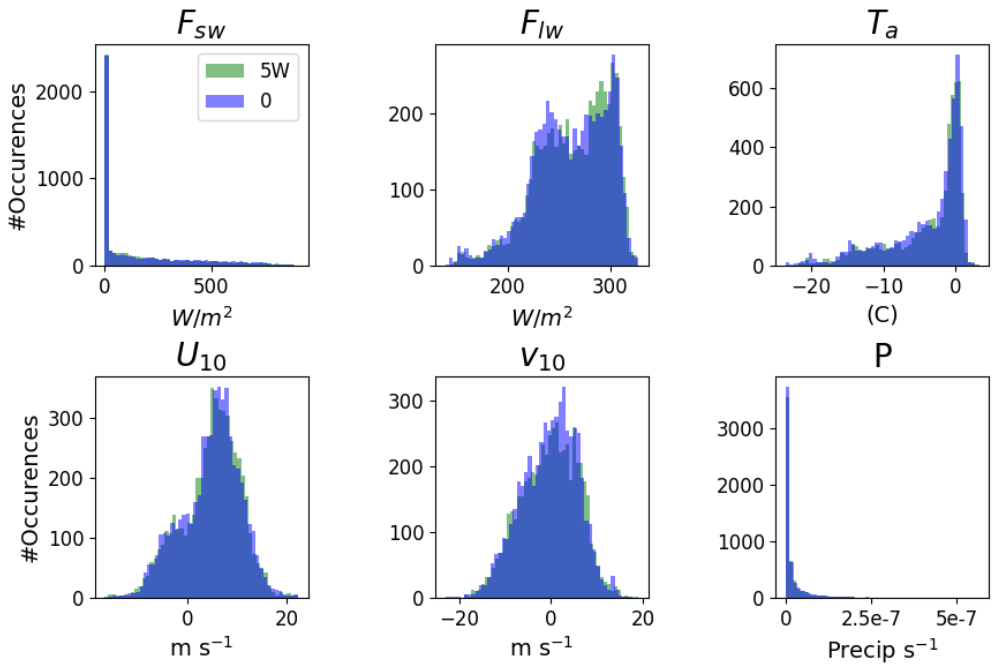


Figure 5.4: Histogram comparison of the reanalysis fields at 60S 0W (light blue) and 60S 5W (green) with the dark blue colouring indicating the overlap. The fields shown are the downwelling shortwave and longwave fluxes, atmospheric surface temperature at 2m, 10m wind speed and precipitation. Each occurrence indicates a value of the hourly time step within the ERA5 reanalysis over the study period at the respective coordinate. Each field has been split up into 50 equal size bins for this comparison.

5.2.3 Atmospheric forcing

To force the 1D model we use surface fields from the ERA5 reanalysis product at an hourly time step. The fields used in our model are the 10m U and V horizontal wind components, 2m temperature and dew-point temperature, downwelling solar and longwave radiation at the surface and total precipitation. We use the atmospheric forcing fields at 60S and 0E. To evaluate the potential variance in forcing along the float drift, and thus any issue with the choice of a single point along the drift, we compare the distribution of values for the various reanalysis fields at two extreme points of the drift period in figure 5.4. Here we see the forcing data is qualitatively similar at both points. Though there is likely to be temporal differences from passing weather systems, we are primarily interested in bulk trends in this study as opposed to the fine scale evolution. Thus for simplicity, we will use forcing fields from 60S and 0E whose time series is shown in figure 5.5.

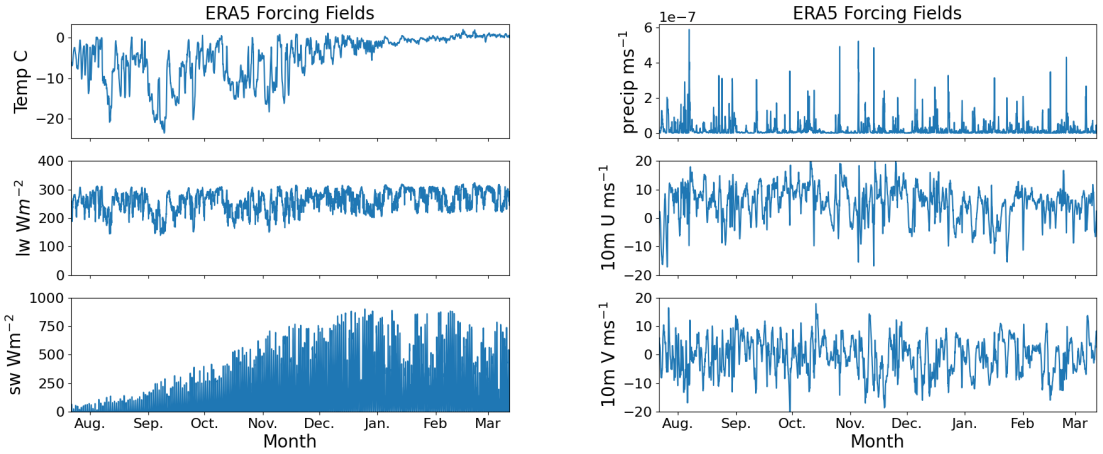


Figure 5.5: Time series of reanalysis fields to be used as surface forcing in the 1D model of §5.4. The left column shows the evolution of the 2m surface temperature field, downwelling longwave radiation, and downwelling shortwave radiation. The right column shows the precipitation rate and the 10-meter meridional and zonal wind speeds.

5.3 Observations of the seasonal evolution

From winter to summer, the increase in solar radiation warms the mixed layer and reduces ice coverage and thickness (Pellichero et al., 2018). This increased solar heating can be seen in figure 5.6 as observed by a vertically profiling SOCCOM float. The mixed layer properties remain relatively constant from mid-winter through to

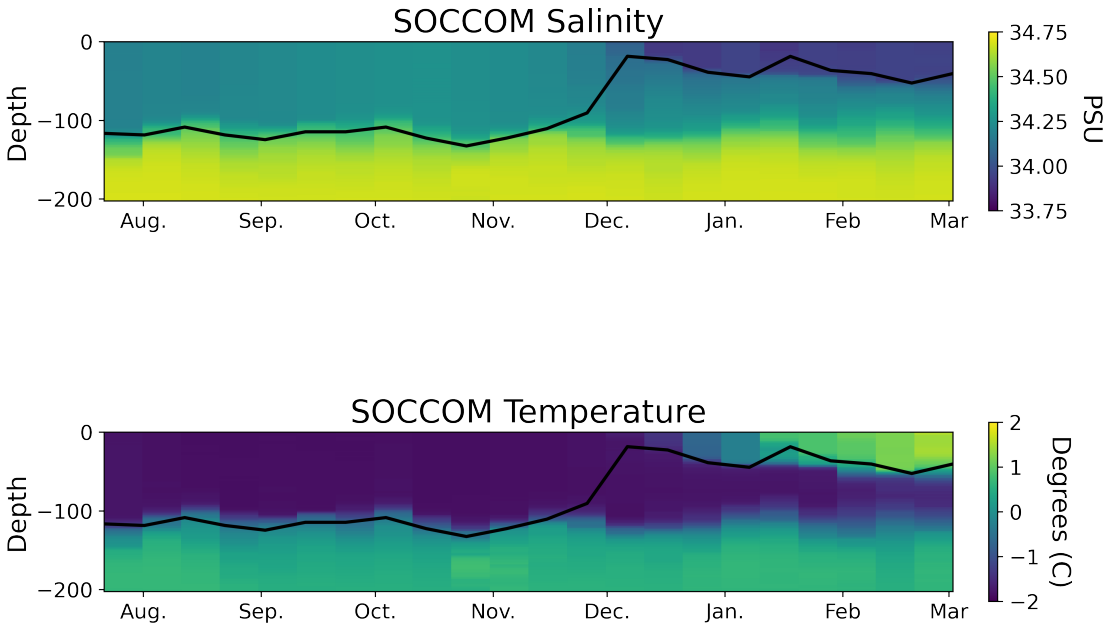


Figure 5.6: Salinity (top) and temperature (bottom) evolution from 22nd of July 2018 until the 6th of March as observed from SOCCOM float 5904467. The overlain black line indicates the calculated mixed layer depth using the criterion $\rho_z - \rho_0 \geq 0.03$ kg m^{-3}

early summer (Aug-November). From December- January, the mixed layer shoals and is accompanied by a surface warming and accompanying freshening due to ice melt. This process restratifies the surface ocean creating a fresher, warmer and shallower (30m) summer mixed layer (SML). Throughout this work we use a difference criterion as in de Boyer Montégut et al. (2004) to estimate the mixed layer depth. This criteria checks when the density at depth, ρ_z, differs from the ocean surface density, ρ_0 by some threshold. Here we are using a threshold of $\Delta\rho = 0.3$ kg m^{-3}.

The largest seasonal signals across the observational period appear in changes of the mixed layer temperature and salinity. These can be visualised both as a function of time and depth (Figure 5.6), but also in temperature and salinity space. Decomposing the SOCCOM profiles in temperature and salinity space as in figure 5.7 allows for a clear visualization of the three main water masses and the mixing lines between them.

In winter, the mixed layer temperature remains at the freezing point of $T_{ww} = -1.77°$ with a mixed layer salinity of approximately $S_{ww} = 34.2$ psu. At small time scales, the temperature may deviate from the freezing point. However, any deviation would be responded to by an increase or decrease in ice formation and a subsequent

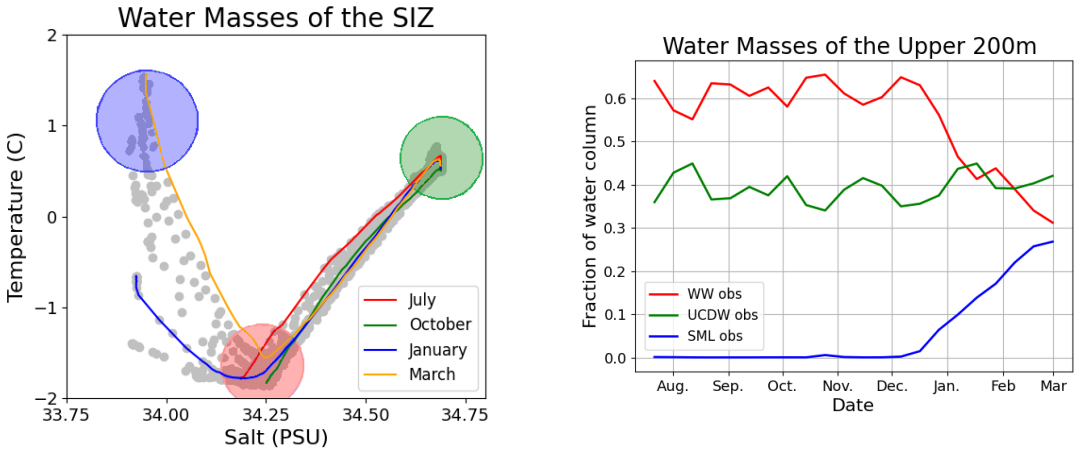


Figure 5.7: Temperature vs salinity plot of all profiles taken by the SOCCOM float during the study period (left) as well as the fraction of the water column they represent in the surface 200m (right). Key water masses are identified by the shaded regions as UCDW (green), WW (red), and the summer mixed layer (blue).

balance between induced convective instability from brine rejection and entrainment of UCDW. In the analysis below, we use values representative of this UCDW layer given by temperature and salinity of $T = 0.65°$ and $S = 34.69$ psu.

After the shoaling of the mixed layer accompanying sea ice melt in the spring, the SML is formed atop the WW layer. The SML has representative temperature and salinity of $T_{sml} = 1.72°$ C and $S_{sml} = 33.95$. The SML is thus around 0.25 psu fresher than the WW and steadily warms from the freezing point to nearly 2 degrees in March. As previously observed, the creation of a shallow mixed layer in summer insulates the WW layer from further modification via surface processes (Pellichero et al., 2018). Once the SML has formed after shoaling of the mixed layer in December, the WW layer appears to thin from both top and bottom suggesting encroachment of the UCDW layer or mixing between the two layers. Previous studies have posited that the mixing of WW and UCDW after the formation of the summer mixed layer is due to isopycnal and diapycnal mixing (Couto et al., 2017).

From the above discussion, we know that the upper ocean evolution of the study region can be characterized by these three primary water masses: 1) the Winter Water (WW) of the deep winter mixed layer, 2) the comparatively fresh and warm summer mixed layer waters (SML) and 3) the UCDW lying below the winter mixed layer. We can take a closer look at the water-mass evolution in the surface 200m using the exact systems method outlined below. This method is named so because the number of equations is the same as the number of unknowns and so the system can

be 'exactly' determined as opposed to the over or under constrained system where the number of variables is less than, or more than the constraints (Strang et al., 1993). This approach is equivalent to the 'composite tracer method' used in Jenkins (1999). In this representation subscripts indicate which of the above mentioned water masses the property belongs to (WW, SML, UCDW), and the subscript *obs* indicates the observed quantity. This method solves the following set of equations

$$X_{WW} + X_{UCDW} + X_{SML} = 1 \tag{5.1}$$

$$T_{WW}X_{WW} + T_{UCDW}X_{UCDW} + T_{SML}X_{SML} = T_{obs} \tag{5.2}$$

$$S_{WW}X_{WW} + S_{UCDW}X_{UCDW} + S_{SML}X_{SML} = S_{obs} \tag{5.3}$$

for each observational/model data point, where X represents the fraction of the grid cell that is made up of a particular water-mass. The characteristic temperature and salinity T and S for the various water masses were determined as follows. For Winter Water, the temperature and salinity of the mixed layer at the start of the model/observational period were taken. For the Summer mixed layer we use properties of the mixed layer at the end of the observational period. Lastly UCDW properties were determined by using the properties at 200m depth within the SOCCOM profile. The water-mass evolution as determined by this method is shown in figure 5.7 alongside a temperature-salinity plot of all data points in the surface 200m of the SOCCOM float data used for this study. The temporal evolution of the water-mass fractions are also shown in figure 5.7; this picture is useful for connecting the times of changing water-mass fraction with other ocean processes. Furthermore, the correlation of changes also suggests which water mass is replacing the reduced fraction of another. For example, in December-January, after the sea ice cover is melted, summer mixed layer formation begins suggesting Winter Water transformation at the surface.

Understanding the processes governing the evolution of these three primary water masses could potentially allow a glimpse into understanding the yet to be explained trend of Antarctic sea ice extent. The model to be developed in the next section will allow us to focus on the role of specific physical processes, and span a parameter space about observationally constrained values to clarify the importance of various processes. We can then compare the contributions of the included processes to the observed time series of upper ocean evolution illustrated above to understand which processes are responsible for the observed evolution of stratification.

5.4 1D ice ocean model

The bulk mixed layer model developed here is based on a hybridization of two frequently used bulk mixed layer models of Kraus and Turner (1967) and Price et al. (1986) as published in Biddle et al. (2017). The current version of this model has been updated to include the more detailed sea ice model of Petty et al. (2013) along with some slight modifications to the handling of mixed layer evolution. In contrast to the model of Petty et al. (2013), our model neglects the treatment of a surface skin layer which mediates exchanges between the atmosphere and upper ocean and instead treats the mixed layer as in direct contact with the air-sea and ice-ocean interface. In this setting, the surface ocean layer properties are equivalent to the mixed layer properties.

Within this model, the ice layer reacts to atmospheric forcing through prescribed heat fluxes and interacts with the ocean through exchanges of salt and heat with the mixed layer. We will introduce the model representation of these two pathways separately. Within a partially ice-covered region, the fluxes of heat and salt are simply additive and weighted by the sea ice fraction C (where $C = 0$ is open ocean and $C = 1$ is completely ice covered) so that the net flux is given by $Q_{net} = CQ_{io} + (1 - C)Q_{ao}$ where Q_{io} is the ice-ocean flux and Q_{ao} is the air-ocean flux . Throughout this section we will use the subscripts, s, i , o to indicate properties of the snow, ice, or ocean respectively and subscript ML refers to properties of the ocean mixed layer. A simplified schematic of the various fluxes of heat in a region with sea ice concentration C is shown in figure 5.8

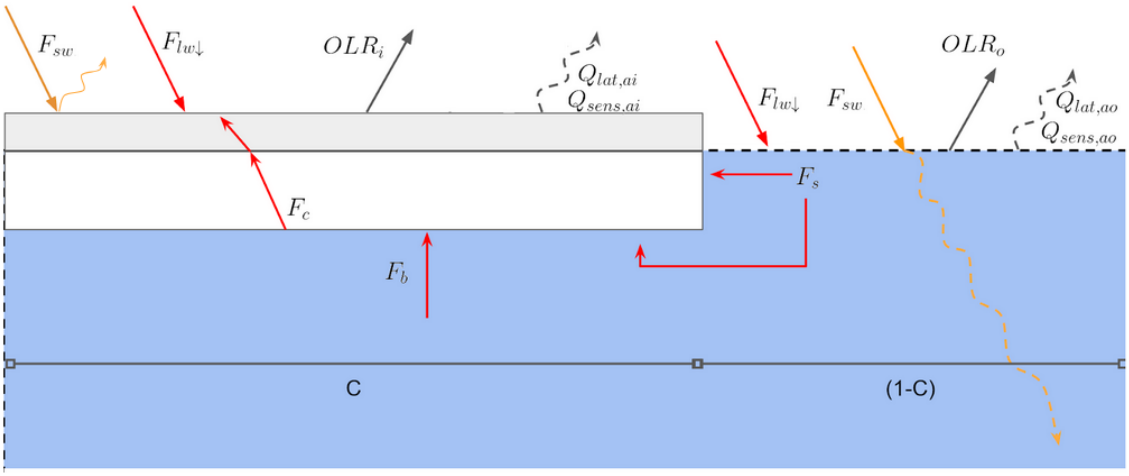


Figure 5.8: Heat fluxes for the ice and ocean interfaces to be discussed in a region with sea ice concentration C. F_{sw} and $F_{lw\downarrow}$ are the downwelling short and longwave radiation terms with a fraction $\alpha_{si}F_sw$ of shortwave reflected from the ice surface with albedo α_{si}. In the open ocean the shortwave radiation that is not reflected penetrates and can be absorbed at depth. At the ice interface, the non reflected short wave radiation is absorbed primarily within the snow and ice. Within this energy balance model this contribution is lumped with the fluxes at the snow/ice-air interface. OLR is shorthand for the outgoing longwave radiation terms which depend on the surface temperature of their respective mediums. Q_{lat} and Q_{sens} are the latent and sensible heat fluxes for the two interfaces with subscripts ai for air-ice/snow interface and ao for air-ocean interface.. F_c is the conductive heat flux through the ice, F_b is the basal heat flux and F_s is the contribution of heat flux absorbed at the surface which subsequently contributes to both basal and lateral melting.

5.4.1 Open Ocean Exchanges

For the fraction $(1 - C)$ of the mixed layer not covered by ice, the heat exchange at the air-sea interface into the mixed layer, $Q_{heat,ao}$ is calculated by

$$\begin{aligned} Q_{heat,ao} =& F_{lw\downarrow} + F_{sw,0} - \epsilon_o\sigma(T_{ML})^4 - \rho_a c_{p,a} C_{d,ao} U_{10}(T_{ML} - T_a) \\ & - \rho_a L_v C_{d,ao} U_{10}(q_{sat}(T_{ML}) - q_a) \end{aligned} \tag{5.4}$$

where $F_{lw\downarrow}$ is the downwelling longwave radiation, $F_{sw,0}$ is the downwelling shortwave radiation absorbed over the depth of the mixed layer (see below), ϵ_o is the ocean emissivity, $\sigma(T_{ML})^4$ is the black body radiation emitted using the ocean surface temperature which in our bulk mixed layer model is T_{ML}, and the Steffan-Boltzmann constant, σ. The fourth term on the right hand side describes sensible heat fluxes with

ρ_a the atmospheric density, $c_{p,a}$ the specific heat capacity of the atmosphere, U_{10} is the 10 meter wind speed, and T_a is the temperature of the atmosphere near the ocean (2m temperature in our case). Similar to Petty et al. (2013), we here approximate the heat transfer coefficient as equal to the air-sea drag coefficient $C_{d,ao}$. The final term describes energy transfer from evaporation, where L_v is the latent heat of vaporisation, $q_{sat}(T_{ML})$ is the saturation specific humidity calculated using the surface ocean temperature at atmospheric pressure P_{atm} using the form $q_{sat}(T) = 0.622 e_s(T)/P_{atm}$ with e_s calculated as in Bolton (1980), and q_a is the specific humidity.

The heat contribution from the shortwave radiation sometimes penetrates deeper then the mixed layer. In our model this heating is represented as

$$F_{sw} = I_0 \left(0.6 e^{-\frac{z}{0.6}} + 0.4 e^{-\frac{z}{20}}\right) \tag{5.5}$$

where I_0 is total downwelling irradiance, and z is the depth in meters. This models the attenuation of solar irradiation with depth (Paulson and Simpson, 1977). This parmaterization approximates the wavelength dependency of the shortwave absorption using two components of decay with attenuation lengths of 0.6m and 20m. In principle these coefficients vary depending on the optical properties of the water type; for this model we have used the 1a type of Jerlov (1968). For z in the mixed layer, the contribution is summed and divided by the mixed layer depth to be applied equally across the mixed layer.

The net salt flux at the air-sea interface is determined by calculating the loss of ocean water implied by the evaporation term in (5.4) and subtracting off the precipitation prescribed by the reanalysis forcing to find the net water flux out of the ocean

$$Q_{salt,ao} = \frac{\rho_a L_v C_{d,ao} U_{10} (q_{sat}(T_{ML}) - q_a)}{(\rho_{fw} L_v)} - P, \tag{5.6}$$

where ρ_{fw} is the density of fresh water. This is then applied to the ocean as a virtual salt flux to the mixed layer for each timestep as

$$\Delta S_{ML} = (1 - C) Q_{salt,ao} S_{ML} \frac{\Delta t}{H_{ML}} \tag{5.7}$$

where Δt is the discretized time, and salinity is distributed over the mixed layer depth H_{ML}. The (1-C) factor accounts for evaporation being driven by fluxes over the ocean only. Similarly for heat

$$\Delta T_{ML} = (1 - C) Q_{heat,ao} \frac{\Delta t}{\rho_{ML} c_o H_{ML}}. \tag{5.8}$$

with c_o the specific heat capacity of the ocean. These fluxes, together with the contributions from the sea ice paramaterizations to be discussed in section 5.4.2, are then input into the bulk mixed layer model to determine the evolution of the mixed layer.

5.4.2 Sea ice model

The sea ice model introduced here is predominantly that of Petty et al. (2013) with some modifications to integrate with our modified ocean model.

To begin, we calculate the snow-covered ice surface temperature, T_s^i, as in Petty et al. (2013) by balancing the radiative, sensible heat, and latent heat fluxes with a conductive heat flux through the ice and overlying snow as

$$\begin{aligned} F_{lw\downarrow} + (1-\alpha_{si})F_{sw\downarrow} - \rho_a c_{p,a} C_{d,ia} U_{10}(T_s^i - T_a) \\ -\rho_a L_s C_{d,ia} U_{10}(q_{sat}(T_s^i) - q_a) - \epsilon_s \sigma (T_s^i)^4 = -F_c(T_s^i)_\uparrow. \end{aligned} \tag{5.9}$$

Here $C_{d,ia}$ is the ice-air turbulent exchange coefficient which we have assumed to be equivalent for sensible and latent heat fluxes, L_s the latent heat of sublimation for snow, ϵ_s is the emissivity of snow, α_{si} is the snow (ice) albedo, and $F_c(T_s^i)_\uparrow$ is the conductive heat flux through the ice-snow system to the snow-air interface.

For the conductive term, a linear temperature gradient through the snow and sea ice has been assumed, as in Semtner (1976), such that

$$F_c = \frac{k_i k_s (T_f - T_s^i)}{(k_i h_s + k_s h_i)} \tag{5.10}$$

where T_f is the freezing point of the underlying mixed layer given by a liquidus curve, k is the conductivity of the respective media and h is its thickness. If there is no snow cover, $h_s = 0$, so (5.10) can be reduced to $F_c = \frac{k_i(T_f - T_i)}{h_i}$. In this model we do not evolve snow thickness and instead leave it as a parameter to be fixed later. For a treatment of evolving snow cover using the model of Petty et al. (2013) we direct the reader to recent work within Frew et al. (2019). Equations 5.9 and 5.10 can be combined to determine the snow surface temperature needed to balance the system each iteration. This model neglects the heat capacity of the ice, c_i, and brine pockets and hence neglects any thermal lag of the interior ice temperature adjusting to changing atmospheric and oceanic temperatures, with the conductive gradient adjusted instantly. Furthermore neglecting the specific heat of the ice likely impacts the overall heat budget and the model determined ice-thickness by 10-20% (Schmidt et al., 2004b; Bitz and Lipscomb, 1999). Both neglected effects are relatively modest

because the Stefan number $L/\rho_i c_i \Delta T$ is usually large for typical ice heat capacity c_i and temperature scale ΔT (Worster and Rees Jones, 2015). In line with the above approximation we also apply the shortwave radiative absorption within the ice into the surface energy budget in (5.4), rather than distributing the heating over the ice interior. In reality the latter internal heating would modify the internal temperature gradient and conductive heat flux to the ice-atmosphere interface; we account for this effect by adding the relevant heating into the surface energy budget and neglecting transmission into the underlying ocean.

In addition to the conductive heat flux, the net heat flux at the ice-ocean interface is effected by turbulent exchange with the mixed layer, and a partitioning of the surface layer heat-flux between lateral and basal melting. The turbulent heat flux at the bottom of the ice, F_b, is given by

$$F_b = \rho_o c_o u_i^* C_{d,io} \left(T_{ML} - T_f\right), \tag{5.11}$$

where c_o is the specific heat capacity of the ocean, the quantity u_i^* is the friction velocity which characterises turbulent exchange and $C_{d,io}$ is the ice ocean drag coefficient. Similar to the air-sea drag coefficient, $C_{d,io}$ is treated as equivalent to the heat transfer coefficient as in Petty et al. (2013). In general the friction velocity is given by $u^* = \sqrt{\tau/\rho}$ with τ the surface stress. As in Petty et al. (2013), we assume that the ice is in free drift and neglect acceleration on short timescales, leading to a force balance between atmospheric wind stress and ice-ocean stress yielding

$$u_i^{*2} = \frac{C_{d,ao}\rho_a}{\rho_o} U_{10}^2 \qquad u_a^{*2} = C_{d,ao} U_{10}^2 \tag{5.12}$$

We neglect wave drag here, which is appropriate if the Froude number based on ridge heights is large. Petty et al. (2013) used the properties of an ocean surface layer to define a heat potential that was used to predict lateral and basal melt contributions from heat absorption in the upper ocean. The current model does not have the extra surface layer, so we adjust the heat potential to use bulk mixed layer properties. We also modify the treatment of partitioning of lateral and basal heat fluxes, so that the present model explicitly resolves a closed energy budget (the treatment of Petty et al. (2013) effectively treats the surface layer as an energy reservoir without tracking stored energy). The present approach was found to yield better agreement with the observed melt out date (where $C \to 0$), compared to early attempts using the heat flux partitioning in Petty et al. (2013) which modelled melt out as one month later than observed. However, earlier melt out in the model here yielded warmer summer

mixed layers, where as the formulation of Petty et al. (2013) more closely matched the summer mixed layer temperature of the observations. This could, in principle, have been compensated by tuning of default parameter values for air sea fluxes over open ocean, but we do not pursue such a tuning exercise here. We proceed here with the energy conserving scheme described below.

The total heat-flux to the ice from the exposed ocean component of the mixed layer with temperature T_{ML} is parameterized by

$$F_s = (1 - C)\rho_o c_o u_o^* C_{d,io}(T_{ML} - T_f). \tag{5.13}$$

Here $(1 - C)$characterizes the fractional surface area of the open ocean surface. This is effectively the heat potential of Petty et al. (2013), but using the mixed layer temperature as the surface temperature. This total heat flux from the exposed ocean surface layer can then be separated into contributions to lateral and basal melting of the sea ice via the parameter R_{lat}, where $R_{lat} = 0$ indicates all melt is lateral, and $R_{lat} = 1$ all melt is basal. Assuming that the total basal heat flux contribution $R_{lat}F_s$ is distributed over the ice-covered area fraction, C, this gives an additional local basal heat flux contribution of

$$F_{sb} = \begin{cases} F_s R_{lat}/C & \text{for } C > 0 \text{ and } T_{ML} > T_f \\ 0 & \text{otherwise.} \end{cases} \tag{5.14}$$

which is applied in addition to F_b from the deeper mixed layer given by (5.11). The remaining lateral partition of F_s contributes to the evolution of the ice coverage, dC/dt, as

$$\frac{dC}{dt} = \begin{cases} \frac{-F_s}{L_f \rho_i h_i} & \text{for } C < C_{max} \text{ and } T_{ML} < T_f \\ \frac{F_s(1-R_{lat})}{L_f \rho_i h_i} & \text{for } C > 0 \text{ and } T_{ML} > T_f \\ 0 & \text{otherwise} \end{cases} \tag{5.15}$$

with L_f the latent heat of fusion of the ice. If $C = C_{max}$ and $T_{ML} < T_f$, the heat from F_s is instead used to grow sea ice vertically as in Petty et al. (2013). The vertical melt rate can be computed from the basal Stefan condition

$$\frac{dh_i}{dt} = (F_c - F_b - F_{sb}) / (\rho_i L_f). \tag{5.16}$$

The salt and heat fluxes to the mixed layer from ice growth and melt are then

$$Q_{salt,io} = \frac{\rho_i}{\rho_{ml}} (S_{ml} - S_i) \left[C \frac{dh_i}{dt} + \frac{dC}{dt} h_i \right] \tag{5.17}$$

due to brine rejection as the ice volume changes, and

$$Q_{heat,io} = -\left(CF_b + F_s\right). \tag{5.18}$$

The net heat and salt fluxes at the ocean surface are thus given by the sums of the ocean and ice fluxes for a partially ice covered ocean. These fluxes will later be used in the Krauss-Turner step for the mixed layer scheme to calculate the TKE budget and determine the entrainment velocity of the mixed layer. In our work, (5.14) differs from the equivalent result of Petty et al. (2013) by a factor of $1/C$. This change ensures the energy budget is closed for the ice and mixed layer. Taking the sum of $\rho_i L_f h_i \times$(5.15)$+\rho_i L_f C \times$(5.16) and substituting (5.14) and the surface energy flux balance (5.9), one obtains the rate of change of latent heat stored in the ice volume, in terms of atmospheric surface fluxes and the energy exchanges (5.18) between the ice and ocean.

One last process in Petty et al. (2013) is that of ice advection into or out of the domain. In general ice advection is described by the divergence of the flux of ice area

$$\xi = \nabla \cdot (C\mathbf{U_i}) \tag{5.19}$$

where $\mathbf{U_i}$ is the ice velocity. For the sake of simplicity we will neglect horizontal gradients in the ice concentration so

$$\xi = C\nabla \cdot \mathbf{U_i}. \tag{5.20}$$

In the current implementation, the quantity $\nabla \cdot \mathbf{U_i}$ is set to be a constant which we will determine in §5.4.4. It is important to note that horizontal gradients in the ice concentration are likely to be important for the SIZ for some processes such as initial ice growth. This is due to adjustment of the surface albedo as a result of equatorward advection of ice from colder, earlier growth regions to the south. The ice advected into the domain is assumed to have the same thickness as ice currently in the region.

5.4.3 Mixed Layer Model

The ocean model used herein is that of Biddle et al. (2017) which utilizes a combination of two classic bulk mixed layer models: the Price-Weller-Pinkel (PWP) model (Price et al., 1986), and the Krauss-Turner (KT) model (Kraus and Turner, 1967). These bulk mixed layer models consider the budgets of heat, salt, and momentum to

determine the Turbulent Kinetic Energy (TKE) budget of the upper ocean and adjust the mixed layer properties to maintain the approximate hydrodynamic stability criterion.

The primary difference between these two bulk mixed layer models is how they parameterize this TKE budget. Five constituent parts can be considered to make up the TKE budget (Gaspar, 1988): the potential energy cost of entrainment of deeper water into the mixed layer at its base, wind and wave production of TKE at the ocean surface, production from shear stress at the mixed layer base, buoyancy forcing from surface fluxes, and dissipation. The KT method computes the effect of wind/wave and buoyancy forcings at the surface together with energy dissipation to calculate an entrainment velocity, which is then used to determine the mixed layer depth. In comparison to this, the PWP model focuses primarily on the parameterization of shear instability to adjust the mixed layer depth. Together these models provide a more complete representation of the upper ocean evolution.

In numerical calculations one of these mixing processes must arbitrarily occur first. In this model we first apply the surface buoyancy fluxes of heat and momentum discussed above for both the open and ice-covered oceans, and then proceed to calculate the mixed layer depth first using KT, and then we check for shear instability with the PWP criteria. At the end of each iteration, we check for convective instability by examining the density at the mixed layer depth and the density in the next deepest grid cell and mix until the mixed layer is lighter than the underlying gridcell.

The KT mixed layer equations independently determine the power input from the surface wind stress, P_w, and power input from buoyancy fluxes, P_b. These quantities are then used to estimate whether the mixed layer can deepen via entrainment of water below the mixed layer, if not then the mixed layer shoals to achieve a balance of energy fluxes. The wind power, P_w, can be estimated using the mixed layer depth H_{ML} as in Kraus and Turner (1967) by

$$P_w = 2m_{kt}e^{\frac{-H_{ML}}{d_w}}(u^*)^3 \tag{5.21}$$

where m_{kt} is the coefficient for power provided by wind, d_w is the dissipation length scale and u^* is the friction velocity given by the weighted sum of the ice and ocean friction velocities as

$$u^* = \sqrt{Cu_i^{*2} + (1-C)u_0^{*2}}. \tag{5.22}$$

Equation (5.21) can physically be seen to capture the work done at the surface by shear stress which then decays exponentially with depth based on the dissipation

length scale. With this interpretation the value of (5.21) is the wind power remaining for mixed layer deepening. As noted in Petty et al. (2013), this assumption may overestimate the contribution of wind mixing to TKE. The buoyancy flux, Bo is given by

$$Bo = g(\alpha_T Q_{heat} - \beta Q_{salt}) \tag{5.23}$$

where α_T is the thermal expansion coefficient and β is the haline contraction coefficient and both are assumed to be constant.

The power of the buoyancy forcing is then computed as

$$P_b = \frac{H_{ML}}{2}\left[(1+n_{kt})Bo - (1-n_{kt})|Bo|\right] \tag{5.24}$$

where n_{kt} is the coefficient for power provided by buoyancy accounting for differing effects of convective mixing and increased stabilization of the stratification. From these, we can compute the vertical entrainment velocity, w_e, by balancing the power provided by mixing and buoyancy forcings with the change in potential energy due to entraining fluid from below the mixed layer, which yields

$$w_e = \frac{(P_w + P_b)}{H_{ML}\left[g\alpha(T_{ML} - T_b) - g\beta(S_{ML} - S_b)\right]} \tag{5.25}$$

where the subscript b denotes the properties of the ocean column just below the mixed layer. If $w_e > 0$ then the model mixed layer is deepened by $w_e \Delta t$ for timestep Δt. In the case of shoaling where $P_w + P_b < 0$, a balance between P_w and P_b is calculated to determine the model mixed layer depth where the wind forcing and buoyancy forcing would be in balance as

$$H_{ML} = \frac{P_w}{-Bo}. \tag{5.26}$$

After the Krauss-Turner step is concluded we proceed to check the Richardson number criteria of PWP. Unlike in the above, for the PWP we require information about how the zonal and meridional ocean velocities U and V vary with depth to determine whether there is stratified shear instability. These velocities are adjusted to account for inertial oscillations due to Earth's rotation, as well as the wind stress at the ocean surface. These steps are applied only to the mixed layer and occur in the following order. Firstly, an inertial oscillation over the first half of the timestep leads to a rotation

$$\tilde{U} = U\cos(\frac{-f\Delta t}{2}) - V\sin(\frac{-f\Delta t}{2}) \tag{5.27}$$

$$\tilde{V} = V\cos(\frac{-f\Delta t}{2}) + U\sin(\frac{-f\Delta t}{2}) \tag{5.28}$$

where $\tilde{U}$ and $\tilde{V}$ are updated values given previous values U and V. Next the wind stress is applied

$$U = \tilde{U} + \frac{\tau_x}{H_{ml}\rho_o}\Delta t \tag{5.29}$$

$$V = \tilde{V} + \frac{\tau_y}{H_{ml}\rho_o}\Delta t \tag{5.30}$$

where τ_x and τ_y are the zonal and meridional wind stress calculated as $\tau = \rho_o u^*|u^*|$ with u^* calculated as above. Following this (5.27) and (5.28) are applied again to complete the velocity calculations. Then we proceed to calculate and enforce the bulk-Richardson and gradient Richardson number criteria. These are used to ensure the mixed layer conditions do not exceed criteria for stratified shear instability and are given as

$$Ri_b = \frac{gh\Delta\rho_o}{\rho_0(\Delta|\mathbf{V}|)^2} \geq 0.65 \tag{5.31}$$

for the bulk Richardson number where $\Delta\rho_o$ and $\Delta|\mathbf{V}|$ are the differences in density and ocean speed between two grid cells. The gradient Richardson number is

$$Ri_G = \frac{g(\Delta\rho_o/\Delta z)}{\rho_o(\Delta|\mathbf{V}|/\Delta z)^2} \geq 0.25. \tag{5.32}$$

with Δz the thickness of a grid cell. If either of these inequalities are not satisfied, the mixed layer is adjusted incrementally until they are met.

The next component of the model of Biddle et al. (2017) evolves the stratification below the mixed layer, by using a uniform vertical diffusion of $\chi = T, S, U, V$.

$$\frac{\partial\chi}{\partial t} = K_\chi \frac{\partial^2\chi}{\partial z^2} \tag{5.33}$$

where K_χ is a constant eddy diffusivity of the quantity χ. This is here modified to include a description of Ekman pumping with constant vertical velocity W_{ek} as

$$\frac{\partial\chi}{\partial t} = K_\chi \frac{\partial^2\chi}{\partial z^2} - W_{ek}\frac{\partial\chi}{\partial z} \tag{5.34}$$

where the Ekman velocity W_{ek} can be calculated using the ocean surface stress as

$$W_{ek} = \mathbf{k}\cdot\nabla\times\left(\frac{\tau}{f\rho_o}\right) \tag{5.35}$$

In order to conserve mass, vertically uniform Ekman upwelling must be accompanied by divergent lateral Ekman transport in the surface mixed layer. However, because

we are neglecting horizontal gradients of temperature and salinity this flow transports no heat or salt and hence does not appear explicitly in the model.

These processes, diffusion and vertical Ekman velocity, are the only two physical processes at work below the mixed layer within the model. At the end of each iteration, static stability at the mixed layer base is checked ($\rho_{ML} < \rho_b$) and if not met, the mixed layer deepens until the inequality is satisfied.

5.4.4 Model Parameters and Initialization.

For a given location, a number of parameters need to be constrained before running the model: initial snow/ice thickness, ice concentration, ice advection, and the coefficient R_{lat} determining partitioning of lateral vs basal melting. To constrain these parameters for our study region we will use the reanalysis products along with observations from SOCCOM floats and satellite ice concentration as mentioned in §5.2 and data from ice mass balance buoys deployed near the study region. A sensitivity study of these and other parameters follows in §5.5.1.

Observational data for the ice thickness of this region is sparse. To establish a reasonable value of ice thickness we used mean values for the Eastern Weddell sea from satellite observations (Kurtz and Markus, 2012) and an assimilation of shipboard measurements (Worby et al., 2008). For snow thickness, we used a lower value within one standard deviation of the mean snow thickness of these same studies. This was done so as to approximate the snow cover in the early winter when our observations start. Furthermore, an ice mass balance buoy (IMEI: 300434063380850) deployed near the study region, though in October 2019, at 58.07.143'S, 0.02.055'W recorded snow depth of 2 cm. From this we decided upon a reasonable ice/snow thickness to be $h_{s,0} = 0.02\ m$ and $h_{i,0} = 0.5\ m$ during the starting month of July 2018. We later vary each of these values to determine the effects of uncertainty and to test the sensitivity to the snow coverage which here is held constant. The fractional ice coverage, C_0 was set at the enforced simulation upper bound of 0.95. The observed ASMR2 sea ice concentration was near 1, though we set 0.95 as an arbitrary cut off to allow for leads or gaps between ice floes that might not be accurately resolved in the ASMR2 data. As mentioned previously, when $C = C_{max}$ any contribution of the surface heat content to ice expansion goes instead to vertical ice growth as in Petty et al. (2013). This can be interpreted to be an increase in ice thickness via ridging at high ice concentrations.

The lateral vs basal partitioning of the surface heat flux is largely unconstrained and in principle depends on a host of factors we do not seek to incorporate in this

model (Tsamados et al., 2015). Furthermore measurements and parameterizations of lateral melt are few and Arctic focused (Steele, 1992). That said, these studies indicate that the majority of this heat goes towards basal melting so that $0.5 < R_{lat} < 1.0$. We here arbitrarily set $R_{lat} = 0.7$ then later conduct sensitivity studies over the range $0.5 < R_{lat} < 1.0$.

The ice advection parameter is constrained by looking at values of the 10m U,V wind fields within the reanalysis data. From these fields we approximate the ice velocity assuming free drift as in Kwok et al. (2017). We neglect impacts of ocean currents on ice drift for simplicity. With this ice velocity field we calculate the divergence in a 5x5 degree area around 60S and 0E during the ice covered period. The time average value of the divergence was then used as part of a constant ice advection term in our model, providing $\nabla \cdot \mathbf{U_i}$ in (5.20).

The constant Ekman upwelling velocity is determined in the same manner as the ice divergence though using the reanalysis wind fields. We also assume a constant atmosphere-ocean drag coefficient to determine the ocean surface stress from the reanalysis wind fields. If we assume the ice to be in free drift, and neglecting acceleration on short timescales, the atmospheric stress on the ice is approximately the ocean stress under ice. We can then use the wind stress field in the region from the ERA5 reanalysis products 10m wind fields over a 5 degree by 5 degree region centered about the model point of 60S and 0E to calculate approximate values for Ekman pumping over the duration of the study We then take the average value of the time series as in the ice divergence formulation. the curl of the stress can then be used to calculate vertical Ekman velocity via (5.35). Here we have also used default values for drag coefficients and so after choosing the region where to evaluate the wind stress there are no new free fitting parameters introduced in this comparison.

The parameter values used in the default configuration are consolidated in table 5.1. In each simulation, the time step Δt is 100 seconds, and each vertical grid-cell is 3 meters, which were chosen so that results do not depend strongly on their values.

$h_s = 0.02m$	$h_{i,0} = 0.5m$	$C_0 = 0.95$
$R_{lat} = 0.7$	$\nabla \mathbf{U}_i = -0.5\text{yr}^{-1}$	$W_{ek} = 1.4 \cdot 10^{-6} m\ s^{-1}$
$K_{T,S} = 10^{-5}$	$K_{u,v} = 5 * K_{T,S}$	$C_{d,ao} = 1.5 \times 10^{-3}$

Table 5.1: Default values for parameters to be used in the default configuration of the model. In the configuration where Ekman pumping is turned off $W_{ek} = 0$ ms^{-1}. Eddy diffusivities are those used in Biddle et al. (2017).

With these constraints on the input parameters, the model is initiated with a SOCCOM float profile using the bias-adjusted CTD measurements from 22/06/2018, 22:25:40 at -59.738° S and -4.711° E. This profile is interpolated onto the computational grid with a vertical spatial discretization of $\Delta z = 3$m. The model is then forced with ERA5 reanalysis fields to specify the atmospheric fluxes to ice and ocean at -60° S, and 0° E with the first forcing timestep taken to be 22nd of July, 2018 at 22:00:00. The reanalysis data is interpolated onto a discretized time step $\Delta t = 5$ minutes. The simulations are then run until 6th of March, 2019 at 01:00:00, with simulation results compared with the float profile time-series throughout the period. As discussed briefly in §5.2, the SOCCOM floats are quasi-lagrangian and thus move following the ocean currents at a particular steering level dependent on the profiling pattern shown in figure 5.3. This likely filters out the leading order effects of many processes featuring barotropic ocean advection, along with removing the component of flow at the steering level in baroclinic mesoscale and submesoscale eddies. However, differential baroclinic flow above and below the steering level are not removed by the float advection, and could drive water property modifications. Such processes may also play important roles in determining the vertical structure of the ocean. These processes are also omitted from the model which treats the evolution of vertical structure at a specific point using primarily 1D processes. The interpretation of a comparison to the float profiles should thus be seen as a characteristic profile of the broader region rather than a complete explanation of the evolution of a profile along its drift.

5.5 Model Results

Within this section we compare simulation runs without Ekman pumping, to those with vertical Ekman transport. We then test the sensitivity to other processes included in the model in §5.5.1.

The default configuration as described in section 5.4 without Ekman pumping captures the seasonal evolution of the mixed layer quite well for such an idealized model, as shown by comparing figure 5.9 to the earlier pseudocolour plots of figure 5.6. In the winter, the reference model has a deep winter mixed layer that is roughly constant, followed by a rapid shoaling of the MLD linked to stratification associated with ice melt during November through December.

We can take a more detailed look at the agreement from the vertical profiles of the temperature and salinity at specific times comparing observations and model in figure 5.10. From these vertical profiles it is evident that while the model without

Ekman pumping captures the seasonal evolution of the upper ocean and mixed layer, the model fails to capture the apparent upwards translation of the UCDW from 120m depth in the start of the time series to $\approx 75m$ at the end of the study period as seen in figure 5.10. The failure to capture this process suggests the presence of additional physics not included in this version of the model. Within the reference configuration of the model, after the spring shoaling, the only physical mechanism operating at the depth of the WW-UCDW interface is diffusion. Examining the model evolution of the WW-UCDW interface in figure 5.9, we see the model leaves the maximum depth of the winter water layer relatively unchanged after the mixed layer shoals in spring, and diffusively smears out the temperature and salinity gradient slightly. This fails to capture observed evolution of the stratification seen at depth below the mixed layer. Capturing the evolution of this WW layer is important as it serves to insulate the surface ocean from the warm UCDW. A shallower UCDW-WW interface in a subsequent melt season could influence sea ice growth through the feedback process suggested in Martinson (1990), whereby convective instability arising from sea ice growth entrains deeper water. Furthermore, a shallower UCDW layer is likely more readily able to flux large amounts of heat to the winter mixed layer due to storm events through the process examined by Wilson et al. (2019).

Within the confines of our model we can either attempt to explain this error through enhancing or varying diffusion throughout the water column or by introducing a new physical mechanism. It is possible that enhanced diapycnal mixing or larger eddy diffusivities are present at the interface between these water masses; however, diagnosing what value this should be is difficult without more sophisticated observations. We therefore instead focus on the inclusion of Ekman pumping which is readily implemented into the model and check the magnitude of the response before discussing estimates of missing processes later.

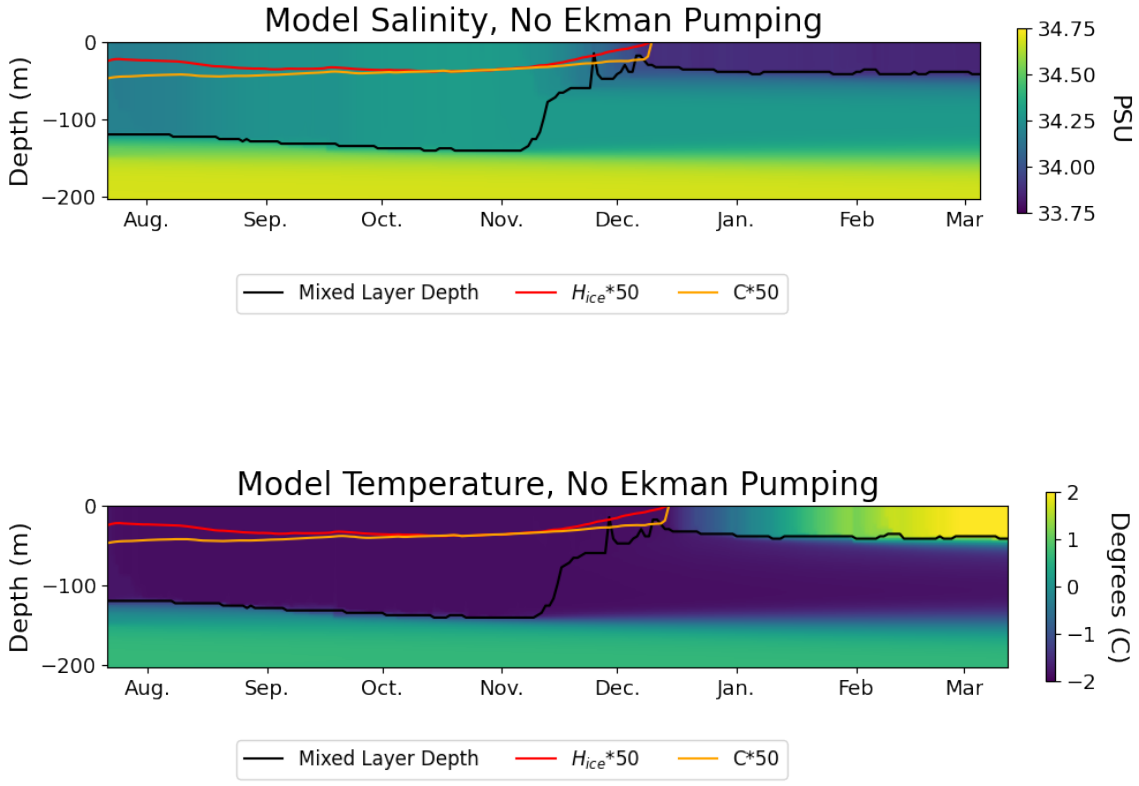


Figure 5.9: Seasonal evolution of salt (top) and temperature (bottom) within the hybrid model as laid out in §5.4 without Ekman pumping. Overlain are the mixed layer depth (black) as well as the ice thickness (red) and ice concentration (yellow) both scaled by a factor of 50 for visualization.

The effects of the inclusion of Ekman pumping into the model can be clearly seen in snapshots of the temperature and salinity profiles at various stages in the evolution of the water column in figure 5.10. In the surface 50m and the deeper ocean below $\approx 150m$ the configurations with and without Ekman pumping yield nearly the same results. In between these two regions however, a few key differences occur. Near the surface, we see that the mixed layer depth is shallower in the model run with Ekman pumping enabled. In the January and March profiles, this appears to be a deviation from the observations. As neither models have an enhanced diffusion at the mixed layer base due to internal wave breaking, or other processes to increase diapycnal mixing, it is possible that this may be remedied in the real-world system by a localized increase in the eddy diffusivities at the mixed layer base.

From 50m to 100m, we see that the thickness of the cold WW layer in the March profile is well characterized by the model run with Ekman pumping. In January, the model captures the upwelling UCDW feature better with constant Ekman pumping than without, though the error here is larger than in the March profile. This is potentially due to temporal variations in the ocean surface stress field and thus temporal variability in the Ekman pumping which has been omitted here for simplicity.

A number of excluded mechanisms could potentially add to the effect of Ekman pumping, and contribute to the observed shoaling of UCDW in the summer, such as mesoscale or submesoscale eddies. Some parameterizations of submesoscale eddies in 1D models have been implemented (Du Plessis et al., 2017), and a similar parameterization could reasonably be implemented for larger mesoscale eddies in a 1D ocean model. However, such parameterizations require information about the lateral gradients in temperature and salinity which are not available here. We can estimate the mixing time scale of mesoscale eddies by the quantity $t_{me} = L^2/K_{eff}$ where L is the mesoscale eddy length scale, and K_{eff} is an effective diffusivity due to mesoscale eddy effects. From Abernathey et al. (2010), values of K_{eff} in the Southern Ocean around 60s are $K_{eff} \approx 500$ m^{2}s^{-1} and a typical mesoscale eddy length scale of $L = 10km$ from Chelton et al. (1998) yields $t_{me} \approx 23$ days. The time period of this study is nearly 10 times this which suggests these eddies most likely contribute to the evolution of this system in addition to the well established mechanism of Ekman pumping we will be examining here. It is possible that the quasi-Lagrangian nature of the float profiles as discussed previously filters out some of the signal from these processes in this study.

A leading order impact of altering the WW-UCDW content in the profiles of figure 5.10 is the resulting change in heat and freshwater content shown in figure 5.11. Both of these quantities have potential to significantly impact the ice state in subsequent years (Wilson et al., 2019; Pellichero et al., 2017). In figure 5.11 we evaluate the impact of Ekman pumping by tracking the evolution of these quantities within both model runs, and comparing to the observations. We see a closer agreement of the model with the Ekman pumping included compared to observations. The model with Ekman upwelling has a water column for which the upper 200 meters contains both more heat and less freshwater than the model runs without, as deeper waters are advected upwards. At a basic level, the addition of heat via a shallower UCDW-WW interface has the potential to limit the winter ice growth through ventilation of UCDW during mixed layer deepening accompanying sea ice formation in the austral fall.

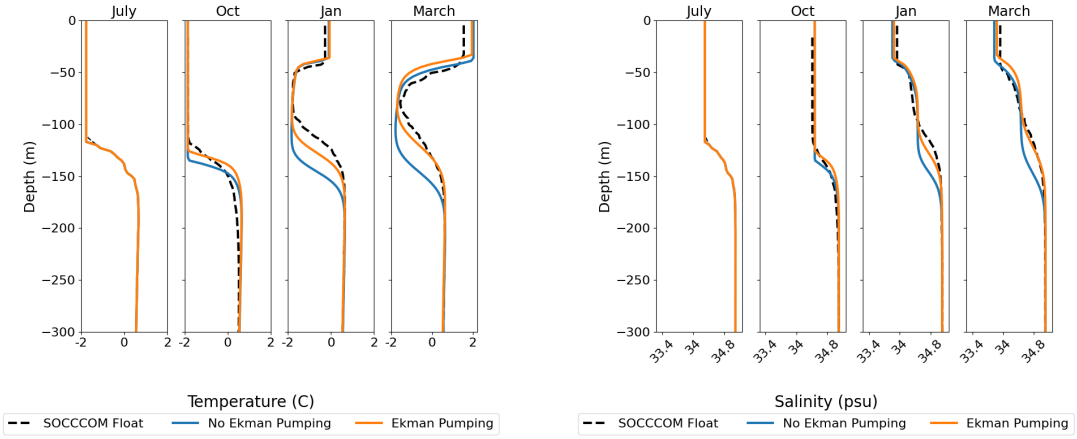
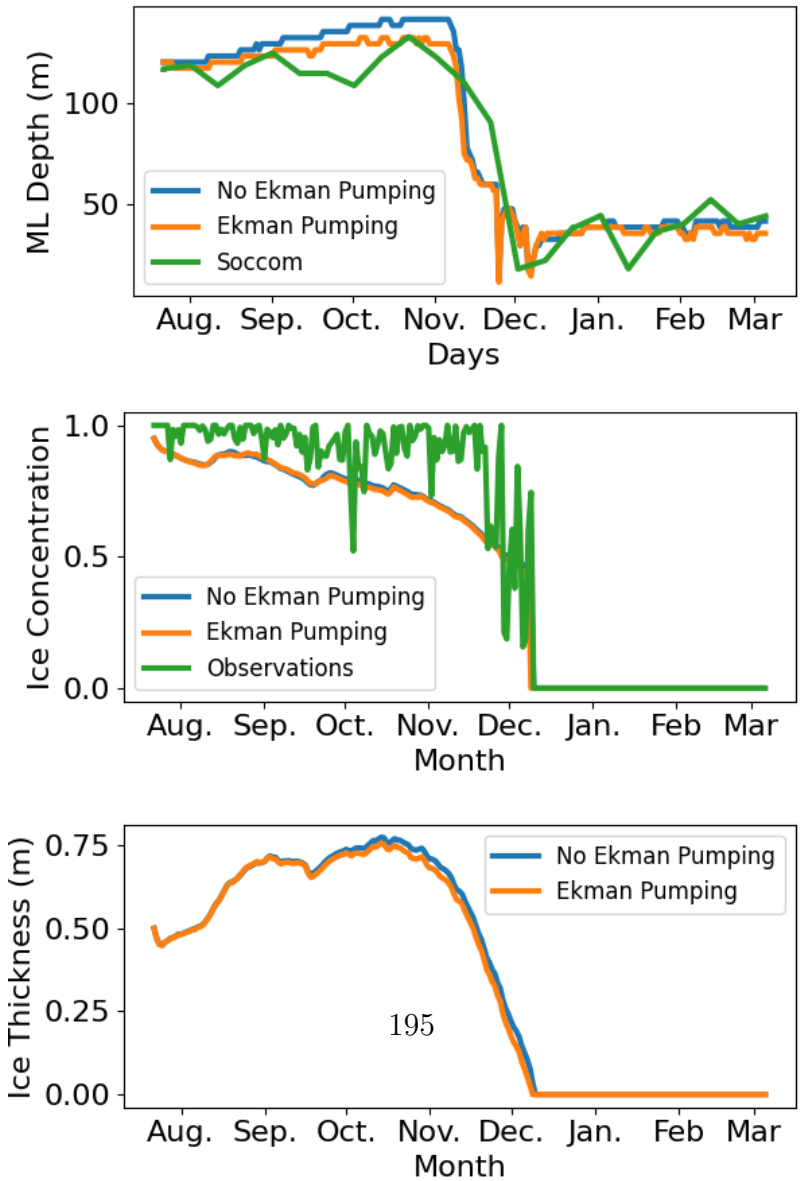


Figure 5.10: Vertical profiles of temperature (left) and salinity (right) at selected points in the time series for the model (dashed black) and model runs without Ekman pumping (blue line) and with (orange line). The months in which each profile was taken are given by the plot titles.



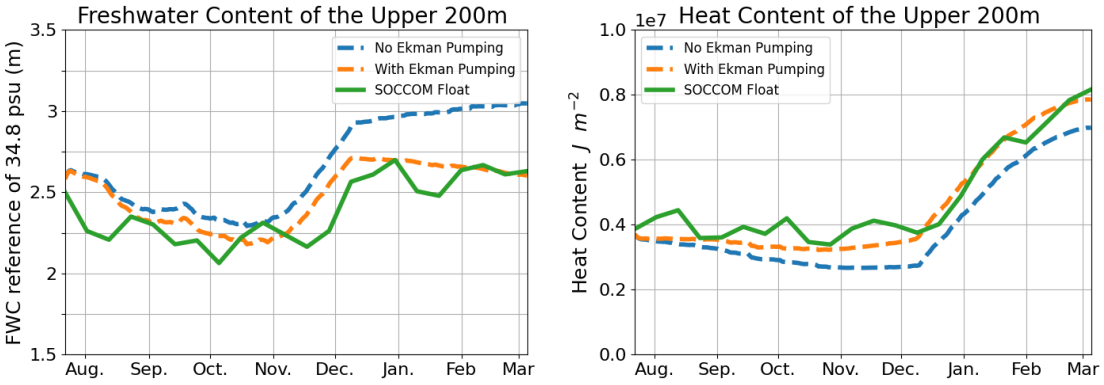


Figure 5.11: Evolution of the freshwater (left) and heat (right) contents of the upper 200m. Liquid freshwater content was calculated using a practical salinity of 34.8. The model reference run without Ekman pumping is shown as a blue dashed line, and the model with Ekman pumping as an orange dashed line, and SOCCOM float observations as a green solid line.

It is possible that these quantities, heat and fresh water content, better match observations for the wrong reasons. To build some assurance we can look at the adjustment of other observable metrics such as the mixed layer depth, and sea ice concentration/thickness when Ekman upwelling is included in the model as shown in figure 5.12. In these comparisons we see minimal variation in the temporal evolution of the ice thickness, or ice concentration. The agreement between modelled and observed ice melt out dates is surprisingly good given the simplicity of the model and that there has been no attempt at tuning parameters and initial conditions beyond standard or observed values, which gives added confidence in the treatment of ice thermodynamics. In both model configurations, the modelled ice decline is more gradual then observations indicating that the simple ice model used here misses some processes contributing to rapid ice decline. The winter mixed layer depth is slightly shallower (10m) and closer to observations in the model run with Ekman pumping.

We also use the exact systems method described above to examine how closely the evolution of the water-mass fraction matches up with the observational data, illustrated in figure 5.13. In the initial phase where sea ice is forming, the SML fraction in both model runs is negligible as expected. The onset of SML formation in both models in mid December lines up with the melt out day (date when $C = 0$) observed in figure 5.12. However, the observed onset of SML formation is approximately a week delayed. This delay could be due to the float sample rate of one profile every ≈ 10 days or from uncertainty in the sea ice concentration data for low ice concentration. Around February the model runs diverged with the Ekman pumping run SML levelling out at

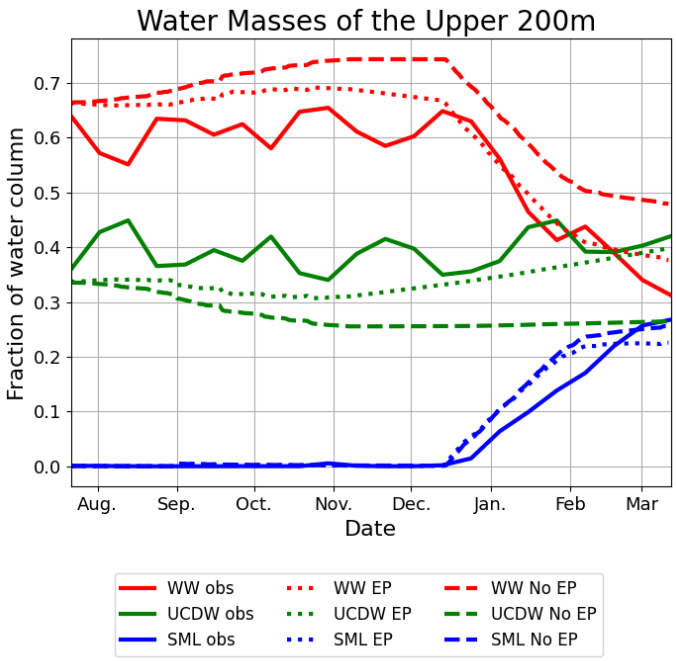


Figure 5.13: Fraction of the upper 200m partitioned into the three main water masses WW (blue), UCDW (orange), SML (green) as determined by the exact systems method for model runs with Ekman Pumping (dotted 'EP'), without Ekman pumping (dashed 'No EP'), and the SOCCOM float observations (solid 'obs')

a lower fraction than both the observations and the model without Ekman Pumping.

For the model run without Ekman pumping, the WW appears to increase from the starting value until the start of SML formation in mid December. This is in contrast with the observations which stay roughly constant, though with oscillations on monthly timescales. This same model run also under predicts the amount of UCDW with the UCDW fraction declining from the start of time-series until levelling out at a constant value around the start of November. This levelling out of the UCDW can be seen to correspond with the initiation of mixed layer shoaling as seen in figure 5.12, suggesting the modification of UCDW in the model without Ekman pumping only occurs with mixed layer deepening in winter.

With Ekman pumping turned on, the model evolution of WW and UCDW better matches the observed fractions throughout the time series. For this configuration, the WW fraction increases slightly until November indicating the start of mixed layer shoaling as in figure 5.12 where it takes a slight downturn. This downturn in WW fraction corresponds with the start of an upturn in UCDW and the point at which UCDW reaches the constant state in the model run without Ekman pumping. Following the cut off of the UCDW layer from direct exchanges with the mixed layer, the

UCDW water fraction increases approximately linearly corresponding to a constant upwelling. The inclusion of Ekman pumping generally improves the comparison to the observed water mass fractions. In particular, the comparison suggests that Ekman pumping appears essential for characterizing the increasing trend for UCDW fraction in summer, specifically it's contribution to displacement and thinning of the WW layer.

To determine if the role of Ekman pumping as seen here is prevalent throughout the SIZ, we can compare the magnitude of the Ekman pumping used in this model to Ekman pumping calculated from observational values of the surface winds in the Southern Ocean as shown in figure 5.14. Here we see that for summer values of the Ekman pumping the average magnitude as calculated by Carranza and Gille (2015) using 12 years of observational data appears largely consistent in magnitude along the latitudinal band of 60s. This suggests that the impact of Ekman pumping seen here may be relevant throughout the SIZ.

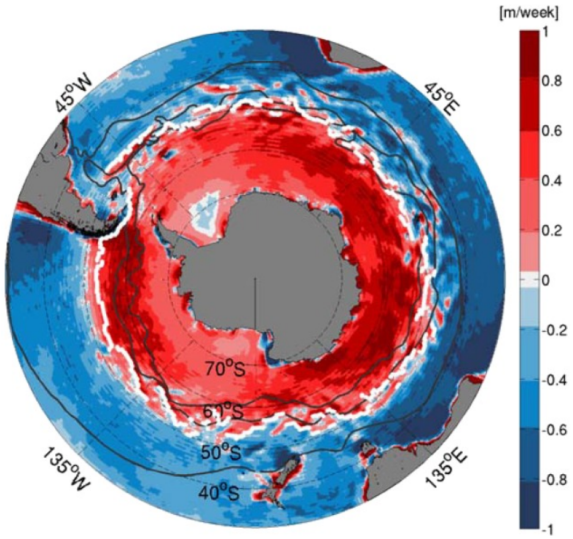


Figure 5.14: Average values of summer (DJF) Ekman pumping (m week^{-1}) for the Southern Ocean reproduced from figure 5a of Carranza and Gille (2015). Data shown is the average value of summer (DJF) Ekman pumping based on 12 years of 'Cross-Calibrated Multi Platform' wind data (2000–2011). Note that 1 m week^{-1} $\approx$ 1.65×10^{-6} m s^{-1} and so the value used in this work 1.40×10^{-6} m s^{-1} $\approx$ 0.85 m week^{-1}.

Both versions of the model fail to capture the apparent monthly oscillation in properties of the upper ocean structure seen here in the UCDW and WW fractions, in the MLD timeseries in figure 5.12, and the heat and saltwater components shown in figure 5.11. It is unlikely that this is due to internal waves due to the monthly

time scales. Similarly, submesoscale eddies often have time periods of order days (Biddle and Swart, 2020). It has been observed that both wind forcing and barotropic eddies in the Southern Ocean have monthly timescales which could contribute to this signal if they simultaneously excite vertically sheared flow or upwelling (Sinha and Abernathey, 2016). In particular, temporal variations in Ekman upwelling have been omitted from the model here. To better understand the importance of Ekman pumping on the observed upper ocean, we can test the sensitivity of the model to the chosen parameter values of table 5.1.

5.5.1 Model Sensitivity

It is important to view the impact of Ekman pumping in the context of other uncertainties and sensitivities of the model. We therefore look at how variations in the other free parameters could impact key model quantities. The values in table 5.1 represent characteristic or canonical values that are mostly observationally constrained, but in reality they vary spatial and temporally in a way not characterized here. Additionally, some parameters may vary as the sea ice state changes. To determine the sensitivity of the results discussed in §5.5 we vary parameters in the ranges given in table 5.2.

$R_{lat} \in [0.5, 1.0]$	$\nabla \cdot \mathbf{U}_i \in [0.2, 0.9]$ yr^{-1}	$H_{i,0} \in [0.1, 1.0]$ m
$A_0 \in [0.5, 0.95]$	$C_{d,a} \in [1, 2] \times 10^{-3}$	$W_{ek} \in [0, 2 \times 10^{-6}]$
$H_s \in [0, 0.25]$ m	$K_{T,S} \in [0.1, 10] \times 10^{-5}$	

Table 5.2: Variation of parameters to be examined in figures 5.16 and 5.15. In the model implementation Ekman upwelling was constrained using a default air-sea drag $C_{d,a} = 1.5 \times 10^{-3}$, Changes in $C_{d,a}$ do not adjust the Ekman upwelling velocity in this sensitivity study but alter the surface fluxes of heat and momentum as well as the mixed layer equations of 5.4.4.

The heat partitioning term, R_{lat} was varied over the range where basal heat was greater than or equal to the lateral heat flux as done in Petty et al. (2013). Variation of $\nabla \cdot \mathbf{U}_i$ and W_{ek} were chosen so as to span the range of values calculated from the reanalysis product over the time period for which the default value of table 5.1 was approximately the mean. $H_{i,0}$ and A_0 were varied so as to examine the potential impact of varied sea-ice states with low $H_{i,0}$ and A_0 seen to represent the effects of potential Antarctic sea ice decline. Variation in $H_{i,0}$ was taken within a standard deviation of the satellite and shipboard measurements reported in Kurtz and Markus (2012) and Worby et al. (2008). The snow thickness, H_s, should vary temporally over

the winter season, however we treated it to be a constant representative of the starting conditions of the study period. This variation was similarly informed within values observed in Kurtz and Markus (2012) and Worby et al. (2008). The model diffusivities were adjusted by an order of magnitude in an attempt to account for changes in the sea state while still being within the range used by other bulk mixed layer models in the Southern Ocean. In the geophysical system, this value is depth dependent and varies spatially and temporally; the variation done here is aimed at separating contributions of the diffusive transformation of UCDW from those resulting from our Ekman pumping characterization.

First examining the changes in water mass fraction shown in figure 5.15, we see the strongest changes occur due to variations in the ice advection, H_{i0}, $C_{d,ao}$, W_{ek} and H_s. Of these parameters only $C_{d,ao}$ and W_{ek} show significant variation in the change of UCDW. As these fractions must sum to 1 this means that the changes in ice advection, H_{i0} and H_s are balanced between WW and SML fractions. An inspection of the surface ocean metrics displayed in figure 5.16 shows that the sensitivity to ice advection, $H_{i,0}$ and H_s is primarily a result of the change in the melt out day occurrence and sea-ice growth. The ice advection into the domain results in a later melt out day, corresponding to a shorter window of SML formation. The change in initial ice thickness shows the same pattern because there is more ice to melt. This is partially but not completely compensated by ice growth, because thin ice grows faster from the larger conductive heat flux (proportional to $k(T_{ML} - T_f)/h_i$). The snow cover has an opposite effect, with increased initial snow cover showing a larger SML fraction balanced by a decrease in WW; this corresponds to an earlier melt out day caused by the impact of insulating snow cover on reduced ice growth in the winter period.

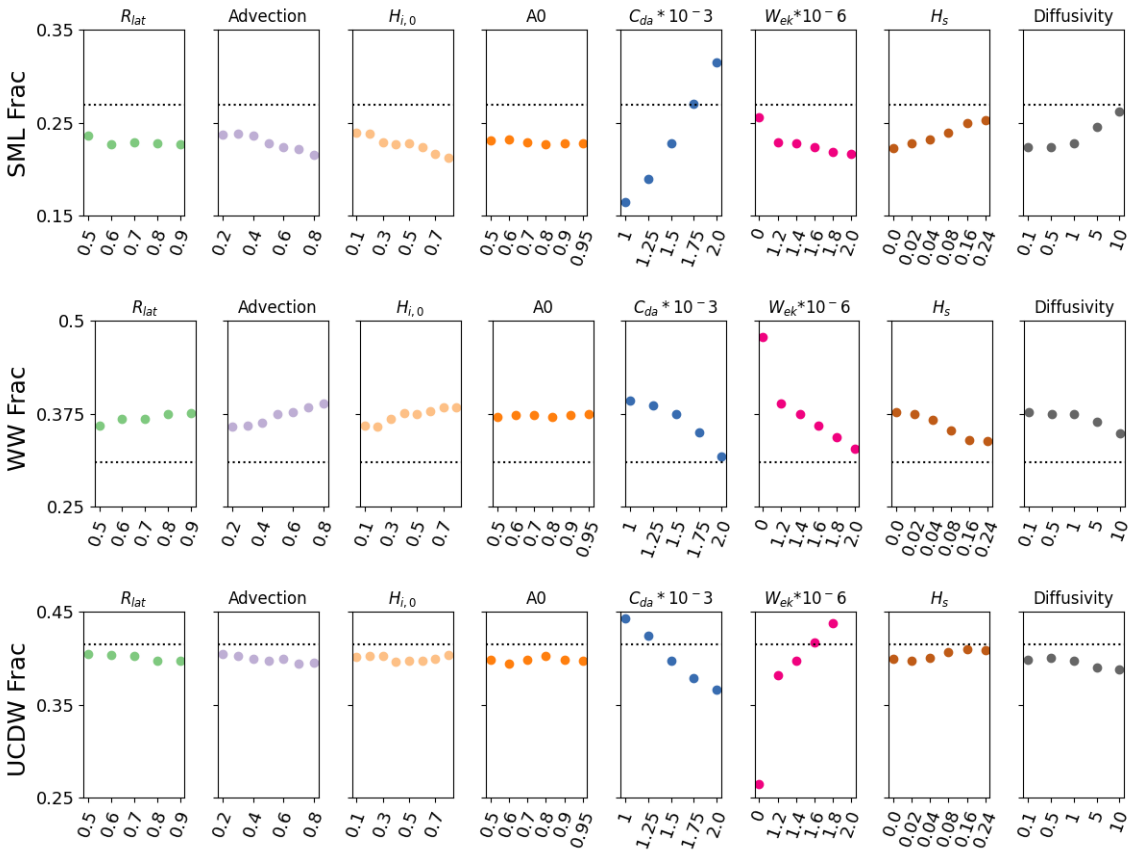


Figure 5.15: Sensitivity of water-mass fraction (Frac) to variations in model parameters. Black dotted lines represent the value derived from the SOCCOM float observations.

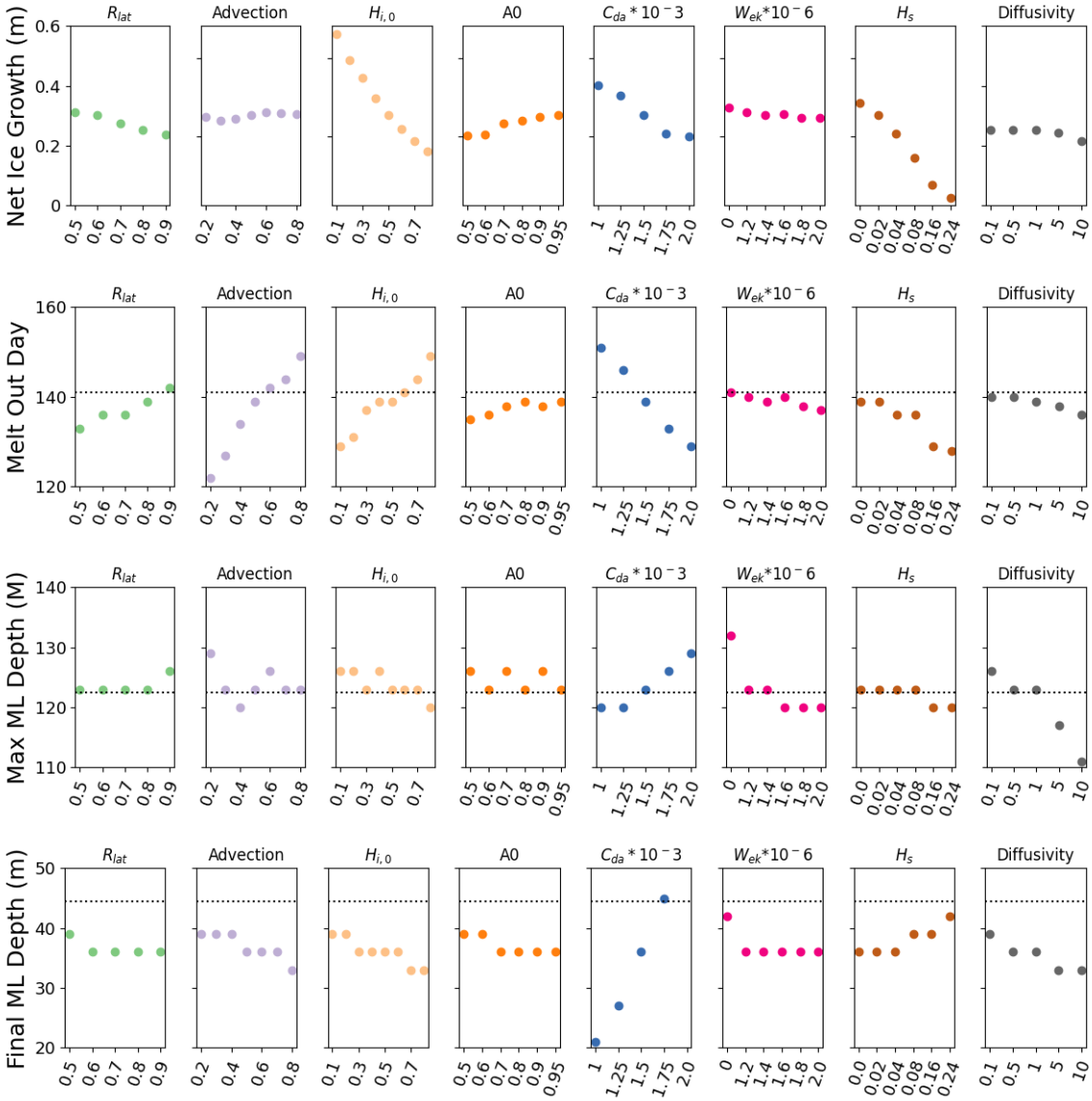


Figure 5.16: Sensitivity of selected metrics to variations in model parameters. Black dotted lines represent the observed value.

Unlike the parameters just examined, variation in the water mass fractions from changing $C_{d,ao}$ and W_{ek} occur in each of the primary water masses. In this sensitivity test, the changes here in $C_{d,ao}$ are ignored when calculating the value of W_{ek}, which is prescribed independently, and so the sensitivities of each are independent within the model. Hence, sensitivity to $C_{d,ao}$ indicates the efficiency of the surface fluxes of heat, salt and momentum. The only pathway for modification of the UCDW layer due to variation in $C_{d,ao}$ is when the UCDW is in direct contact with the mixed layer in the winter. We observe in figure 5.16 that an increase in $C_{d,ao}$ has a corresponding increase in the maximum mixed layer depth, and a deeper mixed layer at the end

of the time series. The former of these serves to indicate the strength of the winter mixed layer, which would allow for more entrainment of deeper UCDW waters. This sensitivity to $C_{d,ao}$ is consistent with enhanced energy input for shear driven mixing from surface winds, and potentially also a net negative (convective destabilizing) buoyancy flux, from enhanced sensible and latent heat loss to the atmosphere. In the full ocean column, increased $C_{d,ao}$ as well as increased W_{ek} may compliment each other and result in a larger transformation rate of UCDW. The Ekman induced upwelling plays a key role in the canonical picture of Southern Ocean overturning and water mass transformation as discussed in §4.1, and the results here suggest such Ekman pumping has a significant interplay with the contribution from seasonal water mass transformation in the seasonal ice zone.

Compared to the effects of $C_{d,ao}$ on the water mass fractions, changes in W_{ek} seem to have little effect on changes to SML indicating that any changes in WW are balanced largely by changes in UCDW. The patterns are broadly consistent with enhanced Ekman upwelling advecting the deep UCDW stratification through a greater portion of the domain, with the winter water increasingly advected upward to experience surface modification and transformation. In the real-world system, the quantity W_{ek} is influenced due to atmospheric patterns, ice concentration, $C_{d,ao}$, and many of the processes that influence ice-ocean drag as discussed in the previous chapters and reviewed thoroughly in Tsamados et al. (2014).

The observed sensitivity of the melt out day to ice advection, H_{i0}, H_s, and $C_{d,ao}$ could have consequences for subsequent ice growth/melt cycles. The duration of summer without sea ice sets the amount of heat the surface ocean is able to absorb and so the melt out day here controls the potential for heating of the ocean surface over the summer period. In subsequent periods of ice formation, this heat must be removed before ice formation can occur. In turn this may affect the net ice growth, and winter mixed layer depth. This points to two potential feedback mechanisms for a weaker ice state: 1) reduction of the period of sea ice formation due to excess heat absorbed in the upper ocean, and 2) shoaling of the UCDW due to weak winter mixing. If there is less ice growth due to the increased heat content of the mixed layer, the UCDW/WW interface may shoal as a result of reduced destabilizing buoyancy flux from brine rejection. A shallower UCDW/WW interface may allow for easier entrainment of the warm UCDW water in future periods of ice growth thus reducing sea ice growth rates similar to the feedback examined in Wilson et al. (2019), and Martinson (1990). Characterization of the long term feedback of either process on the multi-annual ice trends would require a study over longer time periods which is not

conducted here, though the model developed in this chapter could be implemented to study this in future work.

5.6 Conclusion

Whilst the Air-Ice-Ocean system features many inherently three-dimensional processes, simplified 1D models offer a lens with which to examine individual mechanisms contributing to the ocean stratification. Here we have used such a 1D model combining a hybrid bulk mixed layer ocean component from Biddle et al. (2017) with the sea ice model of Petty et al. (2013), and adding a treatment of Ekman pumping. It was found that an adjustment of the treatment of partitioning of lateral and basal ice melt (originally motivated by an attempt to resolve a closed energy budget) also led to more realistic predictions of the ice melt out date. By tracking the water mass evolution in temperature and salinity space, we were able to see that there was an under representation of UCDW in the modelled upper ocean when Ekman pumping was neglected. In the model configuration with Ekman pumping, an improvement in the evolution of the Winter Water and Upper Circumpolar Deepwater in comparison to SOCCOM float observations was observed. This suggests that Ekman pumping is a key mechanism for the evolution of the water column. It is possible that the physics represented in the current model would interact with wave or shear driven turbulence in the deeper stratification leading to a more complex eddy diffusivity or mesoscale or submesoscale eddy effects, but the available observations were insufficient to constrain these effects in the present model. A discussion of the relevant time scales suggests that such eddy-driven mixing would be a higher order effect over seasonal timescales, however. Furthermore, it is possible that the quasi-Lagrangian nature of the float filters out a number of 2D and 3D processes as it drifts with some of these features. This feature has been used to estimate mesoscale eddy fluxes at the so-called parking depth[1] of various floats as in Chapman and Sallée (2017).

We also examined the sensitivity of key diagnostics to model parameters in section 5.5.1. Here it was noted that the evolution of WW and UCDW showed the largest sensitivity to changes in the Ekman upwelling parameter. The insensitivity of this process to other model parameters supports the conclusion of this work that Ekman upwelling is a leading order term in the evolution of UCDW and WW on seasonal timescales. The parameters for initial ice thickness, ice advection rates, and the

[1]The parking depth of float profilers is defined as a depth where the floats often sit for 5-15 days. Typical values of this depth are 500m and 1000m.

snow depth were seen to appreciably alter the melt out day as well as the net ice growth. This may set up a feedback whereby earlier sea-ice melt results in later sea-ice formation at the end of the season. This decreased sea ice formation would result in thinner ice and potentially impact the meridional buoyancy gradients via alterations to the expected northward ice transport within the SIZ. Reduced local ice formation may also allow for the shoaling of UCDW compared to seasons with strong sea ice formation by inhibiting the convective instability arising from reduced brine rejection. Shoaling of the UCDW layer increases the heat content of the surface ocean and may inhibit subsequent ice formation via entrainment. To quantify the potential role of this feedback a more detailed study on local ice formation in the region would be needed as much of the ice at the start of our study is likely ice advected from waters closer to the Antacrctic continent (Pellichero et al., 2018).

The model used in this study has neglected many of the 2D and 3D processes that affect the vertical structure of the ocean. Furthermore, in this work we have neglected the temporal evolution of some key processes. Ice advection, snow thickness, and eddy diffusivity are known to vary spatially and temporally in the region. Exclusion of temporal variation in the ice advection scheme could account for the error seen when comparing the model output ice concentration with the satellite observations shown in figure 5.12. From observations, the ice concentration in the region was seen to vary rapidly on short timescales with the concentration held closer to $C = 1$ until a rapid reduction in ice concentration occurring at melt out. This stands in contrast with the predicted gradual decline of ice concentration from the model output. The neglected temporal variance of the Ekman pumping may contribute to the nearly monthly oscillations seen throughout much of metrics observed by, or derived from, the SOCCOM float observations. These, however, may also be due to synoptic forcing or geophysical wave dynamics causing heaving of the pycnocline. Neglecting the evolution of snow cover most likely results in an over estimate of sea ice growth in the model. This enhanced ice growth in turn may affect entrainment of the UCDW layer in winter by over estimating convective instability due to increased destabilizing buoyancy fluxes from brine rejection. The treatment of eddy diffusivities as constant, depth independent quantities in bulk mixed layer models is common (Price et al., 1986; Wilson et al., 2019; Biddle et al., 2017; Du Plessis et al., 2017; Martinson, 1990). However, actual eddy diffusivities are known to be both spatially and temporally heterogeneous (Abernathey et al., 2010; Marshall et al., 2006; Smith and Marshall, 2009). In particular, enhanced turbulence at the base of the mixed layer as a result of internal wave breaking, near-inertial oscillations, and other processes is known to

occur (Fernández-Castro et al., 2014). It is possible that this neglected variation in diffusivities may contribute to some of the remaining differences between model and observations seen in this study. We here have also neglected double diffusive effects by setting the diffusivities for temperature and salinity the same. It is possible that double diffusive effects could be important for determining any impact from variations in the UCDW depth on longer timescales, as suggested by Abernathey et al. (2016).

Recent studies have established the importance of observed changes in Southern Ocean sea ice extent, thickness, and regional distribution (Parkinson and Cavalieri, 2012; Parkinson, 2019; Cavalieri and Parkinson, 2012), which have the potential to strongly influence surface water-mass transformation in the Southern Ocean (Pellichero et al., 2018; Abernathey et al., 2016). These studies have predominantly examined the processes of water-mass transformation on annual or multi-annual time scales and on basin scales where it is widely acknowledged that Ekman transport and Southern Ocean upwelling play key roles in the overturning circulation. Here we have sought to characterize specific processes that set the seasonal evolution of these quantities. In doing so we have identified the importance of a singular process, Ekman pumping, on the erosion of the WW layer, and the shoaling of the UCDW layer. As Ekman pumping is determined by the ocean surface stress, which is in turn affected by the presence or absence of sea ice, changes in the Antarctic sea-ice state may alter the water-mass transformation rates examined in these studies.

Though this simple model lacks many features of the full system, the insight provided into the potential role of the various processes is useful. This study demonstrates that Ekman pumping is an important contributor to the evolution of upper ocean water masses within the seasonal ice zone. Two primary observations were made in regards to the role of Ekman pumping in the study region: 1) Ekman pumping, together with surface mixing, sets the evolution of the WW layer on seasonal timescales and 2) Including the effects of Ekman pumping in this model resulted in a more saline surface ocean containing more heat, with potential feedbacks on subsequent ice growth-melt cycles. The impact of seasonal surface fluxes and Ekman pumping will undoubtedly act in concert with other processes including eddies or advection of water masses, in order to control the stratification of the seasonally ice covered ocean in the Antarctic. However here we have demonstrated their importance for recreating the observed ocean column, suggesting that explicit investigation of these processes on longer time and length scales is imperative for accurately characterizing the impacts of a changing ice state.

Chapter 6

Conclusions

Both the Arctic and Antarctic sea ice states are undergoing rapid changes and commonly seen to be a bellwether of climate change. Understanding the interactions between sea ice and the underlying ocean is imperative for accurate predictions of regional and global changes. In recent decades, the study of these ice-covered regions has become an increasingly active topic of research. This is in part due to the increased observational capabilities which have been able to provide key insight into the ice-covered oceans (Armitage et al., 2016; von Albedyll et al., 2020; Swart et al., 2019; Riser et al., 2018a; Lee et al., 2012; Treasure et al., 2017; Planck et al., 2019; Toole et al., 2011; Roquet et al., 2013).

As a result of these new observational capabilities, a number of previously understudied physical processes have been identified. Ice tethered profilers and other autonomous profilers have allowed for an increased understanding of the freshwater content and eddy activity in the gyre as discussed in Manucharyan et al. (2016) but study of the ocean velocities was often neglected. Following the detailed estimate of geostrophic velocities in the Beaufort Gyre in Armitage et al. (2016), the importance of the ice-ocean governor was established (Meneghello et al., 2018a). Observations of the ice-ocean boundary layer (Cole et al., 2014, 2018) have provided new insight into the evolving internal wave field in the under ice boundary layer. Similarly, the increased density of under-ice observations in the Antarctic (Riser et al., 2016; Roquet et al., 2013) has allowed for improved understandings of water-mass transformation (Pellichero et al., 2017, 2018; Abernathey et al., 2016). With regards to bulk mixed layer models, the early work often sought to characterize broader feedbacks as in Martinson (1990) whereas these modern observations have allowed studies to examine the role of specific processes (as in Frew et al., 2019; Biddle et al., 2017; Wilson et al., 2019), or regional variations (as in Petty et al., 2013; Du Plessis et al., 2017).

Within this thesis, we have investigated the importance of several understudied aspects of the ice-ocean boundary layer and their corresponding implications for larger regional scale systems. In chapters 3, 4, and 5, three scientific topics were examined using three different mathematical models developed within this thesis work. A lattice Boltzmann framework described and tested in chapter 2 was used in chapter 3 to simulate stratified ocean flow beneath a ridged ice floe. The generation of internal waves was observed to strongly impact the heat and momentum fluxes at the ice-ocean boundary. In chapter 4, these results were used to examine the potential impact of internal wave drag on the vertical structure of an ice-covered gyre using a hierarchy of models. Lastly, in chapter 5, we modified a 1D ice and ocean bulk mixed layer model and compared it to observations in the seasonal ice zone of the Antarctic Ocean, where we identified the importance of vertical Ekman velocity for seasonal water-mass transformation. In this section, we will first review the key results of each chapter, before examining the broader conclusions and implications of this thesis work as a whole, and possibilities for future work.

6.1 Summary of scientific results

6.1.1 Effects of sea ice generated internal waves on the ice-ocean boundary layer

In chapter 3, we examined stably stratified ocean flow beneath a ridged ice floe using the computational infrastructure developed and tested in chapter 2. We began by examining an idealized picture of a cold, fresh, sea ice floe moving over a stagnant ocean stably stratified in both temperature and salinity. Consistent with previous work on stratified shear flow over topography, we found that the key flow regimes are characterized by a Froude number, $Fr_h = \sqrt{\frac{U^2}{hg\beta\Delta S}}$, or equivalently by the parameter $Nh/U = 1/Fr_h$, which depends on the obstacle height h, flow velocity U, and stratification with buoyancy frequency $N = \sqrt{g\beta\Delta S/H}$. Here subcritical flow with $Fr_h < 2$ corresponds to internal wave formation and super critical flow with $Fr_h > 2$ is the evanescent wave regime.

For our model, we observed qualitative and quantitative agreement with results from existing theory for a variety of flow properties. For $Fr_h < 2$ internal waves were observed whose wavelengths increased with Fr_h. At small $Fr_h < 0.5$ flow blocking was observed in agreement with the linear theory of Baines and Guest (1988) and the model results of Winters and Armi (2012). For the triangular ridge considered here this blocking was observed to correspond to an intensified subsurface jet over the

ridge similar to the results of Winters and Armi (2012) for a semi elliptical ridge with internal waves observed down stream of the ridge. For $0.5 < Fr_h < 2$, blocking was not observed, however upstream and downstream internal waves were observed with wavelengths given by $\lambda = 2\pi U/N = 2\pi h Fr_h$ consistent with past theory (Baines, 1998). For $Fr_h > 2$, no internal waves were observed, instead evidence of flow separation from the ridge tip with the downstream side of the obstacle characterized by a pool of stagnant fluid in the shadow of the ridge.

A key result of this model was quantifying the momentum flux at the ice-ocean interface in terms of a drag coefficient $C_{d,io}$ assuming a quadratic drag law. In simulations with $Re = 100, 250, 500$ a range of $0.2 < Fr_h < 100$ was explored. It was found that in the wave-free regime for $Fr_h > 2$, the drag coefficient was approximately constant yielding a neutrally stratified drag coefficient. In the regime with internal waves for $Fr_h < 2$, the drag coefficient was seen to vary by an order of magnitude according to a power law relationship $C_d = C_{d,0} + AFr_h^n$. Power law fits to the data for each Reynolds number yielded exponents $n = -1.77, -2.32, -2.69$ for $Re = 100, 250, 500$ respectively. This range of n is within the range $-3 < n < -1$ predicted by the broader literature (McPhee and Kantha, 1989; Baines, 1998), with n decreasing towards the nonlinear limit $n = -3$ as the Reynolds number increases. A qualitative agreement of $C_{d,0}$ as a function of Reynolds number was established in comparison to the well known Blausius scaling of $C_{d,0} \propto Re^{-1/4}$ for modest Reynolds numbers, although we would expect this to asymptote to a constant value in a well developed turbulent regime (Blasius, 1913; Goldenfeld, 2006). The significant increase of the drag coefficient at low Froude number due to wave drag is likely significant for ice-ocean momentum transfer.

The ice-ocean heat flux of this setup was investigated in §3.3.3 using two configurations with different thermal stratification of the inflow. For the configuration of the model with maximum temperature of the inflow at the top boundary which was motivated by an ice flow moving over a warm radiatively heated summer mixed layer, a maximum value of the heat flux was observed for $Fr_h \approx 0.8$. As Fr_h increased, the heat flux decreased to a constant value approximately 10% lower than the maximum heat flux at $Fr_h \approx 0.8$. As Fr_h decreased for $Fr_h < 0.8$, the heat flux also decreased with a maximum change of $\approx 15\%$ from the maximum heat flux. Whilst the net change to the heat flux is relatively modest, there were interesting spatial patterns. For $Fr_h < 2$, we noted amplified heat transport over the ridge accompanied by oscillatory spatial variations downstream of the obstacle corresponding to the internal wave peaks and troughs. Upstream of the ridge for $Fr_h < 2$, signs of a developing

boundary layer were noted. We also examined a case where the inflow temperature profile is continuous at the ice-ocean boundary, and increases with depth motivated by a winter scenario where the ocean in leads between the ice is cooled from above and close to freezing at the surface. This unstable temperature profile yielded essentially dynamically similar flow to the stable temperature case but modified the heat transfer. For this unstable temperature profile the heat flux for $Re = 500$ was observed to continually increase as $Fr_h \to 0$ in qualitative agreement with the model of Skyllingstad et al. (2003), and the observations of Perovich et al. (2003). A key result of this work is that the order of magnitude changes of drag coefficient at low Froude number were not replicated in the heat flux. Heat flux parameterizations commonly use a friction velocity $u^* \propto \sqrt{C_d}U$, but the work here suggests that it would not be appropriate to include the enhanced wave drag contribution to C_d in such a heat flux parameterization. Conducting a similar investigation into the spatial properties of the heat flux as before revealed that the upstream heat flux was markedly reduced compared to the previous stable temperature case. In both stratification cases the heat flux demonstrated an oscillatory pattern downstream and amplified heat flux over the ridge. Whilst melting feedbacks were not included in the current model, the predicted spatial variations in heat flux may lead to enhanced melting of the ridge, and generation of ice topography by differential rates of phase change downstream of a ridge.

We concluded the work of this chapter by examining the sensitivity of the results to the ridge distance from the inlet, as well as a few differing ridge geometries for the stable temperature stratification. For $Fr_h < 2$, without flow blocking, the total heat flux was nearly independent of the location of the ridge, though the heat flux over the ridge was affected with increased distance from the inflow yielding a reduced heat flux. However, accounting for all variations of heat flux upstream, over and downstream of the ridge, the results are approximately consistent with the total heat flux to the floe corresponding to a uniform background heat flux multiplied by the total length of the floe, plus an increment due to local interactions with the ridge (that depends on Fr_h and Re, but not the precise placement of the ridge). The triangular and Lorentzian witch of Agnesi ridge geometries were observed to produce similar changes in heat and momentum fluxes whilst a significant reduction in heat and momentum flux was observed for the flat ice floe.

The conclusions of this study are largely limited by the modest Reynolds number compared to geophysical values several orders of magnitude larger. Furthermore, the simulations presented here were purely 2D and thus neglect rotational effects,

3D turbulence, and 3D variance in ridge geometry. We also neglected a rigorous treatment of ice melting, upstream evolution of the flow, and ridge porosity. From the broader literature on the topic, we expect these quantities to effect the critical point of the Froude number, as well as the magnitude of the characteristic flow speed by either flow through the ridge, melting of the ridge, or flow around the ridge. Therefore, inclusion of these effects would likely result in a quantitative change in the magnitudes of the changes predicted via spatial and temporal variations in the parameter Nh/U. However, the predictions made here may be seen to represent the mean state of this parameter in the real-world system.

6.1.2 Effects of internal wave drag and rheology on the vertical structure of the Beaufort Gyre.

Having observed the potential for order of magnitude changes in the drag coefficient due to wave drag, in chapter 4 we explored the potential larger scale consequences using an idealized formulation of the Beaufort Gyre. In this endeavour, we adapted a previous ocean theory, developed a new conceptual model of ice deformation with viscous rheology, and made some initial attempts to investigate a coupled ice-ocean model to examine the potential for internal wave drag to affect the vertical structure of the Beaufort Gyre and motion of the overlying ice cover.

I began the analysis by modifying the ocean-only model of Manucharyan and Spall (2016) to include variations in the ice-ocean drag coefficient due to internal wave generation. The model of Manucharyan and Spall (2016) characterized the Beaufort Gyre as a balance between surface accumulation of freshwater due to Ekman transport and mesoscale eddy induced flow at depth arising from baroclinic instabilities. With our modifications, appreciable variations in the freshwater content and isopycnal shape were observed accompanying variations in the wave drag exponent, n, when the relative ice-ocean velocity was assumed fixed. If instead the total ice-ocean torque is fixed, the change to freshwater volume is reduced, but there are still significant changes in the spatial variation of the isopycnal depth which would impact local eddy activity and detailed patterns of geostrophic flow. We then examined the difference in isopycnal depth arising from different choices for how the relative ice-ocean velocity varies with gyre radius. Here two cases were examined, a linear profile, loosely representative of ice in solid body rotation, and a sinusoidal profile which could be seen to approximate a state where the ice velocity decays at the edge of the gyre due to significant friction. An uncertainty study was conducted examining

the potential effect of variations in the default parameter choices within a geophysically motivated range. In line with expectations from recent work of Meneghello et al. (2020), the strongest dependence was observed to be on the ice-ocean relative velocity, with wave drag effects also playing a substantial role in regimes with strong stratification (representative of summer conditions).

In §4.5.1, I developed a theoretical model for axisymmetric sea ice motion over the gyre, assuming a simplified viscous rheology that neglects complications due to plastic ice deformation, but allows the key effect of lateral transmission and accommodation of stresses in the ice. To build initial insight, I then derived an analytical solution for the simplified case of a drag law that varies linearly with velocity. I then developed a numerical continuation method to solve the full nonlinear model of (4.36) for a characteristic winter and summer stratification value, and also in the no-slip and free slip limits for ice boundary conditions at the gyre edge. In the strong stratification regime, we saw that wave drag effects could significantly impact the ice velocity as well as the spatial distribution of ice-ocean stress. It was observed that with stress free boundary conditions, the ice approximately moves via a rigid body rotation (with negligible lateral viscous shear stresses throughout the gyre). In the no-slip limit, both ice velocity and ice-ocean stress were observed to have a similar spatial distribution as the constant drag case, albeit with a shift in peak velocity and stress towards the gyre edge. Despite the spatial similarities, the magnitude of the ice velocity was reduced. However, due to the increased ice-ocean drag coefficient the total stress was observed to increase. A number of partial slip conditions were examined for both stratification cases. These partial slip conditions are loosely motivated by an axisymmetric description of area averaged boundary conditions for the spatial heterogeneity in ice conditions at the gyre extent. As the slip parameter Υ increases, the ice internal stresses increase thus transmitting less of the atmospheric torque to the ocean. It was found that for large Υ, increasing the stratification reduced the ice internal stresses as a result of increased efficiency for momentum transfer at the ice-ocean interface.

A sensitivity study for the model parameters was conducted which concluded the largest sensitivity of the model was due to the atmospheric and ocean velocities which control the magnitude of the forcing. For the larger stratification considered, appreciable sensitivity was found for each of the wave drag parameters, n, A, and $Fr_{h,0}$ along with the sea ice shear viscosity η. For no-slip boundary conditions, both the linear analytic calculation and selected nonlinear numerical solutions show that

reductions in the ice viscosity lead to thinning of the viscous boundary layer at the gyre edge, and an increase in peak velocity.

Using a selection of variable slip runs, I examined the predicted isopycnal depth using the ice-ocean stress calculated by the rheology model. Motivated by existing work on the topic and the established sensitivity to the ocean velocity in both this rheology model, and the previous ocean model, we used this isopycnal slope to calculate a geostrophic velocity. The resultant geostrophic velocity was an order of magnitude larger than the initial profile supplied to the ice model. This suggests that the ocean would have a strong stabilizing response, reducing the relative ice-ocean velocity in line with the ice-ocean governor mechanism (Meneghello et al., 2018b)

In each of the models developed for this section, regimes where wave drag could significantly alter the Beaufort Gyre were observed. These effects manifested in significant changes to the predicted freshwater content of the gyre in §4.4. In §4.5 we observed further significant impact on the spatial profiles of ice velocity and ice-ocean stress as well as on the net ice internal stresses. In regimes where the modified wave drag parameterization did not appreciably alter the net ocean surface stress across the gyre, local enhancement of stress was observed which may affect smaller scale processes at the ocean surface. It is important to note that the impacts identified in sections 4.4 and 4.5 result from one way coupling between ice and ocean, with specified forcing of one component leading to response of the other without a feedback on the original forcing. Hence the results give an initial indication of the potential effects of wave drag on the gyre system, and motivate further study using fully coupled models to fully characterise the impacts after accounting for all feedbacks. An initial attempt to couple these models was presented in §4.A, but numerical issues arose preventing an exhaustive study of this model within this thesis. The model breakdown hinted at a breakdown of the assumptions underpinning the steady TEM theory (with localised outward Ekman pumping likely to transiently drain the gyre) suggesting that a time-dependent model may be necessary to fully capture the feedbacks with strong wave drag.

6.1.3 Seasonal evolution of upper ocean water masses in the Antarctic seasonal ice zone

In chapter 5, we shifted our focus to the Southern Ocean where we investigated the role of ice processes and Ekman pumping on the seasonal transformation of Upper Circumpolar Deep Water (UCDW) and Winter Water (WW) in the seasonal ice zone. The model developed in this chapter drew upon two previous bulk mixed layer and

ice models (Biddle et al., 2017; Petty et al., 2013). The ice model of Petty et al. (2013) was modified to conserve energy in the partitioning of surface ocean heat for lateral and basal melt. A key addition to these models was the implementation of Ekman Pumping into the ocean dynamics.

I first applied the model without the inclusion of Ekman pumping and compared to the seasonal evolution of upper ocean stratification as observed by SOCCOM floats. Here we observed that this version of the model did a reasonable job of characterizing the evolution of the surface mixed layer properties. Additionally, this model successfully recreated the timing of total sea ice melt after incorporating the energy conserving treatment of basal melt. Despite the accuracy seen for mixed layer characterization, it was observed that below 100m the model had large errors in the ocean stratification, heat, and freshwater content in the upper ocean. This configuration without Ekman pumping over-predicted the freshwater content of the surface ocean, and under predicted the heat content. Changes in these heat and salt budgets of the upper ocean could impact the typical mixed layer evolution of the region (Pellichero et al., 2017) or the transformation of circumpolar deep water during winter (Pellichero et al., 2018).

With the inclusion of Ekman upwelling, the overall agreement with observations was significantly improved. This version of the model more accurately recreated the mixed layer depth and properties as well as the stratification throughout the surface 200m over the observational period of the SOCCOM float. This consequently improved the model evolution of the heat and freshwater content of the upper ocean.

Comparing the evolution of the water masses, we found that after the shoaling of the mixed layer in November, the model run without Ekman pumping predicted little change in the UCDW fraction for the rest of the study period. The WW layer was also approximately constant from November until the formation of the summer mixed layer (SML) in mid December (austral summer). In these periods both water masses could only transform via the constant eddy diffusivity of the model. With the inclusion of Ekman pumping, the model accurately characterized the evolution of UCDW and WW layers as observed in the SOCCOM float data.

To examine the sensitivity of the model to the chosen value of parameters, I did a broad uncertainty study examining the final values of the water masses as a deeper ocean metric as well as observed surface ocean metrics such as the sea ice growth, sea ice melt out day, maximum winter mixed layer depth, and the final summer mixed layer depth. From this uncertainty study, we saw strongest sensitivity of the water mass fractions to the Ekman pumping magnitude, and the air-sea drag coefficient.

Of these two sensitivities, only the Ekman pumping predicted the observed WW decrease to be attributable to an increase in UCDW. Each of the surface ocean metrics examined demonstrated insensitivity to changes in the Ekman upwelling velocity.

The results of this section suggest that Ekman pumping alone may be sufficient to explain the observed evolution of UCDW and WW. The model used included no parameterizations of larger scale eddies, or advective processes and idealised the quasi-lagrangian drift of the float as observing ocean properties which were representative of a region near 60S and 0E. In this sense, these results serve to illustrate the characteristic water-mass evolution of the region over a single season. Here we have only looked at one season, and one location, so the full regional significance of this balance awaits full confirmation. However, the results presented are consistent with larger scale theories of Southern Ocean water mass transformation and overturning circulation that rely on wind stress driving Ekman pumping. The results here are indicative that in addition to these processes, Ekman pumping is also relevant to the seasonal evolution of water masses in seasonally ice-covered oceans. It is possible that on longer timescales, the slower processes neglected here may influence the evolution of the SIZ. A straightforward follow on to the work presented would be to apply this model to a region with different characteristic ice cover or vertical structure to verify the robustness of the method. Additionally, examination of multi-annual evolution of the region would provide insight for how alterations to the upper ocean heat and freshwater content as well as the water-mass fraction influences subsequent ice-growth/melt periods.

6.1.4 Future work and broader perspectives

Each topic of this thesis, though different in scope and scale, has been motivated by a single pervasive thread: How do small scale processes of the under-ice boundary layer impact the larger scale ocean structure and evolution. In each chapter a unique computational framework was developed which could be used and extended for a number of straightforward follow on studies. Though outlined in the individual chapters, we will briefly reiterate the key questions here to motivate the broader questions raised by this work.

Chapter 3

1. What are the impacts of double diffusive effects in the molecular sub-layer at the ice-ocean interface on the predicted heat and salt fluxes?
2. How do variations in the aspect ratio of the ridge alter the predicted heat and momentum fluxes?

3. How does the ice roughness evolve under the observed spatial variation in heat? Such an approach would require a description of phase change in the model.

Chapter 4

1. How are the predicted effects of varying drag coefficients due to internal wave drag represented in a fully coupled model?
2. How do the predicted impacts of internal wave drag manifest in the time dependent system?
3. How do variations in the ice-ocean drag coefficient as a result of processes other than wave drag (e.g. varying roughness, concentration, floe size distribution) impact the Beaufort Gyre?

Chapter 5

1. How well does the current model characterize other regions of the SIZ?
2. How do variations in Ekman upwelling rates affect the evolution of the SIZ on multi-annual timescales?
3. What impact does shoaling of the UCDW have on subsequent sea ice growth/melt cycles?

Beyond the questions immediately flagged by this work, some broader questions about the role of sea ice in the polar oceans are discussed below. Specifically, what is the role of the processes examined here in the changing Arctic and Antarctic?

In chapter 3, a relationship between stratification, ice roughness, and ice-ocean fluxes of heat and momentum was established. A changing Arctic will likely see a decrease in ice thickness and roughness (Guarino et al., 2020). This thinning of sea ice will result in the increased mobility of ice floes. Both a reduction in ice roughness, and an increase in ice-ocean relative velocity alter Fr_h in a way that would decrease sea ice generation of internal waves, and the momentum flux. In regions where sea ice wave drag is a large component of the ice-ocean drag (such as those with strong surface stratification), this may cause an unexpected rate of change in ice drift and basal heat transfer. Furthermore, during sea ice retreat in the spring, ice melt will freshen the upper ocean, increasing stratification and the significance of wave drag, which may influence the upper ocean mixing. As ice-concentration continues to decrease, this is potentially cancelled out by an increase in wave-driven mixing which would destratify the upper ocean. In this scenario, the concentration of ice floe edges would increase. The LBM framework used in this chapter could be modified to examine lateral vs basal melt of ice floes and internal wave effects from these floe edges.

The results of chapter 4 offer an additional mechanism of adjustment for the response of the Arctic to thinning ice cover. The predicted reduction in ice concentration and drag may decrease the effective viscosity of sea ice due to decreased frequency and strength of floe interactions. With atmospheric and oceanic velocities fixed, our model predicts increased ice mobility with decreased shear viscosity for a gyre with significant stress at the gyre edge. Observations and model work indicate that there is a strong stabilising feedback on the Beaufort Gyre freshwater content from seasonal variations in the ice velocity (Meneghello et al., 2018a; Wang et al., 2019a). In the winter, the ice cover of the gyre experiences substantial stress at the boundary resulting from coastal land fast ice, and thick ice in the Arctic interior. In contrast to the steady isopycnal model that is appropriate for multi-annual timescales, the sea ice model developed here describes a quasi-steady response on timescales longer than the ice acceleration of a few days (Rallabandi et al., 2017) and is appropriate for characterizing seasonal changes. Furthermore, as the Arctic ice state continues to evolve, this winter configuration may instead be characterized by one of the intermediate values of Υ, the lateral slip parameter examined in figure 4.13. Alterations to the partial slip parameter could eliminate the negative stress at the gyre edge corresponding with Ekman upwelling. Thus, not only is the changing ice state within the gyre important for predicting seasonal variation in vertical Ekman transport, but so too is the ice state of the broader Arctic Ocean.

A more accurate characterization of the gyre rheology would include the effects of plastic rheology. A primary effect of plastic deformation under shear stress is on the spatial variations in velocity (Rallabandi et al., 2017). Accounting for this process may provide pathways for local variations in the sign and magnitude of Ekman upwelling/downwelling in the gyre such as the increased Ekman upwelling observed in Meneghello et al. (2018a) near the Alaskan coast.

It was also observed in chapter 4 that some ocean states were insensitive to the inclusion of wave drag effects. In the real-world system internal wave generation is just one of many processes affecting sea ice drag (Tsamados et al., 2014). We could attempt to examine the effects brought on by variations of the drag coefficient resultant from changing form drag. A potential avenue of inclusion for this mechanism would be to allow for thickness evolution in our rheology model via a stress based ridging scheme or via prescribing the variation based on observed or modelled ridge distributions such as in Tsamados et al. (2014).

Chapter 5 dealt primarily with the Antarctic; however, the transformation of surface waters is of critical importance within the Arctic as well. The potential

entrainment of warm North Atlantic Water in the Arctic Ocean has the ability to contribute to significant melting (Polyakov et al., 2020b,a). It would be potentially interesting to apply the ice ocean bulk mixed layer model in the Arctic marginal ice zone to investigate whether the model captures the evolution of water properties and the ice state equally well there. To enhance the predictive capabilities of our model, we could alter the existing treatment of Ekman pumping as a constant value determined from characteristic air-sea stress to one which evolves based on the surface stress as a function of ice thickness and concentration. With this configuration we could investigate potential unforeseen feedbacks with regards to changing ice state and the fate of the heat within the North Atlantic Water layer at depth.

A further application of this 1D ice ocean model is the prediction of under-ice phytoplankton blooms similar to Horvat et al. (2017). A first step towards this approach would be via the inclusion of a simple nutrient-phytoplankton (NP) model which treats phytoplankton populations as limited by a single limiting nutrient (Mandal et al., 2016). A straightforward treatment of both the limiting nutrient and the phytoplankton would be as passive scalars, although a swimming speed could be implemented to examine specific phytoplankton species. This would require the integration of observations of such a limiting nutrient (often nitrogen, Ayata et al. (2013)). A further modification of our model to examine this problem would be to allow light penetration through the sea ice in addition to the current treatment of light penetration into the ocean column.

Some of the methods used here in an Arctic setting might interestingly be applied to the Antarctic such as application of the rheological model to examine the structure of the Weddell Gyre in the Southern Ocean, consideration of sea ice internal wave generation in the perennial ice pack of the Antarctic, or multi-annual evolution of the seasonal ice zone under changing sea ice states.

Many of the above questions are readily investigated via modifications to the computational and mathematical frameworks developed within this thesis. Furthermore, investigation of these questions serve to fill a demonstrated knowledge gap with regards to understanding the coupling between processes of the under-ice boundary layer and the deeper ocean. The methods developed within this thesis are thus applicable to a varied range of oceanographic problems because the processes studied here are fundamental to any region of the ice-covered oceans.

Bibliography

Ko Aagaard and Eddy C Carmack. The role of sea ice and other fresh water in the Arctic circulation. *Journal of Geophysical Research: Oceans*, 94(C10):14485–14498, 1989.

Ryan Abernathey, John Marshall, Matt Mazloff, and Emily Shuckburgh. Enhancement of mesoscale eddy stirring at steering levels in the Southern Ocean. *Journal of Physical Oceanography*, 40(1):170–184, 2010.

Ryan P Abernathey, Ivana Cerovecki, Paul R Holland, Emily Newsom, Matt Mazloff, and Lynne D Talley. Water-mass transformation by sea ice in the upper branch of the Southern Ocean overturning. *Nature Geoscience*, 9(8):596–601, 2016.

Maria Gaetana Agnesi. *Instituzioni analitiche ad uso della gioventu' italiana*. Nella Regia-ducal corte, 1748.

DA Aguilar and BR Sutherland. Internal wave generation from rough topography. *Physics of Fluids*, 18(6):066603, 2006.

C.K. Aidun and J.R. Clausen. Lattice-boltzman method for complex flows. *Annual Review of Fluid Mechanics*, 42:439–472, 2010. doi: 10.1146/annurev-fluid-121108-145519.

Matthew H Alford, Jody M Klymak, and Glenn S Carter. Breaking internal lee waves at Kaena Ridge, Hawaii. *Geophysical Research Letters*, 41(3):906–912, 2014.

John D Anderson. Ludwig Prandtl's boundary layer. *Physics today*, 58(12):42–48, 2005.

E.L. Andreas et al. Parametrizing turbulent exchange over summer sea ice and the marginal ice zone. *Quarterly Journal of the Royal Meteorological Society*, 136(649): 927–943, 2010.

Thomas W. K. Armitage, Bacon Sheldon, Ridout Andy L., Thomas Sam F., Aksenov Yevgeny, and Wingham Duncan J. Arctic sea surface height variability and

change from satellite radar altimetry and grace, 2003–2014. *Journal of Geophysical Research: Oceans*, 121(6):4303–4322, 2016. doi: 10.1002/2015JC011579.

Thomas WK Armitage, Georgy E Manucharyan, Alek A Petty, Ron Kwok, and Andrew F Thompson. Enhanced eddy activity in the Beaufort Gyre in response to sea ice loss. *Nature Communications*, 11(1):1–8, 2020.

A.M. Artoli et al. Mesoscopic simulations of systolic flow in the human abdominal aorta. *Journal of Biomechanics*, 39:873–884, 2006.

P. Assmy et al. Leads in Arctic pack ice enable early phytoplankton blooms below snow-covered sea ice. *Nature: Scientific Reports*, 7, 2017.

S.-D. Ayata, M. Lévy, O. Aumont, A. Sciandra, J. Sainte-Marie, A. Tagliabue, and O. Bernard. Phytoplankton growth formulation in marine ecosystem models: Should we take into account photo-acclimation and variable stoichiometry in oligotrophic areas? *Journal of Marine Systems*, 125:29–40, 2013. ISSN 0924-7963. doi: https://doi.org/10.1016/j.jmarsys.2012.12.010.

Peter G Baines. *Topographic effects in stratified flows*. Cambridge University Press, 1998.

Peter G Baines and Fiona Guest. The nature of upstream blocking in uniformly stratified flow over long obstacles. *Journal of Fluid Mechanics*, 188:23–45, 1988.

Peter G Baines and Klaus P Hoinka. Stratified flow over two-dimensional topography in fluid of infinite depth: a laboratory simulation. *Journal of the Atmospheric Sciences*, 42(15):1614–1630, 1985.

Stephen E Belcher, Alan LM Grant, Kirsty E Hanley, Baylor Fox-Kemper, Luke Van Roekel, Peter P Sullivan, William G Large, Andy Brown, Adrian Hines, Daley Calvert, et al. A global perspective on Langmuir turbulence in the ocean surface boundary layer. *Geophysical Research Letters*, 39(18), 2012. doi: https://doi.org/10.1029/2012GL052932.

Carl M Bender and Steven A Orszag. *Advanced mathematical methods for scientists and engineers I: Asymptotic methods and perturbation theory*. Springer Science & Business Media, 2013.

Prabhu Lal Bhatnagar, Eugene P Gross, and Max Krook. A model for collision processes in gases. I. small amplitude processes in charged and neutral one-component systems. *Physical review*, 94(3):511, 1954.

LC Biddle and S Swart. The observed seasonal cycle of submesoscale processes in the Antarctic marginal ice zone. *Journal of Geophysical Research: Oceans*, 125(6): e2019JC015587, 2020.

Louise C. Biddle, Karen J. Heywood, Jan Kaiser, and Adrian Jenkins. Glacial Meltwater Identification in the Amundsen Sea. *Journal of Physical Oceanography*, 47 (4):933–954, 04 2017. ISSN 0022-3670. doi: 10.1175/JPO-D-16-0221.1.

Cecilia M Bitz and William H Lipscomb. An energy-conserving thermodynamic model of sea ice. *Journal of Geophysical Research: Oceans*, 104(C7):15669–15677, 1999.

Heinrich Blasius. Das aehnlichkeitsgesetz bei reibungsvorgängen in flüssigkeiten. In *Mitteilungen über Forschungsarbeiten auf dem Gebiete des Ingenieurwesens*, pages 1–41. Springer, 1913.

Ed Blockley, Martin Vancoppenolle, Elizabeth Hunke, Cecilia Bitz, Daniel Feltham, Jean-François Lemieux, Martin Losch, Eric Maisonnave, Dirk Notz, Pierre Rampal, et al. The future of sea ice modeling: where do we go from here? *Bulletin of the American Meteorological Society*, 101(8):E1304–E1311, 2020.

A. Boetius et al. Microbial ecology of the cryosphere: sea ice and glacial habitats. *Nature Reviews. Microbiology*, 13(11):677, 2015.

David Bolton. The Computation of Equivalent Potential Temperature. *Monthly Weather Review*, 108(7):1046–1053, 07 1980.

John R Booker and Francis P Bretherton. The critical layer for internal gravity waves in a shear flow. *Journal of fluid mechanics*, 27(3):513–539, 1967.

M. Bourassa et al. High-latitude ocean and sea ice surface fluxes: Challenges for climate research. *Bulletin of the American Meteorological Society*, 94, 2013.

Guillaume Boutin, Timothy Williams, Pierre Rampal, Einar Olason, and Camille Lique. Wave–sea-ice interactions in a brittle rheological framework. *The Cryosphere*, 15(1):431–457, 2021.

K.E. Brainerd and M.C. Gregg. Surface mixed and mixing layer depths. *Deep Sea Research Part I: Oceanographic Research Papers*, 42(9):1521 – 1543, 1995. ISSN 0967-0637. doi: http://dx.doi.org/10.1016/0967-0637(95)00068-H.

Samuel Brenner, Luc Rainville, Jim Thomson, Jennifer MacKinnon, and Craig Lee. Momentum fluxes across the air-ice-ocean interface in the Beaufort sea. *Earth and Space Science Open Archive*, page 1, 2020. doi: 10.1002/essoar.10502273.2.

M.I. Budyko. The effect of solar radiation variations on the climate of the Earth. *Tellus*, 21(5):611–619, 1969. ISSN 2153-3490. doi: 10.1111/j.2153-3490.1969.tb00466.x.

Cécile Cabanes, Virginie Thierry, and Catherine Lagadec. Improvement of bias detection in argo float conductivity sensors and its application in the North Atlantic. *Deep Sea Research Part I: Oceanographic Research Papers*, 114:128–136, 2016.

Eddy Carmack, Fiona McLaughlin, Michiyo Yamamoto-Kawai, Motoyo Itoh, Koji Shimada, Richard Krishfield, and Andrey Proshutinsky. Freshwater storage in the northern ocean and the special role of the Beaufort gyre. In *Arctic–subArctic ocean fluxes*, pages 145–169. Springer, 2008.

Eddy Carmack, I Polyakov, Laurie Padman, Ilker Fer, E Hunke, Jennifer Hutchings, Jennifer Jackson, D Kelley, Ronald Kwok, Chantelle Layton, et al. Toward quantifying the increasing role of oceanic heat in sea ice loss in the new Arctic. *Bulletin of the American Meteorological Society*, 96(12):2079–2105, 2015.

Eddy C Carmack. The alpha/beta ocean distinction: A perspective on freshwater fluxes, convection, nutrients and productivity in high-latitude seas. *Deep Sea Research Part II: Topical Studies in Oceanography*, 54(23-26):2578–2598, 2007.

Edward C Carmack, Michiyo Yamamoto-Kawai, Thomas WN Haine, Sheldon Bacon, Bodil A Bluhm, Camille Lique, Humfrey Melling, Igor V Polyakov, Fiamma Straneo, M-L Timmermans, et al. Freshwater and its role in the Arctic marine system: Sources, disposition, storage, export, and physical and biogeochemical consequences in the Arctic and global oceans. *Journal of Geophysical Research: Biogeosciences*, 121(3):675–717, 2016.

Magdalena M. Carranza and Sarah T. Gille. Southern ocean wind-driven entrainment enhances satellite chlorophyll-a through the summer. *Journal of Geophysical Research: Oceans*, 120(1):304–323, 2015. doi: https://doi.org/10.1002/2014JC010203.

Giulia Castellani, Martin Losch, Mischa Ungermann, and Ruediger Gerdes. Sea-ice drag as a function of deformation and ice cover: Effects on simulated sea ice and ocean circulation in the Arctic. *Ocean Modelling*, 128:48–66, 2018.

D. J. Cavalieri and C. L. Parkinson. Arctic sea ice variability and trends, 1979–2010. *The Cryosphere*, 6(4):881–889, 2012. doi: 10.5194/tc-6-881-2012.

Christopher Chapman and Jean-Baptiste Sallée. Can we reconstruct mean and eddy fluxes from argo floats? *Ocean Modelling*, 120:83–100, 2017.

J.-B. Charrassin et al. Southern Ocean frontal structure and sea-ice formation rates revealed by elephant seals. *PNAS*, 105:11634–11639, 2008.

Dudley B Chelton, Roland A DeSzoeke, Michael G Schlax, Karim El Naggar, and Nicolas Siwertz. Geographical variability of the first baroclinic rossby radius of deformation. *Journal of Physical Oceanography*, 28(3):433–460, 1998.

S. Chen and G.D. Doolen. Lattice Boltzman method for fluid flows. *Annual Review of Fluid Mechanics*, 30, 1998.

B. Chopard et al. Cellular automata and lattice Boltzmann techniques: An approach to model and simulate complex systems. *Advances in Complex Systems*, 05(02n03): 103–246, 2002. doi: 10.1142/S0219525902000602.

M.-D. Chou. A solar radiation model for use in climate studies. *Journal of the Atmospheric Sciences*, 49(9):762–772, 1992.

B. Chun and A.J.C. Ladd. Interpolated boundary condition for lattice Boltzmann simulations of flows in narrow gaps. *Physical review E*, 75(6):066705, 2007.

R.M. Clever and F.H. Busse. Transition to time-dependent convection. *Journal of Fluid Mechanics*, 65(4):625–645, 1974.

Sylvia T Cole, Mary-Louise Timmermans, John M Toole, Richard A Krishfield, and Fredrik T Thwaites. Ekman veering, internal waves, and turbulence observed under Arctic sea ice. *Journal of Physical Oceanography*, 44(5):1306–1328, 2014.

Sylvia T. Cole, John M. Toole, Luc Rainville, and Craig M. Lee. Internal waves in the Arctic: Influence of ice concentration, ice roughness, and surface layer stratification. *Journal of Geophysical Research: Oceans*, 123(8):5571–5586, 2018. doi: https://doi.org/10.1029/2018JC014096.

Josefino C. Comiso and Fumihiko Nishio. Trends in the sea ice cover using enhanced and compatible AMSR-E, SSM/I, and SMMR data. *Journal of Geophysical Research: Oceans*, 113(C2), 2008. doi: 10.1029/2007JC004257.

MD Coon, GA Maykut, and RS Pritchard. Modeling the pack ice as an elastic-plastic material. 1974.

Sam B Cornish, Yavor Kostov, Helen L Johnson, and Camille Lique. Response of Arctic freshwater to the Arctic oscillation in coupled climate models. *Journal of Climate*, 33(7):2533–2555, 2020.

Nicole Couto, Douglas G Martinson, Josh Kohut, and Oscar Schofield. Distribution of Upper Circumpolar Deep Water on the warming continental shelf of the West

Antarctic Peninsula. *Journal of Geophysical Research: Oceans*, 122(7):5306–5315, 2017.

G.F.N. Cox and W.F. Weeks. Numerical simulations of the profile properties of undeformed first-year sea ice during the growth season. *Journal of Geophysical Research: Oceans*, 93(C10):12449–12460, 1988.

M.F. Cronin and J. Sprintall. Wind and buoyancy-forced upper ocean. In S.A. Thorpe, editor, *Encyclopedia of Ocean Sciences: Elements of Physical Oceanography*, pages 248–256. Elsevier, 2 edition, 2009.

Cornelius Cuvelier, August Segal, Guus Segal, AA van Steenhoven, and A Van Steenhoven. *Finite element methods and Navier-Stokes equations*, volume 22. Springer Science & Business Media, 1986.

E.A. D'Asaro. Turbulence in the upper-ocean mixed layer. *Annual Review of Marine Science*, 6:101–115, 2014.

Eric A D'Asaro and Mark D Morehead. Internal waves and velocity fine structure in the Arctic Ocean. *Journal of Geophysical Research: Oceans*, 96(C7):12725–12738, 1991.

N. R. Davis and P. Wadhams. A statistical analysis of Arctic pressure ridge morphology. *Journal of Geophysical Research: Oceans*, 100(C6):10915–10925, 1995. doi: https://doi.org/10.1029/95JC00007.

Peter ED Davis, Camille Lique, and Helen L Johnson. On the link between Arctic sea ice decline and the freshwater content of the Beaufort Gyre: Insights from a simple process model. *Journal of Climate*, 27(21):8170–8184, 2014.

Clément de Boyer Montégut, Gurvan Madec, Albert S. Fischer, Alban Lazar, and Daniele Iudicone. Mixed layer depth over the global ocean: An examination of profile data and a profile-based climatology. *Journal of Geophysical Research: Oceans*, 109(C12), 2004. doi: 10.1029/2004JC002378.

Sarah Dewey, James Morison, Ronald Kwok, Suzanne Dickinson, David Morison, and Roger Andersen. Arctic ice-ocean coupling and gyre equilibration observed with remote sensing. *Geophysical Research Letters*, 45(3):1499–1508, 2018.

Robert R Dickson, Jens Meincke, Svend-Aage Malmberg, and Arthur J Lee. The "great salinity anomaly" in the northern North Atlantic 1968–1982. *Progress in Oceanography*, 20(2):103–151, 1988.

Martin J Doble, Max D Coon, and Peter Wadhams. Pancake ice formation in the Weddell Sea. *Journal of Geophysical Research: Oceans*, 108(C7), 2003. doi: https://doi.org/10.1029/2002JC001373.

Edward W Doddridge, Gianluca Meneghello, John Marshall, Jeffery Scott, and Camille Lique. A three-way balance in the Beaufort Gyre: The ice-ocean governor, wind stress, and eddy diffusivity. *Journal of Geophysical Research: Oceans*, 124(5):3107–3124, 2019.

M Du Plessis, S Swart, IJ Ansorge, and A Mahadevan. Submesoscale processes promote seasonal restratification in the Subantarctic Ocean. *Journal of Geophysical Research: Oceans*, 122(4):2960–2975, 2017.

D. Dumont, A. Kohout, and L. Bertino. A wave-based model for the marginal ice zone including a floe breaking parameterization. *Journal of Geophysical Research*, 116, 2011. doi: https://doi.org/10.1029/2010JC006682.

Stephen D Eckermann, John Lindeman, Dave Broutman, Jun Ma, and Zafer Boybeyi. Momentum fluxes of gravity waves generated by variable froude number flow over three-dimensional obstacles. *Journal of the atmospheric sciences*, 67(7):2260–2278, 2010.

J.G.M. Eggels and J.A. Somers. Numerical simulation of free convective flow using the lattice-Boltzmann scheme. *International Journal of Heat and Fluid Flow*, 16(5):357 – 364, 1995. ISSN 0142-727X. doi: https://doi.org/10.1016/0142-727X(95)00052-R.

H. Eicken. Ice sampling and basic sea ice core analysis. In H. Eicken, R. Gradinger, M. Salganek, K. Shirasawa, D. Perovich, and M. Lepparanta, editors, *Field Techniques for Sea Ice Research*, pages 117–140. University of Alaska Press, 2009.

Vagn Walfrid Ekman. On dead water. *Norwegian North Polar Expedition, 1893-1896*, pages 1–150, 1904.

Vagn Walfrid Ekman. *On the influence of the Earth's rotation on ocean-currents.* Almqvist & Wiksells boktryckeri, A.-B., 1905.

WJ Emery and Jens Meincke. Global water masses-summary and review. *Oceanologica acta*, 9(4):383–391, 1986.

Daniel L Feltham. Sea ice rheology. *Annu. Rev. Fluid Mech.*, 40:91–112, 2008.

I. Fer and A. Sundfjord. Observations of upper ocean boundary layer dynamics in the marginal ice zone. *Journal of Geophysical Research: Oceans*, 112(C4), 2007. ISSN 2156-2202. doi: 10.1029/2005JC003428.

Ilker Fer. Near-inertial mixing in the central Arctic Ocean. *Journal of Physical Oceanography*, 44(8):2031–2049, 2014.

B Fernández-Castro, B Mouriño-Carballido, VM Benítez-Barrios, P Chouciño, Eugenio Fraile-Nuez, R Graña, M Piedeleu, and A Rodríguez-Santana. Microstructure turbulence and diffusivity parameterization in the tropical and subtropical Atlantic, Pacific and Indian oceans during the Malaspina 2010 expedition. *Deep Sea Research Part I: Oceanographic Research Papers*, 94:15–30, 2014.

Raffaele Ferrari and Carl Wunsch. Ocean circulation kinetic energy: Reservoirs, sources, and sinks. *Annual Review of Fluid Mechanics*, 41(1):253–282, 2009. doi: 10.1146/annurev.fluid.40.111406.102139.

Johan Fourdrinoy, Clément Caplier, Yann Devaux, Germain Rousseaux, Areti Gianni, Ierotheos Zacharias, Isabelle Jouteur, Paul-Marius Martin, Julien Dambrine, Madalina Petcu, and Morgan Pierre. The naval battle of Actium and the myth of the ship-holder: the effect of bathymetry. In *5th MASHCON - International Conference on Ship Manoeuvring in Shallow and Confined Water with non-exclusive focus on manoeuvring in waves, wind and current*, pages 104 – 133, May 2019. doi: hal-02139218.

Johan Fourdrinoy, Julien Dambrine, Madalina Petcu, Morgan Pierre, and Germain Rousseaux. The dual nature of the dead-water phenomenology: Nansen versus ekman wave-making drags. *Proceedings of the National Academy of Sciences*, 117 (29):16770–16775, 2020.

R. C. Frew, D. L. Feltham, P. R. Holland, and A. A. Petty. Sea ice–ocean feedbacks in the Antarctic shelf seas. *Journal of Physical Oceanography*, 49(9):2423–2446, 2019. doi: 10.1175/JPO-D-18-0229.1.

Philippe Gaspar. Modeling the seasonal cycle of the upper ocean. *Journal of Physical Oceanography*, 18(2):161–180, 1988.

Peter R Gent and James C Mcwilliams. Isopycnal mixing in ocean circulation models. *Journal of Physical Oceanography*, 20(1):150–155, 1990.

KA Giles, SW Laxon, DJ Wingham, DW Wallis, WB Krabill, CJ Leuschen, D McAdoo, SS Manizade, and RK Raney. Combined airborne laser and radar

altimeter measurements over the Fram Strait in May 2002. *Remote Sensing of Environment*, 111(2-3):182–194, 2007.

Katharine A Giles, Seymour W Laxon, Andy L Ridout, Duncan J Wingham, and Sheldon Bacon. Western Arctic ocean freshwater storage increased by wind-driven spin-up of the Beaufort Gyre. *Nature Geoscience*, 5(3):194–197, 2012.

Nigel Goldenfeld. Roughness-induced critical phenomena in a turbulent flow. *Physical Review Letters*, 96(4):044503, 2006.

S Goldstein. On the stability of superposed streams of fluids of different densities. *Proc. R. Soc. Lond. A*, 132(820):524–548, 1931.

D. Gregory, G. J. Shutts, and J. R. Mitchell. A new gravity-wave-drag scheme incorporating anisotropic orography and low-level wave breaking: Impact upon the climate of the uk meteorological office unified model. *Quarterly Journal of the Royal Meteorological Society*, 124(546):463–493, 1998. doi: https://doi.org/10.1002/qj.49712454606.

Roger Grimshaw. Internal gravity waves: critical layer absorption in a rotating fluid. *Journal of Fluid Mechanics*, 70(2):287–304, 1975.

Roger Grimshaw and KR Helfrich. Internal solitary wave generation by tidal flow over topography. *Journal of Fluid Mechanics*, 839:387–407, 2018.

Maria-Vittoria Guarino, Louise C Sime, David Schröeder, Irene Malmierca-Vallet, Erica Rosenblum, Mark Ringer, Jeff Ridley, Danny Feltham, Cecilia Bitz, Eric J Steig, et al. Sea-ice-free Arctic during the last interglacial supports fast future loss. *Nature Climate Change*, 10(10):928–932, 2020.

Z. Guo, B. Shi, and C. Zheng. A coupled lattice BGK model for the Boussinesq equations. *International Journal for Numerical Methods in Fluids*, 39(4):325–342, 2002.

J. Haapala et al. Small-scale horizontal variability of snow, sea-ice thickness and freeboard in the first-year ice region north of svalbard. *Annals of Glaciology*, 54 (62):261–266, 2013.

C. Haas et al. Synoptic airborne thickness surveys reveal state of Arctic sea ice cover. *Geophysical Research Letters*, 37(9), 2010. doi: https://doi.org/10.1029/2010GL042652.

Thomas WN Haine, Beth Curry, Rüdiger Gerdes, Edmond Hansen, Michael Karcher, Craig Lee, Bert Rudels, Gunnar Spreen, Laura de Steur, Kial D Stewart, et al.

Arctic freshwater export: Status, mechanisms, and prospects. *Global and Planetary Change*, 125:13–35, 2015.

Chris Halle and Robert Pinkel. Internal wave variability in the Beaufort Sea during the winter of 1993/1994. *Journal of Geophysical Research: Oceans*, 108(C7), 2003.

C.D. Hamilton et al. Predictions replaced by facts: a keystone species' behavioural responses to declining Arctic sea-ice. *Biology letters*, 11(11):20150803, 2015.

Ramsey R Harcourt. An improved second-moment closure model of Langmuir turbulence. *Journal of Physical Oceanography*, 45(1):84–103, 2015.

O. Harsem, A. Eide, and K. Heen. Factors influencing future oil and gas prospects in the Arctic. *Energy Policy*, 39, 2011.

Bernhard Haurwitz. *Zur theorie der wellenbewegungen in luft und wasser*. Geophysikalischen Institut der Universität Leipzig, 1931.

Xiaoyi He and Li-Shi Luo. Theory of the lattice Boltzmann method: From the Boltzmann equation to the lattice Boltzmann equation. *Physical review E*, 56(6): 6811, 1997.

Xiaoyi He, Shiyi Chen, and Gary D. Doolen. A novel thermal model for the lattice Boltzmann method in incompressible limit. *Journal of Computational Physics*, 146 (1):282 – 300, 1998. ISSN 0021-9991. doi: https://doi.org/10.1006/jcph.1998.6057.

Harold DBS Heorton, Michel Tsamados, ST Cole, Ana MG Ferreira, Andrea Berbellini, M Fox, and Thomas WK Armitage. Retrieving sea ice drag coefficients and turning angles from in situ and satellite observations using an inverse modeling framework. *Journal of Geophysical Research: Oceans*, 124(8):6388–6413, 2019.

WD Hibler. A dynamic thermodynamic sea ice model. *Journal of Physical Oceanography*, 9(4):815–846, 1979.

WD Hibler and WB Tucker. Seasonal variations in apparent sea ice viscosity on the geophysical scale. *Geophysical Research Letters*, 4(2):87–90, 1977.

F J Higuera and Javier Jiménez. Boltzmann approach to lattice gas simulations. *Europhysics Letters*, 9(7):663, 1989.

David M Holland and Adrian Jenkins. Modeling thermodynamic ice–ocean interactions at the base of an ice shelf. *Journal of Physical Oceanography*, 29(8):1787–1800, 1999.

M.M. Holland et al. Future abrubt reductions in the summer Arctic sea ice. *Geophysical Research Letters*, 33, 2006.

James Holte and Lynne Talley. A new algorithm for finding mixed layer depths with applications to Argo data and Subantarctic Mode Water formation. *Journal of Atmospheric and Oceanic Technology*, 26(9):1920–1939, 2009.

C. Horvat and E. Tziperman. A prognostic model of the sea-ice floe size and thickness distribution. *The Cryosphere*, 9, 2015. doi: https://doi.org/10.5194/tc-9-2119-2015.

C. Horvat et al. The frequency and extent of sub-ice phytoplankton blooms in the Arctic ocean. *Science Advances*, 3(3):e1601191, 2017.

Elizabeth C Hunke. Viscous–plastic sea ice dynamics with the EVP model: Linearization issues. *Journal of Computational Physics*, 170(1):18–38, 2001.

Elizabeth C Hunke and John K Dukowicz. An elastic–viscous–plastic model for sea ice dynamics. *Journal of Physical Oceanography*, 27(9):1849–1867, 1997.

Herbert E Huppert and John W Miles. Lee waves in a stratified flow Part 3. semi-elliptical obstacle. *Journal of Fluid Mechanics*, 35(3):481–496, 1969.

Jennifer K Hutchings, Andrew Roberts, Cathleen A Geiger, and Jacqueline Richter-Menge. Spatial and temporal characterization of sea-ice deformation. *Annals of Glaciology*, 52(57):360–368, 2011.

Nils Hutter, Martin Losch, and Dimitris Menemenlis. Scaling properties of Arctic sea ice deformation in a high-resolution viscous-plastic sea ice model and in satellite observations. *Journal of Geophysical Research: Oceans*, 123(1):672–687, 2018.

Nikolay G. Iakovlev. *Arctic Ocean Modeling: The Consistent Physics on the Path to the High Spatial Resolution*, pages 559–567. Springer International Publishing, Cham, 2018. ISBN 978-3-319-71934-4. doi: 10.1007/978-3-319-71934-4$_3$5.

Toshiki Iwasaki, Shinichi Yamada, and Kazumasa Tada. A parameterization scheme of orographic gravity wave drag with two different vertical partitionings Part I: Impacts on medium-range forecasts. *Journal of the Meteorological Society of Japan. Ser. II*, 67(1):11–27, 1989.

Stanley S. Jacobs. Bottom water production and its links with the thermohaline circulation. *Antarctic Science*, 16(4):427–437, 2004. doi: 10.1017/S095410200400224X.

Stanley S Jacobs and Josefino C Comiso. Climate variability in the Amundsen and Bellingshausen seas. *Journal of Climate*, 10(4):697–709, 1997.

L. Jahanshaloo, E. Pouryazdanpanah, and N.A. Che Sidik. A review on the application of the lattice Boltzmann method for turbulent flow simulation. *Numerical Heat Transfer, Part A: Applications*, 64(11):938–953, 2013.

G. S. Janowitz. The barotropic rossby wave drag due to an isolated topography. *Journal of Atmospheric Sciences*, 34(5), 1977.

Adrian Jenkins. The impact of melting ice on ocean waters. *Journal of physical oceanography*, 29(9):2370–2381, 1999.

Nils Gunnar Jerlov. *Optical oceanography*. Elsevier, 1968.

Gregory C. Johnson, Sunke Schmidtko, and John M. Lyman. Relative contributions of temperature and salinity to seasonal mixed layer density changes and horizontal density gradients. *Journal of Geophysical Research: Oceans*, 117(C4), 2012. doi: https://doi.org/10.1029/2011JC007651.

I. Jones and B.C. Kenney. The scaling of velocity fluctuations in the surface mixed layer. *Journal of Geophysical Research*, 82(9):1392–1396, 1977.

Walter L. Jones. Propagation of internal gravity waves in fluids with shear flow and rotation. *Journal of Fluid Mechanics*, 30(3):439–448, 1967. doi: 10.1017/S0022112067001521.

M. Kahru et al. Effects of sea ice cover on satellite-detected primary production in the Arctic ocean. *Biology Letters*, 12, 2016.

Elizabeth W. S. Kam, Ronald M. C. So, and Randolph C. K. Leung. Lattice Boltzman method simulation of aeroacoustics and nonreflecting boundary conditions. *AIAA Journal*, 45(7):1703–1712, 2007.

Lakshmi H Kantha and Carol Anne Clayson. An improved mixed layer model for geophysical applications. *Journal of Geophysical Research: Oceans*, 99(C12):25235–25266, 1994.

Thomas Keitzl, Juan-Pedro Mellado, and Dirk Notz. Impact of thermally driven turbulence on the bottom melting of ice. *Journal of Physical Oceanography*, 46(4): 1171–1187, 2016.

Teddie L. Keller. Implications of the hydrostatic assumption on atmospheric gravity waves. *Journal of Atmospheric Sciences*, 51(13):1915 – 1929, 01 Jul. 1994. doi: 10.1175/1520-0469(1994)051¡1915:IOTHAO¿2.0.CO;2.

William W Kellogg. Climatic feedback mechanisms involving the polar regions. *Climate of the Arctic*, 111:116, 1975.

Jessica S Kenigson, Renske Gelderloos, and Georgy E Manucharyan. Vertical structure of the Beaufort gyre halocline and the crucial role of the depth-dependent eddy diffusivity. *Journal of Physical Oceanography*, 51(3):845–860, 2021.

Stefan Kern and Gunnar Spreen. Uncertainties in Antarctic sea-ice thickness retrieval from ICESat. *Annals of Glaciology*, 56(69):107–119, 2015.

Jinwon Kim and L Mahrt. Momentum transport by gravity waves. *Journal of Atmospheric Sciences*, 49(9):735–748, 1992.

Jody M Klymak. Nonpropagating form drag and turbulence due to stratified flow over large-scale abyssal hill topography. *Journal of Physical Oceanography*, 48(10):2383–2395, 2018.

Jody M Klymak and Sonya M Legg. A simple mixing scheme for models that resolve breaking internal waves. *Ocean Modelling*, 33(3-4):224–234, 2010.

A.L. Kohout et al. Storm-induced sea-ice breakup and the implications for ice extent. *Nature*, 509(7502):604, 2014.

Myung-Seo Koo, Hyun-Joo Choi, and Ji-Young Han. A parameterization of turbulent-scale and mesoscale orographic drag in a global atmospheric model. *Journal of Geophysical Research: Atmospheres*, 123(16):8400–8417, 2018. doi: https://doi.org/10.1029/2017JD028176.

E. B. Kraus and J. S. Turner. A one-dimensional model of the seasonal thermocline ii. the general theory and its consequences. *Tellus*, 19(1):98–106, 1967. doi: 10.1111/j.2153-3490.1967.tb01462.x.

N. T. Kurtz and T. Markus. Satellite observations of antarctic sea ice thickness and volume. *Journal of Geophysical Research: Oceans*, 117(C8), 2012. doi: https://doi.org/10.1029/2012JC008141.

R. Kwok and N. Untersteiner. The thinning of Arctic sea ice. *Physics Today*, 64, 2011.

Ron Kwok. Arctic sea ice thickness, volume, and multiyear ice coverage: losses and coupled variability (1958–2018). *Environmental Research Letters*, 13(10):105005, 2018.

Ron Kwok, H Jay Zwally, and Donghui Yi. ICESat observations of Arctic sea ice: A first look. *Geophysical Research Letters*, 31(16), 2004. doi: https://doi.org/10.1029/2004GL020309.

Ron Kwok, Shirley S Pang, Sahra Kacimi, and Eddy C Carmack. Sea ice drift in the Southern Ocean: Regional patterns, variability, and trends. *Elementa: Science of the Anthropocene*, 5, 2017. doi: 10.1525/elementa.226.

A.J.C. Ladd. Numerical simulations of particulate suspensions via a discretized Boltzmann equation. Part 1. theoretical foundation. *Journal of Fluid Mechanics*, 271, 1994.

Yu Chau Lam. Masters thesis:drag and momentum fluxes produced by mountain waves. *University of Reading Department of Mathematics*, 2013.

W. G. Large, J. C. McWilliams, and S. C. Doney. Oceanic vertical mixing: A review and a model with a nonlocal boundary layer parameterization. *Reviews of Geophysics*, 32 (4):363–403, 1994. doi: 10.1029/94RG01872.

Jonas Latt. Choice of units in lattice Boltzmann simulations. 2008. URL `http://lbmethod.org/_media/howtos:lbunits.pdf`.

Craig Lee. Stratified ocean dynamics of the Arctic Ocean (SODA). In *Ocean Sciences Meeting 2020*. AGU, 2020.

Craig M Lee, Sylvia Cole, Martin Doble, Lee Freitag, Phil Hwang, Steve Jayne, Martin Jeffries, Rick Krishfield, Ted Maksym, and Wieslaw Maslowski. Marginal ice zone (miz) program: Science and experiment plan. Technical report, WASHINGTON UNIV SEATTLE APPLIED PHYSICS LAB, 2012.

Sonya Legg. Mixing by oceanic lee waves. *Annual Review of Fluid Mechanics*, 53: 173–201, 2021. doi: 10.1146/annurev-fluid-051220-043904.

B. Light, G.A. Maykut, and T.C. Grenfell. Effects of temperature on the microstructure of first-year Arctic sea ice. *Journal of Geophysical Research*, 108:3051, 2003. doi: 10.1029/2001JC000887.

PF Linden. The deepening of a mixed layer in a stratified fluid. *Journal of Fluid Mechanics*, 71(2):385–405, 1975.

Richard S Lindzen. Supersaturation of vertically propagating internal gravity waves. *Journal of Atmospheric Sciences*, 45(4):705–711, 1988.

F.B. Lipps. Numerical simulation of three-dimensional Bénard convection in air. *Journal of Fluid Mechanics*, 75(1):113–148, 1976.

William H Lipscomb, Elizabeth C Hunke, Wieslaw Maslowski, and Jaromir Jakacki. Ridging, strength, and stability in high-resolution sea ice models. *Journal of Geophysical Research: Oceans*, 112(C3), 2007. doi: https://doi.org/10.1029/2005JC003355.

Camille Lique, Helen L Johnson, and Peter ED Davis. On the interplay between the circulation in the surface and the intermediate layers of the Arctic Ocean. *Journal of Physical Oceanography*, 45(5):1393–1409, 2015.

Robert R Long. Some aspects of the flow of stratified fluids: I. a theoretical investigation. *Tellus*, 5(1):42–58, 1953.

François Lott, Bruno Deremble, and Clément Soufflet. Mountain waves produced by a stratified shear flow with a boundary layer. Part II: Form drag, wave drag, and transition from downstream sheltering to upstream blocking. *Journal of the Atmospheric Sciences*, 78(4):1101 – 1112, 2021. doi: 10.1175/JAS-D-20-0144.1.

P. Lu et al. Influence of melt-pond depth and ice thickness on Arctic sea-ice albedo and light transmittance. *Cold Regions Science and Technology*, 124:1–10, 2016.

Peng Lu, Zhijun Li, Bin Cheng, and Matti Leppäranta. A parameterization of the ice-ocean drag coefficient. *Journal of Geophysical Research: Oceans*, 116(C7), 2011. doi: https://doi.org/10.1029/2010JC006878.

B Lund, Hans C Graber, POG Persson, M Smith, M Doble, J Thomson, and P Wadhams. Arctic sea ice drift measured by shipboard marine radar. *Journal of Geophysical Research: Oceans*, 123(6):4298–4321, 2018.

Jennifer A MacKinnon, Zhongxiang Zhao, Caitlin B Whalen, Amy F Waterhouse, David S Trossman, Oliver M Sun, Louis C St. Laurent, Harper L Simmons, Kurt Polzin, Robert Pinkel, et al. Climate process team on internal wave–driven ocean mixing. *Bulletin of the American Meteorological Society*, 98(11):2429–2454, 2017.

Alena Malyarenko, Andrew J Wells, Patricia J Langhorne, Natalie J Robinson, Michael JM Williams, and Keith W Nicholls. A synthesis of thermodynamic ablation at ice-ocean interfaces from theory, observations and models. *Ocean Modelling*, page 101692, 2020.

Sandip Mandal, Hikaru Homma, Anupam Priyadarshi, Hans Burchard, S. Lan Smith, Kai W. Wirtz, and Hidekatsu Yamazaki. A 1D physical–biological model of the impact of highly intermittent phytoplankton distributions. *Journal of Plankton Research*, 38 (4):964–976, 03 2016. doi: 10.1093/plankt/fbw019.

GE Manucharyan and Pål Erik Isachsen. Critical role of continental slopes in halocline and eddy dynamics of the Ekman-driven Beaufort Gyre. *Journal of Geophysical Research: Oceans*, 124(4):2679–2696, 2019.

Georgy E Manucharyan and Michael A Spall. Wind-driven freshwater buildup and release in the Beaufort Gyre constrained by mesoscale eddies. *Geophysical Research Letters*, 43(1):273–282, 2016.

Georgy E. Manucharyan, Michael A. Spall, and Andrew F. Thompson. A theory of the wind-driven Beaufort Gyre variability. *Journal of Physical Oceanography*, 46(11): 3263–3278, 2016. doi: 10.1175/JPO-D-16-0091.1.

John Marshall and Timour Radko. Residual-mean solutions for the Antarctic Circumpolar Current and its associated overturning circulation. *Journal of Physical Oceanography*, 33(11):2341–2354, 2003.

John Marshall and Kevin Speer. Closure of the meridional overturning circulation through southern ocean upwelling. *Nature Geoscience*, 5(3):171–180, 2012.

John Marshall, Emily Shuckburgh, Helen Jones, and Chris Hill. Estimates and implications of surface eddy diffusivity in the Southern Ocean derived from tracer transport. *Journal of physical oceanography*, 36(9):1806–1821, 2006.

Torge Martin, Michael Steele, and Jinlun Zhang. Seasonality and long-term trend of Arctic Ocean surface stress in a model. *Journal of Geophysical Research: Oceans*, 119(3):1723–1738, 2014.

Torge Martin, Michel Tsamados, David Schroeder, and Daniel L Feltham. The impact of variable sea ice roughness on changes in Arctic Ocean surface stress: A model study. *Journal of Geophysical Research: Oceans*, 121(3):1931–1952, 2016.

D.O. Martinez et al. Comparison of spectral method and lattice Boltzmann simulations of two-dimensional hydrodynamics. *Physics of Fluids*, 6(3):1285–1298, 1994.

Douglas G Martinson. Evolution of the Southern Ocean winter mixed layer and sea ice: Open ocean deepwater formation and ventilation. *Journal of Geophysical Research: Oceans*, 95(C7):11641–11654, 1990.

Douglas G Martinson and Richard A Iannuzzi. Antarctic ocean-ice interaction: Implications from ocean bulk property distributions in the Weddell Gyre. *Antarctic sea ice: physical processes, interactions and variability*, 74:243–271, 1998.

A. Mashayek, H. Salehipour, D. Bouffard, C. P. Caulfield, R. Ferrari, M. Nikurashin, W. R. Peltier, and W. D. Smyth. Efficiency of turbulent mixing in the abyssal ocean circulation. *Geophysical Research Letters*, 44(12):6296–6306, 2017. doi: https://doi.org/10.1002/2016GL072452.

R. Massom et al. Change and variablity in east Antarctic sea ice seasonality, 1979/80-2009/10. *PLoS ONE*, 8, 2013. doi: 10.1371/journal.pone.0064756.

G. A. Maykut and Miles G. McPhee. Solar heating of the Arctic mixed layer. *Journal of Geophysical Research: Oceans*, 100(C12):24691–24703, 1995. doi: https://doi.org/10.1029/95JC02554.

G.A. Maykut and N. Untersteiner. Some results from a time-dependent thermodynamic model of sea ice. *Journal of Geophysical Research (1896-1977)*, 76(6):1550–1575, 1971.

Trevor J McDougall. Thermobaricity, cabbeling, and water-mass conversion. *Journal of Geophysical Research: Oceans*, 92(C5):5448–5464, 1987.

N. A. McFarlane. The effect of orographically excited gravity wave drag on the general circulation of the lower stratosphere and troposphere. *Journal of Atmospheric Sciences*, 44(14):1775 – 1800, 15 Jul. 1987. doi: 10.1175/1520-0469(1987)044¡1775:TEOOEG¿2.0.CO;2.

M.G. McPhee. Turbulent heat flux in the upper ocean under sea ice. *Journal of Geophysical Research: Oceans*, 97(C4):5365–5379, 1992.

Miles McPhee. *Air-ice-ocean interaction: Turbulent ocean boundary layer exchange processes*. Springer Science & Business Media, 2008.

Miles G McPhee and Lakshmi H Kantha. Generation of internal waves by sea ice. *Journal of Geophysical Research: Oceans*, 94(C3):3287–3302, 1989.

Miles G McPhee, Gary A Maykut, and James H Morison. Dynamics and thermodynamics of the ice/upper ocean system in the marginal ice zone of the Greenland Sea. *Journal of Geophysical Research: Oceans*, 92(C7):7017–7031, 1987.

Miles G. McPhee, Takashi Kikuchi, James H. Morison, and Timothy P. Stanton. Ocean-to-ice heat flux at the North Pole environmental observatory. *Geophysical Research Letters*, 30(24), 2003. doi: https://doi.org/10.1029/2003GL018580.

W.E. Meador and W.R. Weaver. Two-stream approximations to radiative transfer in planetary atmospheres: A unified description of existing methods and a new improvement. *Journal of the Atmospheric Sciences*, 37(3):630–643, 1980.

R. Mei, L.-S. Luo, and W. Shyy. An accurate curved boundary treatment in the lattice Boltzmann method. *Journal of Computational Physics*, 155(2):307–330, 1999.

N. Melia, K. Haines, and E. Hawkins. Sea ice decline and 21st century trans-Arctic shipping routes. *Geophysical Research Letters*, 43(18):9720–9728, 2016.

George L Mellor and Tetsuji Yamada. Development of a turbulence closure model for geophysical fluid problems. *Reviews of Geophysics*, 20(4):851–875, 1982.

W Kendall Melville. The role of surface-wave breaking in air-sea interaction. *Annual review of fluid mechanics*, 28(1):279–321, 1996.

Gianluca Meneghello, John Marshall, Jean-Michel Campin, Edward Doddridge, and Mary-Louise Timmermans. The ice-ocean governor: Ice-ocean stress feedback limits Beaufort Gyre spin-up. *Geophysical Research Letters*, 45(20):11–293, 2018a.

Gianluca Meneghello, John Marshall, Mary-Louise Timmermans, and Jeffery Scott. Observations of seasonal upwelling and downwelling in the Beaufort Sea mediated by sea ice. *Journal of Physical Oceanography*, 48(4):795–805, 2018b. doi: 10.1175/JPO-D-17-0188.1.

Gianluca Meneghello, Edward Doddridge, John Marshall, Jeffery Scott, and Jean-Michel Campin. Exploring the role of the "ice–ocean governor" and mesoscale eddies in the equilibration of the Beaufort Gyre: Lessons from observations. *Journal of Physical Oceanography*, 50(1):269–277, 2020.

John W Miles and Herbert E Huppert. Lee waves in a stratified flow. Part 2. semi-circular obstacle. *Journal of Fluid Mechanics*, 33(4):803–814, 1968.

S.C. Mishra and H.K. Roy. Solving transient conduction and radiation heat transfer problems using the lattice Boltzmann method and the finite volume method. *Journal of Computational Physics*, 223(1):89–107, 2007.

AA Mohamad. *Lattice Boltzmann Method*, volume 70. Springer, 2011.

James H Morison, Miles G McPhee, and Gary A Maykut. Boundary layer, upper ocean, and ice observations in the Greenland Sea marginal ice zone. *Journal of Geophysical Research: Oceans*, 92(C7):6987–7011, 1987.

RC Musgrave, JA MacKinnon, R Pinkel, AF Waterhouse, and J Nash. Tidally driven processes leading to near-field turbulence in a channel at the crest of the mendocino escarpment. *Journal of Physical Oceanography*, 46(4):1137–1155, 2016.

A. Mussa et al. Lattice Boltzmann simulations of 2d laminar flows past two tandem cylinders. *Journal of Computational Physics*, 228(4):983–999, 2009.

Vishnu Nandan, Torsten Geldsetzer, John Yackel, Mallik Mahmud, Randall Scharien, Stephen Howell, Joshua King, Robert Ricker, and Brent Else. Effect of snow salinity on CryoSat-2 Arctic first-year sea ice freeboard measurements. *Geophysical Research Letters*, 44(20):10–419, 2017.

Fridtjof Nansen. *Fridtjof Nansen's" Farthest North.": Being the Record of a Voyage of Exploration of the Ship Fram, 1893-96 and of a Fifteen Months' Sleigh Journey by Dr. Nansen and Lieut, Johansen*, volume 1. Macmillan and Company, Limited, 1897.

Carmen J Nappo. Gravity waves in the middle and upper atmosphere. In *International Geophysics*, volume 102, pages 181–199. Elsevier, 2012.

National Snow and Ice Data Center. All about sea ice. *https://nsidc.org/data/seaice_index/*, 2020.

RAJ Neggers, Jan Chylik, Ulrike Egerer, H Griesche, Vera Schemann, Patric Seifert, Holger Siebert, and Andreas Macke. Local and remote controls on Arctic mixed-layer evolution. *Journal of Advances in Modeling Earth Systems*, 11(7):2214–2237, 2019.

J Nikuradse. Forschung auf dem gebiete des ingenieurwesens. *Verein Deutsche Ingenieure*, 4:361, 1933.

PP Niller. One-dimensional models of the upper ocean. modeling and prediction of the upper layers of the ocean, eb kraus, ed, 1977.

D. Notz and J. Stroeve. Observed Arctic sea-ice loss directly follows anthropogenic CO2 emission. *Science*, 354(6313):747–750, 2016.

D. Notz and M.G. Worster. Desalination processes of sea ice revisited. *Journal of Geophysical Research: Oceans*, 114(C5), 2009. doi: https://doi.org/10.1029/2008JC004885.

Dirk Notz, Miles G McPhee, M Grae Worster, Gary A Maykut, K Heinke Schlünzen, and Hajo Eicken. Impact of underwater-ice evolution on Arctic summer sea ice. *Journal of Geophysical Research: Oceans*, 108(C7), 2003. doi: https://doi.org/10.1029/2001JC001173.

Andre Nuber, Lasse Rabenstein, Jochen A Lehmann-Horn, Marian Hertrich, Stefan Hendricks, Andy Mahoney, and Hajo Eicken. Water content estimates of a first-year sea-ice pressure ridge keel from surface-nuclear magnetic resonance tomography. *Annals of Glaciology*, 54(64):33–43, 2013.

M. Nuttal. *Protecting the Arctic: Indigenous Peoples and Cultural Survival*. Routledge, 1998.

James J O'Brien. A note on the vertical structure of the eddy exchange coefficient in the planetary boundary layer. *J. Atmos. Sci*, 27(8):1213–1215, 1970.

T. N. Palmer, G. J. Shutts, and R. Swinbank. Alleviation of a systematic westerly bias in general circulation and numerical weather prediction models through an orographic

gravity wave drag parametrization. *Quarterly Journal of the Royal Meteorological Society*, 112(474):1001–1039, 1986. doi: 10.1002/qj.49711247406.

C. L. Parkinson and D. J. Cavalieri. Antarctic sea ice variability and trends, 1979–2010. *The Cryosphere*, 6(4):871–880, 2012. doi: 10.5194/tc-6-871-2012.

Claire L Parkinson. *Arctic sea ice, 1973-1976: Satellite passive-microwave observations*, volume 490. Scientific and Technical Information Branch, National Aeronautics and Space, 1987.

Claire L Parkinson. A 40-y record reveals gradual Antarctic sea ice increases followed by decreases at rates far exceeding the rates seen in the Arctic. *Proceedings of the National Academy of Sciences*, 116(29):14414–14423, 2019.

R.R. Parmerter and M.D Coon. Model of pressure ridge formation in sea ice. *Journal of Geophysical Research*, 77(33):6565–6575, 1972.

Clayton A. Paulson and James J. Simpson. Irradiance measurements in the upper ocean. *Journal of Physical Oceanography*, 7(6):952–956, 1977. doi: 10.1175/1520-0485(1977)007¡0952:IMITUO¿2.0.CO;2.

Etienne Pauthenet, Fabien Roquet, Gurvan Madec, Jean-Baptiste Sallée, and David Nerini. The thermohaline modes of the global ocean. *Journal of Physical Oceanography*, 49(10):2535 – 2552, 2019. doi: 10.1175/JPO-D-19-0120.1.

Violaine Pellichero, Jean-Baptiste Sallée, Sunke Schmidtko, Fabien Roquet, and Jean-Benoît Charrassin. The ocean mixed layer under Southern Ocean sea-ice: Seasonal cycle and forcing. *Journal of Geophysical Research: Oceans*, 122(2):1608–1633, 2017. doi: 10.1002/2016JC011970.

Violaine Pellichero, Jean-Baptiste Sallée, Christopher C Chapman, and Stephanie M Downes. The Southern Ocean meridional overturning in the sea-ice sector is driven by freshwater fluxes. *Nature communications*, 9(1):1–9, 2018.

D. Perovich and K. Jones. The seasonal evolution of sea ice floe size distribution. *Journal of Geophysical Research*, 119(12):8767–8777, 2014.

D.K. Perovich and C. Polashenski. Albedo evolution of seasonal Arctic sea ice. *Geophysical Research Letters*, 39, 2012.

D.K. Perovich et al. Thin and thinner: Sea ice mass balance measurements during SHEBA. *Journal of Geophysical Research: Oceans*, 108(C3), 2003. doi: https://doi.org/10.1029/2001JC001079.

A. Peters et al. Multiscale simulation of cardiovascular flows on the ibm blue gene/p: full heart-circulation system at near red-blood cell resolution. *Computer Physics Communications*, pages 1–10 volume = 180, comment = ,, 2009.

Algot K. Peterson, Ilker Fer, Miles G. McPhee, and Achim Randelhoff. Turbulent heat and momentum fluxes in the upper ocean under Arctic sea ice. *Journal of Geophysical Research: Oceans*, 122(2):1439–1456, 2017. ISSN 2169-9291. doi: 10.1002/2016JC012283.

Alek A. Petty, Daniel L. Feltham, and Paul R. Holland. Impact of atmospheric forcing on Antarctic continental shelf water masses. *Journal of Physical Oceanography*, 43 (5):920–940, 2013. doi: 10.1175/JPO-D-12-0172.1.

Alek A Petty, Michel C Tsamados, Nathan T Kurtz, Sinead L Farrell, Thomas Newman, Jeremy P Harbeck, Daniel L Feltham, and Jackie A Richter-Menge. Characterizing Arctic sea ice topography using high-resolution IceBridge data. *The Cryosphere*, 10 (3):1161–1179, 2016.

Felix Pithan and Thorsten Mauritsen. Arctic amplification dominated by temperature feedbacks in contemporary climate models. *Nature Geoscience*, 7(3):181–184, 2014.

Cameron J Planck, James Whitlock, Chris Polashenski, and Donald Perovich. The evolution of the seasonal ice mass balance buoy. *Cold Regions Science and Technology*, 165:102792, 2019.

R. Alan Plumb and Raffaele Ferrari. Transformed Eulerian-mean theory. Part I: Non-quasigeostrophic theory for eddies on a zonal-mean flow. *Journal of Physical Oceanography*, 35(2):165–174, 2005. doi: 10.1175/JPO-2669.1.

C. Polashenski, D. Perovich, and Z. Courville. The mechanisms of sea ice melt pond formation and evolution. *Journal of Geophysical Research*, 117, 2012.

C. Polashenski et al. Percolation blockage: A process that enables melt pond formation on first year Arctic sea ice. *Journal of Geophysical Research: Oceans*, 122(1):413–440, 2017. ISSN 2169-9291. doi: 10.1002/2016JC011994.

Igor V Polyakov, Tom P Rippeth, Ilker Fer, Matthew B Alkire, Till M Baumann, Eddy C Carmack, Randi Ingvaldsen, Vladimir V Ivanov, Markus Janout, Sigrid Lind, et al. Weakening of cold halocline layer exposes sea ice to oceanic heat in the eastern Arctic Ocean. *Journal of Climate*, 33(18):8107–8123, 2020a.

Igor V Polyakov, Tom P Rippeth, Ilker Fer, Till M Baumann, Eddy C Carmack, Vladimir V Ivanov, Markus Janout, Laurie Padman, Andrey V Pnyushkov, and

Robert Rember. Intensification of near-surface currents and shear in the Eastern Arctic Ocean. *Geophysical Research Letters*, 47(16):e2020GL089469, 2020b.

E. Post et al. Ecological consequences of sea-ice decline. *Science*, 341, 2013.

L Prandtl. über flüssigkeitsbewegung bei sehr kleiner reibung. *Intern. Math. Kongr. Heidelberg*, 3(2):484–491, 1905.

James F. Price, Robert A. Weller, and Robert Pinkel. Diurnal cycling: Observations and models of the upper ocean response to diurnal heating, cooling, and wind mixing. *Journal of Geophysical Research: Oceans*, 91(C7):8411–8427, 1986. doi: 10.1029/JC091iC07p08411.

J.F. Price, C.N.K. Mooers, and J.C. Van Leer. Observation and simulation of storm-induced mixed-layer deepening. *Journal of Physical Oceanography*, 8(4):582–599, 1978.

A Proshutinsky, RH Bourke, and FA McLaughlin. The role of the Beaufort Gyre in Arctic climate variability: Seasonal to decadal climate scales. *Geophysical Research Letters*, 29(23):15–1, 2002.

A Proshutinsky, R Krishfield, JM Toole, M-L Timmermans, W Williams, S Zimmermann, M Yamamoto-Kawai, TWK Armitage, D Dukhovskoy, E Golubeva, et al. Analysis of the Beaufort Gyre freshwater content in 2003–2018. *Journal of Geophysical Research: Oceans*, 124(12):9658–9689, 2019.

A Proshutinsky, R Krishfield, and M-L Timmermans. Introduction to special collection on Arctic Ocean modeling and observational synthesis (FAMOS) 2: Beaufort Gyre phenomenon. *Journal of Geophysical Research: Oceans*, 125(2), 2020.

Andrei Y Proshutinsky and Mark A Johnson. Two circulation regimes of the wind-driven Arctic Ocean. *Journal of Geophysical Research: Oceans*, 102(C6):12493–12514, 1997.

Andrey Proshutinsky, Richard Krishfield, and David Barber. Preface to special section on Beaufort Gyre climate system exploration studies: Documenting key parameters to understand environmental variability. *Journal of Geophysical Research: Oceans*, 114(C1), 2009a. doi: https://doi.org/10.1029/2008JC005162.

Andrey Proshutinsky, Richard Krishfield, Mary-Louise Timmermans, John Toole, Eddy Carmack, Fiona McLaughlin, William J Williams, Sarah Zimmermann, Motoyo Itoh, and Koji Shimada. Beaufort Gyre freshwater reservoir: State and variability from observations. *Journal of Geophysical Research: Oceans*, 114(C1), 2009b. doi: https://doi.org/10.1029/2008JC005104.

T Prowse, Arvid Bring, Johanna Mård, E Carmack, M Holland, A Instanes, T Vihma, and FJ Wrona. Arctic freshwater synthesis: Summary of key emerging issues. *Journal of Geophysical Research: Biogeosciences*, 120(10):1887–1893, 2015.

Timour Radko. *Double-diffusive convection*. Cambridge University Press, 2013.

Bhargav Rallabandi, Zhong Zheng, Michael Winton, and Howard A Stone. Formation of sea ice bridges in narrow straits in response to wind and water stresses. *Journal of Geophysical Research: Oceans*, 122(7):5588–5610, 2017.

Richard J Reed and William J Campbell. Theory and observations of the drift of ice station alpha. Technical report, WASHINGTON UNIV SEATTLE, 1960.

David W Rees Jones and Andrew J Wells. Frazil-ice growth rate and dynamics in mixed layers and sub-ice-shelf plumes. *The Cryosphere*, 12(1):25–38, 2018.

Heather Regan, Camille Lique, Claude Talandier, and Gianluca Meneghello. Response of total and eddy kinetic energy to the recent spinup of the Beaufort Gyre. *Journal of Physical Oceanography*, 50(3):575–594, 2020.

Emma C. Reid, Thomas M. DeCarlo, Anne L. Cohen, George T. F. Wong, Steven J. Lentz, Aryan Safaie, Austin Hall, and Kristen A. Davis. Internal waves influence the thermal and nutrient environment on a shallow coral reef. *Limnology and Oceanography*, 64(5):1949–1965, 2019. doi: https://doi.org/10.1002/lno.11162.

Tom P Rippeth, Ben J Lincoln, Yueng-Djern Lenn, JA Mattias Green, Arild Sundfjord, and Sheldon Bacon. Tide-mediated warming of Arctic halocline by Atlantic heat fluxes over rough topography. *Nature Geoscience*, 8(3):191–194, 2015.

Stephen C Riser, Howard J Freeland, Dean Roemmich, Susan Wijffels, Ariel Troisi, Mathieu Belbéoch, Denis Gilbert, Jianping Xu, Sylvie Pouliquen, Ann Thresher, et al. Fifteen years of ocean observations with the global argo array. *Nature Climate Change*, 6(2):145–153, 2016.

Stephen C Riser, Dana Swift, and Robert Drucker. Profiling floats in soccom: Technical capabilities for studying the southern ocean. *Journal of Geophysical Research: Oceans*, 123(6):4055–4073, 2018a.

Stephen C. Riser, Dana Swift, and Robert Drucker. Profiling floats in soccom: Technical capabilities for studying the southern ocean. *Journal of Geophysical Research: Oceans*, 123(6):4055–4073, 2018b. doi: https://doi.org/10.1002/2017JC013419. URL `https://agupubs.onlinelibrary.wiley.com/doi/abs/10.1002/2017JC013419`.

Lettie A Roach, Jakob Dörr, Caroline R Holmes, François Massonnet, Edward W Blockley, Dirk Notz, Thomas Rackow, Marilyn N Raphael, Siobhan P O'Farrell, David A Bailey, et al. Antarctic sea ice area in CMIP6. *Geophysical Research Letters*, 47(9): e2019GL086729, 2020.

Andrew F Roberts, Elizabeth C Hunke, Samy M Kamal, William H Lipscomb, Christopher Horvat, and Wieslaw Maslowski. A variational method for sea ice ridging in Earth system models. *Journal of Advances in Modeling Earth Systems*, 11(3):771–805, 2019.

Fabien Roquet, Carl Wunsch, Gael Forget, Patrick Heimbach, Christophe Guinet, Gilles Reverdin, Jean-Benoit Charrassin, Frederic Bailleul, Daniel P Costa, Luis A Huckstadt, et al. Estimates of the Southern Ocean general circulation improved by animal-borne instruments. *Geophysical Research Letters*, 40(23):6176–6180, 2013.

DA Rothrock. The pressure term in the constitutive law of an ice pack. *AIDJEX Bull*, 2:28–32, 1970.

DA Rothrock and AS Thorndike. Geometric properties of the underside of sea ice. *Journal of Geophysical Research: Oceans*, 85(C7):3955–3963, 1980.

Drew A Rothrock. The energetics of the plastic deformation of pack ice by ridging. *Journal of Geophysical Research*, 80(33):4514–4519, 1975.

David Roylance. Engineering viscoelasticity. *Department of Materials Science and Engineering–Massachusetts Institute of Technology, Cambridge MA*, 2139:1–37, 2001.

B. Rudels, L.G. Anderson, and E.P. Jones. Formation and evolution of the surface mixed layer and halocline of the Arctic Ocean. *Journal of Geophysical Research: Oceans*, 101(C4):8807–8821, 1996.

MI Ruzin. The wind drift of ice in a heterogeneous pressure field. *Tr. Arkt. Antartkt. Inst*, 226:123–35, 1959.

Benjamin T. Saenz and Kevin R. Arrigo. Annual primary production in Antarctic sea ice during 2005–2006 from a sea ice state estimate. *Journal of Geophysical Research: Oceans*, 119(6):3645–3678, 2014. doi: 10.1002/2013JC009677.

J.-B. Sallée et al. Assessment of Southern Ocean water mass circulation and characteristics in CMIP5 models: Historical bias and forcing response. *Journal of Geophysical Research: Oceans*, 118(4):1830–1844, 2013.

Jean-Baptiste Sallée, Kevin Speer, Steve Rintoul, and Susan Wijffels. Southern Ocean thermocline ventilation. *Journal of Physical Oceanography*, 40(3):509–529, 2010.

M. Schäfer et al. Benchmark computations of laminar flow around a cylinder. In *Flow simulation with high-performance computers II*, pages 547–566. Springer, 1996.

Hermann Schlichting and Klaus Gersten. *Boundary-layer theory*. Springer, 2016.

Gavin A. Schmidt, Cecilia M. Bitz, Uwe Mikolajewicz, and L.-Bruno Tremblay. Ice–ocean boundary conditions for coupled models. *Ocean Modelling*, 7(1):59–74, 2004a. ISSN 1463-5003. doi: https://doi.org/10.1016/S1463-5003(03)00030-1.

Gavin A Schmidt, Cecilia M Bitz, Uwe Mikolajewicz, and L-Bruno Tremblay. Ice–ocean boundary conditions for coupled models. *Ocean Modelling*, 7(1-2):59–74, 2004b.

Christian Schoof and Ian Hewitt. Ice-sheet dynamics. *Annual Review of Fluid Mechanics*, 45:217–239, 2013.

C. Schultz, S. C. Doney, W. G. Zhang, H. Regan, P. Holland, M. P. Meredith, and S. Stammerjohn. Modeling of the influence of sea ice cycle and Langmuir circulation on the upper ocean mixed layer depth and freshwater distribution at the West Antarctic peninsula. *Journal of Geophysical Research: Oceans*, 125(8):e2020JC016109, 2020. doi: https://doi.org/10.1029/2020JC016109.

A.J. Semtner. A model for the thermodynamic growth of sea ice in numerical investigations of climate. *Journal of Physical of Oceanography*, 379:379 – 389, 1976.

Jaemyeong Mango Seo, Jong-Jin Baik, and Hye-Yeong Chun. Theoretical investigation of nonhydrostatic effects on convectively forced flows: Propagating and evanescent gravity-wave modes. *Physics of Fluids*, 30(12):126604, 2018.

Mark C Serreze and Andrew P Barrett. Characteristics of the Beaufort Sea high. *Journal of Climate*, 24(1):159–182, 2011.

MC Serreze, AP Barrett, JC Stroeve, DN Kindig, and MM Holland. The emergence of surface-based Arctic amplification. *The Cryosphere*, 3(1):11, 2009.

M.H. Sharqawy, J.H. Lienhard, and S.M. Zubair. Thermophysical properties of seawater: a review of existing correlations and data. *Desalination and Water Treatment*, 16(1-3):354–380, 2010.

NC Shibley, M-L Timmermans, JR Carpenter, and JM Toole. Spatial variability of the Arctic Ocean's double-diffusive staircase. *Journal of Geophysical Research: Oceans*, 122(2):980–994, 2017.

Kunio Shirasawa and R Grant Ingram. Characteristics of the turbulent oceanic boundary layer under sea ice. Part 1: A review of the ice-ocean boundary layer. *Journal of Marine Systems*, 2(1-2):153–160, 1991.

Anirban Sinha and Ryan P Abernathey. Time scales of Southern Ocean eddy equilibration. *Journal of Physical Oceanography*, 46(9):2785–2805, 2016.

A. Sirevaag. Turbulent exchange coefficients for the ice/ocean interface in case of rapid melting. *Geophysical Research Letters*, 36(4), 2009. doi: https://doi.org/10.1029/2008GL036587.

E.D. Skyllingstad et al. Effects of keels on ice bottom turbulence exchange. *Journal of Geophysical Research: Oceans*, 108(C12), 2003. doi: https://doi.org/10.1029/2002JC001488.

Thomas Slater, Isobel R Lawrence, Inès N Otosaka, Andrew Shepherd, Noel Gourmelen, Livia Jakob, Paul Tepes, Lin Gilbert, and Peter Nienow. Earth's ice imbalance. *The Cryosphere*, 15(1):233–246, 2021.

K Shafer Smith and John Marshall. Evidence for enhanced eddy mixing at middepth in the Southern Ocean. *Journal of Physical Oceanography*, 39(1):50–69, 2009.

S. Smith et al. Polynyas and leads: An overview of physical processes and environment. *Journal of Geophysical Research: Oceans*, 95(C6):9461–9479, 1990.

H Solomon. A study of ice dynamics relevant to AIDJEX. *AIDJEX Bull*, 2(33-50), 1970.

Kevin Speer, Stephen R Rintoul, and Bernadette Sloyan. The diabatic Deacon cell. *Journal of Physical Oceanography*, 30(12):3212–3222, 2000.

G. Spreen, L. Kaleschke, and G. Heygster. Sea ice remote sensing using AMSR-E 89-GHz channels. *Journal of Geophysical Research: Oceans*, 113(C2), 2008. doi: 10.1029/2005JC003384.

T. Stanton et al. Observational study of relationships between incoming radiation, open water fraction, and ocean-to-ice heat flux in the transpolar drift: 2002–2010. *Journal of Geophysical Research*, 117, 2012.

Michael Steele. Sea ice melting and floe geometry in a simple ice-ocean model. *Journal of Geophysical Research: Oceans*, 97(C11):17729–17738, 1992. doi: 10.1029/92JC01755.

Joël Stein. Investigation of the regime diagram of hydrostatic flow over a mountain with a primitive equation model. Part I: Two-dimensional flows. *Monthly weather review*, 120(12):2962–2976, 1992.

Nadja Steiner, Markus Harder, and Peter Lemke. Sea-ice roughness and drag coefficients in a dynamic–thermodynamic sea-ice model for the Arctic. *Tellus A*, 51(5):964–978, 1999.

Gilbert Strang, Gilbert Strang, Gilbert Strang, and Gilbert Strang. *Introduction to linear algebra*, volume 3. Wellesley-Cambridge Press Wellesley, MA, 1993.

J.C. Stroeve, J.E. Box, and T. Haran. Evaluation of the MODIS (MOD10A1) daily snow albedo product over the Greenland ice sheet. *Remote Sensing of Environment*, 105(2):155–171, 2006.

S. Succi. The lattice Boltzmann equation: For fluid dynamics and beyond. 2001.

Shantong Sun and Ian Eisenman. Observed Antarctic sea ice expansion reproduced in a climate model after correcting biases in sea ice drift velocity. *Nature communications*, 12(1):1–6, 2021.

Bruce R Sutherland, Stuart B Dalziel, Graham O Hughes, and PF Linden. Visualization and measurement of internal waves by 'synthetic schlieren'. Part 1. vertically oscillating cylinder. *Journal of fluid mechanics*, 390:93–126, 1999.

G. Sutherland, B. Ward, and K.H. Christensen. Wave-turbulence scaling in the ocean mixed layer. *Ocean Science*, 9(4):597, 2013.

Sebastiaan Swart, Sarah T. Gille, Bruno Delille, Simon Josey, Matthew Mazloff, Louise Newman, Andrew F. Thompson, Jim Thomson, Brian Ward, Marcel D. du Plessis, Elizabeth C. Kent, James Girton, Luke Gregor, Petra Heil, Patrick Hyder, Luciano Ponzi Pezzi, Ronald Buss de Souza, Veronica Tamsitt, Robert A. Weller, and Christopher J. Zappa. Constraining Southern Ocean air-sea-ice fluxes through enhanced observations. *Frontiers in Marine Science*, 6:421, 2019. ISSN 2296-7745. doi: 10.3389/fmars.2019.00421.

Atusi Tani. On the first initial-boundary value problem of compressible viscous fluid motion. *Publications of the Research Institute for Mathematical Sciences*, 13(1):193–253, 1977a.

Itiro Tani. History of boundary layer theory. *Annual review of fluid mechanics*, 9(1): 87–111, 1977b.

Geoffrey Ingram Taylor. Effect of variation in density on the stability of superposed streams of fluid. *Proc. R. Soc. Lond. A*, 132(820):499–523, 1931.

P.D. Taylor and D.L. Feltham. A model of melt pond evolution on sea ice. *Journal of Geophysical Ressearch*, 109, 2004.

P.K. Taylor. Heat and momentum fluxes at the sea surface. In S.A. Thorpe, editor, *Encyclopedia of Ocean Sciences: Elements of Physical Oceanography*, pages 127–134. Elsevier, 2 edition, 2009.

MAC Teixeira and Jose L Argain. The dependence of mountain wave reflection on the abruptness of atmospheric profile variations. *Quarterly Journal of the Royal Meteorological Society*, 146(729):1685–1701, 2020.

Miguel A. C. Teixeira. The physics of orographic gravity wave drag. *Frontiers in Physics*, 2:43, 2014. ISSN 2296-424X. doi: 10.3389/fphy.2014.00043.

Miguel AC Teixeira and Chau Lam Yu. The gravity wave momentum flux in hydrostatic flow with directional shear over elliptical mountains. *European Journal of Mechanics-B/Fluids*, 47:16–31, 2014.

D. Thomas and G Dieckmann. Sea ice. 2010.

Alan S Thorndike, Drew A Rothrock, Gary A Maykut, and Roger Colony. The thickness distribution of sea ice. *Journal of Geophysical Research*, 80(33):4501–4513, 1975.

S.A. Thorpe. Langmuir circulation. *Annu. Rev. Fluid Mech.*, 36:55–79, 2004.

G.W. Timco and W.F. Weeks. A review of the engineering properties of sea ice. *Cold Regions Science and Technology*, 60:107–129, 2010.

M-L Timmermans, Andrey Proshutinsky, Richard A Krishfield, Donald K Perovich, Jackie A Richter-Menge, Timothy P Stanton, and John M Toole. Surface freshening in the Arctic Ocean's Eurasian Basin: An apparent consequence of recent change in the wind-driven circulation. *Journal of Geophysical Research: Oceans*, 116(C8), 2011. doi: https://doi.org/10.1029/2011JC006975.

M.-L. Timmermans et al. Ice-Tethered Profiler observations of the double-diffusive staircase in the Canada Basin thermocline. *Journal of Geophysical Research*, 113, 2008. doi: https://doi.org/10.1029/2008JC004829.

Mary-Louise Timmermans and John Marshall. Understanding Arctic Ocean circulation: A review of ocean dynamics in a changing climate. *Journal of Geophysical Research: Oceans*, 125(4):e2018JC014378, 2020.

J.M. Toole et al. Influences of the ocean surface mixed layer and thermohaline stratification on Arctic sea ice in the central canada basin. *Journal of Geophysical Research*, 115, 2010.

John M Toole, Richard A Krishfield, Mary-Louise Timmermans, and Andrey Proshutinsky. The ice-tethered profiler: Argo of the arctic. *Oceanography*, 24(3):126–135, 2011.

Srikanth Toppaladoddi and John S Wettlaufer. Statistical mechanics and the climatology of the Arctic sea ice thickness distribution. *Journal of statistical physics*, 167 (3-4):683–702, 2017.

Srikanth Toppaladoddi, Sauro Succi, and John S Wettlaufer. Tailoring boundary geometry to optimize heat transport in turbulent convection. *EPL (Europhysics Letters)*, 111(4):44005, 2015.

Takahiro Toyoda, Nariaki Hirose, L Shogo Urakawa, Hiroyuki Tsujino, Hideyuki Nakano, Norihisa Usui, Yosuke Fujii, Kei Sakamoto, and Goro Yamanaka. Effects of inclusion of adjoint sea ice rheology on backward sensitivity evolution examined using an adjoint ocean–sea ice model. *Monthly Weather Review*, 147(6):2145–2162, 2019.

Anne M Treasure, Fabien Roquet, Isabelle J Ansorge, Marthán N Bester, Lars Boehme, Horst Bornemann, Jean-Benoit Charrassin, Damien Chevallier, Daniel P Costa, Mike A Fedak, et al. Marine mammals exploring the oceans pole to pole: a review of the meop consortium. *Oceanography*, 30(2):132–138, 2017.

L Bruno Tremblay and LA Mysak. Modeling sea ice as a granular material, including the dilatancy effect. *Journal of Physical Oceanography*, 27(11):2342–2360, 1997.

David S Trossman, Brian K Arbic, James G Richman, Stephen T Garner, Steven R Jayne, and Alan J Wallcraft. Impact of topographic internal lee wave drag on an eddying global ocean model. *Ocean Modelling*, 97:109–128, 2016.

Michel Tsamados, Daniel L. Feltham, David Schroeder, Daniela Flocco, Sinead L. Farrell, Nathan Kurtz, Seymour W. Laxon, and Sheldon Bacon. Impact of variable atmospheric and oceanic form drag on simulations of Arctic sea ice. *Journal of Physical Oceanography*, 44(5):1329–1353, 2014. doi: 10.1175/JPO-D-13-0215.1.

Michel Tsamados, Daniel Feltham, Alek Petty, David Schroeder, and Daniela Flocco. Processes controlling surface, bottom and lateral melt of Arctic sea ice in a state of the art sea ice model. *Philosophical Transactions of the Royal Society A: Mathematical, Physical and Engineering Sciences*, 373(2052):20140167, 2015. doi: 10.1098/rsta.2014.0167.

John Turner, Thomas J. Bracegirdle, Tony Phillips, Gareth J. Marshall, and J. Scott Hosking. An initial assessment of Antarctic sea ice extent in the CMIP5 models. *Journal of Climate*, 26(5):1473–1484, 2013. doi: 10.1175/JCLI-D-12-00068.1.

Ices Unesco and IAPSO SCOR. Background papers and supporting data on the international equation of state of seawater 1980, 1981.

G.K. Vallis. *Atmospheric and oceanic fluid dynamics*. Cambridge University Press, 2017.

Luke Van Roekel, Alistair J Adcroft, Gokhan Danabasoglu, Stephen M Griffies, Brian Kauffman, William Large, Michael Levy, Brandon G Reichl, Todd Ringler, and Martin Schmidt. The KPP boundary layer scheme for the ocean: Revisiting its formulation and benchmarking one-dimensional simulations relative to LES. *Journal of Advances in Modeling Earth Systems*, 10(11):2647–2685, 2018.

Dominic Vella and JS Wettlaufer. Explaining the patterns formed by ice floe interactions. *Journal of Geophysical Research: Oceans*, 113(C11), 2008. doi: https://doi.org/10.1029/2008JC004781.

Timo Vihma. Effects of Arctic sea ice decline on weather and climate: A review. *Surveys in Geophysics*, 35(5):1175–1214, 2014.

Luisa von Albedyll, Christian Haas, and Wolfgang Dierking. Linking sea ice deformation to ice thickness redistribution using high-resolution satellite and airborne observations. *The Cryosphere Discussions*, pages 1–33, 2020.

P. Wadhams and N.R. Davis. Further evidence of ice thinning in the Arctic Ocean. *Geophysical Research Letters*, 27(24):3973–3975, 2000.

P. Wadhams et al. Changing characteristics of Arctic pressure ridges. *Polar Science*, 6 (1):71–77, 2012.

Peter Wadhams. *The Seasonal Ice Zone*, pages 825–991. Springer US, Boston, MA, 1986. doi: 10.1007/978-1-4899-5352-$0_1$5.

Gosta Walin. On the relation between sea-surface heat flow and thermal circulation in the ocean. *Tellus*, 34(2):187–195, 1982. doi: https://doi.org/10.1111/j.2153-3490.1982.tb01806.x.

Qiang Wang, Claudia Wekerle, Sergey Danilov, Nikolay Koldunov, Dmitry Sidorenko, Dmitry Sein, Benjamin Rabe, and Thomas Jung. Arctic sea ice decline significantly contributed to the unprecedented liquid freshwater accumulation in the Beaufort Gyre of the Arctic Ocean. *Geophysical Research Letters*, 45(10):4956–4964, 2018.

Qiang Wang, John Marshall, Jeffery Scott, Gianluca Meneghello, Sergey Danilov, and Thomas Jung. On the feedback of ice–ocean stress coupling from geostrophic currents in an anticyclonic wind regime over the Beaufort Gyre. *Journal of Physical Oceanography*, 49(2):369–383, 2019a.

Qiang Wang, Claudia Wekerle, Sergey Danilov, Dmitry Sidorenko, Nikolay Koldunov, Dmitry Sein, Benjamin Rabe, and Thomas Jung. Recent sea ice decline did not

significantly increase the total liquid freshwater content of the Arctic Ocean. *Journal of Climate*, 32(1):15–32, 2019b.

George Neville Watson. *A treatise on the theory of Bessel functions*. Cambridge university press, 1995.

W.F. Weeks. *On Sea Ice*. University of Alaska Press, 2010.

Alexander V Wilchinsky and Daniel L Feltham. Anisotropic model for granulated sea ice dynamics. *Journal of the Mechanics and Physics of Solids*, 54(6):1147–1185, 2006.

G.D. Williams et al. The suppression of Antarctic Bottom Water formation by melting ice shelves in Prydz Bay. *Nature Communications*, 7, 2016. doi: 10.1038/ncomms12577.

Earle A. Wilson, Stephen C. Riser, Ethan C. Campbell, and Annie P. S. Wong. Winter upper-ocean stability and ice–ocean feedbacks in the sea ice–covered Southern Ocean. *Journal of Physical Oceanography*, 49(4):1099–1117, 2019. doi: 10.1175/JPO-D-18-0184.1.

Kraig B Winters. The turbulent transition of a supercritical downslope flow: sensitivity to downstream conditions. *Journal of Fluid Mechanics*, 792:997, 2016.

Kraig B Winters and Laurence Armi. Hydraulic control of continuously stratified flow over an obstacle. *Journal of fluid mechanics*, 700:502, 2012.

Anthony P. Worby, Cathleen A. Geiger, Matthew J. Paget, Michael L. Van Woert, Stephen F. Ackley, and Tracy L. DeLiberty. Thickness distribution of antarctic sea ice. *Journal of Geophysical Research: Oceans*, 113(C5), 2008. doi: https://doi.org/10.1029/2007JC004254.

M Grae Worster and David W Rees Jones. Sea-ice thermodynamics and brine drainage. *Philosophical Transactions of the Royal Society A: Mathematical, Physical and Engineering Sciences*, 373(2045):20140166, 2015.

MG Wurtele, RD Sharman, and TL Keller. Analysis and simulations of a troposphere–stratosphere gravity wave model. Part I. *Journal of Atmospheric Sciences*, 44(21): 3269–3281, 1987.

Xin Xu, Yuan Wang, and Ming Xue. Momentum flux and flux divergence of gravity waves in directional shear flows over three-dimensional mountains. *Journal of the Atmospheric Sciences*, 69(12):3733–3744, 2012.

M Yamamoto-Kawai, FA McLaughlin, EC Carmack, S Nishino, and K Shimada. Freshwater budget of the Canada Basin, Arctic Ocean, from salinity, δ180,

and nutrients. *Journal of Geophysical Research: Oceans*, 113(C1), 2008. doi: https://doi.org/10.1029/2006JC003858.

M Yamamoto-Kawai, FA McLaughlin, EC Carmack, S Nishino, K Shimada, and N Kurita. Surface freshening of the Canada Basin, 2003–2007: River runoff versus sea ice meltwater. *Journal of Geophysical Research: Oceans*, 114(C1), 2009. doi: https://doi.org/10.1029/2008JC005000.

Michiyo Yamamoto-Kawai, Noriyuki Tanaka, and Sergey Pivovarov. Freshwater and brine behaviors in the Arctic Ocean deduced from historical data of δ180 and alkalinity (1929–2002 ad). *Journal of Geophysical Research: Oceans*, 110(C10), 2005. doi: https://doi.org/10.1029/2004JC002793.

J. Zhang et al. Sea ice floe size distribution in the marginal ice zone: Theory and numerical experiments. *Journal of Geophysical research: Oceans*, 120, 2015.

Jinlun Zhang. Sea ice properties in high-resolution sea ice models. *Journal of Geophysical Research: Oceans*, 126(1):e2020JC016686, 2021.

Likun Zhang, Maarten C. Buijsman, Eva Comino, and Harry L. Swinney. Internal wave generation by tidal flow over periodically and randomly distributed seamounts. *Journal of Geophysical Research: Oceans*, 122(6):5063–5074, 2017. doi: https://doi.org/10.1002/2017JC012884.

Wenli Zhong, Michael Steele, Jinlun Zhang, and Jinping Zhao. Greater role of geostrophic currents in Ekman dynamics in the western Arctic ocean as a mechanism for Beaufort gyre stabilization. *Journal of Geophysical Research: Oceans*, 123 (1):149–165, 2018.

S. Zippel and J. Thomson. Air-sea interactions in the marginal ice zone. *Elem Sci Anth*, 4, 2016. doi: 10.12952/journal.elementa.000095.

Q. Zou and X. He. On pressure and velocity boundary conditions for the lattice Boltzmann BGK model. *Phys, Fluids*, 9:1591–1598, 1997.